



UNIVERSITY OF
BIRMINGHAM

The effect of turbulence in the built environment on wind turbine aerodynamics

Giulio Vita

Ph.D. Dissertation
in Wind Engineering

Supervisors:

Dr Hassan Hemida

Prof Charalambos C. Baniotopoulos

School of Engineering
Department of Civil Engineering
University of Birmingham
United Kingdom

UNIVERSITY OF
BIRMINGHAM

University of Birmingham Research Archive

e-theses repository

This unpublished thesis/dissertation is copyright of the author and/or third parties. The intellectual property rights of the author or third parties in respect of this work are as defined by The Copyright Designs and Patents Act 1988 or as modified by any successor legislation.

Any use made of information contained in this thesis/dissertation must be in accordance with that legislation and must be properly acknowledged. Further distribution or reproduction in any format is prohibited without the permission of the copyright holder.

A Nora e al nostro 'Fagiolino'

To Nora and our 'tiny Bean'

‘Σκίδνησι καὶ πάλιν συνάγει καὶ πρόσεισι καὶ ἄπεισι.’

{fresh waters are ever flowing in upon you}

Ἡράκλειτος, DK 91a

‘Cu semina ventu arricùogghi timpesta’

{Sow the wind and reap the whirlwind}

Sicilian saying

‘置かれた場所で咲きなさい’

{Okareta basho de sakinasai - Bloom where God has planted you}

Japanese saying

Acknowledgments

Writing the acknowledgements of this work is like having a refreshing sorbet after a huge meal: it allows one to savour with the mind the accomplished endeavour and bid farewell.

This Ph.D. done in conjunction with the Project “Aeolus4future” has not only provided me with the knowledge of conducting and evaluating research, even less understanding turbulent flows. It has allowed me to grow greatly as a man, cherishing and treasuring my achievements to aim even higher in life. To have the honour to befriend and be part of the life of fantastic people. To travel across Europe and feel always at home and welcome. To have collected memories to treasure and share to children and grandchildren. To build a prosperous life in a city which I now consider my third home.

My first thought goes to the European Commission. Projects like the H2020 Framework and the Marie Skłodowska-Curie Actions allow many young professionals like me to start building their lives, while studying for their Ph.D. or working at the university, without having to pause it to follow their passions.

A huge thank goes to Prof Claudio Borri, who has mentored me during my university studies and has convinced me not without effort to apply for this position. I wish for us a fruitful relation in the near future. A special thank goes also to Dr Hassan Hemida and Prof Lambis Baniotopoulos. Thank you both, for your patience, your teachings, your thoughts, your help making me a better person and better researcher. You made me feel at home even when home seemed very far.

I also thank Prof Mark Sterling, Prof Chris Baker, Dr Mike Jesson, and Dr Andrew Quinn for allowing me to work on the EPSRC Project ‘Urban Winds’. Thanks to the other CIs for their support in showing me how to do real research: Drs Genora Joseph, David Soper, Zhenru Shu, and Mingzhe He.

I also thank Dr Thomas Andrienne, Dr Ashvinkumar Chaudhari, Prof Bert Blocken, Dr Enzo Marino, Dr Claudio Mannini for welcoming me as a visiting researcher at their wind tunnel and computational labs at the University of Liège (BE), the Lappeenranta University of Technology (FI) and the University of Florence (IT). I have expanded my academic horizons in ways I could not imagine.

Thanks from the heart to my ‘Aeolus4future’ family! Best ever representative Slobodanka. Cheerful Agota. Funny Mirjana. Popular Ana. Obnoxious Gonçalo. Attractive Gabriel. Genius Rahim. Neapolitan Milan. Singer MohammadReza. Party animal Andreu. Professional Ali. Second to last my

Acknowledgments

thoughts go to Cansev, for our interminable openFOAM and openHEART Skype sessions. Last and most certainly not least my love goes to Rana, matchless travel partner, considerate and caring friend, acquired member of the family. You have all been vital to this achievement: Hope we keep in touch! Heartfelt thanks to my University of Birmingham family, the bestest Civil Engineering Department ever. To the friendships from the first days, Michaela, Danial, Simon, and Nick. To the more recent friendships, Anam, Carlo, Nina, Koohyar, Zhuang, Panos, Nour: thanks guys to make my time every day! To Ryan and the WES escapes to London! To Bruño and how to be amazing at CFD and fabada! To Rachel and how to be super British and super wholehearted. To Nafsika and how to properly holidaying and complaining. To Rafael and how to ‘What are you talking about’? To Steffi, professor of laughter, tornadoes, and friendship! To my boyfriend Fred, for the awesome food, the travelling, fast cars and all the love! Big thanks also to the Marie Curie Association and the Lunch at Staff House proud components: Federica, Marco, Jorge, Andrea, Gianluca, Ceren, Paula, Zanna, Eduardo.

My thoughts and prayers go to Alice and Simone, and their wonderful family. I will always bring with me all the happy memories and warmth of your friendship: siete nel mio cuore e ci vediamo presto!

Thanks to all my other friends in Birmingham (luckily, you have quite piled up over the years). Although you spend most of your time (seriously?) in Cadbury, Arup, WSP or RWDI, you are always up to hang out! You are all in my thoughts, too many too be listed here but so easy to rely on!

A special thank goes also to my best men retard Gabriele and stinky Gianmarco, to my partner of old days Gabriele B., and to my beloved friends: Nik, Irene, Ginevra, Chiara, Niccolò, Luca, Nadia & Cate.

I am most grateful to my family, for you have taught me how to value tough work, commitment and myself. Senza di voi, il vostro amore incondizionato, la vostra infinita pazienza, la vostra stima e supporto, non sarei arrivato a concludere questo lavoro e a mirare in alto come mi avete mostrato voi.

Grazie Mamma, Papá, Noemi e Valerio.

But all what is written in these pages I owe to my wonderful wife Nora. Together we have managed to do everything in our full-optional life. We’ve gone through a lot and we’ll keep going through a lot. To her and to our miracle of a daughter I dedicate this work. I look forward to closing this PhD chapter to embark in a truly new adventure always with you, my love. Ti amo!

Grazie di cuore a tutti voi!

Abstract

Urban Wind Energy is a niche of Wind Energy showing an unstoppable trend of growth in its share in the tumultuous DIY energy market. Urban Wind Energy consists of positioning wind turbines within the built environment. The idea is to match energy production and consumption site so to increase the efficiency of the system as energy losses and costs due to the transportation, conversion and delivery of energy are virtually zeroed. Many aficionados advocate the advantage of such a technology for the environment and argue that a greater diffusion might overcome its flaws as a newborn technology.

However, no urban wind application to date is known to have been successful in providing but a derisory amount of 'clean' energy. The reason for this fiasco lies in the way research in urban wind energy is conducted, i.e. mostly concerned either in improving the efficiency of wind energy converters, or the assessment of the available wind resource. Very few works have considered the technical implications of placing a wind energy converter, one of the most complex aerodynamic devices, in a complex inflow such as that found in built environments, of which very little is known in terms of its turbulence environment. In fact, it has long been acknowledged that the power output, the fatigue limit state or the total service-life downtime of a wind turbine is well correlated with turbulence at the inflow.

This thesis provides a different perspective in tackling this problem by dissecting the issue in its fundamental components. The paucity of results on the interaction of a turbulent inflow with an aerodynamic device, i.e. between a turbulent flow as measurable in a windy position within the built environment and wind turbine aerodynamics, prompts to ask what is the fundamental reason for the lack of results and the assumption that turbulence can be well neglected when designing a traditional wind turbine rotor. The answer to this question is the difficulty in providing a suitable turbulent inlet in experimental and numerical simulations, which is representative of an atmospheric turbulent flow. This means most of the time dealing with flows having turbulence intensities of up to $\sim 25\%$ combined with a variable integral length scale of $\sim 20-250$ m, depending on the location of interest. If a traditional urban horizontal axis wind turbine is considered, e.g. having a power of $\sim 1-20$ kW, this translates into a diameter of $\sim 5-10$ m, which in turn implies a wind turbine aerofoil of $\sim 0.1-1$ m, i.e. at least one order

of magnitude smaller than the integral length scale. Such ratios are virtually impossible to test in traditional wind tunnel experiments.

The present Ph.D. research is therefore motivated by the necessity of finding a methodology to replicate this kind of flow and test it on a model wind turbine aerofoil to understand the aerodynamic implications of placing a wind turbine in the built environment.

Results presented in this thesis are divided into two main parts, resembling the twofold nature of this problem.

In the first part (Part II in the following), the capability of both wind tunnel testing and numerical modelling is tested towards the prediction of turbulence found in suitable locations across the built environment, both idealised or realistic. Results show indeed how turbulence intensity is significant even at considerable height above high-rise buildings in an urban context.

In the second part (Part III in the following), a model wind turbine aerofoil is placed in a turbulent flow resembling the characteristics as found in the built environment, which translates to a ratio between the integral length scale and the characteristic size of the body of ~ 3 . This value is close to a possible configuration in the built environment. Results show that indeed an effect of turbulence on the aerodynamic performance of the wind turbine aerofoil is present even at the largest integral length scales, confuting the diffused opinion that turbulence effects can be neglected for large integral length scales, i.e. assuming *a priori* that the high-frequency energy of a large scale turbulent flow is not able to interact with the boundary and shear layer of a bluff body, such as is a stalled wind turbine aerofoil. Results also confirm that numerical simulations, i.e. Large Eddy Simulation, is well mature and capable of reproducing a wide range of turbulence statistics as found in the urban environment. Indeed its performance against full-scale data has been found competing if not superior to traditional wind tunnel testing when the flow pattern in the built environment is investigated.

A methodological framework is proposed in the conclusions of this work to integrate both experimental and numerical methodologies to overcome each other limitations.

Contents

Acknowledgments.....	7
Abstract.....	9
Contents	11
Figures.....	15
Chapter 1 Introduction	21
1.1. Motivation for research.....	21
1.2. Aim of research and objectives.....	27
1.3. Limitations of the research.....	28
1.4. Thesis Outline	29
Chapter 2 Literature and Methodology Background	31
2.1. Wind Energy research trends	31
2.2. Urban Wind Energy Research.....	36
2.2.1. Urban Wind and Turbulence.....	41
2.2.2. Urban Wind Turbines.....	48
2.3. Background on research methodology.....	60
2.3.1. Full Scale Tests	60
2.3.2. Wind Tunnel Testing	61
2.3.3. Computational Fluid Dynamics	61
2.4. Research gap	64
2.5. Back-to-Basics: a novel methodology for urban wind energy research.....	66
2.5.1. Scaling Wind Turbine and Wind Resource.....	66
2.5.1. An integrated experimental-numerical methodology.....	69
Chapter 3 Generating large length scale turbulence using passive grids in wind tunnel.....	71
3.1. Grid turbulence generation in wind tunnel testing.....	72
3.2. Methodology	76

3.2.1.	Experimental setup.....	76
3.2.2.	Design of Passive Grids	77
3.2.3.	Calculation of statistics	80
3.3.	Results and discussion	82
3.3.1.	Turbulence Decay	83
3.3.2.	Isotropy	88
3.3.3.	Gaussianity.....	91
3.3.4.	Independently varied statistics	93
3.4.	Conclusions.....	99
Chapter 4 Turbulence environment over a typical high-rise building.....		101
4.1.	Urban Wind Energy, High rise Buildings and the built environment.....	102
4.2.	Methodology	108
4.2.1.	Experimental Setup at Ruhr Universität Bochum.....	108
4.2.2.	Numerical setup	110
4.3.	Results.....	111
4.3.1.	Experimental validation testcase.....	111
4.3.2.	Numerical flow pattern	115
4.3.3.	RANS and LES results.....	117
4.4.	Discussion and Conclusion	124
Chapter 5 Turbulence Environment around high-rise buildings in the University of Birmingham Campus		127
5.1.	Numerical simulation of realistic built environments.....	128
5.2.	Background.....	135
5.2.1.	Physical Simulation.....	136
5.2.2.	Numerical Simulation	137
5.3.	Methodology	138
5.3.1.	Full Scale Validation test-case.....	139

5.3.2.	Physical Simulation.....	140
5.3.3.	Numerical Simulation	143
5.3.4.	Processing of fluctuating wind speed data	150
5.4.	Pedestrian Level Wind Results	151
5.5.	Rooftop level wind results	154
5.6.	Discussion and Conclusions.....	160
Chapter 6 The effect of integral length scale of turbulence on a wind turbine aerofoil		163
6.1.	Effect of turbulence on bluff bodies and wind energy converters	164
6.1.1.	Motivation (background wind energy deals with turbulence)	164
6.1.2.	Effect of turbulence on bluff bodies.....	165
6.1.3.	Effect of turbulence on wind turbine aerofoils	167
6.2.	Methodology	169
6.2.1.	Experimental setup: the DU96w180 aerofoil model.....	169
6.2.1.	Experimental setup: the inflow	171
6.2.2.	Statistical Moments and Proper orthogonal decomposition.....	174
6.3.	Results: Reynolds effects and stall mechanism	176
6.4.	Undisturbed case.....	177
6.5.	Effect of turbulence in attached flow conditions	179
6.6.	Effect of turbulence intensity on surface pressure	180
6.6.1.	Small length scale $L_w/c < 0.6$	180
6.6.2.	Length scale close to chord length $0.8 < L_w/c < 1.4$	180
6.6.1.	Large Length Scale $L_w > 2.6$	183
6.7.	Effect of integral length scale on surface pressure.....	185
6.7.1.	Low Turbulence Intensity $I_u < 5\%$ (LS1).....	186
6.7.2.	Medium Turbulence Intensity $7 < I_u < 10\%$	187
6.7.3.	High Turbulence Intensity $I_u > 14\%$	188
6.8.	Separation point position	189

6.9. Force coefficients.....	190
6.9.1. Post-stall $\alpha=14$ deg.....	191
6.9.2. Full-stall $\alpha=24$ deg.....	192
6.10. Proper Orthogonal Decomposition	194
6.11. Conclusions.....	197
Chapter 7 The effect of large integral length scale of turbulence on a wind turbine aerofoil using LES.....	199
7.1. Generation of inlet turbulence in Large Eddy Simulation	200
7.2. Methodology	204
7.3. Preliminary results and discussion.....	209
7.3.1. Inlet statistics	209
7.3.2. Flow pattern	214
7.3.3. Pressure coefficient.....	216
7.4. Conclusions and take out points.....	217
Chapter 8 Conclusions	219
8.1. Original Research Contribution	221
8.2. Further steps of the research	222
References.....	225

Figures

Figure 1.1. The ‘upscaling’ strategy of future wind energy converters. Typical wind turbine sizes compared to buildings in London.	23
Figure 2.1. Cumulative Power Capacity in the EU from 2008 to 2018. Courtesy: WindEurope.....	31
Figure 2.2. Share of newly installed capacity in the EU in 2018. Source: Platts, SolarPowerEurope. Courtesy: WindEurope.....	32
Figure 2.3. Actual generated energy from onshore and offshore wind in the EU in 2018. Courtesy: WindEurope.	33
Figure 2.4. Cost distribution for WTs referred to different wind climates. Reproduced with permission from (Fuglsang et al., 2002).	35
Figure 2.5. (Left) Location of operational and planned wind farms in the UK; (Right) Simulation of Levelised Cost of Energy of Wind across the UK (adapted from Hdidouan and Staffell, 2017).	35
Figure 2.6 – a) Strata SE1 Tower, in Elephant and Castle, London, UK; b) The Bahrain World Trade Centre, in Manama, BH.....	38
Figure 2.7 –Classification of Urban Wind Energy application based on the possible relationships of wind turbines with a building.	39
Figure 2.8. Southern view of the Vattenfall Horns Rev 1 offshore wind farm taken on the 12 February 2008. Courtesy: Vattenfall. Photographer: Christian Steiness.	40
Figure 2.9. Urban plume downwind a large urban settlement and the vertical layers of the UBL.....	42
Figure 2.10 a)Probability Density Function (PDF) of wind speed fluctuations found within the atmospheric boundary layer, with “fat tails” and non-Gaussian distribution; b) PDF of WT power output and wind speed. Reproduced with permission from (Milan et al., 2013; Mücke et al., 2011). .	44
Figure 2.11. Blade Element Momentum Theory diagram. ϑ is the pitch angle; α the angle of attack; ω the angular velocity of the rotor; r the distance of annular rings; u_0 is the wind speed; w_i the apparent wind speed used to take into account unsteady effects; $u_{rel}=u_0 \times \omega r \times w_i$ is the real wind speed, vectorial product of the wind speeds and the rotational speed of the rotor; L and D are respectively the Lift and Drag forces.	49
Figure 2.12. Flow pattern over a WT blade, showing the separation area on the suction (upper) side of a Wind Turbine blade, and the centrifugal deviation of attached flow due to rotation.	50
Figure 2.13. Evolution of stall mechanism with angle of attack α	51
Figure 2.14. Typical distribution of Lift coefficient against angle of attack α . 1) flow is attached; 2) trailing edge separation with steep drop of lift; 3) full stall development with leading edge separation.	51
Figure 2.15. A typical classical experimental setup for the study of flow pattern variations under a turbulent inflow. Here the blunt plate experimental set of a classical experiment (Sasaki and Kiya, 1985).	54
Figure 2.16. Massive separated flow over a bluff body for smooth flow (solid line) and turbulent flow (dashed line), showing variability of the effect of turbulence with shape aspect ratio (Simiu and Scanlan, 1986).	55
Figure 2.17. Lift coefficient variation under varying turbulent intensity of inflow, for a) static and b) dynamic (with comparison) condition. Reproduced with permission from (Amandolèse and Széchényi, 2004).	56

Figure 2.18. Log-log diagram of the Energy spectrum $E(k)$ of turbulent length waves, k , with indication of its three domains: 1. Largest energy containing eddies; 2. Inertial subrange; 3. Smallest dissipative eddies. For each CFD model: referred to solved and modelled energy cascade. 63

Figure 2.19. The Research Gap. A twofold problem. Correctly addressing the turbulence pattern of the inflow; and understanding the scales affecting the aerodynamic performance of a WT aerofoil in the built environment. 65

Figure 2.20. Methodological framework to integrate wind tunnel and CFD results to assess the effect of turbulent flows as found in a realistic urban environment on wind turbine aerodynamics..... 69

Figure 3.1. Experimental setup: the aeronautical Test Section (TS1) of the Wind Tunnel of the University of Liège..... 76

Figure 3.2. Schematic (front and side view) of the set of four grids #, with bar b and mesh M size. ... 77

Figure 3.3. Preliminary design of the flow field. The symbols vary based on the different mesh size, while the filling is relevant to the chosen setup. The red lines and symbols indicate possible alignments for the statistics. 78

Figure 3.4 a) Turbulence Intensity decay with empirical fitting after Roach (1987) for grids #2 and #3 (- -) and after Laneville (1979) for grid #4 (- -). Least Square fitting of data is also provided for grids #2 and #3 (—) and grid #4 (—) as detailed in the text. b) Integral length scale decay with least square (—) and empirical fitting after Roach (1987) (- -) as detailed in the text. Markers are filled with a grey hatch if $x \geq 9.1$ m and coloured after wind speed (Table 3.4). 83

Figure 3.5 a) Taylor microscale decay and c) Taylor microscale against distance, with empirical fit as detailed in and b) Kolmogorov the text (Table 3.1) (—, - -). Colours after wind speed (Table 3.4). a) Turbulence Intensity decay with empirical fitting after Roach (1987) for grids #2 and #3 (- -) and after Laneville (1979) for grid #4 (- -). Least Square fitting of data is also provided for grids #2 and #3 (—) and grid #4 (—) as detailed in the text. b) Integral length scale decay with least square (—) and empirical fitting after Roach (1987) (- -) as detailed in the text. Markers are filled with a grey hatch if $x \geq 9.1$ m and coloured after wind speed (Table 3.4). 84

Figure 3.6 Turbulent Reynolds number relative to a) Taylor and b) integral scale against mesh distance, with fit of data (—) and fit by Kurian and Fransson (2009) (- -). Colours after distance (Table 3.4). 85

Figure 3.7. a) Integral and Taylor scale ratio dependence on the turbulent Reynolds number, with fit relation after Isaza et al. (2014) (—); b) Mean velocity ratio against mesh distance, with least square fit for grids #1, #2, and #3 (- -), and for grid #4 (—). Colours after distance (Table 3.4). 86

Figure 3.8 Turbulence Intensity anisotropy, a) horizontal and b) vertical component against non-dimensional mesh distance in logarithmic scale. Colours after distance (Table 3.4). 88

Figure 3.9 Integral length scale anisotropy for a) horizontal and b) vertical component against mesh distance. Colours after distance (Table 3.4). 89

Figure 3.10 Taylor microscale anisotropy for a) horizontal and b) vertical component against mesh distance. Colours after distance (Table 3.4). 89

Figure 3.11 a) Anisotropy invariant map; b) zoom close to the isotropy condition. c) Second and d) third invariant plotted against x . Colours after a), b) wind speed and c), d) distance (Table 3.4). 90

Figure 3.12 Skewness of velocity components for all grids and velocities. Colours after distance (Table 3.4). 92

Figure 3.13 Kurtosis of velocity components for all grids and velocities. Colours after distance (Table 3.4). 93

Figure 3.14 Turbulence Intensity versus Integral Length Scale of turbulence in a) non-dimensional, and b) dimensional form. Least square fit of all data (- -; - -; - -; - -; for grids #1, #2, #3 and #4, respectively),

and of data at $x \leq 4$ m (\rightarrow) is plotted together with Equation 12 (\rightarrow ; \rightarrow ; \rightarrow ; \rightarrow for grids #1, #2, #3 and #4, respectively). Circles and dashed black lines in b) refer to Table 3.5..... 95

Figure 3.15 Wave number spectrum a) at the inlet of the expansion $x = 4$ m, and b) at the outlet $x = 9.1$ m; Continuous line for grid #1 (\rightarrow), #2 (\rightarrow), #3 (\rightarrow), and #4 (\rightarrow); dashed line for von Kármán fitting; (\rightarrow) -5/3 power law..... 96

Figure 3.16. Power Spectral Density of turbulence for positions a) $x/M = 5$, b) $x/M = 10$ and c) $x/M > 25$ and wind speed $u_{rot} = 15$ m/s. Continuous line for grid #1 \rightarrow , #2 \rightarrow , #3 \rightarrow , and #4 \rightarrow ; dashed line for von Kármán fitting..... 97

Figure 3.17 Non-dimensional PSD of all velocity components at $x = 9.1$ m and for $u_r = 15$ m/s; Continuous line for grid #1 \rightarrow , #2 \rightarrow , #3 \rightarrow , and #4 \rightarrow ; dashed line for von Kármán fitting..... 97

Figure 3.18. Power Spectral Density of velocity for constant integral length scale (a, b, c, d) and turbulence intensity (e, f, g, h); Colours as reported in Table 3.5..... 98

Figure 4.1. a,b) WT and buildings: i) on rooftop, ii) on façade, iii) integrated, iv) in vicinity; c) flow enhancer (Hemida, 2014). 103

Figure 4.2. Choice of the most suitable typology of wind turbine based on the computation of regions of the flow having given characteristics (Toja-Silva et al., 2015b)..... 105

Figure 4.3. (Top) the different scales of the urban boundary layer (adapted from Piringer et al., 2007); (bottom) different typologies of turbulence around buildings (Haan and Kareem, 2009) 106

Figure 4.4. Wind Tunnel of the Ruhr-University Bochum 108

Figure 4.5. Photo of the wind tunnel with the model mounted on a turning table..... 109

Figure 4.6. Wind-tunnel velocity profile ahead of the model 110

Figure 4.7. a) Fluctuating and b) steady inlet domains for LES. 110

Figure 4.8. Velocity vectors, u and w as measured at pos. 1 and 2. 112

Figure 4.9. Mean velocity respectively at position 1 a) and 2 b), with experimental results (line for k - ω , dashed for les); c) streamlines of averaged velocity field for les model. 113

Figure 4.10. Horizontal and Vertical Turbulence intensity for Position (left) 1 and (right) 2..... 114

Figure 4.11. Integral and Taylor- s length scale of turbulence for Position (left) 1 and (right) 2. The Taylor- s microscale is plotted with a factor of 10. 114

Figure 4.12. Iso-contours of the mean velocity field for the LES simulation. 115

Figure 4.13. a), b) Vortex core visualisation (Q invariant $1/s^2$), with flow pattern identification; c) vortex core visualisation (swirling strength $1/s$) and d) structured block grid of the high-rise building model..... 116

Figure 4.14. Flow pattern in terms of velocity-invariant $Q = 0.1$ in the case of (left) steady and (right) fluctuating inlet for the (top) RANS and (bottom) LES cases. 117

Figure 4.15. Horizontal mean velocity for Position 1 and 2. Continuous line for turbulent inlet, dashed for steady and comparison with experimental results..... 118

Figure 4.16. Horizontal turbulence intensity for Positions 1 and 2. 119

Figure 4.17. Vertical turbulence intensity for Positions 1 and 2..... 119

Figure 4.18. Velocity invariants for the assessment of flow anisotropy. Results for experimental setup and LES with turbulent inlet conditions..... 120

Figure 4.19. Time histories for Position 1 at $z/D = 0.3$ for experimental, LES and no inlet LES cases. 121

Figure 4.20. Non-dimensional Power Spectral Density for Positions 1 and 2 at two height $z/D = 0.1$ and 0.6 122

Figure 4.21. autocorrelation coefficient for Position 1 at two heights $z/D = 0.1$ and 0.6 122

Figure 4.22. Integral length scale of turbulence for Positions 1 and 2. 123

Figure 4.23. Taylor’s microscale of turbulence for Positions (left)1 and (right) 2. 124

Figure 5.1. University of Birmingham Campus. (Left) aerial view as of 2015. (Right) view of geometry with landmarks and reference locations. 138

Figure 5.2. Full Scale Experiment. (Left) Map of UoB campus, with footpath alignment at the base of the BB and reference point position on top of the MT, with cardinal directions; (centre) Aerial view of footpath and position of 8 sonic anemometers; (Right) view of sonic anemometers as installed during the measurement campaign. 139

Figure 5.3. (Left) overview of wind tunnel test setup. (top) HWA placed according to 8 locations in full-scale. (Bottom) Cobra Probe for reference point measurement. 141

Figure 5.4. Detail of experimental setup with indication of wind direction for the storm Ophelia. (Left) Biosciences Building and (Right) Muirhead Tower. 142

Figure 5.5. Properties of approaching atmospheric boundary layer (ABL) flow. (Left) vertical profiles of mean wind speed and turbulence intensity; (Right) power spectral density of wind speed measured at reference height upstream the model. 142

Figure 5.6. (Left) Wind tunnel domain. (Right) Alternative computational domain: whole wind tunnel geometry. 143

Figure 5.7. (Left) General view of the computational unstructured mesh, with refined topology along the footpath. (Right) Detail of mesh on the Biosciences Tower. 144

Figure 5.8 – Inlet velocity statistics downstream of precursor domain. a) Mean velocity; b) variance and covariance; c) integral length scale. H in this case is the height of the Muirhead tower. 145

Figure 5.9. Mesh independency study a) Mean velocity; b) standard deviation; c) Integral length scale. 146

Figure 5.10. Mean, standard deviation, turbulent kinetic energy, and integral length scale along the 8 measurement positions on the pedestrian test route indicated in Figure 5.2. CFD results refer to LES and are compared to EXP and FUL data. 151

Figure 5.11. Mean and standard deviation field over the 8 measurement positions. (upper row) RANS case; (lower row) LES case. Black lines are mean velocity streamlines 153

Figure 5.12 (left) Flow pattern along the footpath, showing the downwash at the BB southern façade with the jet nearby Position 2, the recirculation region which affects Positions 4-to-7 and the wake flow at the northern side. (right) 99th Percentile of the velocity magnitude. 154

Figure 5.13. Mean horizontal and vertical velocity at the rooftop of the Muirhead tower (left) and Biosciences building (right). 155

Figure 5.14. Horizontal and vertical standard deviation at the rooftop of the Muirhead tower (left) and Biosciences building (right). 156

Figure 5.15. Turbulent Kinetic Energy at the rooftop of the Muirhead tower (left) and Biosciences building (right). 156

Figure 5.16. Integral length scale of turbulence at the rooftop of the Muirhead tower (left) and Biosciences building (right) compared with integral length scale as found at the inlet flow. 157

Figure 5.17. Anisotropy of velocity in terms of velocity invariants at the rooftop of the Muirhead tower (left) and Biosciences building (right) 158

Figure 5.18. Skewness and kurtosis of horizontal velocity at the rooftop of the Muirhead tower (left) and Biosciences building (right) 159

Figure 5.19. Gust wind speed at the rooftop of the Muirhead tower (top-left) and Biosciences building (top-right) and along the pedestrian route (bottom). 160

Figure 6.1. Power coefficient of a HAWT as measured, predicted and designed (Pagnini et al., 2015) 164

Figure 6.2 – Experimental setup at the university of Liège..... 169

Figure 6.3. The DU 96w180 aerofoil and the position of the pressure taps..... 170

Figure 6.4. Energy Ratio of the Proper Orthogonal Decomposition..... 175

Figure 6.5. Stall Mechanism and comparison with experimental data from literature..... 176

Figure 6.6. Undisturbed case. (Top) Mean surface Pressure Coefficient for 3 Angles of attack used in this study, compared with results from (Timmer, 2010; Timmer and van Rooij, 2003). (Bottom) Standard deviation of surface pressure coefficient..... 177

Figure 6.7. (Top) Proper Orthogonal Decomposition of the undisturbed case, spatial generalised modes. (Bottom) energy spectra of the time generalised coordinates. Comparison with undisturbed case 178

Figure 6.8. Mean pressure coefficient on the aerofoil. Compared with undisturbed case and results from Timmer..... 181

Figure 6.9. Standard deviation of pressure coefficient..... 182

Figure 6.10 skewness of pressure coefficient..... 183

Figure 6.11. kurtosis of pressure coefficient..... 184

Figure 6.12. Mean pressure coefficient c_p for the three angles of attack and LS1-4..... 185

Figure 6.13. Standard deviation for the three angles of attack and LS1-4..... 186

Figure 6.14. Skewness for the three angles of attack and LS1-4 187

Figure 6.15. Kurtosis for the three angles of attack and LS1-4..... 188

Figure 6.16. Effect of turbulence on Separation Point x_S for 4 and 24 deg. Results marked as in Table 6.5. 189

Figure 6.17. Normalised force coefficients for $\alpha=14$ deg against turbulence parameter $I(L/c)$ 191

Figure 6.18. Probability Density Function of Lift coefficient for cases as in..... 192

Figure 6.19. Normalised mean and standard deviation of force coefficients against turbulence parameter $I(L/c)$ 193

Figure 6.20. Probability Density Function of Lift coefficient for cases as in..... 193

Figure 6.21. First 4 POD modes (rows) for TII-5 (columns). Colors as in 194

Figure 6.22. First 4 POD modes (rows) for LS1-4 (columns). Colors as in Table 3.5. 195

Figure 7.1 Precursor turbulence generation techniques, (top) virtual wind tunnel, (bottom) double recycling/rescaling domain method, with flow mapping at the inlet of the geometry of interest (Immer, 2016). 201

Figure 7.2. Synthetic turbulence generation, (top) Synthetic Eddy Method approach of synthetic vortex mapping (Jarrin et al., 2006; Poletto et al., 2013); (bottom) Digital noise Filtering Method of introducing a random white noise, filter it to achieve wanted turbulence statistics and scale it according to the model geometry (Immer, 2016; Klein et al., 2003) 202

Figure 7.3. Computational domain with inlet surface and solid region and distance from the aerofoil model..... 204

Figure 7.4. Schematic of the structured hexahedral mesh topology around the aerofoil..... 205

Figure 7.5. Effect of domain size on mean pressure and boundary layer thickness at $0.99c$ 206

Figure 7.6. Effect of orthogonal mesh refinement on surface pressure coefficient. 206

Figure 7.7. Structural hexahedral mesh for the aerofoil with chord $c=0.125$ m. (top) side view and (bottom) view of the topology around the aerofoil boundary layer. 207

Figure 7.8. Structured hexahedral mesh for the aerofoil having chord $c=0.05$ m. (bottom) side and (top) top view. 208

Figure 7.9. Topology of the computational mesh around the aerofoil with short chord length 208

Figure 7.10. y^+ instantaneous value along the suction side of both C125 and C25 aerofoil models. 209

Figures

Figure 7.11. Mean velocity along the computational domain, compared with experimental results. 210

Figure 7.12. Turbulence intensity decay along the computational domain, compared with experimental results, for both the along wind and across wind directions. 211

Figure 7.13. Longitudinal and Transversal integral length scale decay, compared with experimental results. 212

Figure 7.14. Velocity Invariants for C125, C25 and EXP. 212

Figure 7.15. Velocity Skewness and kurtosis compared with experimental results. 213

Figure 7.16. Energy Spectra compared with experiments. 214

Figure 7.17. (top) vorticity of C25(above) and C25 (below). (bottom) dimensional mean velocity for C25 (left) and C125 (right), with streamlines showing the flow pattern. 215

Figure 7.18. Surface pressure coefficient at the suction side for C25 and C125, compared with the experimental case and the undisturbed experimental case. 216

Chapter 1

Introduction

1.1. Motivation for research

The World Population dwelling in urban areas is expected to increase steadfastly by 2.5 billion inhabitants in around 30 years (United Nations - Department of Economic and Social Affairs - Population Division, 2019). This means an impressive 68% out of 9.77 billion people will be living in cities compared to the current 55% out of 7.38 billion. This change is expected to occur mostly in the least developed parts of the world, where life standards are set to increase, meaning more people will be able to access services and welfare, hence using more energy (Seto et al., 2014). To accommodate this soaring demand of energy, the key for sustainable development, as auspicated by the United Nations, does not lie uniquely in the energy policy realm:

“It’s the architecture, stupid!”

With this wake up call, Mazria (2003) showed that buildings are responsible for the largest usage of energy, and improving the way they are designed is the most efficient way to tackle energy consumption. Although nowadays this is a well-established and irrefutable concept, progress needs to be made in the way end-users transform the energy provided by producers (Norman et al., 2006; Zhao and Magoulès, 2012). The provision of energy remains essential for sustainable development (Lund, 2007), and a complete overhaul of the policies in place is still considered necessary to guarantee

services. Phasing out fossil fuel generators is key to sustainability. However, fossil fuels still provide 85% of the overall consumed energy, because they are still and properly considered the most reliable source of energy available (Hansen et al., 2019; Junker et al., 2018).

Technology progress is undergoing an inexorable transition from the pursue of ‘innovation’ towards ‘exnovation’ (David, 2017; Davidson, 2019) or the fulfilment of the ‘global energy justice’ concept (Finley-Brook and Holloman, 2016; Goldthau and Sovacool, 2012; McCauley et al., 2019), and future performant buildings and intelligent energy provision are at the forefront of this transition.

The concept of Smart City (Hatuka et al., 2018) is highly relevant when discussing the future of energy policy and energy sustainability (Haarstad and Wathne, 2019). The ‘smartness’ of future cities lies in several qualities:

- the capacity to be autonomous, i.e. requiring minimum resources from the environment, preserving it (Galvao et al., 2015; Norman, 2018);
- the resilience, i.e. the ability to adapt and respond to favourable or adverse conditions (Antrobus, 2011; Rajasekar et al., 2018);
- the ability to fulfil sustainable development goals (Wendling et al., 2018).

In smart cities, the energy strategy is strongly interlaced with buildings, not mere passive interfaces between energy consumers and producers, but intelligent entities, able to actively interact with service grids, e.g. by conveniently storing and releasing energy, or even by producing it (Kolokotsa, 2016; Kylili and Fokaides, 2015). As buildings are estimated to absorb 40 to 60 % of the total energy produced worldwide (Chel and Kaushik, 2018), the repercussions of pursuing smart energy policies are set to impact heavily on society and the economy.

In the (r)evolution of energy policy and smart cities, the role of renewable energy systems is certainly implicit (Bandyopadhyay, 2019; Blazquez et al., 2018; Jacobsson et al., 2009; Liu et al., 2018). At the present, the shift to 100% renewable energy is desirable and theorised as possible, but far from straightforward. An intelligent strategy for the renewable energy mix, storage, distribution grid or self-production needs to be further developed to abolish fossil fuels without unacceptable disruption for the population (Bogdanov et al., 2019; Drysdale et al., 2019; Hansen et al., 2019; Peter, 2019). Wind Energy

is quite promising in leading this transition, as the most advanced and performant renewable technology available (deLlano-Paz et al., 2015), with an impressive record in the European Union (Walsh and Pineda, 2019).

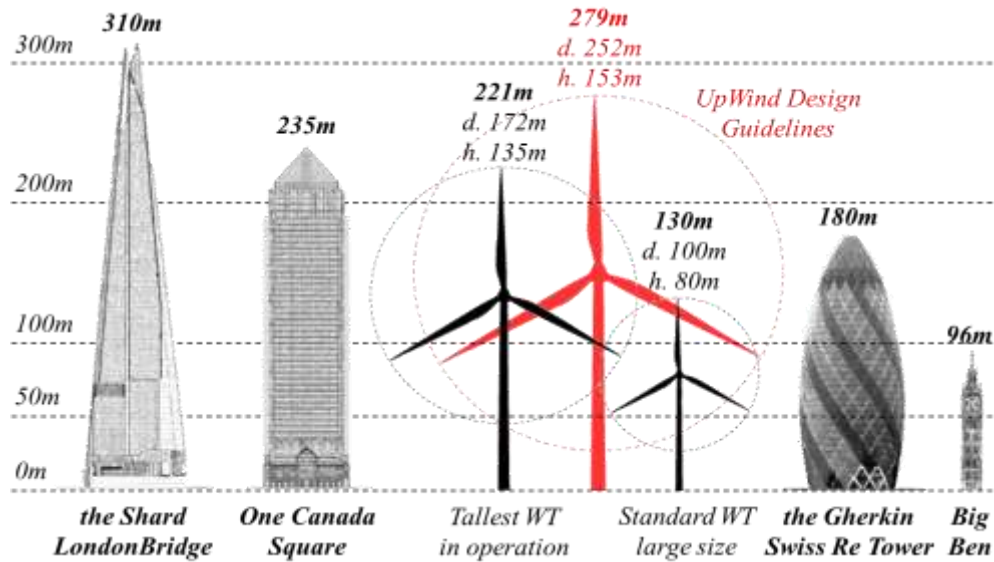


Figure 1.1. The ‘upscaling’ strategy of future wind energy converters.
Typical wind turbine sizes compared to buildings in London.

The Wind Energy Industry has traditionally interpreted innovation and progress of the technology with ‘upscaling’, or ‘concentrated energy generation’, i.e. the ability of increasing the size of rotors, to increase power efficiency (Baniotopoulos et al., 2011; Stathopoulos et al., 2018). In fact, the beneficial contribution in terms of levelised energy costs deriving from producing more energy with a single device, might be offset by the exponential increase in the cost of the components to realise a larger device, as shown in Figure 1.1 (Sieros et al., 2012; Stathopoulos et al., 2018). An alternative approach to upscaling is the ‘distributed energy generation’ and the ‘downscaling’ of converters, i.e. the tailored placement of smaller devices within a vast area (Ackermann et al., 2001; Dabiri et al., 2015). The industry is quite reluctant to improving the performance of small devices, possibly due to the energy market of the developed world they mostly operate in at present. However, ‘downscaling’ might be crucial in the energy evolution of areas lacking an adequate distribution network, or where energy demand is unmet, giving the population the possibility of generating the energy needed locally, without the need of state infrastructures (Samu et al., 2019). Also in the developed world, small devices could be used within the scope of smart cities, with buildings as partial generators contributing to the local energy production or consumption (Grosspietsch et al., 2019).

Although promising, distributed energy generation through downscaling remains a concept, as many challenges are to be addressed to start implementation at industrial level (Stathopoulos and Alrawashdeh, 2019). Nevertheless, the so-called ‘small wind energy market’ has found a recognised place in the conceptual planning of smart cities, due to wind being always present in the urban energy mix fabric (Simões and Estanqueiro, 2016). The faith of some investors and proprietors might justify why the small wind market does not show any sign of attenuation, despite the questionable success of applications (Evans et al., 2011; Gsänger and Pitteloud, 2015; Stankovic et al., 2009; Tummala et al., 2016).

Urban wind energy is the niche of wind energy designated to the study of wind energy converters placed in the built environment, poised to improve the performance and increase the viability of the technology. Despite the fiasco of the few available applications, urban wind energy is anything but a dead end of wind energy research, as available results do not yet allow for conclusions to be yet drawn on the feasibility of the technology (Stathopoulos and Alrawashdeh, 2019). The reason for the steady success of the debate is the huge impact a reliable way of wind micro-harvesting would have on urban planning, especially in developing countries (Mainali and Silveira, 2013).

Most of the research works in Urban Wind Energy are briefly referred to in Chapter 2 and reviewed thoroughly in recent literature (Hemida, 2016; Hemida et al., 2014; Ishugah et al., 2014; KC et al., 2019; Micallef and van Bussel, 2018; Millward-Hopkins et al., 2012; Šarkić Glumac et al., 2018; Stathopoulos et al., 2018; Stathopoulos and Alrawashdeh, 2019; Tadie Fogaing et al., 2019; Toja-Silva et al., 2018). All works argue the necessity for extensive and additional fundamental research to be carried out for small wind turbines to approach the performance of traditional wind energy. However, a pathway to success is noticeable in the sense that the field is gradually becoming more self-aware and focused, parting itself from the empiricism of first applications.

Urban wind energy research can be split into two main areas (Stathopoulos et al., 2018):

- Focus on the inflow: Urban aerodynamics and the estimation of the urban wind resource;
- Focus on the device: Design and optimisation of dedicated urban wind turbines.

Urban flows are caused by the wind impinging with buildings in the built environment (Emeis, 2013).

The aerodynamic interaction between buildings, or bluff bodies, and their wakes causes turbulence to

occur, having specific characteristics, distinct from those of turbulence naturally found in the Atmospheric Boundary Layer, or ‘atmospheric turbulence’. It is normally referred to as signature turbulence (Roshko, 1955). However, signature turbulence varies greatly with the bluff body, i.e. building, considered, and it also interacts with additional turbulence generated due to thermal or chemical phenomena, such as atmospheric stability, the ‘urban heat island’ or pollution (Droste et al., 2018; Kanda, 2007; Piringer et al., 2007; Roth, 2000). At present, knowledge is (very) limited on urban aerodynamics and turbulence, and crucial engineering guidelines for the design and positioning of wind turbines, which are a guarantee to the success of applications, are far from drafting.

The European Academy of Wind Energy (EAWWE) has recently published an important document, which states the long-term research challenges yet to be overcome in wind energy (van Kuik et al., 2016). Among the long list of scientific challenges, two voices are applicable to urban wind energy:

“2-2: To understand small-scale turbulence for instationary atmospheric and complex orographic conditions”.

“3-2: To achieve an understanding of 3D flow pattern and their dynamics on rotor blades including emerging turbulence”.

Challenge 2-2 clearly reflects the need of basic research on the inflow characteristics, i.e. the wind resource, especially when addressing the scale difference between the scale of the atmospheric turbulence, the energy cascade and its relation with the scale of the rotor.

On the other hand, Challenge 3-2 shows that more research on the hypotheses surrounding the design of rotors is needed, especially regarding the complexity of aerodynamic phenomena and the interaction with the downstream flow, i.e. the wake aerodynamics.

Both these aspects show the parallel with urban wind energy aerodynamics, and its connection with the whole wind energy sector: a progress in urban wind energy might not be an end in itself, but give considerable input to unresolved aerodynamic issues in the whole sector.

What is surprisingly missing in urban wind energy research is a convincing link between these two apparently separate worlds. Or rather, the recognition that some sort of interaction between turbulence in the urban wind and the aerodynamics of a wind energy converter might be responsible for the observed lack in performance of the technology. In fact, a connection between turbulent inflow and

performance is rather accepted in the wind energy community (Milan et al., 2013), regarding the fatigue behaviour (Bernhammer et al., 2016; Thomsen and Sørensen, 1999) or the power output (Kaiser et al., 2007; Sunderland et al., 2013). In particular, the wind energy community is interested in wind farms and how wind turbine wakes affect the performance of downstream rotors (Kim et al., 2015; Thomsen and Sørensen, 1999; Wu and Porté-Agel, 2012). However, a thorough understanding of the basic aerodynamic mechanism under which turbulent scales in the inflow interact with the boundary layer of blades affecting performance is yet to be reached.

Surprisingly, the issue of a turbulent inflow influencing aerodynamic performance is considered marginal in wind energy literature, and the debate, although ongoing, is stalled. The reasons for the paucity of results lie in several factors. Firstly, the preferred approach in positioning wind farms is to avoid or strongly limit turbulence at the inlet of rotors, after the early experiences of 1970s large wind farms (Mulvaney et al., 2013). Furthermore, controlling wind statistics at the inlet of physical and numerical simulations is a very complex matter with a very limited applicability for large traditional wind farms, prompting the wind energy industry to justify the use of laminar inflows in the design of wind energy converters.

If the approach of avoiding turbulence might have been reasonable for traditional onshore or offshore wind farms, located in windy and relatively undisturbed areas (Emeis, 2013), under no circumstances this is a viable strategy for the highly turbulent urban boundary layer or in complex terrain locations. Small wind turbines placed on top or near obstacles is necessarily going to deal with signature turbulence during their service life.

Improving the understanding of the basic aerodynamic mechanism under which turbulence affects aerodynamic performance is the motivation of this research. A novel methodology to assess and/or predict this interaction is essential for progress in the technology of urban wind energy and resolve the traditional separation of the research on device performance and site conditions, which is likely to be responsible for the low efficiency of small wind applications.

1.2. Aim of research and objectives

The aim of the research is to improve the understanding of turbulence characteristics within the built environment and the related aerodynamic performance of wind turbines. Particular emphasis is given to the integral length scale of turbulence found in the inflow and its relation with the aerodynamic behaviour of static wind turbine aerofoils.

To fulfil the proposed aim, six objectives are identified as follows:

- (O1.) To assess the gap in research about wind turbine aerodynamics, by critically review literature in the field of urban wind energy, and the effects of free-stream turbulence on bluff bodies. O1 is developed in Chapter 2;
- (O2.) To create an urban wind-like inflow in wind tunnels, using the passive grid technique, to vary turbulence intensity (TI) and the integral length scale of turbulence (LS) separately. O2 is developed in Chapter 3;
- (O3.) To develop a numerical framework based on Large Eddy Simulation (LES), to investigate the signature turbulence above a model high-rise building, with validation from available experimental data (Hemida et al., 2014). O3 is developed in Chapter 4;
- (O4.) To develop a numerical model to investigate the signature turbulence at different locations over a realistic urban geometry, i.e. the University of Birmingham Campus, with a suitable experimental validation strategy. O4 is developed in Chapter 5;
- (O5.) To investigate the independent effect of turbulence intensity and integral length scale as generated in O2 on the aerodynamic performance of a wind turbine aerofoil. O5 is developed in Chapter 6;
- (O6.) To extend results obtained for the model wind turbine aerofoil in O5 to match turbulence characteristics found in O3 and O4 using inlet turbulence generation techniques for LES. O6 is developed in Chapter 7.

All Objectives have been fulfilled within the scope of the European Innovative Training Network “Aeolus4future”. O2 and O5 have been conducted in February 2017 during a Secondment at the Wind Tunnel Lab of the University of Liège (BE). Validation of O3 has been provided in a collaborative

activity with the Wind Tunnel Lab of the Ruhr University of Bochum (DE). O4 has been fulfilled within the EPSRC Project “Pedestrian Wind Danger around tall buildings in the urban environment” with the University of Birmingham Fluid Research Group. O7 has been developed in collaboration with the von Kármán Institute of Fluid Dynamics (BE), leading to the choice of the aerofoil DU96w180, and the secondment at the Lappeenranta University of Technology (FI) about inlet generation techniques for LES and advanced usage of OpenFOAM.

1.3. Limitations of the research

The field of study of the Ph.D. research is the bluff body aerodynamics, applied to wind turbine aerodynamics, and building aerodynamics. The work scientifically contributes to the subject of applied fluid dynamics with both wind tunnel testing and computational fluid dynamics.

Although motivated by the lack of understanding in basic flow mechanisms involved with urban wind energy, the scope of this work is not intended to justify or overcome limitations in the urban wind energy technology. Urban wind energy is largely based on research directly related to the performance of converters, such as the correction of the power output to account for turbulence effects, or positioning strategies of wind turbines within the built environment. Therefore, the conclusions of this study are not immediately applicable to the amendment or upgrade of the current binding international standards on the design of wind energy converters to be installed in the urban environment. The IEC 61400 (Part 1:2005 and AMD Part 1:2010 Design requirements; Part 2:2013 Small Wind Turbines;) or the DNV-GL (DNVGL-ST-0376 Rotor blades for wind turbines; DNVGL-ST-0437 Loads and site conditions for wind turbines) are the current reference standards for the wind energy industry.

This work is limited to investigating the basic physical mechanism that causes the different response wind turbines are known to experience in the presence of a turbulence. Turbulence is here intended as the signature turbulence from the flow pattern around buildings, regardless of other sources of turbulence such as thermally induced by the urban heat island, which might indeed have a substantial effect on performance.

Henceforth, any reference to urban wind energy is to be interpreted as one of the possible applications for an improvement in the knowledge of the aerodynamic performance of aerofoils placed in a turbulent

flow. Eventually, results presented in this work might be extended to improve the reliability of engineering models to take into account the effect of signature turbulence in the calculations of wind turbine performance, possibly increasing their accuracy and reliability compared to the negligibility of effects currently accepted in design practice.

1.4. Thesis Outline

The thesis is structured as a collection of original and stand-alone research papers resembling the objectives given in Section 1.2. When applicable, a disclaimer is present at the beginning of each chapter, if the work or part of it has been published elsewhere by the author himself and other co-authors and reproduced with permission, as requested by the University of Birmingham Plagiarism Guidelines. In Chapter 2, the literature background on urban wind energy, building aerodynamics and the role of free-stream turbulence in wind turbine aerodynamics is reported in terms of main findings and briefly discussed with reference to relevant literature. Additionally, a brief background on the methods used in the thesis is provided, with reference to literature and textbooks and the parts of the thesis where they are implemented.

In the rest of the thesis, chapters are structured so to include an introduction comprising of a detailed and up-to-date literature review on the specific scope of the objective under study, which is justified in terms of research gap addressed and novelty. A detailed methodology for the fulfilment of the objective is then given, and relevant results and findings are presented and discussed. A conclusion for each chapter is given in terms of the original research contribution and how it relates to the subsequent chapter of the thesis.

In Chapter 3, an experimental study on a possibility of enhancing the scope of wind tunnel testing to reach turbulence characteristics as found in the built environment is reported in fulfilment of the scope of O2.

In Chapter 4, an investigation on the signature turbulence as found at the top of a high-rise building in order to discuss what suitable turbulence characteristics are to be reproduced with the technique developed in Chapter 3 to obtain a real representation of turbulence in the built environment.

In Chapter 5, the same investigation as in Chapter 4 is applied to a realistic urban environment. Both pedestrian and roof-top level of high-rise buildings are considered in order to quantify turbulence characteristics and how adequate CFD simulations and wind tunnel testing are respectively to assess wind conditions. Reference for this chapter is a full-scale measurement campaign at the University of Birmingham Campus.

In Chapter 6, the experimental technique developed in Chapter 3 is used to vary the turbulence characteristics upstream of a wind turbine aerofoil. A possible mechanism for the effect of large length scale turbulence is formulated.

In Chapter 7, a brief investigation on the possibility of extending the experimental scope of Chapter 3 with the use of inlet turbulence generation techniques for Large Eddy Simulation is performed, and relevant preliminary results are presented towards the development of an experimental-numerical approach for the modelling of the effect of turbulence found in the built environment on bluff bodies.

Conclusions are given in Chapter 8, with direct reference to the objectives of the study given in the present Chapter 1.

Chapter 2

Literature and Methodology Background

Chapter 2 is based on the Proceedings of the WINERCOST'16 Conference (Vita, Hemida and Baniotopoulos, 2016), with appropriate referencing and the permission of the other co-authors. It is also noted that the contents of this Chapter does not provide the literature review or the methodology of the work, which are separately treated in extensive detail in the relevant Chapters.

2.1. Wind Energy research trends

Wind represents the second largest source of energy of the European Union (EU) in 2018, with a total installed capacity of 178.8 GW, covering over 14% of EU's energy demand, with 362 TWh of energy generated. Figure 2.1 shows annual wind power installations have been increasing steadily from 3.2 GW of new power capacity in 2000, to 11.7 GW in 2018, with a share of 18.8% of total installed power capacity (952 GW) (Walsh and Pineda, 2019). Of the installed power, 160 GW is onshore and 18.5 GW offshore, with investments of respectively €16.3bn and €10.3bn.

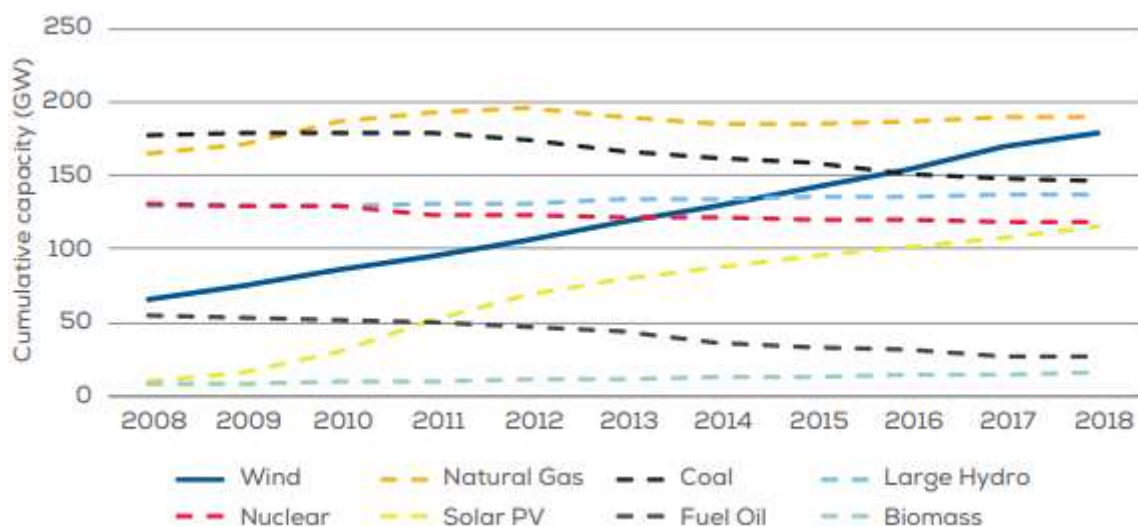


Figure 2.1. Cumulative Power Capacity in the EU from 2008 to 2018. Courtesy: WindEurope.

Figure 2.2 shows that 95% of new power capacity in the EU comes from renewable energy, while fossil fuel is almost absent, as decommissioning involves 2.9GW of power capacity (Walsh and Pineda, 2019). These statistics match with the EU Horizon 2020 target of having at least 20% of power from renewables by 2020, which has been already met by almost every country in the EU, prompting the Commission to speed up the approval of new targets for 2030 (Resch et al., 2019).

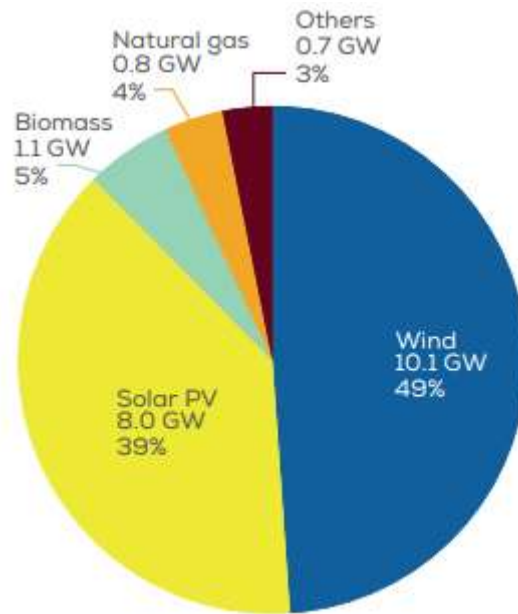


Figure 2.2. Share of newly installed capacity in the EU in 2018.
Source: Platts, SolarPowerEurope. Courtesy: WindEurope.

Wind power supplied to utilities comes almost exclusively from large wind farms, mostly onshore and increasingly offshore. Large wind energy converters are in fact very efficient and optimised such that a stable capacity factor of 24% of their rated power could be achieved in 2018 (37% for offshore) (Hdidouan and Staffell, 2017). It is more often documented how during peak days up to a third of the EU energy consumption is entirely supplied by wind (six days in 2018, with the best ever rate on the 8th December 2018).

Figure 2.3 shows that most of the installed rated power remains unused throughout the year. This is due to the variability of the wind resource, which in turns points to the redefinition of the very concept of rated power and efficiency in the traditional term (Carrasco et al., 2006; Estrella et al., 2019). Recent energy policy research predicts that following the complete decommissioning of fossil fuel power

plants, a societal and technological switch for the energy production is to take place (Davidson, 2019; McCauley et al., 2019; Sheikh et al., 2016). The technological switch will have to provide power generation that is flexible and tailored to respond to the variability of the energy source; harvesting it as long as it is available or needed, wherever available; while possibly storing it (Díaz-González et al., 2012; Díaz et al., 2019; Lund, 2007). Wind Energy is at the forefront of this switch, although much research is needed on the interoperability, reliability and effectiveness of wind farms (Jacobson and Delucchi, 2011).

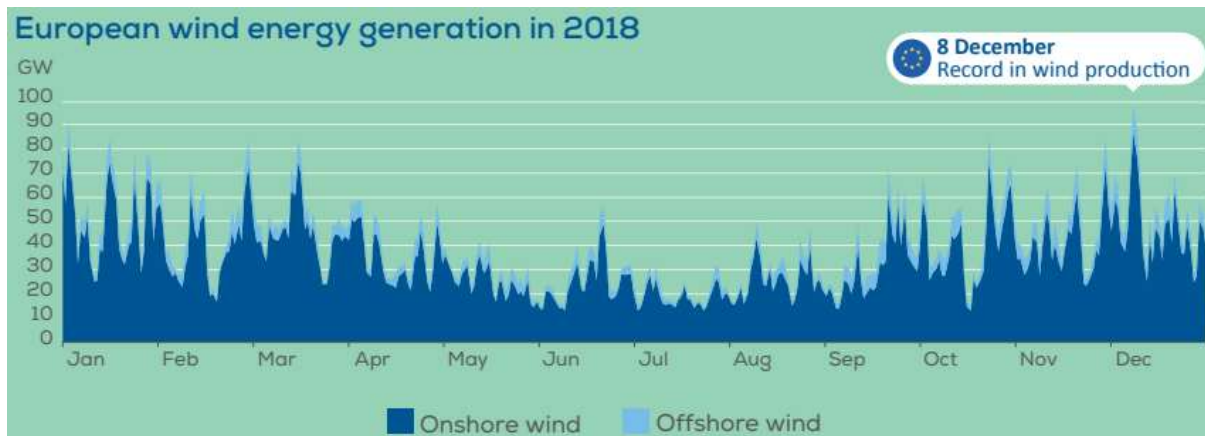


Figure 2.3. Actual generated energy from onshore and offshore wind in the EU in 2018. Courtesy: WindEurope.

In terms of the technology, wind energy research challenges are exhaustively dealt with in a recent work giving cause for reflection in the wind energy community (van Kuik et al., 2016). Paraphrasing results from the presented research achievements, a multifaceted trend can be recognised in wind energy.

i) Harvesting of energy in unconventional locations.

Complex terrains or locations in proximity of built up areas have become more popular in the last decade for the setting up of wind farms (Chamorro and Porté-Agel, 2011), as the availability of suitable windy plains reduces (Hevia-Koch and Ladenburg, 2019). Forest canopies, hillcrests, open areas in the vicinity of manmade structures, orography, or even in close proximity to urban areas represent possible locations with wind characteristics different from traditional plain locations (Kruyt et al., 2018). In fact, the site has been regarded as the most precious resource a wind farm possesses since first industrial scale applications (Lalas, 1985).

- ii) The increase in size of the new generation of wind turbines.

In light of the limited service life of WTs and the value of wind rich sites, a popular strategy is to repower existing wind farms with larger devices (Hou et al., 2017). The purpose is to raise the mean velocity at hub height, as a surge in power output and height of modern rotors is currently readily available (up to 164-171m/8.8-7.1MW diameter/rated-power for Vestas and Samsung respectively), with the next generation of converters designed for 250m/10MW (Fichaux et al., 2011). While large rotors are effective in increasing the production of a wind farm while reducing overall costs (Sieros et al., 2012), applications are in fact limited because of the transportation of the large-sized components in mostly remote locations (Martínez et al., 2009).

- iii) The enhancement of the power efficiency of rotors.

The classical three bladed rotor has reached remarkable optimisation results over the past decades (Hansen, 2015). However, in parallel to the effort in improving HAWTs, other typologies of rotors have been studied and experimented to overcoming the limitations of three bladed HAWTs (Tummala et al., 2016). The small wind industry has continuously led research on alternatives to traditional three bladed rotors (mostly VAWT and HAWT up to 25-100 kW). However, devices commercialised and sold for household installations show a great degree of empiricism, especially since they are normally placed in the close vicinity or on top of buildings, with a complex flow normally not assessed in detail. As a result, the economic gain in self-producing wind energy is negatively affected. Research on small devices (particularly VAWTs) has been recently progressing towards a more scientific optimisation of the aerodynamics of rotors (Rezaeiha et al., 2018), but the performance of small wind devices is still far from providing a viable trustworthy alternative to in providing an asset for the generation of energy at the consumption site (Tummala et al., 2016).

Wind energy research trends show how the technology is evolving to improve the conceptual coupling between the design of rotors and the specific wind resource found at the site of installation. In fact, Figure 2.4 shows that the cost of a wind turbine is strictly correlated with the installation site (Fuglsang et al., 2002). Rather than the type of device, the inflow defines the type of technology and therefore the most important issue to tackle when looking at progress opportunities. As exemplified in Figure 2.4,

wind speed is by far the most important parameter, but in unconventional locations other parameters might play an important role, such as atmospheric turbulence (Jangamshetti and Ran, 2001).

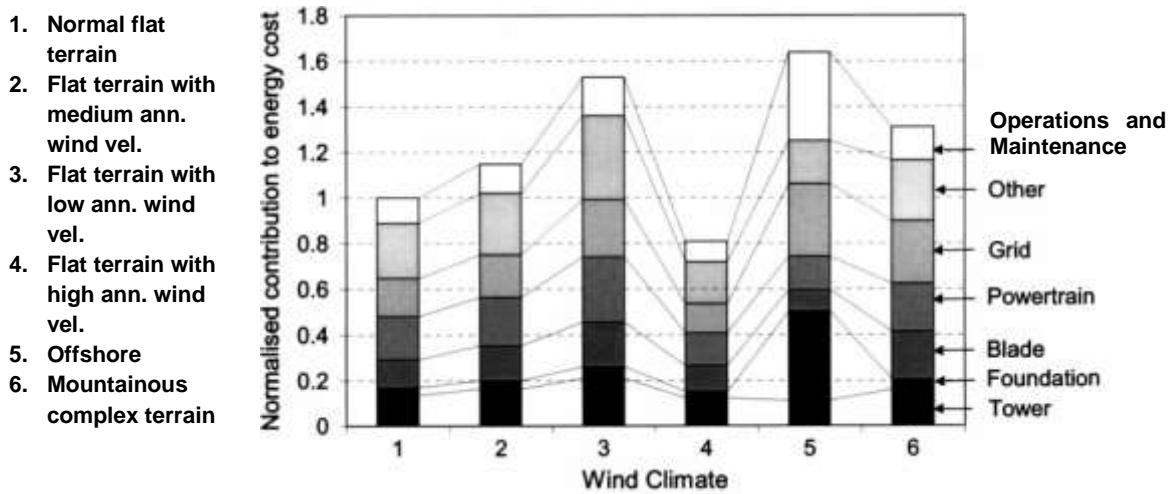


Figure 2.4. Cost distribution for WTs referred to different wind climates. Reproduced with permission from (Fuglsang et al., 2002).

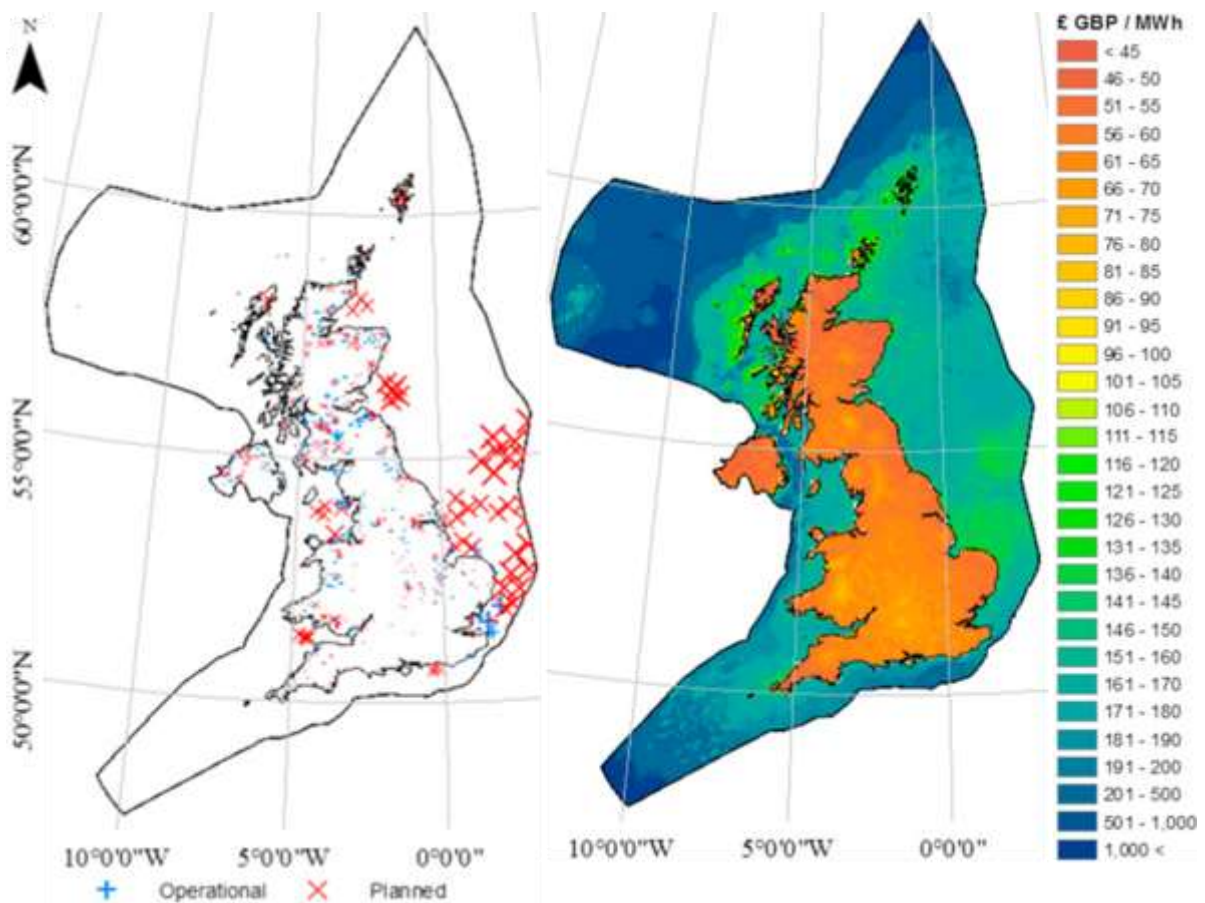


Figure 2.5. (Left) Location of operational and planned wind farms in the UK; (Right) Simulation of Levelised Cost of Energy of Wind across the UK (adapted from Hdidouan and Staffell, 2017).

The cost of renewable energy is the most pressing obstacle to the spreading of the technology. Figure 2.5. shows that the levelised cost of wind energy has a causal relation with the location considered in the United Kingdom (Hdidouan and Staffell, 2017). Onshore, the cost of energy varies from less than 45 £/MWh (Scotland and coastal areas) to roughly 100 £/MWh (Wales and the Midlands). The study also shows that offshore wind farms are only planned where costs are comparable to onshore ones.

The wind energy industry is therefore poised to improve productivity while reducing costs through a tailored design of devices to actively respond to the specific characteristics of the wind resource found on either existing or new unconventional installation sites.

2.2. Urban Wind Energy Research

In Chapter 1, the motivations for this study show that an alternative approach to ‘upscaling’ can be theorised. With the ‘Distributed Power Generation’ a multitude of small or micro power plants is connected to an optimised intelligent grid (Ackermann et al., 2001; Dabiri et al., 2015). The ‘Downscaling’ of devices permits production and consumption site to coincide, with a cut in the cost of grid, maintenance and components. This great potential might be the reason why the small wind energy market has been expanding steadily for the past ten years with no signs of crisis (Gsänger and Pitteloud, 2015). As buildings consume most of the energy, the city becomes the elected installation site (Sieros et al., 2012; Stathopoulos et al., 2018). Small and medium scale (15kW-100kW) wind turbines (WTs) could also be flanked by other small scale renewables such as solar photovoltaic panels, or combined heat power systems, to provide the urban energy mix of future smart cities (Baniotopoulos and Borri, 2015).

Urban Wind Energy is the niche of wind energy aimed at studying the positioning of WTs within the built environment. Traditionally, the research realm of ‘Urban Wind Energy’ overlaps with that of ‘Small Wind Turbines’. However, the two concepts are not analogous (Mertens, 2006). In fact, it is the typology of inflow that defines the technology and not the type or size of the device installed (Stankovic et al., 2009). The commercial penetration of small devices sold as urban wind turbines directed to private customers has led to the current situation of dealing with a consistent number of applications in locations normally visible to the public being not operating, or producing derisory amounts of energy

(Hamza, 2015). The effect of unsuccessful urban wind energy projects harms the image of the wind energy sector as a whole (Devine-Wright, 2005). In fact, one of the problems the wind energy industry faces is the community opposition to large wind farms, and a significant percentage of applications do not gain approval due to social acceptance (Hall et al., 2013). Among the reasons for the public aversion to wind turbines is the preservation of the rural landscape, or preconception about the supposed poor performance of devices, fed by local news on the urban wind energy technology (Evans et al., 2011). Moreover, part of the public is known to support wind energy as a concept, but contrasts with the installation of WTs if insisting on their property or community. This phenomenon is known as 'nimbyism', a neologism coming from the 'not-in-my-back-yard' expression which summarises the shift in culture and policy needed for the public. It is up to government to issue policies to foster renewable energy and set distributed energy generation goals (Devine-Wright, 2005; Martin, 2009).

It is up to wind energy research to provide a solid case for changes in policy. To date there is no justification to push for urban wind energy application at industrial level, as virtually no urban wind application has been able to provide but a derisory amount of clean energy (Ishugah et al., 2014).

Despite the off-putting outcome of applications, urban wind energy is still a well debated topic in wind energy research, due to the huge impact a reliable way of micro-harvesting might have on urban planning, especially in developing countries (Mainali and Silveira, 2013).

In the following, two milestone urban wind energy applications are discussed in detail to describe the practical challenges of harvesting wind in the built environment.

The 2010 completed Strata SE1 building in London (Figure 2.6a) hosts a set of wind turbines at its razor-shaped rooftop, designed to partially cover the energy need of the underneath luxury apartments. After construction, it was hailed as one of the most sustainable and innovative buildings ever made. However, occupants requested immediately to halt the operation of the three five-bladed turbines at night, due to the unbearable level of noise and vibration. After a year of discontinuous operation due to the many faults causing high costs of maintenance, the wind turbines were completely shut down. The reason for this disastrous publicity for the wind energy sector was attributed to flaws in the design of both the shape of the building, the installation of the wind turbines in ducts, and generally the high empiricism of this first remarkable, but not ready, experiment in urban wind energy (Bogle, 2011).

The Bahrain World Trade Centre (WTC) (Figure 2.6b) was also designed to host three large wind turbines installed between its 240m tall twin towers. Unlike the Strata SE1, the Bahrain WTC is shaped to act as an energy collector, straightening and redirecting the wind to be harvested. Nevertheless, it has been estimated that errors in the design such as the orientation of the collector with respect to dominant winds causes a 30% decrease in the energy being produced (Stathopoulos et al., 2018).

The Strata SE1 shows how intuition and empiricism are not key to success, and it should be an example not to be followed. The Bahrain WTC shows instead a pioneering and promising strategy to harvest wind from buildings, shaping them to exploit and possibly enhance the wind resource. However, the technology is still limited from the lack in understanding how wind interacts with buildings and wind turbine aerodynamics (Stathopoulos and Alrawashdeh, 2019).

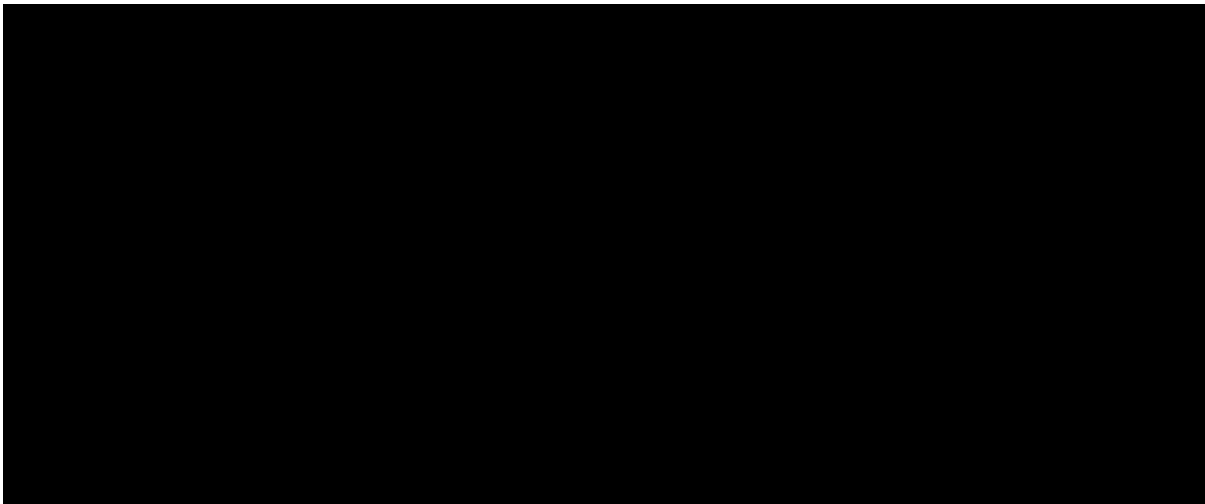


*Figure 2.6 – a) Strata SE1 Tower, in Elephant and Castle, London, UK;
b) The Bahrain World Trade Centre, in Manama, BH*

Several classifications have been proposed in the literature to identify the ways Urban Wind Energy (UWE) can be harvested (Stankovic et al., 2009). Focusing on power capacity aspects, three forms of Urban Wind Energy are recognisable:

- Distributed Wind Turbines, DWT. Energy generation with DWTs is a relatively theoretical concept, which includes the large majority of current urban wind energy applications. It can be defined as the integrated feeding to the grid by a whole totality of small devices harvesting energy from a large and non-uniform area (Lund and Østergaard, 2000). This definition poses challenges especially for the limits posed to the electricity grid (Ackermann et al., 2001);

- Industrial size WT's placed in urban premises. Medium-to-large WT's can be placed in highly turbulent sites, either in the proximity of buildings or major infrastructures (Oppenheim et al., 2004). It can be accounted as a special case of location in complex terrains (Kozmar et al., 2016).
- Building Augmented Wind Turbines, BAWT (sometimes Building Environment WT's, BEWT) include all those applications, which directly interfere with the building structure, using its shape as a local catalyser for the inflow wind (Grant et al., 2008; Stankovic et al., 2009);

Figure 2.7b shows an alternative The aforementioned classification can also stress the mutual positioning of Urban Wind Turbines (UWT) with a building. Four typical situations can be reported:

- WT's mounted on top of buildings (Fig. 2b-i);
- WT's mounted on the façade of buildings (Fig. 2b-ii);
- BAWTs, i.e. the shape of the building is adapted to the presence of WT's (Fig. 2b-iii);
- WT's mounted in the vicinity of buildings (Fig. 2b-iv).

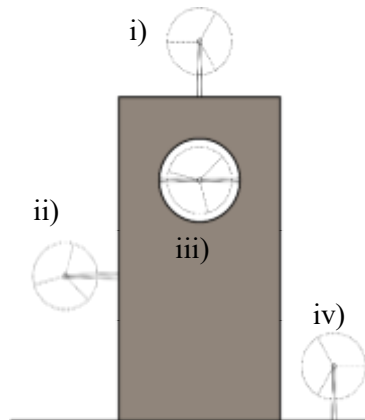


Figure 2.7 –Classification of Urban Wind Energy application based on the possible relationships of wind turbines with a building.

What associates all typologies is the direct interaction with the flow pattern around the building and how this is affected with the variability of the Urban Boundary Layer. The positioning of UWTs in order to maximize energy yield has to be strongly tied on a thorough understanding of the local features of the flow (Kareem and Wu, 2013).

Harvesting wind close to a building might seem a far-fetched option, as urban wind speed is normally lower than over plain terrain locations. However, in specific locations within the built environment

wind speed can locally increase enormously (Stathopoulos et al., 2018). This energy can be enhanced and harvested by tailoring the positioning of small devices with the assessment of the flow pattern around the building (Grauthoff, 1991).

Research in urban wind energy is mostly concerned either with improving the efficiency of small devices, especially VAWTs (Rezaeiha et al., 2017), or the assessment of the available wind resource (Stathopoulos et al., 2018). The flow pattern near a building is analogous to the flow pattern around any bluff body: a recirculation zone, a stagnating zone, a boundary and shear layer, and an accelerated flow region are present. Most UWE research is concerned with characterising the wind pattern over simple urban or neighbourhood configurations (Khayrullina et al., 2013), or over suitable idealised configurations such as high-rise buildings (Hemida et al., 2015, 2014) and street canyons (Walker, 2011). Very few works have instead considered a more thorough approach to investigate the aerodynamic interaction of a WT with a complex inflow (Sicot et al., 2008).



Figure 2.8. Southern view of the Vattenfall Horns Rev 1 offshore wind farm taken on the 12 February 2008. Courtesy: Vattenfall. Photographer: Christian Steiness.

Research efforts on the effect of atmospheric turbulence on wind turbines are not exclusively confined to the built environment. Figure 2.8 shows the Vattenfall Horns Rev offshore wind farm as photographed by C. Steiness on the 12th February 2008. The unicity of the meteorological conditions on that day made possible for the wakes of the wind turbines in operation to be visible, showing that even in the offshore environment an interaction with a highly turbulent flow can indeed take place due to wind turbine wakes (Hasager et al., 2013; Subramanian et al., 2016).

2.2.1. Urban Wind and Turbulence

Urban Boundary Layer

Buildings, as all civil engineering applications, lie inside the lowest 1-2 km layer of the troposphere, which is heavily characterised by highly turbulent flows. This is because of the vertical exchange of momentum, heat and humidity between the surface of earth and the lower part of the atmospheric boundary layer (ABL) (Panofsky and Dutton, 1984). At large wind speed, the ABL becomes fully turbulent, with a depth highly dependent on wind characteristics. This applies both to night and daytime, although atmospheric stability is an important issue for the ABL (Lee, 1979). The size of the so-called mixing depth, which is the total height of the ABL, may vary from several km in the daytime (unstable conditions) to few hundreds of meters during the night (stable conditions) (Emeis, 2013). By neglecting the effects of surface temperature and heat transfer within the ABL, then the so-called neutral conditions take place. However, full-scale measurements have confirmed that neutral conditions are found for less than the 30 % of the total lifetime of a WT (Hand et al., 2003). The Richardson number $\mathcal{R}i$ is a valuable parameter to be correlated with a reference WT's response in order to assess these effects (Hand et al., 2003). Although the role of atmospheric stability on wind energy is debated in literature, neutral ABL conditions are traditionally accepted and used in assessing the wind resource.

The ABL is divided into two sub-layers: the surface layer, SL, and the Prandtl layer, PL (Panofsky and Dutton, 1984). WTs are traditionally placed inside the SL, but for larger devices and in stable conditions both sublayers might be involved. This causes an important wind shear over the rotor area, together with of turbulence intensity up to 30 %, having a wide spectrum of turbulent length scales (Emeis,

2013). The atmospheric turbulence over flat terrains, hills and sea-surface has been for a long time investigated, hence we refer to the existing classic literature on the topic (Stull, 1988).

As the ABL interjects an urban conglomerate, a rather different subject has been developed in the recent years specifically studying the so-called Urban Boundary Layer (UBL) (Piringer et al., 2007). The urban environment and its meteorology is a challenge for research as it evolves together with urban settlements (Tanner and Harpham, 2014). As cities are in constant growth, the UBL is affected by human activities, such as the exhaustion of pollutants or the heating and ventilation of buildings. This causes additional turbulence in the wind in addition to signature turbulence from obstacles, a process that is known as ‘Urban Heat Island’.

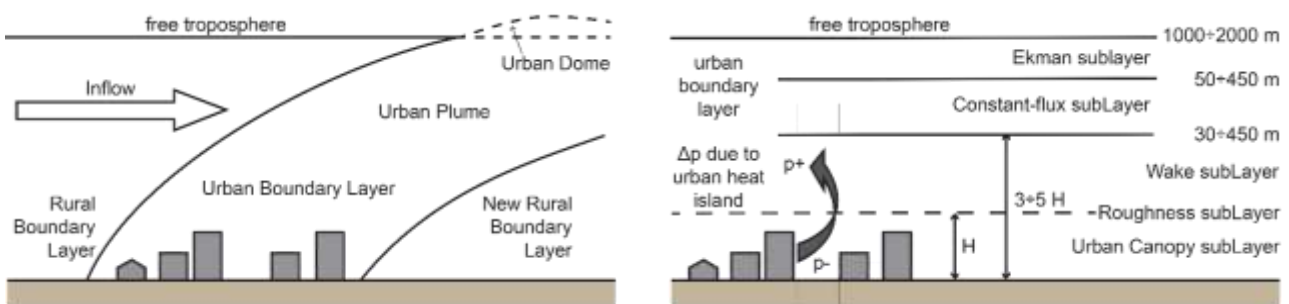


Figure 2.9. Urban plume downwind a large urban settlement and the vertical layers of the UBL.

Figure 2.9 schematises the complex secondary circulation of the wind towards the urban heat island due to local high temperature spots, large roughness elements, sealed areas with stagnant flow, reduced permeability to wind and heat storage, which all contribute to enhanced turbulence intensities and strong heat fluxes (Atkinson, 2003; Roth, 2000). As a result, the depth of the boundary layer increases, the so-called ‘Urban Dome’, where a stable nocturnal boundary layer is also prevented (Hidalgo et al., 2008; Kanda, 2007). Due to the complex urban physics, the UBL has a specific stratification compared to the ABL, as shown in Figure 2.9 (Piringer et al., 2007; Roth, 2000):

- the urban canopy layer, UCL, up to mean top of buildings H ;
- the wake layer, 3 to 5 times the mean building height;
- the constant flux layer or inertial sub-layer, which is akin to the Prandtl layer;
- the Ekman layer, where the wind direction adapts to the geostrophic winds.

For large WTs to be placed within the UBL, a crude estimation of the wind resource might be provided from simplified urban wind profiles, which are available (Emeis, 2013). However, small WTs have a different scale, as they are normally entirely placed within the urban canopy layer, i.e. on or near a building. Unfortunately, the wind speed and turbulence characteristics of the flow around buildings cannot be easily predicted using the boundary layer theory or any simplified analytical approach, as they normally show a broad variability from case to case (Hemida et al., 2015, 2014; Stathopoulos et al., 2018; Toja-Silva et al., 2015a). Therefore, an improved and integrated approach is needed, as the local effects provided by isolated buildings or particular features of the heat and humidity flux play a preponderant role for small WTs (Baniotopoulos et al., 2011; Miao et al., 2009).

Again, this crucial matter is not limited to wind turbines in the urban environment only. In fact, turbulence generated in the built environment may significantly affect the ABL profile for several km of distance from the urban settlement itself, potentially affecting nearby wind farms, although not immediately placed in built sites (Christiansen and Hasager, 2005).

Turbulence characteristics

As turbulence is generated in the built environment, turbulent wind encounters a wind turbine. Thus, a turbulent inflow condition can be defined in terms of wind speed and turbulence characteristics (Stathopoulos et al., 2018). Rigorous research on turbulence characteristics in the built environment has been limited to the scope of wind loading on structures, hence lacking the level of detail needed to address the positioning and performance of small wind turbines (Baniotopoulos and Stathopoulos, 2007). Despite the steady increase in the popularity of urban wind energy, research on turbulence characteristics present in the built environment has been very limited, and consensus on the topic is far from been achieved (Ishugah et al., 2014; KC et al., 2019; Stathopoulos and Alrawashdeh, 2019).

The reason for the lack in convincing results on the nature of urban turbulent inflows might lie on the derivation of this subject from aeronautics. Rotor blades provide the interface between the device and wind in the same exact way as an airplane wing. However, the latter is specifically designed to operate in low (or absent) turbulence, mostly at the Ekman layer (Buresti, 2012; Burton et al., 2011). If turbulence is present, the integral length scale is normally very large, much larger than the characteristic

size of the blade, which is the chord. Therefore, aeronautical blades are not designed or tested against atmospheric turbulence, and neither are wind turbine blades (Burton et al., 2011; Fichaux et al., 2011; Hau, 2013; Peeringa et al., 2015). Turbulent inflows interacting with a traditional onshore wind farm might feature a turbulence intensity varying from $\sim 5\%$ of coastal areas to $\sim 25\%$ on on-shore complex terrain (Antoniou et al., 1992). In the built environment even larger values are to be expected, depending obviously on the distance from obstacles (Emeis, 2013; KC et al., 2019). However, the motivation upon turbulence effects are considered negligible lies in the integral length scale of turbulence. As for traditional wind farms, a range from 0.001 m to almost 500 m is to be expected due to the physical mechanisms acting in the ABL and the energy cascade (Kaimal et al., 1976). Wind Energy Meteorology is indeed interested in analysing in detail the integral length scale, as a mean of assessing gustiness of the harvested wind resource (Emeis, 2014, 2013; Hansen et al., 2012; Hu et al., 2018). If the length scale is large enough, e.g. comparable to the rotor diameter or larger, the turbulence in the inflow acts as a slow variation of the wind direction from the perspective of the rotor. Then, the wind velocity becomes unsteady or intermittent and as a result the scope of the classical statistics of the wind speed is limited. In fact, typical wind velocity measurements at wind farm locations show that the normal Gaussian statistical description of turbulence is not applicable, as fat tails in the Weibull distribution of the wind velocity (Figure 2.10a), or spikiness (Figure 2.10b) are observed (Gottschall and Peinke, 2007; Milan et al., 2013; Mücke et al., 2011).

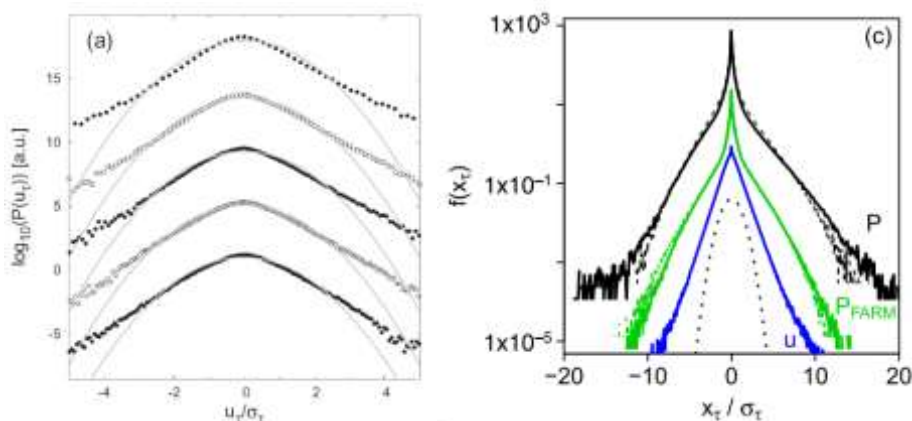


Figure 2.10 a) Probability Density Function (PDF) of wind speed fluctuations found within the atmospheric boundary layer, with “fat tails” and non-Gaussian distribution; b) PDF of WT power output and wind speed. Reproduced with permission from (Milan et al., 2013; Mücke et al., 2011).

Furthermore, after a wind turbine is installed, unsteadiness in the wind resource is also affected by signature turbulence generated from the wake of upstream wind turbines (Vermeer et al., 2003), hence affecting the performance of the whole wind farm (Luhur et al., 2015).

Turbulence in the built environment is affected by the surrounding to a greater extent than in the undisturbed ABL found in traditional wind farms. Therefore, the pattern of turbulence intensity and integral length scale is profoundly different (Micallef and van Bussel, 2018; Stathopoulos et al., 2018). Urban wind flow research has seen recently a surge in the number of investigations due to the ready availability of numerical tools (Toja-Silva et al., 2018) and recognised correlation of poor performance with the lack of knowledge of the inflow (Stathopoulos et al., 2018). Available studies have indeed provided some reference for the positioning of wind turbines and the assessment of the mean wind speed, identifying areas where obstacles may act beneficially to enhance the wind resource (Abohela et al., 2013; Tabrizi et al., 2014; Toja-Silva et al., 2015a, 2015b). However, the scope of these studies is mostly limited to analyse the influence of the shape of the building, or the roof, and to assess the best location position based on maximising the wind speed while minimising the turbulence intensity. All available studies pay attention to the wind turbine, its performance and to find strategies where to place it based on a priori set limitations. A comprehensive and detailed study on the characterisation of the urban wind resource is missing. The reason for this surprising gap in the research is to be found in the uncertainty of both numerical and physical simulations. In fact, suitable validation with experimental or full-scale data needs to be provided, as it is to date largely disregarded due to the very few application and a general lack of interest from the mainstream wind energy industry (KC et al., 2019).

Current Standards

Despite the very limited knowledge of the urban wind resource, or the so far unacceptable performance of urban wind applications, or the very limited interest of the wind energy industry, the number of urban wind energy applications has been showing a steady increase over the past decade (Gsänger and Pitteloud, 2015). Wind Turbines, as mechanical devices, have to abide by law requirements in terms of safety, durability and performance. The International standard IEC 61400 is the most approved and applied standard for the design and certification of small wind turbines (Evans et al., 2017; KC et al.,

2019; Tabrizi et al., 2015). In Table 2.1, a list of the most relevant national and international standards on the design and certification of small wind turbines is provided. National standards and the international DNV-GL Standard normally refer to the IEC 61400 series. As wind turbines are placed in the built environment, a great deal of information provided by the IEC 61400 standard is related to the assessment of the urban wind resource and its turbulence characteristics.

Table 2.1. Available international and international standards on small wind turbines.

<i>Standard</i>	<i>Description</i>	<i>Year</i>
<i>IEC 61400-1</i>	<i>Wind energy generation systems - Part 1: Design requirements</i>	<i>2019-02</i>
<i>IEC 61400-2</i>	<i>Ed.3, Small Wind Turbines</i>	<i>2013-12</i>
<i>IEC 61400-22</i>	<i>Wind turbines - Part 22: Conformity Testing and Certification</i>	<i>2010-05</i>
<i>Renewable UK DECC – Dep. Of Energy & Climate Change</i>	<i>Small Wind Turbine Standard Microgeneration Certification Scheme (MCS)</i>	<i>2014-01 2014</i>
<i>AWEA – American Wind Energy Association</i>	<i>Small Wind Turbine Performance and Safety Standard</i>	<i>2009</i>
<i>Danish Energy Authority</i>	<i>Danish Executive Order from the Danish Energy Authority No. 73</i>	<i>2013</i>
<i>DNVGL-SE-0441</i>	<i>Guideline for the Certification of Wind Turbines</i>	<i>2016-06</i>
<i>DNVGL-ST-0125</i>	<i>Technical Note for Grid Code Compliance</i>	<i>2016-03</i>
<i>DIBt – Deutsches Institut für Bautechnik</i>	<i>German Type Approval according to DIBt-Regulation “Richtlinie für Windenergieanlagen Einwirkungen und Stand sicherheitsnachweise für Turm und Gründung“</i>	<i>Reihe B, Heft 8, Fassung 2012</i>
<i>NEN-EN-IEC 62305 Nieuwe Europese Normen</i>	<i>Lightning Protection – Small wind turbines</i>	<i>2009</i>

The IEC 61400-2:2013 standard specifically deals with small wind turbines and the description of mean and maximum wind field models, and turbulence characteristics required to calculate loads and hence performance of the device (*IEC 61400-2:2013 Wind turbines - Part 2: Small wind turbines*, 2013). While this standard is similar to the IEC 61400-1:2019, which gives indications for wind turbines in general, significant changes are provided to make it applicable specifically to small wind turbines (*IEC 61400-1:2019 Wind energy generation systems - Part 1: Design requirements*, 2019).

A thorough review of the specifications contained in the standards is out of the scope of this work, and more detailed information can be found in relevant literature on the topic (Evans et al., 2017; KC et al.,

2019; Micallef and van Bussel, 2018; Stensgaard Toft et al., 2016). However, it might be worthwhile to give a brief summary on the applicability and accuracy of IEC 61400-2 indications in regards to the real urban wind resource. The standard IEC 61400-2 defines a Normal Turbulence Model (NTM) for the turbulence characteristics, which has been defined based on extensive measurements of open terrain full-scale observations (Stork et al., 1998). The current formulation for the turbulence intensity yields:

$$I_u = \frac{\sigma_u}{U} \quad (2.1),$$

where σ_u is the standard deviation of wind speed at hub height, given by

$$\sigma_u = \frac{I_{15}(15+aU)}{(a+1)} \quad (2.2).$$

I_{15} is the 90th percentile of the characteristic turbulence intensity at hub height, a is a slope parameter, U is the 10-min average of the wind speed at hub height. In Table 2.2, values for I_{15} , a and U , are specified depending on relevant wind turbine classes. U_{ref} is the reference design wind speed.

Table 2.2. Turbulence parameters for wind turbine classes I-IV (IEC 61400-2:2013).

	Wind Turbine Classes			
	I	II	III	IV
U_{ref} (m/s)	50	42.5	37.5	30
U (m/s)	10	8.5	7.5	6
I_{15} (%)	18	18	18	18
a	2	2	2	2

Rearranging Equation (2.2). the following expression is found for the turbulence intensity

$$I_u = \frac{0.9}{U} + 0.12 \quad (2.3).$$

Equation (2.3) is used by the IEC 61400-2 as a way of calculating a limit for wind turbines to operate, namely 18 %. These indications on the turbulence characteristics are mutated from the IEC 61400-1 standard for traditional open terrain wind farms. However, several studies have confirmed that the wind at urban locations prone to the installation of wind turbines experience far higher turbulence intensities up to ~35 %, while assumptions on spectra and methodology to analyse results are difficultly matched with full-scale data (Evans et al., 2017; KC et al., 2019; Tabrizi et al., 2015). Furthermore, any indication on the integral length scale is missing, showing that this parameter is not considered of

interest, while in fact it contributes greatly to the understanding of the intermittency turbulence causes to wind speed (Milan et al., 2013) and the related effect of wind turbine performance (Lee et al., 2012; Luhur et al., 2015; Sunderland et al., 2013) Indications contained in the IEC 61400-2 need to be corroborated with additional research on turbulence in the built environment, with the same rigourity as research conducted on open terrain sites for the past decades.

2.2.2. Urban Wind Turbines

Aerodynamic Performance

The rotor of a wind turbine converts the kinetic energy carried by the wind flow into rotational kinetic energy to be transformed into electricity through a power generator placed at the hub of the wind turbine (Burton et al., 2011; Hau, 2013). Pioneering research on wind turbine rotors of the first applications was borrowed from classical aeronautics (Hau, 2013). However, airplane wings and wind turbine rotors experience a different flow pattern behaviour. In fact, wind turbines are placed in the lowest part of the atmospheric boundary layer, exposed to highly unsteady inflow conditions and rather low wind speeds, while being the largest self-propelled structures ever built. Therefore, wind energy research has evolved into an autonomous subject (Burton et al., 2011; Gasch and Twele, 2012; Hau, 2013).

The traditional wind turbine typology is the three-bladed horizontal axis wind turbine (HAWT). This technology has been specifically optimised to maximise power performance of onshore wind farms set out in open terrain (Burton et al., 2011). This typology has some limitations and disadvantage which are overshadowed by the efficiency of the system. Small Wind Turbines placed in the built environment are subjected to a whole difference configuration. The intermittent, highly fluctuating wind direction and speed of the built environment poses many challenges to the control system of a HAWT, and therefore other configurations are likely. Alternatively blades can be arranged onto a vertical axis wind turbine (VAWT), which is rather insensitive to wind direction and it is able to operate at low wind speeds (Rezaeiha et al., 2018). Both HAWT and VAWT have been subjected to scrutiny to understand which typology is most suited to highly turbulent environments with regards to the aerodynamic performance (Pagnini et al., 2015). A thorough review of wind turbine aerodynamics is out of the scope of the present work, and more details can be found in relevant literature (Hansen, 2015; Snel, 2003).

What is clear from wind energy applications is that steady wind is an off-design condition. Numerous phenomena contribute to the unsteadiness of the wind inflow, strongly affecting the behaviour of a WT (Leishman, 2002a). Despite the number of successful applications, the complexity of the aerodynamic behaviour causes many aerodynamic challenges yet to be overcome (Hansen, 2015; Hansen and Aagaard Madsen, 2011; van Kuik et al., 2006, 2016).

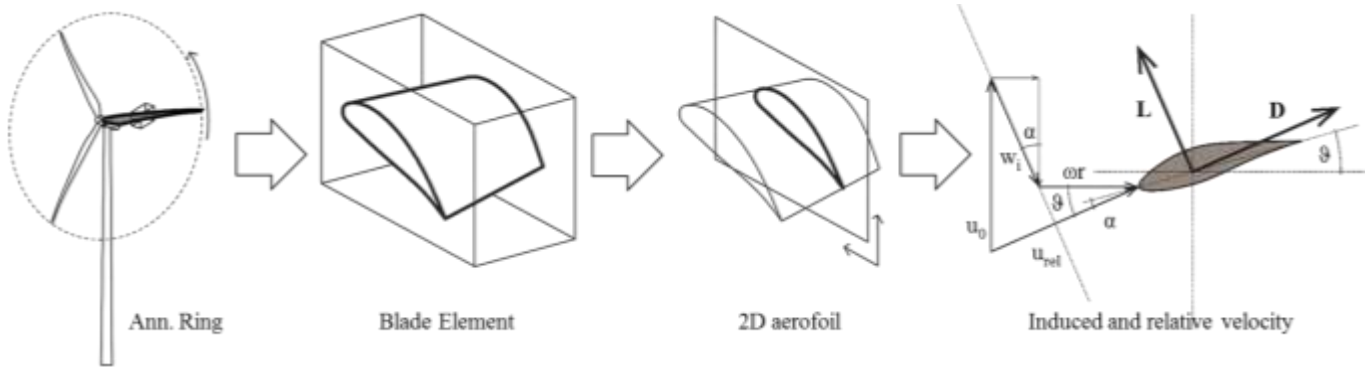


Figure 2.11. Blade Element Momentum Theory diagram. θ is the pitch angle; α the angle of attack; ω the angular velocity of the rotor; r the distance of annular rings; u_0 is the wind speed; w_i the apparent wind speed used to take into account unsteady effects; $u_{rel} = u_0 \times \omega r \times w_i$ is the real wind speed, vectorial product of the wind speeds and the rotational speed of the rotor; L and D are respectively the Lift and Drag forces.

Figure 2.11 shows a schematic of the Blade Element Momentum (BEM) theory, which is used to calculate aerodynamic forces on the wind turbine blades. The rotor is decomposed into annular rings having a distance r from the hub and thickness δr . The annular ring intercepts a blade element, which is then collapsed into its 2D cross-section, the aerofoil. All forces are calculated based on 2D aerofoil data, hence the real unknown in the BEM method is the angle of attack. The reliability of aerofoil data for wind turbine aerodynamic is still a debated topic (Tangler, 2002, 2004). The rotational velocity vector ωr is composed together with the wind speed u_0 . An additional wind speed, named apparent wind speed w_i is used to take into account all unsteady effects. Unsteady effects have been extensively studied, and many analytical models have been developed to flank the BEM method. In the following some of the most important sources for unsteadiness are listed.

- Yawed flow, i.e. the azimuthal misalignment between the rotor axis and the wind direction;
- Tower shadowing, i.e. the dynamical phenomenon, which occurs on the blades when they get through the tower during rotation;
- Flow interferences with upstream wakes, i.e. particular flow patterns in aligned wind turbines;

- Rotational augmentation, i.e. enhancement of aerodynamic properties due to rotation;
- Root and tip vortices, and general three-dimensional effects;
- Roughness of blades, in particular of the leading edge, due to debris or insects or micro-dents;
- Aerofoil geometry and blade planform and twisting;
- Atmospheric Boundary Layer properties, such as wind shear over the rotor, i.e. the vertical gradient of wind velocity distribution, fluctuations in wind speed due to turbulence in the inflow, or intermittent wind, such as gusts or extreme events.

These topics represent current active research in the aerodynamics of WTs (Hansen, 2015; Hansen and Aagaard Madsen, 2011; Rasmussen et al., 2003; Snel, 2003; van Kuik et al., 2016).

Unsteady phenomena have also a great impact on control strategies. Nowadays, active full-span pitch control is the standard method in the control system of industrial wind turbines, while in the urban environment fixed pitch or passive stall is more common. For small and medium WTs, the pitch angle is modified for the blades altogether, accordingly with the free-stream wind speed. For larger WTs, more advanced systems are used, such as the individual pitch control, IPC. This way, the heavy differences in the loading of the single blades due to wind shear and the differences in wind fluctuations at the top and the bottom of the rotor, are weakened (Burton et al., 2011). To a more complex control system are associated higher maintenance costs, which are normally offset by savings on the construction of the blades (Gasch and Tvele, 2012).

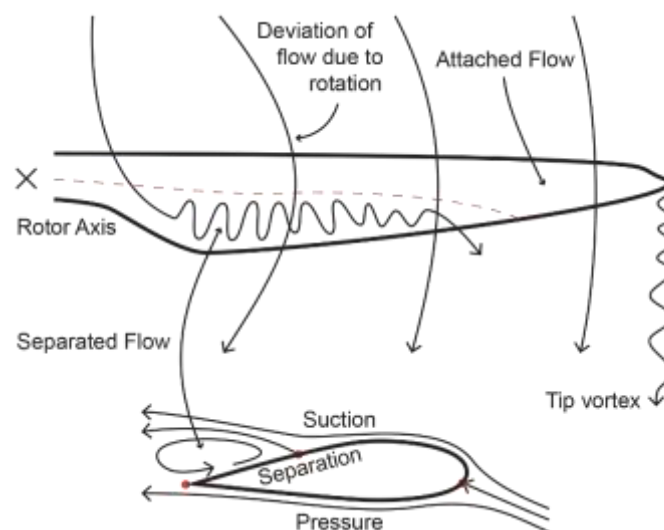


Figure 2.12. Flow pattern over a WT blade, showing the separation area on the suction (upper) side of a Wind Turbine blade, and the centrifugal deviation of attached flow due to rotation.

Presuming to have uniform inflow, with the variation of the angle of attack, aerofoils experience a broad range of aerodynamic loading along the blade span. Figure 2.12 shows a typical flow pattern on a wind turbine blade. At every section the aerofoil experiences a stagnation point and at least a separation point. If the separation point coincides with the trailing edge of the aerofoil, the flow is attached and the aerofoil is analogous to a theoretical aerofoil producing lift for heavier-than-air flight (Buresti, 2012). When the angle of attack α is sufficiently high, two separation points occur and the flow is separated. In correspondence of a specific angle of attack, the aerodynamic behaviour experiences a sharp change, usually a sudden drop in the lift, and static stall occurs. For higher angles of attack, stall continues developing until full stall is present, which means the separation point is close to the leading edge of the aerofoil. In literature, full stall is sometimes erroneously referred to as deep stall (Buresti, 2012). If the angle of attack varies in an unsteady way, the flow pattern completely changes, and dynamic stall occurs (Leishman, 2002b). In aeronautical literature, dynamic stall is normally referred as deep stall. The deep stall condition has been given a dramatic attention in recent wind energy research, since important discrepancies in the expected durability of wind turbines and the resulting one were noticed (Guntur et al., 2016).

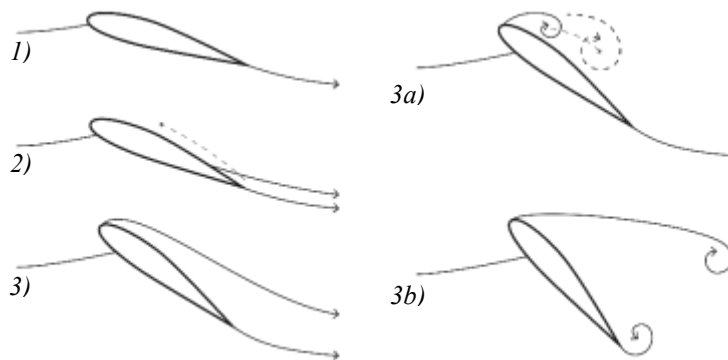


Figure 2.13. Evolution of stall mechanism with angle of attack α .
 1) $\alpha \leq \alpha_{cr}$ the flow is fully attached; 2) Trailing edge separation with separation point moving forward with increasing α ; 3) Full stall with separation point on leading edge. In presence of dynamic pitching different flow patterns are experienced.
 3a) Dynamic stall Vortex; 3b) Aft Dynamic Stall Vortex (Hölling et al., 2014; Leishman, 2002a).

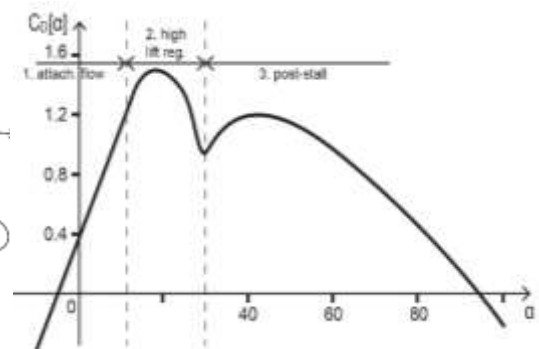


Figure 2.14. Typical distribution of Lift coefficient against angle of attack α .

1) flow is attached; 2) trailing edge separation with steep drop of lift;
 3) full stall development with leading edge separation.

Figure 2.13 shows a schematic of the flow pattern on an aerofoil under static and dynamic stall. The flow over dynamically stalled WT blades presents a vortex pattern on the suction surface of the aerofoil, i.e. dynamic stall and aft dynamic stall vortices (DSV and ADSV). Deep stall is inevitable in VAWTs, as the direction of wind does not match that of the aerofoil, and this is the main reason of their lower power coefficient (Almohammadi et al., 2015). Also HAWT might experience deep stall, even if pitch control and twisting of the blades is used, for example during control system activities such as the dynamic pitching of aerofoils, or temporary yawed flow conditions (which is a very common operating condition for WTs in arrays and clusters). Also wind shear and atmospheric turbulence might cause wind gusts which affect the stall mechanism of a wind turbine blade (Hansen, 2015). In addition to the characteristics of the incoming flow, also aerofoil geometry, and the frequency and amplitude of pitching might provide a strong effect on the behaviour. Though much knowledge is available on static and dynamic stall, experiments have been mostly performed on helicopters, with the aim of avoiding it, while in wind turbines this is an inevitable condition (Leishman, 2000).

Figure 2.14 shows a typical shape for the lift curve with a marked stall mechanism. In aeronautical engineering, the lift curve is normally studied concerning the maximum lift coefficient or the angle of attack at which it occurs. Wind turbine aerodynamics are instead interested in a broader scope. Bluff body aerodynamics studies massive separated-reattached flows over non-streamlined bodies, with a flow pattern that experiences most recirculation and shear regions all over the surfaces of the body. Instead, classical aerodynamics is bound to aeronautical problems, i.e. streamlined bodies, with mainly attached flow with a rather different pattern and assessment methods. WT blades are in-between traditional aerofoils and bluff bodies: the flow remains attached for a meaningful part of the service life, while it is separated for the largest amount of time, experiencing static or dynamic stall, whose complex development and dynamics is yet to be fully mastered (Buresti, 2012; Burton et al., 2011; Hau, 2013). The stall mechanism has been detected since the very first wind energy applications. The Danish Concept used stall in order to limit the power coefficient for the highest wind speeds. However, it resulted in higher loading on structural elements and irregular distribution of torque. For this reason, both the tower and the drivetrain/generator complex experienced high vibration rate and, hence, fatigue. This has resulted in premature failures and unexpected shutdowns. Lack of knowledge on the stall

mechanism has brought manufacturers to prefer pitch control systems, instead of stall control (Hau, 2013). To improve performance under stall, vortex generators, leading edge trimmers, or localised roughness are implemented as passive control systems to improve overall performance and eliminating the rate of furling at higher wind speeds (Hansen and Aagaard Madsen, 2011). Even though modern WT's have improved considerably, lack of comprehension over stall and dynamic stall is still considered the main aspect to intervene over expensive controlling systems, and short life-cycle (Rasmussen et al., 2003; van Kuik et al., 2016).

In stall, the angle of attack and the rate of decrease/increase of the lift coefficient drop/recovery are extremely variable depending on several aerodynamic features (Timmer, 2010):

- Aerofoil typology, i.e. the blade cross-section, usually variable span-wise;
- Pitch angle of blade, ϑ , i.e. the geometric inclination of the blade-chord with respect to the plan of rotation. This is the main parameter regarding power control system;
- Angle of attack, α , i.e. the relative angle between the chord line of aerofoil and the apparent direction of flow, which depends basically on the tip speed ratio, λ ;
- Blade and leading edge roughness;
- Rotation of blades, i.e. centrifugal and Coriolis effects yielding rotational augmentation;
- Tip and root region highly three-dimensional behaviour;
- Unsteady inflow, i.e. inlet turbulence intensity and diverse length scales of turbulence.

This list is intentionally very similar to the previous list of different causes for unsteadiness, to show how stall is the key aerodynamic phenomenon to interpret and act upon the aerodynamic performance of an aerofoil under an unsteady inflow.

In fact, failures of wind farms placed in complex terrains, unpredictability of the power resource under a given wind speed, high maintenance costs and lack of performance might depend on insufficient description on how unsteadiness in the ABL, i.e. turbulence, affects the stall mechanism and therefore the aerodynamic behaviour.

Effect of turbulence on bluff bodies

Inflow turbulence is known to interact with a bluff body, modifying its aerodynamic performance in a similar way as the Reynolds effect acts on many bluff bodies (Zdravkovich, 1997). Research on the effect of free stream turbulence characteristics has been quite popular in the 1980s (Bearman and Morel, 1983; Roshko, 1993; Saathoff and Melbourne, 1987). Recent works on the effect of turbulence are instead quite limited, and a possible reason for this is the intrinsic difficulty in varying turbulence characteristics in wind tunnel testing, which in turn does not allow to replicate or scale accurately conditions found in the atmospheric boundary layer (Haan et al., 1998).

Inflow turbulence has two effects on the boundary layer of a bluff body (Simiu and Scanlan, 1986):

- Triggering of laminar-to-turbulent transition of the boundary layer, lowering Lift;
- Increase of transport of momentum between the boundary layer region and the undisturbed flow, thus increasing the resistance against adverse pressure gradient and delaying separation, increasing maximum Lift and increasing Drag.

Research on the effect of turbulence on separation-reattachment flow pattern, and turbulent shear flows was thoroughly conducted for backward facing steps, forward facing steps, and blunt plates, in a variety of different configurations (Figure 2.15). They offer a good prototype for fine-tuning and assessing more complex flow behaviour.

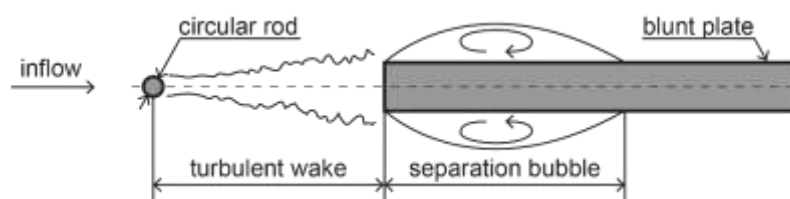


Figure 2.15. A typical classical experimental setup for the study of flow pattern variations under a turbulent inflow. Here the blunt plate experimental set of a classical experiment (Sasaki and Kiya, 1985).

Results agree upon turbulence intensity having a strong correlation with the separation bubble length (or reattachment length), even compared to other parameters, such as roughness (Bearman and Morel, 1983; Essel and Tachie, 2015). An agreed motivation for this is that turbulence energises the shear layer hence diminishing the dimension of the separation bubble (Kiya and Sasaki, 1985; Sasaki and Kiya, 1983). Figure 2.16 clarifies the effect of turbulence on a rectangular prism with growing aspect ratio,

with specific reference to the wake contraction due to the enhanced turbulent mixing of the shear layer (Laneville et al., 1975; Simiu and Scanlan, 1986). A shorter contracted wake is related to a higher Drag coefficient, therefore turbulence contract the wake and increases Drag. However, depending on the aerodynamic of the separation bubble, a reattachment might occur which in turn energises the wake and lowers Drag in turbulence. This means that in engineering applications, the effect of Drag is all but trivial, and it needs to be assessed carefully.

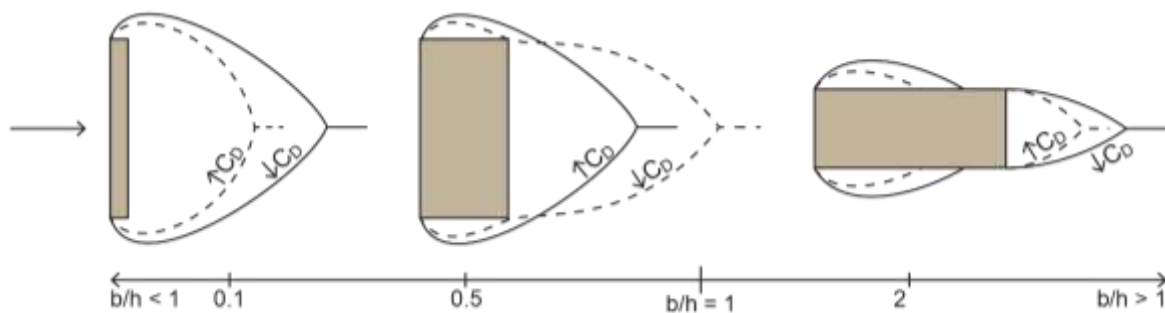


Figure 2.16. Massive separated flow over a bluff body for smooth flow (solid line) and turbulent flow (dashed line), showing variability of the effect of turbulence with shape aspect ratio (Simiu and Scanlan, 1986).

In Chapter 3, more relevant literature on the topic is reviewed. All works agree that turbulence intensity is the main parameter to cause the interaction to occur. However, studies are sometimes baffled in their conclusions on whether this effect can be neglected or not based on the integral length scale, and a clear agreement on the issue is far to be reached.

Effect of turbulence on wind turbine blades

As stated in the previous, a stalled aerofoil is somewhat analogous to a bluff body, as it has a pattern of stagnation, separation and reattachment. In the exact same way as a bluff body, turbulence also interacts with a stalled aerofoil. Turbulence effects on wind turbine aerofoils have received some attention in recent years, detaching from the classical aeronautical accepted concept that turbulence effects are to be neglected. Reliable 2D aerofoil data are at the core of the BEM method, and if an effect is present, which has not been proved so far for atmospheric flows, the accuracy of the methodology would indeed benefit from a progress in the understanding of the interaction (Hansen and Aagaard Madsen, 2011). A thorough discussion upon available literature on the effect of turbulence on aerofoils is available in Chapter 3. However, some details are given in this chapter regarding research trends on the effect of turbulence on wind turbine aerofoil to highlight successes and limitations of relevant research.

Research on inflow turbulence and its effect on the flow pattern over an aerofoil has received some attention in earlier works on the topic (Hoffmann, 1991; Huang and Lee, 1999; McKeough, 1976; Mueller et al., 1983). First investigations have tested experimentally several chord lengths and aerofoil profiles, aspect ratios or the thickness-to-chord ratio, surface roughness, and Reynolds regimes. Traditional wind tunnel testing and flow visualization techniques have been mostly performed for the investigation. All studies confirm an increase in the lift coefficient in turbulence, with a limited effect on the drag coefficient. However, most studies use pressure taps to investigate the variation of the force, which only allow for the shape drag and not the friction drag to be measured. Another finding is the disappearance of the laminar separation bubble, if present.

What differentiate modern studies from the first applications is the consideration of the angle of attack α as a parameter. α is indeed the governing parameter for the stall mechanism of aerofoils, which is particularly interesting for wind turbine blades.

Studies on wind turbine blades have experienced a surge in popularity in the last decade (Sicot et al., 2006b). Reasons for this might be the renewed interest in wake aerodynamics and optimisation of wind farm setup (Wu and Porté-Agel, 2012); the challenging aerodynamics of wind farms placed in complex terrain sites (Conan et al., 2016); and the popularity of small wind turbines and urban wind energy (Stathopoulos et al., 2018).

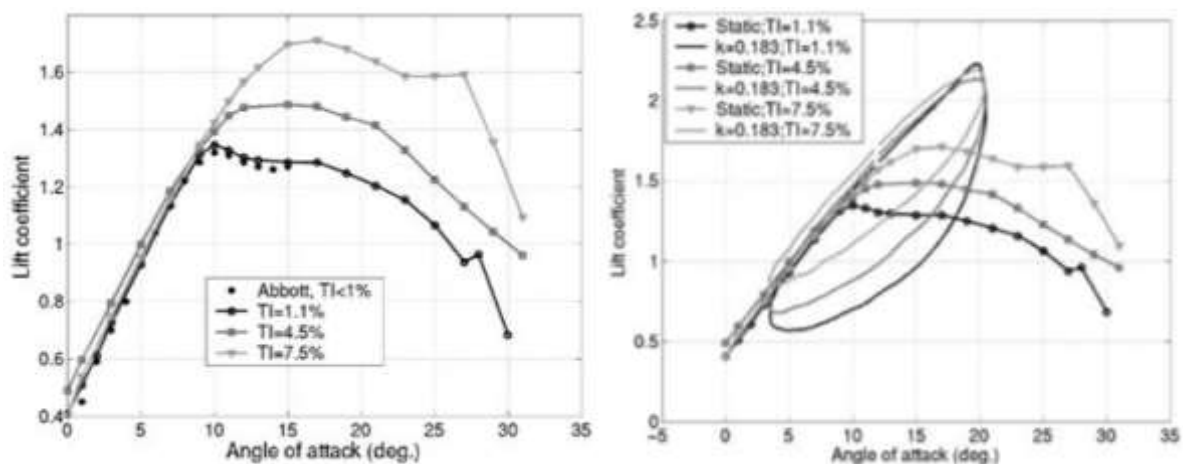


Figure 2.17. Lift coefficient variation under varying turbulent intensity of inflow, for a) static and b) dynamic (with comparison) condition. Reproduced with permission from (Amandolèse and Széchenyi, 2004).

Figure 2.17 shows the effect of turbulence on the stall mechanism for a wind turbine aerofoil in static and deep stall according to one of the earliest studies on wind turbine aerofoils (Amandolèse and

Széchényi, 2004). The turbulence intensity is varied together with the angle of attack. Results confirm results from previous experiments, i.e. the maximum Lift increase. However, in the case of deep stall turbulence shrinks the hysteric curve. What is particularly interesting in Figure 2.17 is the linear part of the lift coefficient curve, which seems not to be affected by turbulence.

More systematic works on wind turbines studied the steady and the unsteady properties of the separation flow over a pitching aerofoil (Devinant et al., 2002; Sicot et al., 2006a). Being submerged in the ABL or placed in clusters, WT's experience a broad range of turbulence intensities, which have to be carefully weighted up. Besides confirming the increase in lift, these studies have shown that in high turbulence the aerodynamic performance is not affected by variations in the Reynolds number. However, it is not clear whether this is due to non-uniformity and wind shear in the inlet wind profile used or truly depending on the turbulence intensity. The authors explained that oscillations in the position of the separation point occur edge-wise, hence affecting the behaviour and impeding the flow to interact with the boundary layer on the aerofoil.

The rotational motion of blades also influences stall. This is called rotational augmentation, and its effect is to delay stall due to the combined effect of the Coriolis forces span-wise and centrifugal pumping edge-wise (Gross et al., 2012), but its physical mechanism is yet under argument (Guntur et al., 2016). Nevertheless, if compared to inflow turbulence, the effects of rotational augmentation on the overall aerodynamic loading seem to be negligible (Sicot et al., 2008).

Both HAWT and VAWT have been considered. But there are some fundamental differences: while for a VAWT the clue is given to the power efficiency, to HAWT the detailed assessment of the aerodynamic unsteady loading is at issue. Nevertheless, the power coefficient depends essentially on the Reynolds number and on the mean wind speed, while structural issues are rather more important.

Usually the increase in lift caused by turbulent intensity goes along an increase of drag, but this varies strongly with the typology of aerofoil. A comprehensive evaluation of the stall mechanism development with regards of the free-stream turbulence should also consider the role of not only the turbulence intensity (being careful about the definition of the time-record), but also of length scale and isotropy, which can lead to broad variation in results (Lubitz, 2014). Reviewed experiments do not give a physical explanation on the actual role of turbulence characteristics. It is commonly accepted that turbulence

intensity gives the flow enough energy to remain attached to the suction surface of aerofoils for a longer time, hence enhancing lift and overall aerodynamic performance. In literature it is not confirmed whether this is the case for every turbulent length scale considered, however an effect is still noticeable if the length scale is comparable with the chord length (Maldonado et al., 2015).

Although wind tunnel testing remain the preferred methodology to investigate effects of turbulence, also numerical simulations have been implemented (Kim and Xie, 2016). CFD represents a powerful tool for the description of stall mechanism, since one can highlight the importance of effects such as three-dimensionality on the overall power performance, while ideally not being limited by the size of the computational domain to explore the turbulence variability found in the ABL (Almohammadi et al., 2015; Gilling et al., 2009).

What associates all works so far is a questionable choice of the chosen inlet turbulence characteristics. Firstly, no sufficient discussion is attempted on the role of the integral length scale of turbulence, while not appropriate knowledge and motivation is available for the choice of the turbulence intensities to be tested. Values found in literature are mostly due to limitations in the generation of turbulence in wind tunnel testing for live size blades and devices, which normally allows for turbulence in the inflow not to be scalable with real full scale conditions.

The critical evaluation of the few presented works suggests the following weaknesses in the research:

- Role of turbulent isotropy and comparison with actual atmospheric turbulence characteristics (isotropy of turbulence is not a natural condition of wind flow, but it is the only studied condition in wind tunnels);
- Role of intermittent statistics of wind on overall structural reliance and power efficiency, i.e. due to larger length scales or gusts;
- Study of turbulent effects based on their length scales (usually wind tunnel experiments present length scale which is comparable to chord length, while in the ABL usually bigger scales are found);
- Study of reduced frequency and tip speed ratio variation occurring for fluctuation in wind velocity, i.e. the asynchronous response of a structure under intermittent loading (fatigue issues);

- Study of coupling effect of rotation effects and turbulent inflow, i.e. rotational augmentation under varying inflow conditions (it is normally accepted for helicopter to consider the rotation as not having effects on stall mechanism, but a coupled evaluation seems to miss);
- Study of three-dimensional effects and two-dimensional data (BEM theory for the design of aerofoil) in order to assess precise power output efficiency and structural reliability;
- Comparison between simulation models (many research are based on RANS and turbulence models in an attempt to validate their applicability to specific problems. For wind turbines, an achievement is missing. It is not clear, whether it is necessary to model the whole turbine with rotating meshes, or to predict actual separation points without laminar-to-turbulent transition models, or further to consider the effect of aero-elasticity of blades in the flow-field, with the implementation of FSI algorithms).

2.3. Background on research methodology

In the previous sections, a meaningful link between the lack of performance and lack in knowledge on wind turbine aerodynamics has been found, with several weaknesses in available results. Although this aspect is going to be developed more in detail in the main body of the thesis, a digression on the available methodologies to test the effect of turbulence is presented in this Section to show advantages and drawbacks of methods with regards to this complex problem.

There are essentially three methodologies used by researchers: full-scale measurements, experimental testing and computational simulation.

2.3.1. Full Scale Tests

There are several attempts in the literature to get valuable results from a full-scale wind turbine, whether placed in a real wind farm, in an urban context (Pagnini et al., 2015), or a testcase built for this purpose (Lubitz, 2014). In particular, even with high resolution measurements of both wind speed and energy output, the results are difficult to generalize. Turbulent gusts affect wind alignment, aerofoil performance and furling limit, which is a major issue especially for small WT, which usually are used in such tests. The impact of turbulence on power output may become less consistent than other issues, such as cutting off and furling effects. This occurs because free-stream turbulence at high speed, near cut-off, causes gusts. Small WTs usually experience intermittent furling with consequently significant hunting for the main wind direction and off-axis orientation, with reduction of power generation, which are difficult to relate directly with free-stream turbulence. Nevertheless turbulence is present even in low turbulence areas due to atmospheric non-stable conditions for over 60 % of the service life of a wind turbine (Hand et al., 2003). This gives that turbulent structures may need specific statistics of wind, depending on their own extremely variable distribution, which needs to take into account of stability effects. A possible way for stability to be taken into account is the use of the Richardson number Ri definition, correlating the fluctuating component of wind with the dynamic loading (Luhur et al., 2015).

2.3.2. *Wind Tunnel Testing*

Wind tunnel testing has been, and still remains, the fundamental investigation mean used in wind engineering for getting further insight on bluff aerodynamics issues. WT aerodynamics is not an exception, and many experiments focus on assessing the effects of inflow turbulence over whole WTs or WT blades or aerofoils, with or without concurrent phenomena. However the way inflow turbulence is created, strongly affects results (Kang et al., 2003). Though it is necessary to reproduce actual site conditions, usually passive or active grids are used, which produce homogeneous isotropic turbulence that rather poorly represents atmospheric conditions (Cekli and van de Water, 2010). Furthermore a significant effort has been put over turbulence intensity modelling, without taking care of turbulent length scales, which perhaps have an important effects on the aerodynamic response of a WT blade (Maldonado et al., 2015). An extensive review of the limitations of wind tunnel testing is given in Chapter 3.

2.3.3. *Computational Fluid Dynamics*

A promising method for getting more insight in the actual aerodynamics of WTs is Computational Fluid-Dynamics (CFD). While CFD has been representing a very important branch in the subject of wake aerodynamics, there are only few applications concerning inflow turbulence (Patrino and Ricci, 2017). This is mainly because of the intrinsic difficulty in modelling verisimilar boundary conditions, such as body forces (Vasaturo et al., 2018). In aerodynamics, a wrongful assumption for the boundary conditions can significantly affect the reliability of results. While for a laminar inflow defining a profile for the wind speed is deterministic, for turbulent inflow, it is necessary to describe accurately the fluctuating component of inlet velocity. Atmospheric turbulence modelling strongly depends on the proper definition of inflow turbulence. A smattering of this important aspect of CFD simulation of turbulent inflow is proposed in the following, with additional details in Chapters 4, 5 and 7.

Two categories of numerical inlet exist in practice:

- recycle/rescale methods;
- synthetic approaches.

The recycle-rescale method provides an inlet from computed data from a specific region downwards the simulation or an auxiliary simulation. Three methods are comprised in this category: periodic boundary conditions, PBC, pre-computed method and internal mapping method. The PBC method re-uses outlet data as inlet condition, and it is very useful for a repeated geometry. The precomputed method uses an external further mesh in order to develop desired level of turbulence to then be applied as inlet in the actual simulation. The internal mapping consists of the collection of flow data from a point downwards to be applied as inlet. The latter solution is the most evolved, but it introduces an error that can be controlled by imposing the divergence-free condition (Chaudhari, 2014; Immer, 2016).

The synthetic approach is a more refined method that is based on the calculation of artificial fluctuations on the statistical properties, which are imposed to the actual computational domain. They are free from the disadvantages of the recycling methods, the introduction of periodicity of fluctuation and overall error, because a random signal is generated. Several recent studies focus on this method, pointing out that a physical meaning free random turbulence generation is equivalent to a white noise, hence having no tangible difference with the laminar inflow and decaying very rapidly (Gilling et al., 2009). A coherent structure of the flow is necessary, and the last proposed method focus on its modelling. To impose spatial and temporal correlation two approaches exist: the spectral method and the algebraic method (Tabor and Baba-Ahmadi, 2010)

Once boundary conditions are set, several techniques to model turbulence exist which might be used to detect the effects on the aerofoil boundary layer and its wake. The wind resource is almost entirely modelled using Reynolds Averaged Navier-Stokes (Toja-Silva et al., 2018). A very quick introduction on the state-of-art of available models is given as follows:

- URANS. By averaging the Navier-Stokes equations, it is only possible to model the turbulence by computing the eddy viscosity, hence solving only the largest turbulent scales. So far, it has been heavily implemented in all aerodynamics applications, for its computational cheapness. However, even introducing more accurate turbulence models, a validation is always needed since results might show large error margins (Mehta et al., 2014).

- LES. The largest energy carrying scales are fully resolved, while the smallest scales are modelled through filtering of the Navier-Stokes. It has become recently more popular, due to availability of larger computing resources, without having the concern of the reliability of the turbulence model for that specific CFD problem (Sagaut, 2006).
- DES. It is a hybrid of RANS and LES, which consists of running RANS in boundary layer and LES in the separated regions for the largest scales. This model has shown issues regarding the quick decay of turbulence, but it is a cheaper alternative to most expensive LES and provides the possibility to introduce laminar-to-turbulent transition models.
- DNS. All range of wave number is solved, giving as drawback the extremely expensive computational demand. Only few applications are effective, but it is considered reliable, as it solves numerically the N-S equations.

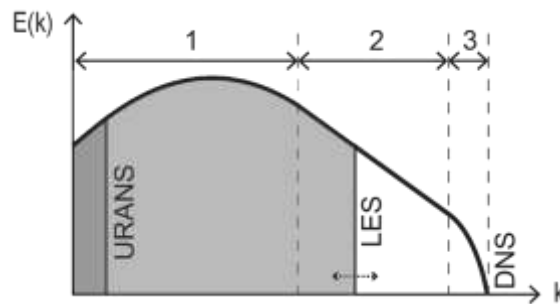


Figure 2.18. Log-log diagram of the Energy spectrum $E(k)$ of turbulent length waves, k , with indication of its three domains: 1. Largest energy containing eddies; 2. Inertial subrange; 3. Smallest dissipative eddies. For each CFD model: referred to solved and modelled energy cascade.

Figure 2.18 shows turbulence models in terms of the energy cascade they are capable to solve. URANS is only able to provide physical solution of the largest energy containing scales, and therefore not suitable to model inflow atmospheric turbulence. In fact, the number of length scales involved is Reynolds number dependant, and one may consider different options, being aware of hypotheses and risks, to save computational effort in order to get optimized, but accurate, results (Blocken, 2018). For the actual state of the art of the computational means, which have shown good results, a thorough review can be found in relevant works (Sørensen and Shen, 2002; Wu and Porté-Agel, 2012).

2.4. Research gap

The brief survey of background literature presented in this Chapter shows that some aspects of research on Urban Wind Energy aerodynamics needs to be addressed for the technology to improve.

A fundamental question might be formulated to summarise the issues at stake:

*How does the highly unsteady flow present in the urban environment
affect the aerodynamic behaviour of wind turbines?*

To correctly interpret this question, its twofold aspects need to be considered:

- What are the turbulence characteristics of an urban flow?
- In what way does urban turbulence affect the aerodynamic performance of a wind turbine?

A comprehensive study on the basic aerodynamic mechanism for which turbulent coherent structures (and what kind of) affect the performance of wind turbines and their rotors has been attempted a number of times, but without a clear and convincing discussion on the mechanism under which turbulence affects performance. In particular, cited references miss the link between performance and integral length scale of turbulence as a governing parameter in the basic mechanism causing the interaction. The reason for this gap in the research, as stated, can be explained with the difficulty in scaling the ABL in wind tunnel testing if a real size device or aerofoil is to be tested.

The potential of CFD is also not fully exploited in relevant literature, as although many techniques exist which have performed well in solving a variety of engineering applications, the lack of information and confidence on the wind resource present in the built environment does not allow for a rigorous numerical investigation to be set out.

Figure 2.19 schematises the research gap this work is aimed to address. An aerofoil subjected to atmospheric wind with a broad range of length scales is affected in its aerodynamic performance. Two parameters are essentially affected by the unsteady inflow: the real angle of attack and the aerodynamic forces. Large length scales are responsible for the angle of attack to vary unsteadily. However, it is not clear from the literature whether smaller scales also contribute to the aerodynamic performance, or if larger scales are capable of acting upon the aerodynamic coefficients as well. The graph also points out at the possible role of turbulence intensity as a trigger to the effect of turbulence on the aerodynamics.

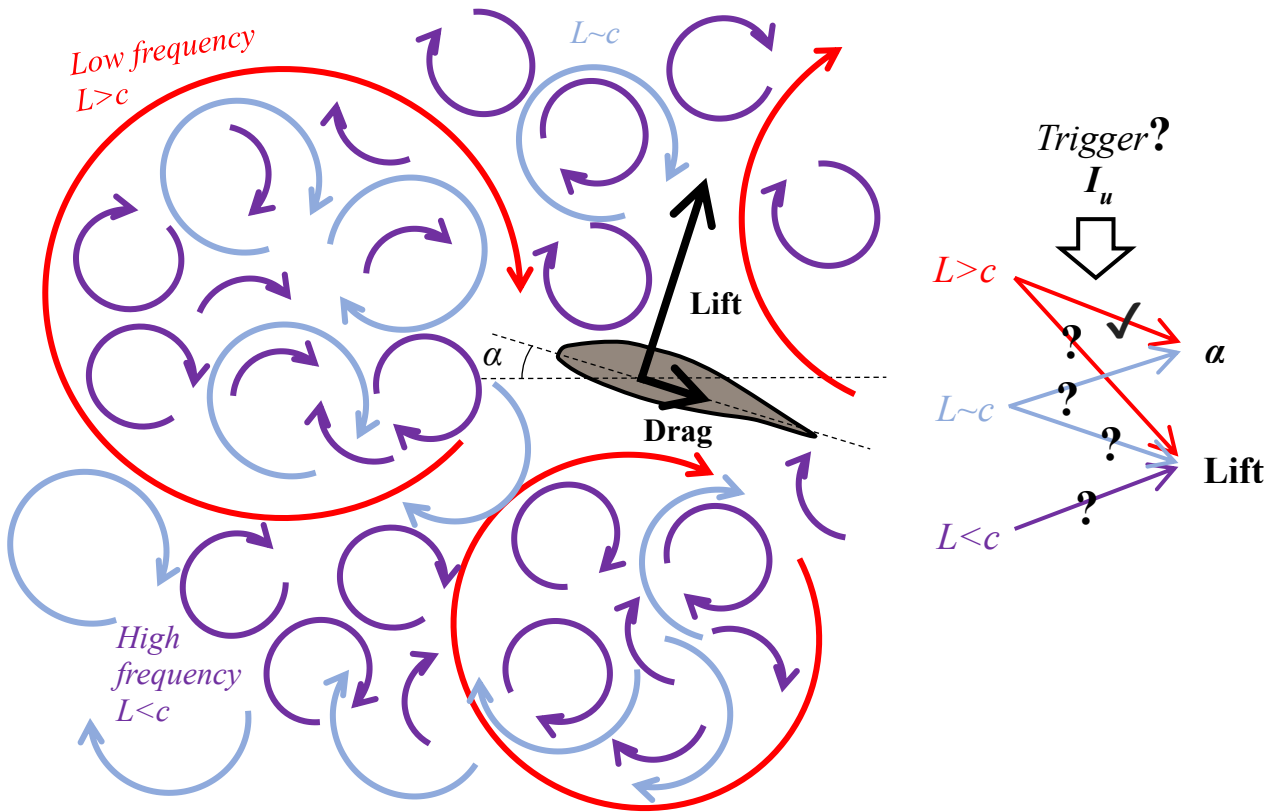


Figure 2.19. The Research Gap. A twofold problem. Correctly addressing the turbulence pattern of the inflow; and understanding the scales affecting the aerodynamic performance of a WT aerofoil in the built environment.

2.5. Back-to-Basics: a novel methodology for urban wind energy research

This Chapter has highlighted a causal connection of the lack in performance of urban wind energy with the lack in the understanding of the physical mechanism of turbulent coherent structures affecting the aerodynamic performance of a wind turbine aerofoil.

To reconsider the way this issue has been addressed in literature so far, going “back-to-basics” seems a sensible approach to progress knowledge and provide input for future research.

This thesis is structured to follow a methodology based on the back-to-basics approach. In practical terms, this means the issue with the lack of performance of urban wind energy is analysed in depth and the weak aspect, in this case the aerofoil response to the various turbulent length scales contained in the inflow, is investigated in detail.

This thesis provides a novel methodology to model wind turbine aerofoils subjected to a realistic turbulent inflow. ‘Realistic’ is here intended as a turbulent inflow where not only the turbulence intensity, but also other turbulence characteristics are taken into consideration, for example the integral length scale.

In this section, the general methodology of the work is clarified in particular concerning the scaling issues in modelling wind turbines and the wind resource; and the steps of the work used to combine physical and numerical simulation techniques.

2.5.1. Scaling Wind Turbine and Wind Resource

The relationship between the reduced scale of experiments and the realistic environmental conditions has represented a major concern for physical simulations of wind effect on structures from the first applications of boundary layer wind tunnels to test wind conditions around buildings or urban blocks (Simiu and Scanlan, 1986). This issue cannot be easily overcome. As discussed in the present chapter, as full-scale tests are limited, engineering practice is required to do experiments with tests based on similarity (Stathopoulos, 2002; Stathopoulos et al., 1992). Whether Reynolds similarity, or its alternatives (Schlichting and Gersten, 2000), are considered, practitioners need to carefully balance the choice of scale with the accuracy in reproducing realistic wind conditions, while allowing the use of

instrumentation to measure efficiently wind speed, surface pressure, or further parameters (Wu and Stathopoulos, 1993).

In short, it is rather easy to scale down the geometry of a wind tunnel model, while sensors have a given size and cannot be normally adapted to each and every configuration tested.

Practice over the past 50 years has found $1:300$ to be a suitable compromise between modelling a sensible wind profile, whilst using available instrumentation.

The scale limitations of physical simulation are obviously not shared by numerical simulations, as full-scale domains can be modelled adapting geometric, velocity and time scale for validation with wind tunnel testing (Blocken, 2014; Stathopoulos, 2002).

Another common application for experimental wind tunnels is the testing of devices. In this case, wind shear is normally not needed. Hence, the fetch length of the tunnel is missing and laminar inflow conditions are normally used. The scale of a device to the ABL profile is incompatible and wind shear effects are not present. Therefore, the scale of models for device in the wind tunnel normally ranges $1:10$ to $1:1$ depending on the object considered. In that case, turbulence is missing from the inflow, which does not match with the environmental conditions. However, the integral length scale is much larger than the characteristics size of the device and turbulence effects are considered negligible (which is an aspect which might require more insight, as shown in Section 2.2.2).

This thesis aims at testing a device, a wind turbine aerofoil having a hypothetical $1:10$ scale, subjected to the turbulence found in the urban environment, which can only be investigated with a $1:300$ model. Table 2.3 provides a range for the scales used in the various parts of the thesis to tackle the problem in investigating accurately turbulence and its effects. Chapter 3 is instrumental to the aim of the work, as it provides a mean in assessing the limits for wind tunnels in varying the turbulent inflow when testing a device. The indicative scale of Table 2.3 refers to environmental measurements obtained in Chapters 4 and 5. In short, this means traditional wind tunnels are limited to generate 25-35 cm in length scales, while in the built environment 2.5-3.5 m are commonly found above the roof of high-rise buildings.

The chord of the device for this thesis has been fixed to a third of the length scale to 12.5 cm, due to the necessity of fitting the model with pressure taps to measure the aerodynamic force coefficients, which again is a limit provided by the instrumentation.

Table 2.3. Impact of scaling for every objective.

* Hypothetical scale based on the size a typical urban wind turbine blade.

** Scale of inflow matching the hypothetical scale of the wind turbine.

<i>Objective and Chapter</i>	<i>Turbine or Resource</i>	<i>Scale</i>	<i>Impact of scale on tests</i>
<i>O2; Ch.3</i>	<i>Grid Turbulent inflow (EXP)</i>	<i>1:10*</i>	<i>Absence of Reynolds effects; Limited turbulence statistics possible.</i>
<i>O3; Ch.4</i>	<i>Highrise Inflow (EXP/CFD)</i>	<i>1:300</i>	<i>Limitation in scale: blockage, wind profile;</i>
<i>O4; Ch.5</i>	<i>Realistic City Inflow (EXP/CFD)</i>	<i>1:300</i>	<i>Presence of Reynolds effects on the inflow;</i>
<i>O5; Ch.6</i>	<i>Aerofoil (EXP)</i>	<i>1:10*</i>	<i>Limited turbulence statistics; Absence of Reynolds effects in turbulence</i>
<i>O6; Ch.7</i>	<i>Aerofoil & Grid Turbulence (CFD)</i>	<i>1:1**</i>	<i>Overcome limitations of EXP; Inflow scale uniformed to device scale</i>

Table 2.3 also provides some information on the scalability of an inflow computed from a 1:300 physical or numerical simulation, to a 1:1 or 1:10 turbulent inflow used to test the aerodynamic performance of a device. As discussed in detail in Chapter 6, Reynolds effects are found to be negligible when turbulence intensity is higher than 4 %, which in turn means turbulence can be scaled differently to wind speed according to the present results without losing generality.

In closing, an important issue with scale is the isotropy of the flow. While the ABL anisotropy is predicted accurately using wind tunnel testing as shown in Chapter 4 and 5, the turbulent inflow generation techniques have only been tested under isotropic conditions, testing the ability of the technique to generate turbulence characteristics. A future topic of investigation might be the anisotropy of the flow in the urban environment to be considered for testing devices. In this study, isotropy is indeed found to increase closer to the building (Chapter 4), reassuring on the validity of grid turbulence in generating a suitable turbulent inflow representative of the built environment for Chapter 6 and 7.

Due to scaling, the validation of numerical results is of extreme importance, as validation test-cases obtained through wind tunnel testing are not representative of realistic wind conditions. In Chapter 7 a strategy is proposed to validate both the turbulent inflow and the numerical setup so that the numerical simulation might be used to overcome wind tunnel limitations.

2.5.1. An integrated experimental-numerical methodology

This thesis provides a methodological framework to reproduce a turbulent inflow representative of the built environment integrating both wind tunnel and numerical simulation.

Figure 2.20 shows the functioning of the framework. The wind resource, or the turbulence characteristics in locations of interest (high-rise buildings, as studied in Chapters 4 and 5) are found using physical and numerical simulations. Tests need to be developed so that not only the mean approaching atmospheric flow U_∞ and the relevant local wind speed U are accurately predicted, but also turbulence characteristics, such as turbulence intensity I_u and integral length scale L_u . These statistics are computed following calculation procedures extensively discussed in Chapter 3.

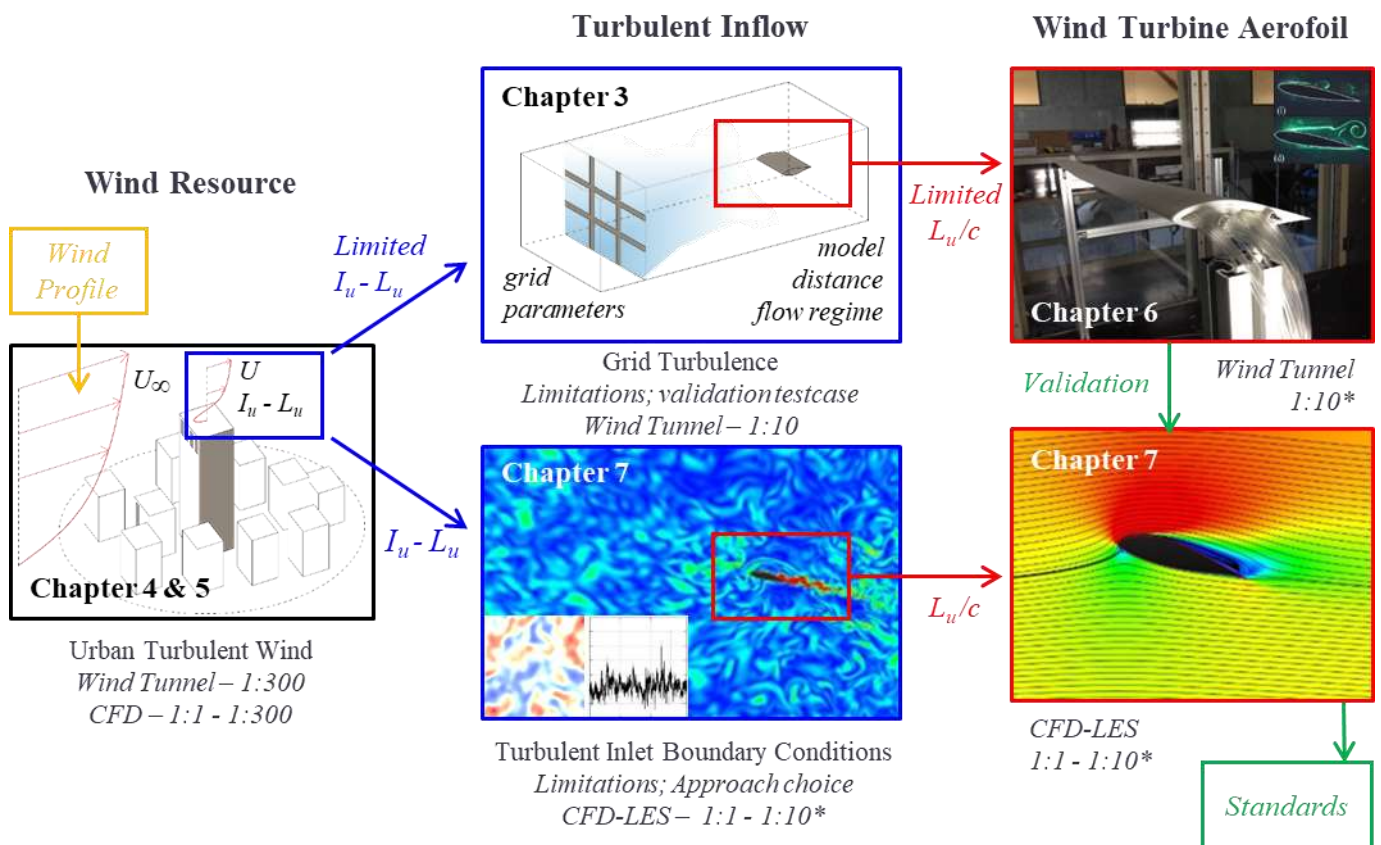


Figure 2.20. Methodological framework to integrate wind tunnel and CFD results to assess the effect of turbulent flows as found in a realistic urban environment on wind turbine aerodynamics.

Assessing the wind resource allows to fine tune the turbulent inflow for the assessment of the aerofoil aerodynamic performance. Chapter 3 confirms that wind tunnel testing has strong limitations in modelling turbulence characteristics analogous to the built environment, if the scale of the model

aerofoil is kept such that it is possible to instrument it. Chapter 7 confirms instead that it is possible to model a high quality turbulent inflow using turbulent inlet boundary conditions.

In Chapter 6, the behaviour of the boundary layer of the wind turbine aerofoil is tested in the wind tunnel setup of Chapter 3. In Chapter 7, the scope of the wind tunnel is extended by testing a model aerofoil having a size compatible to the length-scale-to-chord ratio found in the built environment, i.e. $L/c \sim 10-20$.

The aim of wind tunnel testing is to approach statistics found in the urban environment, but also to provide a validation test case for numerical simulations, which are designed specifically to overcome experimental limitations.

All steps of the research are discussed in detail in the following, in an effort to provide an alternative methodology to investigate the lack of performance of urban wind energy. Going back-to-basics and improving the understanding of the physical interaction of a wind turbine aerofoil with a urban turbulent inflow might provide the link between performance and inflow, which is missing by looking at overall performance of wind turbines.

Results on aerofoils might be implemented in aerofoil data used in Blade Element Momentum models to fine tune the assessment of performance and augment the reliability of urban wind turbines.

Chapter 3

Generating large length scale turbulence using passive grids in wind tunnel

It is noted that the majority of Chapter 3 has been published in Vita et al. (2018) and is reproduced with the permission of the co-authors.

To be able to replicate the urban wind condition to test wind turbine aerofoils under a realistic turbulent inflow is an unresolved challenge of urban wind energy. In industrial aerodynamics wind tunnel testing, a turbulent inflow is usually obtained using passive grids. However, to obtain an atmospheric-like flow field, relatively large length scales ($L \sim 30$ cm) and high turbulence intensities ($I \sim 15$ %) need to be reproduced. In this Chapter, the limitations of grid turbulence to be representative of a urban inflow are investigated. The passive grid technique has been used in combination with a downstream expansion test section to explore the possibility of expanding the scope of traditional grid turbulence, with the possibility of varying both turbulence intensity and integral length scale independently. Four passive grids with different mesh and bar sizes have been used with four wind velocities and five downstream measurement positions. Results show that the flow field is isotropic and homogeneous for distances less than what is recommended in literature ($x/M \sim 5$). The effect of the expansion on the turbulence characteristics is also shown for the first time. The study confirms that by adding an expansion test section it is possible to increase both turbulence intensity and integral length scale downstream from the grid, with limited impact on the overall flow quality in terms of anisotropy and energy spectra.

3.1. Grid turbulence generation in wind tunnel testing

The generation of controlled statistics of turbulence at the inlet of wind tunnel tests is of paramount importance for many aerodynamic applications. Research on bluff body aerodynamics (Bearman and Morel, 1983; Nakamura et al., 1988), turbulence decay (Comte-Bellot and Corrsin, 1966), turbulence interaction noise (Kim et al., 2016) or wind energy (Sicot et al., 2008) requires Free Stream Turbulence (FST) with a rather faceted spectrum of length scales and turbulence intensities to be generated at the inlet. Several approaches can be used for this purpose, such as grid generated turbulence, thermal driven turbulence, the use of cross jets, and actuated foils. While each of these methods has some advantages and disadvantages, grid generated turbulence is considered as the most effective and reliable source of a turbulent inflow for wind tunnel testing (Batchelor, 1953; Hinze, 1975). At least three families of grids are found in the literature: passive, active, and fractal grids.

The use of a passive grid (PG) has been the elected technique of generating turbulence at the inlet of wind tunnel tests since the first pioneering works on turbulence decay (de Karman and Howarth, 1938; Simmons and Salter, 1934; Taylor, 1935). Grid turbulence is generated by the shedding of vortices downstream of bars. The upstream quiescent flow undergoes a transition to a homogeneous and isotropic turbulent flow, characterised with slow rotating vortices which roughly scale to the size of the bars of the grid $L_u \sim b$ (Davidson, 2004). Once the flow is fully developed, turbulence decay dominates the statistics. The rate of decay has been set by Baines and Peterson (1951) and Vickery (1966) to $-5/7$, while Laneville (1973) has instead proposed a value of $-8/9$. Mohamed and LaRue (1990) pointed out that two distinct regions of the flow exist, namely the far-field region, where turbulence decay is the main feature of the flow, and the near-field region, where production and a strong effect of the initial conditions are present (George, 2012). All PGs undergo such an analogous behaviour. Circular rods or square bars, arranged in square meshed or parallel arrays as well as perforated plates are used to build PGs with a variety of details, sizes and materials. Their effects have been systematically addressed by Roach (1987). However, the main classification of PGs is based on the dependence of the downstream turbulence on the Reynolds number, which is predominantly dictated by the shape of bars. Circular rods have a wake pattern that varies greatly with the Reynolds number or their roughness, while blunt bars

feature a given separation at sharp corners (Bearman and Morel, 1983). Square bars compared to rectangular ones are more Reynolds sensitive, as flow re-attachment occurs more easily, modifying their wake (Nakamura, 1993). Smoothing or trimming the corners of square or rectangular bars has a limited impact on the turbulence characteristics (Nakamura et al., 1988). Although the use of rectangular bars is discouraged by some authors (Hancock and Bradshaw, 1983), others did not encounter any significant issues (Bearman and Morel, 1983; Nakamura, 1993; Nakamura et al., 1988; Vickery, 1966). The bar typology can be associated with different concepts for the construction of grids: Bi-planar grids (two sets of parallel bars placed side-by-side); Mono-planar grids (two set of overlapping parallel bars); A single set of parallel bars, either vertical or horizontal. Hancock and Bradshaw (1983) found that a bi-planar grid is preferable as mono-planar grids produce a highly unsteady non-uniform flow, possibly because of the larger separated region behind each intersection. Bearman and Morel (1983) argued that the non-uniformity of the flow decays in a much faster way for mono-planar grids than that of the bi-planar grid. However, the two grid options generate a similar turbulent flow (Nakamura et al., 1988; Roach, 1987). Nevertheless, the effect of the detailing of the grid is no longer apparent when the turbulent flow is fully developed. At what distance this occurs is still debated in research (Isaza et al., 2014). A mesh distance of $x/M > 10$ is considered by many authors (Bearman and Morel, 1983; Gartshore, 1984; Laneville, 1973; Saathoff and Melbourne, 1997; Vickery, 1966), but it is arguable whether this indication is sufficient to assume an independence of statistics with respect to the chosen detailing of the grid (Frenkiel et al., 1979).

The active grid (AG) concept uses a number of winglets mounted on a series of shafts, which rotate to generate a highly turbulent isotropic flow downstream of the grid (Makita, 1991; Makita and Sassa, 1991). This complicated setup has been further developed (Brzek et al., 2009; Cal et al., 2010) to produce integral length scales in the order of the cross-section size of the wind tunnel $L_u \sim H$ (Mydlarski and Warhaft, 2006). The turbulence characteristics can be adjusted by altering the rotating speed of the winglelet-shafts (Cekli and van de Water, 2010; Kang et al., 2003; Larssen and Devenport, 2011). AGs have also been successfully used recently in research on wind energy (Maldonado et al., 2015).

The fractal grid (FG) concept has been recently developed to produce higher turbulence intensities and integral length scales up to $L_u \sim H/10$ as well as limiting the distance from the grid at which the flow

can be considered fully developed (Hurst and Vassilicos, 2007; Seoud and Vassilicos, 2007). A fractal grid of N th order is created from a fractal generating pattern of complexity S , whose geometry is iterated N times. Mesh and bar sizes are varied accordingly. This technique is similar to that of the passive grid generation. However, a production region exists close to the grid where turbulence statistics develop toward a peak value. This does not occur for passive grids (Melina et al., 2016). The flow behind FGs resembles that of the near-field of passive grids. While the implementation of FGs for bluff body aerodynamics is being explored (Nedić and Vassilicos, 2015), PGs are more commonly used.

Thus far, many studies have investigated the effects of free stream turbulence for a variety of applications. However, only a few of them have attempted to address the effect of the turbulent statistics, taken independently of one another (Arie et al., 1981; Lee, 1975; Morenko and Fedyaev, 2017; Peyrin and Kondjoyan, 2002; Younis and Ting, 2012). If PG is the methodology of choice to generate inlet turbulence, a thorough study of the turbulence statistics at the inlet is sometimes only briefly mentioned, or omitted altogether. This might depend on the limited significance of the results, since low turbulence intensities ($<5\%$) are normally available for large integral length scales (>20 cm) (Roach, 1987), while in the atmosphere higher turbulence intensities ($>15\%$) are found (Antoniou et al., 1992; Kaimal et al., 1976). In order to achieve higher values for the turbulence intensity, the only possible way is to reduce the measuring distance from the grid, keeping the mesh and bar size sufficiently large to yield suitable length scales even close to the grid. However, the homogeneity and isotropy condition may not be achieved. It could be argued whether the distance limitation given in literature of $x/M > 10$ could be reformulated for those studies not aimed at turbulence decay. Roach (1987) has warned that such limitations might be overconservative, suggesting that a homogeneous and isotropic, although not fully decaying, flow might be found closer to the grid.

Nevertheless, turbulence statistics of grid turbulence show a deviation from the condition of isotropy. Comte-Bellot and Corrsin (1966) confirmed the validity of the exponential decay law of de Karman and Howarth (1938), however they used a slight contraction of the wind tunnel section to achieve turbulence intensity isotropy. Although the inhomogeneity caused by the contraction does not affect the energy transfer of the decay rate, it was noted that integral length scale isotropy is more difficult to obtain. Later, several works have introduced a contraction section downstream of the PG. While most

studies about the effect of a contraction on turbulent flows focus on the design of wind tunnels (Uberoi, 1956), some more recent works (Bereketab et al., 2000; Mish and Devenport, 2006; Swalwell et al., 2004; Wang et al., 2014) apply a contraction to adjust the isotropy for the inlet of bluff body aerodynamics applications. However, this approach causes a damping of turbulence downstream of the contraction, which in turn does not guarantee isotropy condition to be met for all statistics (Kurian and Fransson, 2009). Together with contractions, also expansion test sections, or diffusers, are broadly used in wind tunnels. Diffusers are placed as exit sections downstream of the working section, to create a pressure rise. Wide-angle diffusers are also needed upstream to allow for a contraction to be placed at the inlet to obtain a desirable steady flow (Bradshaw and Pankhurst, 1964). A diffuser is usually placed downstream or upstream of fans, as they need to be 2-3 times larger than the test-section to achieve a high quality flow field (Mehta, 1979). Diffusers have been tested regarding the performance in recovering pressure with reference to free stream turbulence (Hoffmann, 1981), but to the knowledge of the authors their use as a mean of modifying turbulent inlet statistics in wind tunnel testing is not yet reported in literature.

This paper introduces a novel method of varying turbulence statistics at the inlet of wind tunnel tests using an expansion section. The literature review has clarified that the generation of an atmospheric-like inflow is a challenging issue in the investigation of the effect of turbulence on bluff body aerodynamics, especially in obtaining large integral length scale turbulence ($L_u \sim 0.3$ m) combined with high turbulence intensity ($I_u \sim 15$ %). In the following, the grid generated turbulent flow upstream and downstream of an expansion test section is investigated. The aim is to show the possibility of modulating the turbulent flow to enhance statistics, without compromising them in terms of isotropy and gaussianity. The possibility of varying independently the various statistics is also assessed to understand their compatibility with atmospheric turbulence. Thanks to a thorough study of the turbulence decay mechanism, a simple empirical relation is proposed to predict the turbulence statistics at the outlet of the expansion. In Section 2, the experimental setup is reported together with the methodology to calculate results presented in Section 3. The feasibility of using an expansion together with grid generated turbulence has been assessed with the study of turbulence decay, isotropy, gaussianity, and energy spectra, and conclusions are given in Section 4.

3.2. Methodology

3.2.1. Experimental setup

The experiments were carried out in the multi-disciplinary wind tunnel of the University of Liège. The wind tunnel was operated in closed-loop configuration. The 1.50 m high and 1.95 m wide aeronautical test section (TS1) has a total length of 5 m. The 4×4 m contraction at the inlet nozzle, together with a series of honeycomb and a series of fine-grid screens, allows a remarkably low turbulence level (0.15 %). The flow is accelerated by the 440 kW, 2.8 m diameter rotor that can drive the flow at velocity between 1 m/s and 65 m/s in closed-loop configuration. Figure 3.1 shows a schematic of the test section. The 5 m long TS1 has a 5.1 m expansion to bind the aeronautical cross-section to the larger atmospheric boundary layer cross section TS2 which is 2.5 m wide and 1.8 m high. Therefore, a part of the TS2 section was also used for the measurements.

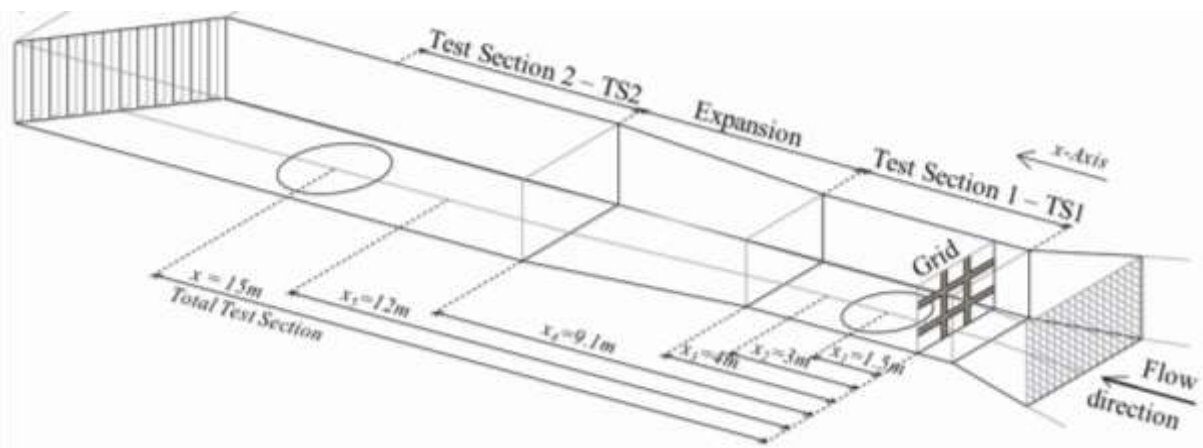


Figure 3.1. Experimental setup: the aeronautical Test Section (TS1) of the Wind Tunnel of the University of Liège

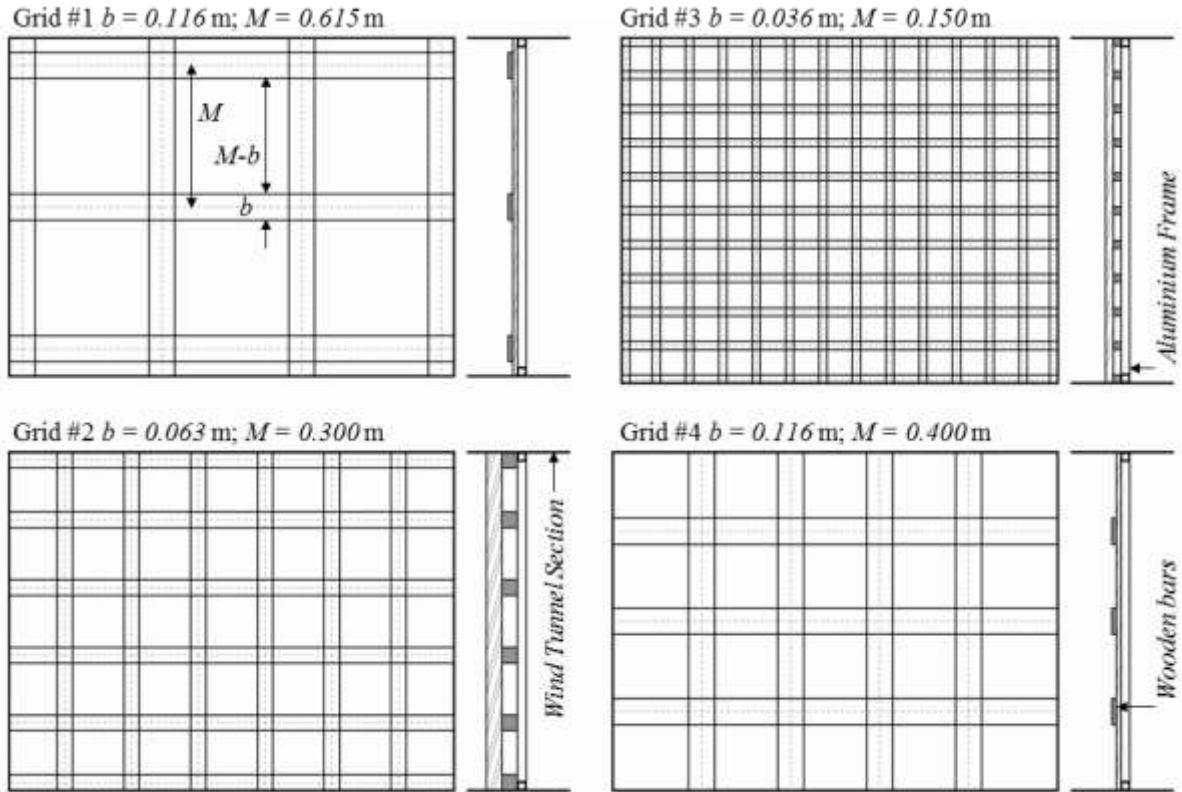


Figure 3.2. Schematic (front and side view) of the set of four grids #, with bar b and mesh M size.

3.2.2. Design of Passive Grids

The design of a turbulent inflow to be generated with a PG requires a careful choice of at least three parameters: the width b of the bars, the mesh size M (i.e. the distance between the centreline of the bars), and the downstream distance x to the grid (Figure 3.2 and Figure 3.3), where the measurements are performed. Vickery (1966) provides an indication for the optimal mesh size of $M = L/8$, where L is the length of the test section. The ratio b/M can be chosen based on the definition of grid drag (Laneville, 1973)

$$c_D = \frac{b/M (2 - b/M)}{(1 - b/M)^4} \quad (3.4).$$

Laneville (1973) recommends to keep c_D between 3 and 4. Consistently, Vickery (1966) suggested $c_D \sim 3.4$, while for Baines and Peterson (1951) $c_D > 3.4$. The grid drag is connected to the definition of porosity β (or its dual, solidity) by:

$$\beta = (1 - b/M)^2 \quad (3.5).$$

Bearman and Morel (1983) advised a value of at least 0.5 for β , which is also confirmed by Nakamura et al. (1988) and Roach (1987). However, using $\beta=0.5$ leads to $c_D < 2$, which is a more common value to be found in research on bluff body aerodynamics. Using these brief indications, Roach (1987) has given some guidelines for designing PGs based on fitting empirical constants to a large set of data, bar sizes and grids. However, the general validity of these guidelines is not assured, since conclusions were drawn from a limited set of wind tunnels. Nevertheless, simple design guidelines provide a useful tool for a preliminary estimation of the PG configurations. The empirical formulae derived by Roach (1987) are reported in Table 3.1 for turbulence intensities I_u and I_v , integral length scale L_u and Taylor microscale λ_u , where the subscripts u , v and w indicate respectively the stream-wise, horizontal and vertical components.

Table 3.1 Empirical relations for turbulence characteristics (after Roach, 1987)

Empirical expression	$I_u = A(x/b)^{-5/7}$	$I_v = AB(x/b)^{-5/7}$	$L_u/b = C(x/b)^{1/2}$	$\left(\frac{\lambda_u}{b}\right)^2 = \frac{14F(x/b)}{Re_b}$
Constants	$A=1.13$	$B=0.89$	$C=0.20$	$F=1$ or $F=1.21$

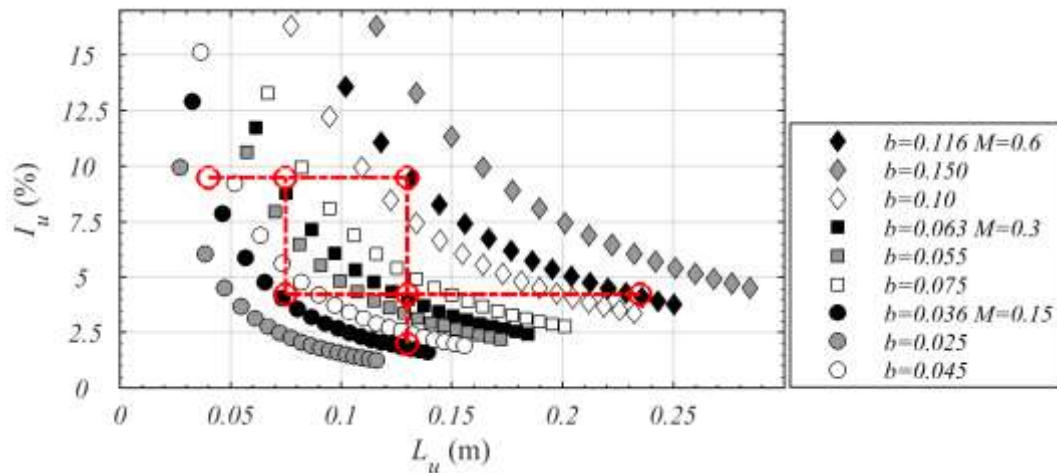


Figure 3.3. Preliminary design of the flow field. The symbols vary based on the different mesh size, while the filling is relevant to the chosen setup. The red lines and symbols indicate possible alignments for the statistics.

The set of grids have been designed by a preliminary choice of the target turbulent characteristics. Following this approach, several ratios of distances and grid sizes have been studied using the empirical formulae of Table 3.1. Despite this simplification, the setup is still rather complex. The proposed setup and the estimated length scales and intensities are indicated in Figure 3.3. Possible alignments of separately varied statistics are indicated (in red). It is evident how difficult can be to achieve $L_u \sim 0.25$ m

together with $I_u \sim 10-15\%$. Only a set of three grids is provided here, while in the final experiment a set of four bi-planar square PGs is used.

The geometry and the turbulent statistics for the different grids are reported in Table 3.2. All results in the table refer to the distance of $x/M=10$, except for grid #1. All grids are placed in the same position $x=0$, i.e. at the inlet of TS1, without the use of any downstream contraction.

Table 3.2 Geometry of grids as shown in Figure 3.2(b)
with turbulence statistics at $x/M=10$ ($x/M=6.5$ for grid #1) and $U_r=15\text{m/s}$.

Grid	b [m]	M [m]	M/b [-]	β [-]	C_d [-]	x/M [-]	I_u [%]	L_u/b [-]	λ_u/b [-]	I_u/I_v ~ 1	L_u/L_v ~ 2	λ_u/λ_v $\sim \sqrt{2}$
#1	0.116	0.615	5.30	0.66	0.79	6.5	15.0	1.51	0.43	1.22	2.46	1.412
#2	0.063	0.30	4.76	0.62	0.97	10	8.35	1.81	0.68	1.14	2.13	1.320
#3	0.036	0.15	4.17	0.58	1.27	10	9.0	1.84	0.91	1.19	1.86	1.135
#4	0.116	0.4	3.45	0.5	1.95	10	11.0	1.39	0.32	1.2	1.81	1.0

A set of wooden bars have been overlapped in a bi-planar array and fixed firmly to an aluminium frame screwed to the inlet of TS1 Figure 3.2. The flow has been measured at 5 different positions, as indicated in Table 3.3, which have been shifted to respect the requirement of $x/M > 5$.

Table 3.3 Position of measurements and mesh distance.

Position reference	x (m)	x/M #1	x/M #2	x/M #3	x/M #4
x_1	1.5	-	5	10	-
x_2	3	4.8	10	20	7.5
x_3	4	6.5	13.34	26.67	10
x_4	9.1	14.8	30.34	60.67	22.75
x_5	11.1	-	-	-	30

A total number of 15 measurements have been made for 4 different rotor wind speeds U_r , for a total of 60 tests. The different sets of grids are shown in Figure 3.2. The name of the grids and their different mesh sizes are also represented. The velocity measurements have been performed at the half-height of the wind tunnel $h = 0.74$ m. Measurements have been also made at the additional height of $h=1.07$ m to briefly assess the uniformity of the flow. This adds up to 9×4 tests for a total number of 96 tests.

Measurements have been made using a dynamic multi-hole pressure probe (Cobra Probe by Turbulent Flow Instrumentation inc., TFI), which allows the measurement of the three components of flow

velocity from 2 to 100 m/s ± 1 m/s within a flow angle of ± 45 deg with a sampling frequency of up to 2 kHz. A proprietary software (TFI Device Control) is used as a data acquisition system (A/D card) to operate the probe. The sampling frequency chosen for this experiment is 500 Hz over a duration of the recorded signal of $t = 60.0$ s. This gives a range of non-dimensional time units, Ut/b , between 1,000 and 33,500, where U is the average velocity, b the bar width and t the duration of the signal. The wind speed has been varied from 5 to 20 m/s in four steps.

3.2.3. Calculation of statistics

The turbulent flow is described using both one- and two-point statistics for the stream-wise, horizontal and vertical components of velocity u , v and w . The fluctuating velocity u is calculated using the Reynolds decomposition $u = u(t) - U$, where $u(t)$ is the velocity realisation as measured, and $U = \overline{u(t)}$ is the mean velocity. One-point statistics include the statistical moments, such as the variance $\overline{u^2}$, the standard deviation $\sqrt{\overline{u^2}}$, the skewness $S_u = \overline{u^3} / (\overline{u^2})^{3/2}$, the flatness (or kurtosis) $K_u = \overline{u^4} / (\overline{u^2})^2$, and the excess kurtosis $\gamma_u = K_u - 3$. The energy in a turbulent flow field can be assessed from $\sqrt{\overline{u^2}}$, in the form of turbulence intensity:

$$I_u = \sqrt{\overline{u^2}} / U; I_v = \sqrt{\overline{v^2}} / U; I_w = \sqrt{\overline{w^2}} / U \quad (3.6).$$

The integral length scale L_u is a measure of the largest energy containing vortices. L_u can be estimated from the autocorrelation coefficient $\rho(\tau) = R_{uu}(\tau) / \overline{u^2}$, where $R_{uu}(\tau) = \overline{u(t)u(t + \tau)}$ is the autocorrelation function, and τ is the time lag. In this case $L_u = UT_u$ where T_u is the integral time scale, obtained from the area subtended by the $\rho(\tau)$ curve, which is usually approximated with:

$$L_u = U \int_0^{\tau_0} \rho(\tau) d\tau \quad (7),$$

where $\rho(\tau_0) = 0$. T_u can also be estimated using a simplified relation, where $\rho(T_u) = 1/e$ (Conan, 2012).

The power spectral density or spectrum E_u is defined from the Wiener-Khintchine theorem:

$$E_u(n) = \frac{1}{2\pi} \int_{-\infty}^{\infty} e^{-int} R_{uu}(\tau) d\tau \quad (8),$$

where n is the frequency. L_u can be estimated using the best fit of E_u with the von Kármán formula:

$$E_u(n) = \frac{4L_u \overline{u^2} / U}{(1 + 70.8(nL_u/U)^2)^{5/6}} \quad (9),$$

which only applies for homogeneous isotropic turbulence. All approaches yield results with a relative error <15 %, hence the l/e rule is used in the following.

Since turbulence is composed of a broad band of frequencies, it is important to have also a reference to the energy distribution for a given frequency band. The Taylor microscale λ_u is commonly used for this purpose, as it represents the largest dissipative length scale. λ_u can be found from the dissipation rate ε :

$$\varepsilon = 15\nu \int_0^\infty \kappa^2 E_u(\kappa) d\kappa \quad (10),$$

where $\kappa = 2\pi n/U$ is the wave number and $E_u(\kappa) = UE_u(n)/2\pi$ is the wave number power spectral density.

In isotropic turbulence, the following relation applies:

$$\frac{l}{\lambda_u^2} = \frac{\varepsilon}{15\nu u^2} = \frac{l}{u^2} \int_0^\infty \kappa^2 E_u(\kappa) d\kappa = \frac{2\pi^2}{U^2 u^2} \int n^2 E_u dn \quad (11),$$

where E_u might represent either the computed or the fitted spectrum. However, Roach (1987) warns that in order to obtain an accurate estimation of ε using the relations which are valid for homogeneous isotropic turbulence, a sampling rate of 10-100 kHz has to be chosen when collecting the data, which is often unpractical. Alternatively, ε can be estimated fitting the spectrum with its inertial sub-range $E_u(\kappa) = C\varepsilon^{2/3} \kappa^{-5/3}$ (Pope, 2000). The multiplicative constant is $C = 18/55 C_\kappa \sim 0.49$ for the stream-wise spectrum and $C = 24/55 C_\kappa \sim 0.65$ for the horizontal spectrum. $C_\kappa \sim 1.5$ is the Kolmogorov universal constant (Sreenivasan, 1995). Another way of calculating λ_u is using the Taylor's hypothesis and the intercept of $\rho(\tau)$ with a parabola at the origin (Pope, 2000):

$$\lambda_u^2 = \overline{u^2} / \overline{(\partial u / \partial x)^2} = U^2 \overline{u^2} / \overline{(du/dt)^2} \quad (12).$$

Both Equations 8 and 9 are estimations based on assumptions, and a careful study should be undertaken for the most suitable approach. In this work, Equation 9 has been chosen for the calculation of λ_u . The smallest turbulent motion, named Kolmogorov microscale η , is another useful value which is defined from the dissipation rate ε :

$$\eta = (\nu^3 / \varepsilon)^{1/4} \quad (13).$$

The transversal and horizontal integral and Taylor length scales, respectively L_v , L_w , λ_v , and λ_w , are calculated with formulae, analogous to the previously introduced ones (Hinze, 1975; Pope, 2000).

Further conclusions on the behaviour of a turbulent flow can be drawn by calculating the Reynolds stress tensor $\overline{u_i u_j}$. In particular, the tensor a_{ij} , first introduced by Lumley (1979), gives a measure of the deviation of the flow field from the isotropy definition of $\overline{u_i u_j} = 1/3 q^2 \delta_{ij}$, where $q^2 = 2k = \overline{u_k u_k}$ is twice the turbulent kinetic energy. The anisotropy tensor a_{ij} is defined by

$$a_{ij} = \frac{\overline{u_i u_j}}{q^2} - \frac{1}{3} \delta_{ij} \quad (14).$$

The second and third invariant of a_{ij} , respectively $II_a = a_{ij} a_{ji}$ and $III_a = a_{ij} a_{jk} a_{ki}$, are used to define an anisotropy invariant map, which defines precisely the rate and the typology of turbulent flow (Jovanović, 2004), varying from pure isotropy $II_a = III_a = 0$ to one-component turbulence. This map has confirmed that grid turbulence yields a highly isotropic flow field (Geyer et al., 2016).

3.3. Results and discussion

Results are presented in this section considering the following topics of investigation: the decay of turbulence, the isotropy and the gaussianity of the flow, and the spectrum of statistics varied separately one another. Results are presented in scatter plots and the symbols used to refer to the different parameters are introduced in Table 3.4. Four different symbols are used indicating the four different grids and the colour represents either the wind speed used, or the distance referred to the expansion test section, when wind speed does not affect the statistics. In Table 3.4, the legend for results is reported.

Table 3.4 Legend for results

Grid Symbols		Wind Speed u_r (m/s)	Distance
#1	+	5	$x/M \leq 10$
#2	□	10	$x \geq 9.1$ m
#3	○	15	$x/M > 10 \cup$
#4	◇	20	$x < 9.1$ m

Results are plotted against the distance from the grid x . In literature, x is often translated into mesh distance x/M or Reynolds mesh distance $x/M 1/Re_M$ first introduced by Comte-Bellot and Corrsin (1966). The bar size b can be also used to define x/b or $x/b 1/Re_b$, however results are better fitted using

the mesh distance. The mesh Reynolds number reads $Re_M = UM/\nu$, and it highlights any dependence from the wind speed. Another useful parameter is the turbulent Reynolds number, which can be defined using λ_u or L_u , which yield $Re_\lambda = \sqrt{u^2}\lambda_u/\nu$ and $Re_A = \sqrt{u^2}L_u/\nu$, respectively. Re_λ and Re_A are used to underline the role of dissipation in the development of statistics. Whenever suitable, data is fitted with the approach used in von Kármán and Howarth (1938) using the formula $f(x) = Ax^p$.

3.3.1. Turbulence Decay

The decay of turbulence is shown in Figure 3.4 a) and b), and Figure 3.5 a) and b) in terms of I_u , L_u/M , λ_u/M , and η/M , respectively. The data is plotted along with the predictive formulae reported in Table 3.1, which have been converted to the mesh distance. It has been found that the data collapses better using x/M rather than x/b . The empirical formulae have also been compared with the least square fit of the data.

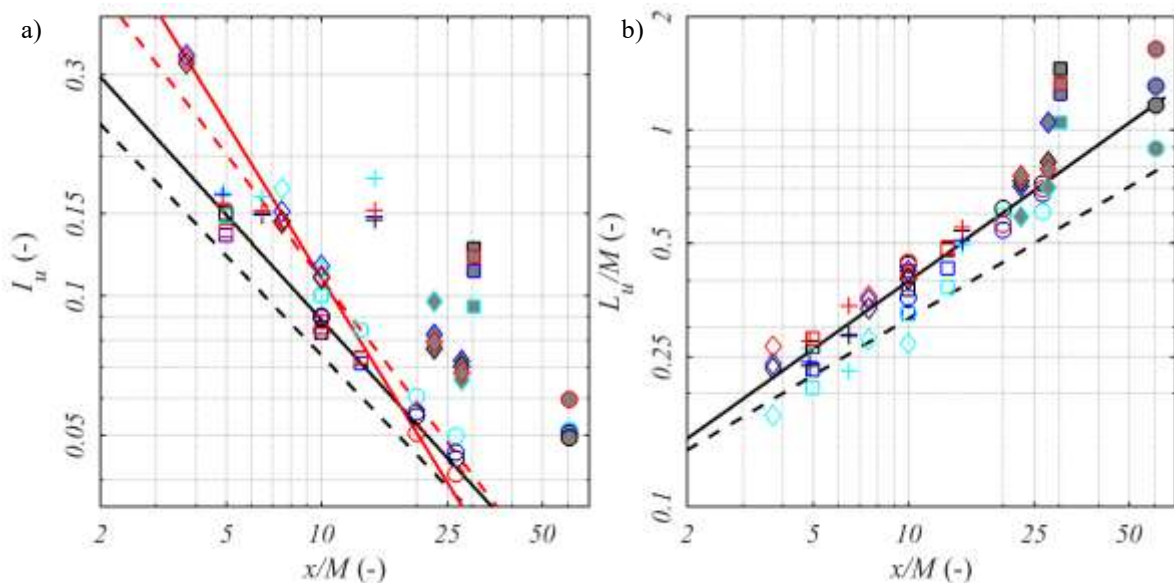


Figure 3.4 a) Turbulence Intensity decay with empirical fitting after Roach (1987) for grids #2 and #3 (—) and after Laneville (1979) for grid #4 (---). Least Square fitting of data is also provided for grids #2 and #3 (—) and grid #4 (—) as detailed in the text. b) Integral length scale decay with least square (—) and empirical fitting after Roach (1987) (—) as detailed in the text. Markers are filled with a grey hatch if $x \geq 9.1$ m and coloured after wind speed (Table 3.4).

In Figure 3.4 a), the decay of I_u is plotted against the mesh distance x/M . Turbulence Intensity decays in a similar way for grids #2 and #3. The empirical formula given by Roach (1987) is close to the least square fit of the data $I_u = 0.5(x/M)^{-3/4}$. Grid #4 shows a similar behaviour, although I_u decays faster.

The least square fit of the data $I_u = 1.41(x/M)^{-1.11}$ is closer to the formula $I_u = 2.54(x/b)^{-8/9}$ given by Laneville (1979). This difference in the behaviour seems to depend on the porosity β , respectively 0.62 and 0.58 for grids #2 and #3, and 0.50 for grid #4. Grid #1 shows a rather different behaviour, and a fit of the data reads $I_u = 0.2(x/M)^{-1}$, which is not plotted in Figure 3.4 a). A likely explanation for this may be the large size of the mesh compared to the wind tunnel section, which in turn causes the mean flow to be highly non-uniform. This is the reason for the inclusion of grid #4, in the experimental setup.

In Figure 3.4 b), the decay of L_u is plotted against x/M . In this case all grids behave consistently, and the fit of the data yields $L_u/M = 0.1(x/M)^{3/5}$, while the empirical formula given by Roach (1987) slightly underestimates L_u/M . In Figure 3.4, data is coloured after wind speed to highlight possible Reynolds effects. All results behave consistently for every wind speed, and only a small scatter of the data is noticeable for $U_r = 5$ m/s (data in cyan in Figure 3.4). This is possibly due to the limitations of Cobra probes in measuring velocities ~ 2 m/s, therefore this velocity range is eliminated in the next figures.

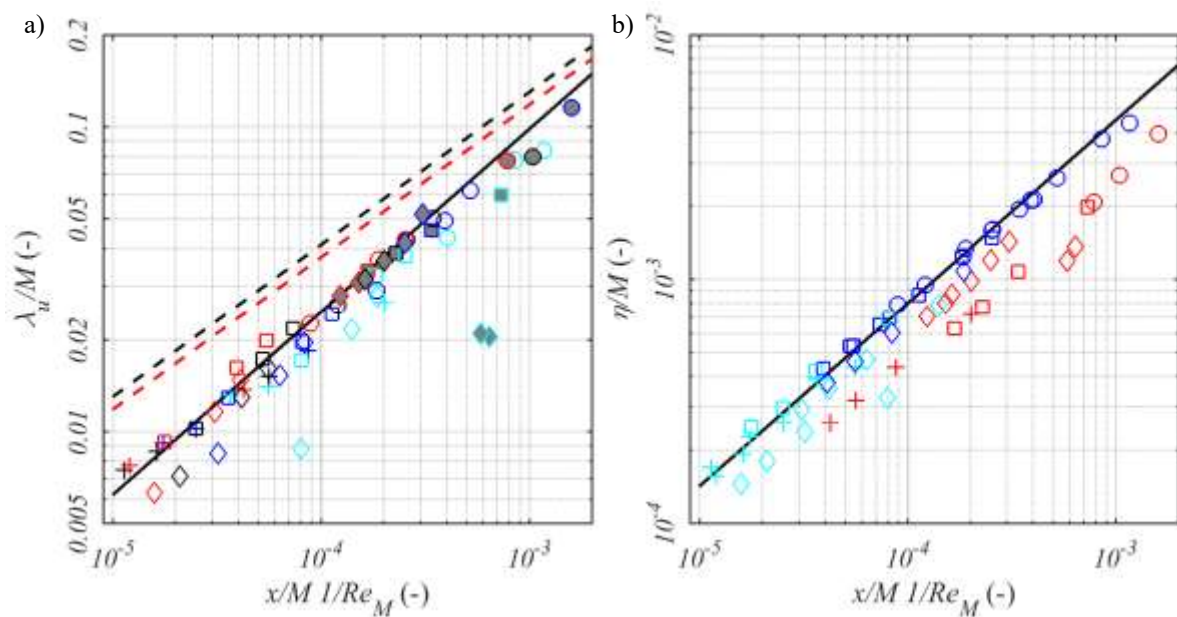


Figure 3.5 a) Taylor microscale decay and c) Taylor microscale against distance, with empirical fit as detailed in and b) Kolmogorov the text (Table 3.1) (—, - -). Colours after wind speed (Table 3.4). a) Turbulence Intensity decay with empirical fitting after Roach (1987) for grids #2 and #3 (- -) and after Laneville (1979) for grid #4 (- -). Least Square fitting of data is also provided for grids #2 and #3 (—) and grid #4 (—) as detailed in the text. b) Integral length scale decay with least square (—) and empirical fitting after Roach (1987) (- -) as detailed in the text. Markers are filled with a grey hatch if $x \geq 9.1$ m and coloured after wind speed (Table 3.4).

The Taylor λ_u/M and Kolmogorov η/M microscales are plotted in Figure 3.5 a) and b), respectively. The empirical formulae overestimate λ_u/M when F is taken as given in Table 3.1, i.e. $F=1$ for isotropic turbulence or $F=1.21$ otherwise. A formula which fits all grids at all distances for this setup is $\lambda_u/M=(14 \ 3/2 \ x/M1/Re_M)^{3/5}$. In the same way, η/M can be accurately predicted for all data using the formula $\eta/M=0.8(x/M1/Re_M)^{1/2}$, which holds for homogeneous turbulence (Pope, 2000).

The behaviour of the length scale decay can be also interpreted with Figure 3.6 also, where the turbulent Reynolds numbers Re_λ and Re_λ are plotted against $x/M1/Re_M$. All data taken at $x \leq 4$ m is fitted by $Re_\lambda=6.97(x/M1/Re_M)^{-0.38}$ and $Re_\lambda=5.6(x/M1/Re_M)^{-0.72}$, regardless of distance or grid typology. Re_λ is very close to the results of Kurian and Fransson (2009), although they used grids with different bar shapes, while Re_λ seems to converge towards their fit only at highest mesh distances. This confirms that the behaviour of the small scales has rather universal properties, which are independent of the initial conditions in which turbulence is created. The decay of the large scales seems to vary with the typology of the grid, at least for $5 \leq x/M \leq 10$, but the decay law seems not to depend on the porosity of the grid.

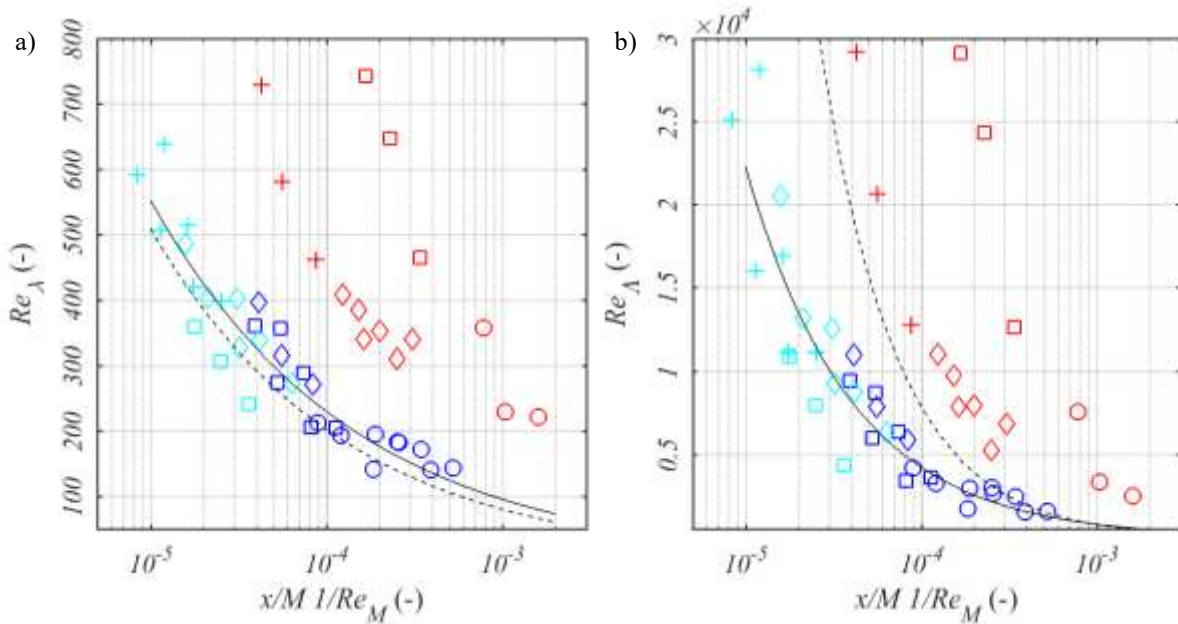


Figure 3.6 Turbulent Reynolds number relative to a) Taylor and b) integral scale against mesh distance, with fit of data (—) and fit by Kurian and Fransson (2009) (- -). Colours after distance (Table 3.4).

The ratio of integral and Taylor length scale, as shown in Figure 3.7 a), is proportional to the local turbulent Reynolds number Re_λ , with a proportionality coefficient of $C \sim 0.08$. Isaza et al. (2014) argue that $L_u/\lambda_u \propto Re_\lambda$ means that the data is measured in the far-field region of the flow, where only

dissipation takes place and the effect of initial conditions posed by the construction of the grids have vanished. The constant of proportionality is given by $C = C_\epsilon/K$ where $C_\epsilon = \epsilon L_u/S_u$ and K is a fitting constant. No effect of the different wind speeds is noticeable. Therefore, data is coloured based on the distance to the grid.

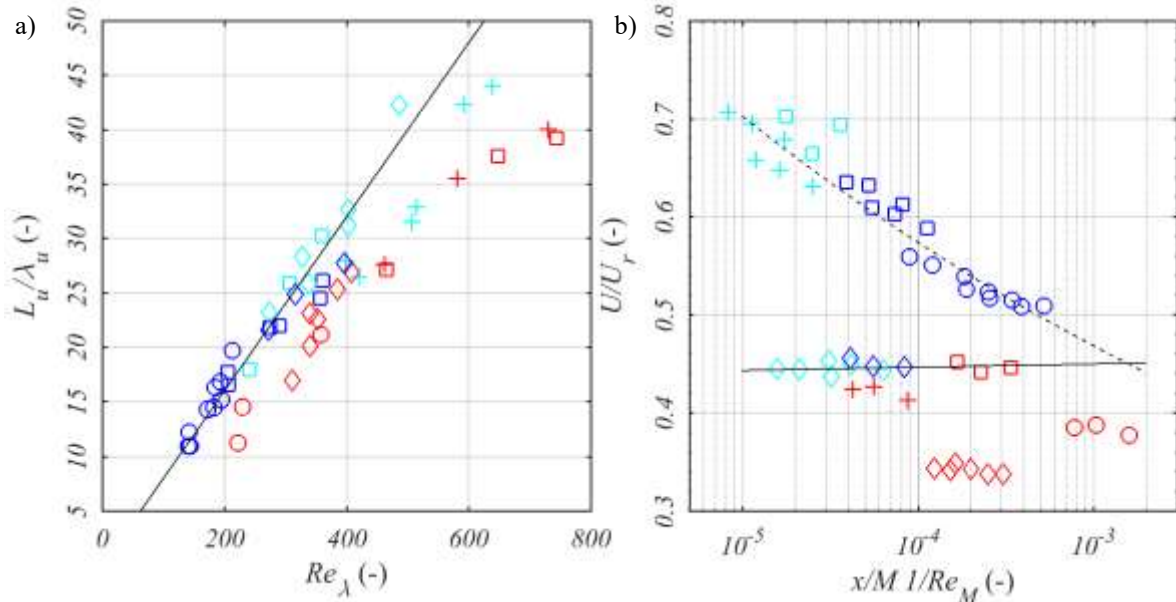


Figure 3.7. a) Integral and Taylor scale ratio dependence on the turbulent Reynolds number, with fit relation after Isaza et al. (2014) (—); b) Mean velocity ratio against mesh distance, with least square fit for grids #1, #2, and #3 (- -), and for grid #4 (—). Colours after distance (Table 3.4).

In Figure 3.4, Figure 3.5, Figure 3.6 and Figure 3.7, some data deviate from the empirical formulae in an apparent scatter. This is marked with a grey hatch in Figure 3.4 a) and b), and Figure 3.5 a). All the measurements which show this behaviour are taken at $x \geq 9.1$ m, i.e. at the outlet of the expansion test section of the wind tunnel of Liège. At $x \geq 9.1$ m, I_u recovers to values measured closer to the grid, while L_u increases with respect of what expected for such a setup. The increase rate of λ_u is comparable for all grids, unlike the other statistics. This confirms that dissipation is a phenomenon which exclusively depends on the Reynolds regime of the flow. Remarkably, the expansion has a very limited effect on the decay rate of λ_u , since the non-dimensional plot shows that the data is only affected by the Reynolds number, and this confirms that λ_u is extremely susceptible to changes in the wind speed. In Figure 3.6, the effect of the expansion is more visible, as data taken at $x \geq 9.1$ m is shifted from the empirical fit. Unlike data taken upstream to the expansion, a different slope is noticeable for different grid typologies. This could be explained with a definition of a parameter $x_L = 4/M$, where $x = 4$ m is the distance from the

grid of the inlet of the expansion section, which reads $x_L=6.50, 13.34, 26.67$, and 10 for grid #1, #2, #3, and #4, respectively. x_L represents the state of the flow at which the expansion section is encountered, which varies with the geometry of the grid. Turbulence generated by grids #2 and #3 encounters the expansion inlet for $x/M > 10$, unlike grids #1 and #4, and a different effect on the decay mechanism is expected.

The effect of the expansion on the turbulent flow field can be explained looking at the mean flow evolution with distance. In the investigation of turbulence decay, passive grids are designed to limit any gradients in the mean velocity so that only dissipative phenomena take place (George, 1992). However, this is achieved when any production process has vanished, i.e. at $x/M \gg 10$. At these distances turbulence characteristics are not representative of atmospheric turbulence, and distances of $x/M \sim 10$ are most commonly found in research on bluff body aerodynamics. In this region, a change in the mean flow cannot be ruled out in principle. The change of the mean flow with distance is plotted in Figure 3.7 b). The mean velocity taken at the centreline of the wind tunnel U is divided by the reference wind speed U_r as given in Table 3.4. Besides the uniform case, the mean flow profile might resemble that of a jet or a wake, depending on the porosity of the grid. For self-preserving jets, an inversely proportional relation is defined: $U/U_r = C_U(x/M)^{-1}$ (Hussein et al., 1994). It is therefore reasonable to assume a relation of the type $U/U_r = C_U(x/M - 1/Re_M)^n$ for grid generated turbulence, where C_U and n vary with the grid geometry (Pope, 2000). In this work, the fitting coefficients read $C_U=0.25$ and $n= -0.09$ for grids #1, #2 and #3, and $C_U=0.45$ and $n= 0.03$ for grid #4. For $n < 0$ the mean flow resembles a jet, while for $n > 0$ a wake-like profile is present. Therefore, the flow regime which is created is strongly affected by the initial conditions, and it seems that a lower porosity is beneficial in obtaining a more uniform flow. Nevertheless, the effect of the expansion on the mean flow might help understanding its effect on the turbulence decay. In Figure 3.7 b), a sudden drop in the mean velocity occurs at $x=9.1$ m (data in red). The Venturi effect which occurs due to the change in the cross-section causes the mean velocity to decrease, and the turbulent vortices to stretch. Results presented in this Section do not show different behaviours for different Reynolds regimes, and the turbulence decay only depends on distance.

The effect of the expansion on grid generated turbulence seems to be limited to the rate of decay of turbulence, due to the changes occurring in the mean flow. Little effect is noticed on the small scales, confirming that dissipation is only affected by the Reynolds regime and not the initial conditions in which turbulence is created, namely the geometry of the grid.

3.3.2. Isotropy

The isotropy of a turbulent flow field can be assessed through turbulence intensity (Comte-Bellot and Corrsin, 1966), Taylor microscale and integral length scale (Roach, 1987), or a more comprehensive approach, such as the anisotropy invariant map (Banerjee et al., 2007).

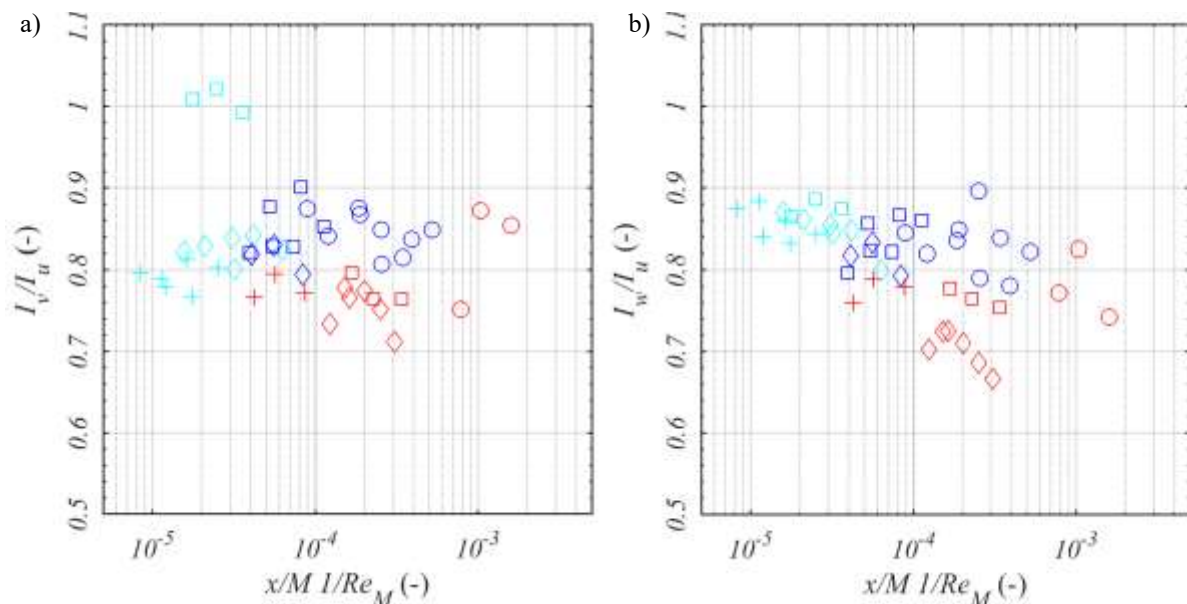


Figure 3.8 Turbulence Intensity anisotropy, a) horizontal and b) vertical component against non-dimensional mesh distance in logarithmic scale. Colours after distance (Table 3.4).

The isotropy of turbulence intensity is defined as the ratio of the standard deviation for the different velocity components, i.e. $I_v/I_u \approx I_w/I_u \approx I$. The isotropy of turbulence intensity is illustrated in Figure 3.8 a) and b) against $x/M 1/Re_M$. for both the horizontal and vertical component, v and w . The data show that distance does not improve isotropy substantially. Isotropy reaches $\approx 80\%$ for I_u/I_v and $\approx 90\%$ for I_u/I_w already relatively close to the grids, around $x/M \sim 5$.

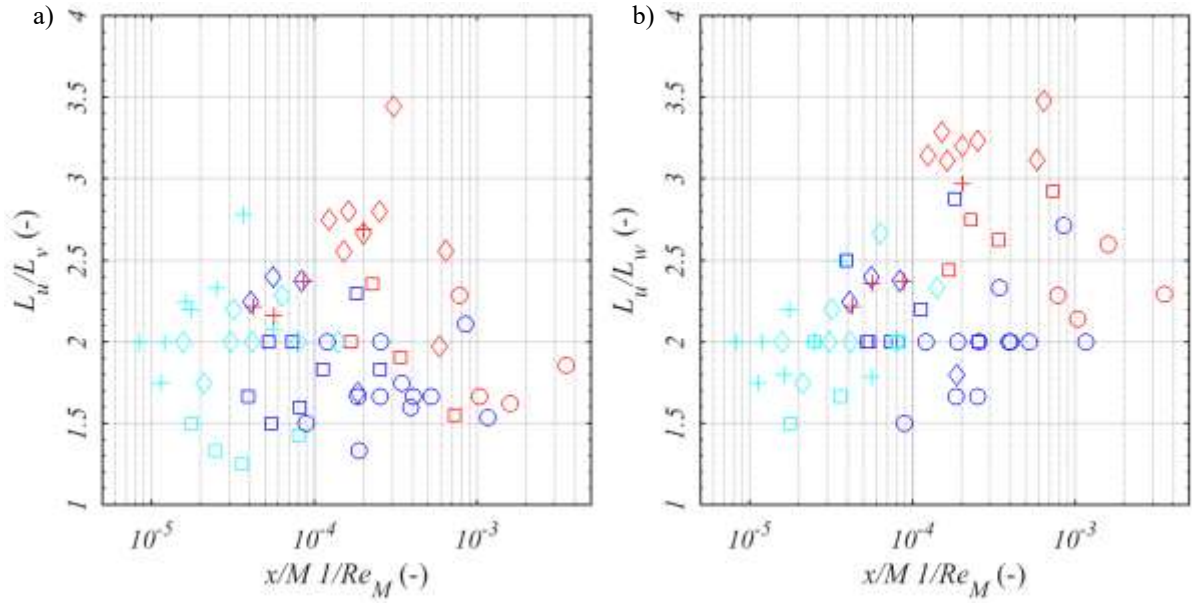


Figure 3.9 Integral length scale anisotropy for a) horizontal and b) vertical component against mesh distance. Colours after distance (Table 3.4).

The integral length scale isotropy condition reads $L_u/L_v \approx L_u/L_w \approx 2$. Both in Figure 3.9 a) and b), the isotropy rates L_u/L_v and L_u/L_w are very close to the theoretical condition for most data at around $x/M \sim 10$.

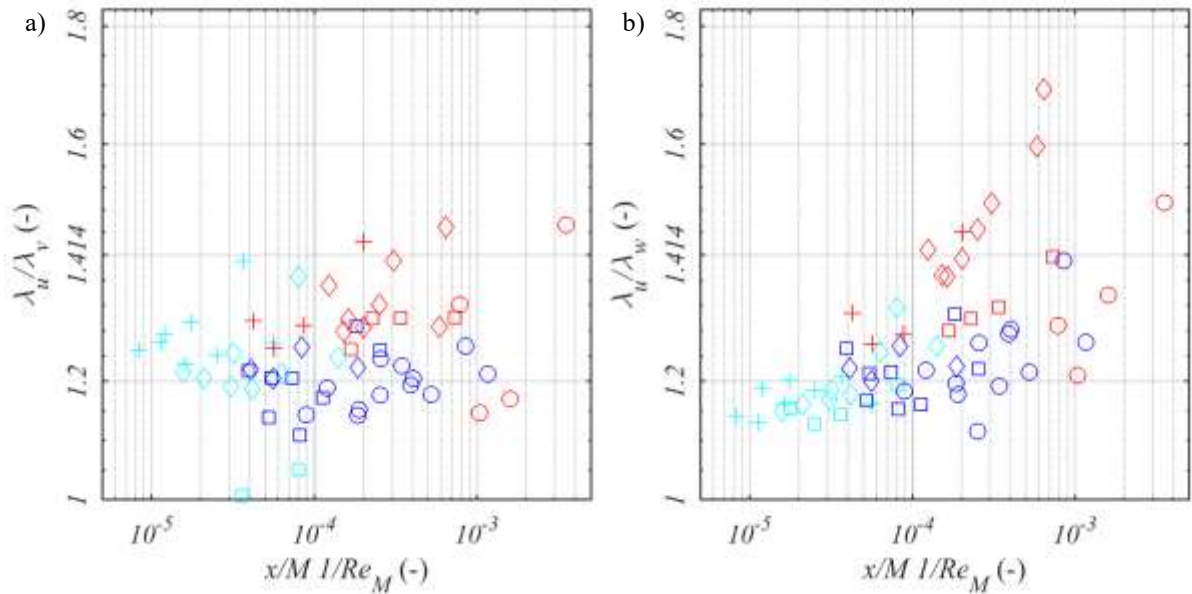


Figure 3.10 Taylor microscale anisotropy for a) horizontal and b) vertical component against mesh distance. Colours after distance (Table 3.4).

The isotropy condition for the Taylor microscale reads $\lambda_u/\lambda_v \approx \lambda_u/\lambda_w \approx \sqrt{2} \approx 1.414$, and it is plotted in Figure 3.10 against $x/M 1/Re_M$. Most data show a value of around ~ 1.2 for both components regardless of the distance from the grid.

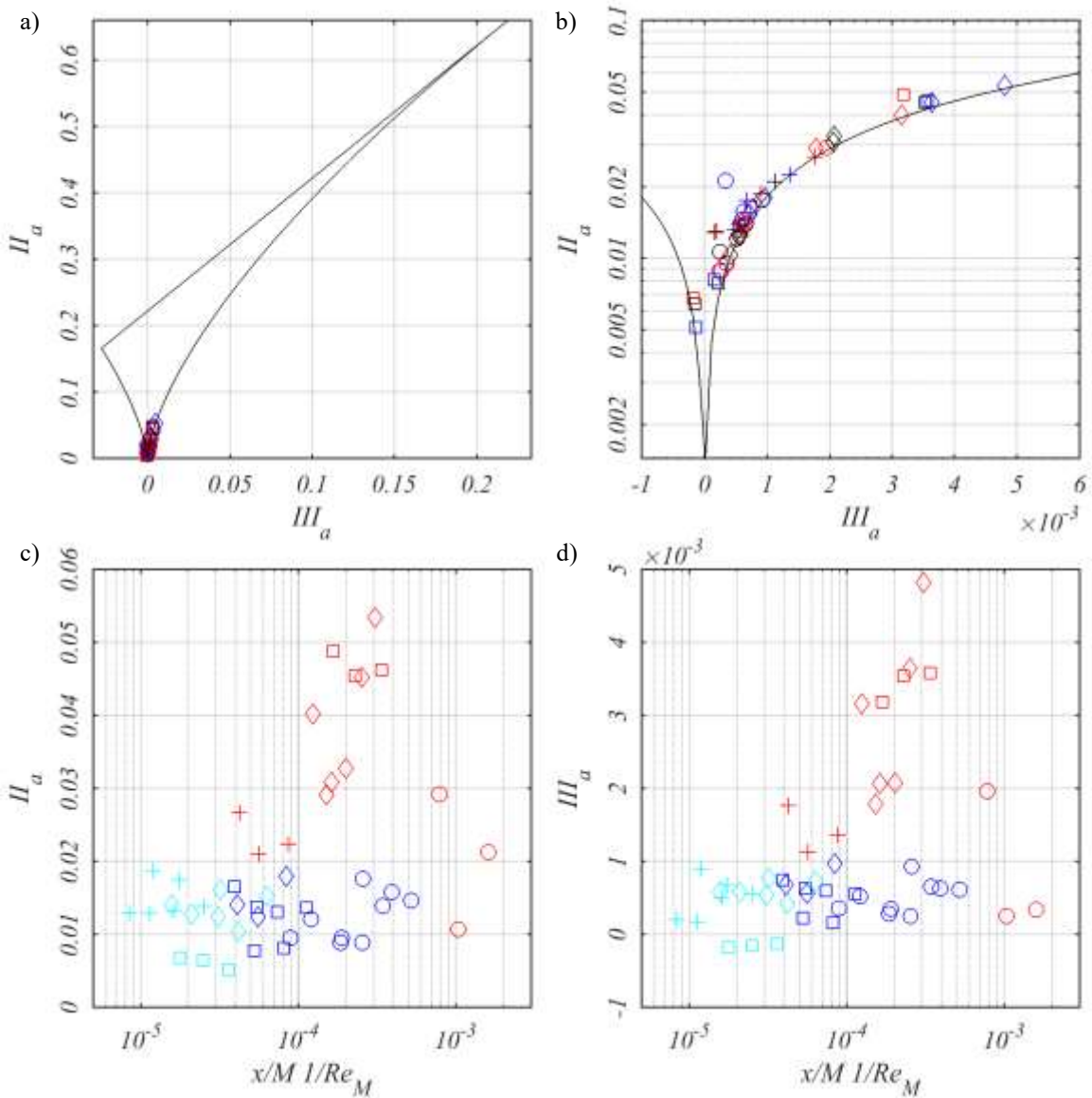


Figure 3.11 a) Anisotropy invariant map; b) zoom close to the isotropy condition. c) Second and d) third invariant plotted against x . Colours after a), b) wind speed and c), d) distance (Table 3.4).

It is rather difficult to draw conclusions on the effect of the expansion on the isotropy of the flow from Figure 3.8, Figure 3.9, and Figure 3.10, as results seems to contradict each another. The anisotropy of I_u seems to confirm that the expansion increases the anisotropy. This increase seems stronger for L_u as most data measured at $x \geq 9.1$ m deviates significantly from 2. However, the expansion seems to improve the isotropy when looking at λ_u . Therefore, no convincing trends are found using the ratio of the different components of the statistics. Nevertheless, the results shown in Figure 3.8, 3.9 and Figure 3.10 are aligned to results found in literature for grid turbulence measured at distances $x/M > 10$. Kurian and Fransson, (2009) have found good level of isotropy for $x/M > 30$, however this longer distance can

be due to the bar type used in the measurements (woven metal wires). Nevertheless, high isotropy has been observed for large wind tunnel configurations, for high (Kistler and Vrebalovich, 2006) and low Reynolds numbers (Wang et al., 2014), as well as for small wind tunnel configurations (Laneville, 1973). However, only few studies investigated distances $x/M < 10$ with regard to the isotropy of the flow, as the estimation of the difference in the decay rate from the near- and far-field region is most commonly considered (Mohamed and Larue, 1990).

A more comprehensive view of the anisotropy rate of the flow is given by considering the second II_a and third III_a invariants of the a_{ij} tensor, as defined in Equation (11). An anisotropy invariant map is shown in Figure 3.11 a) and b). To understand the effect of the distance on the anisotropy, II_a and III_a are plotted separately against the mesh distance in Figure 3.11 c) and d). A very good rate of isotropy is found for all grids, regardless of distance, as the invariants of the data taken at $x \leq 4$ m are close to the condition of perfect isotropy, $II_a = III_a = 0$, this is also true for $x/M \sim 5-10$, which confirms that a non-uniform flow field might still present highly isotropic turbulence. In Figure 3.11 c) and d), data taken at $x \geq 9.1$ m (shown in red) diverges from the isotropy condition, being closer to mildly axisymmetric turbulence, a condition which is typical for vortices being stretched as they are forced through an expansion (or a contraction) (Batchelor, 1953). It is interesting to note that for the empty wind tunnel $II_a = 0.5$ and $III_a = 0.15$, which holds for highly axisymmetric turbulence.

The flow field shows a high isotropy closer to the grid than what is commonly suggested in literature, at $x/M \sim 5$ instead of $x/M \sim 10$. This result might represent a favourable feature in the investigation of the effect of atmospheric-like turbulence on bluff body aerodynamics. The expansion of the test section has a limited effect in the isotropy of turbulence, as the anisotropy indicates a light axial-symmetry. This result confirms that the quality of the turbulence flow field is comparable upstream and downstream of a slow variation in the cross-section of the wind tunnel.

3.3.3. *Gaussianity*

In homogeneous and isotropic turbulence, the probability distribution function is analogous to the normal distribution. This has been shown to hold true even for decaying grid generated turbulence

(Wilczek et al., 2011). This means the skewness of the velocity components yields $S_u=S_v=S_w=0$ and the kurtosis $K_u=K_v=K_w=3$. The latter, in particular, only applies if the flow is purely gaussian.

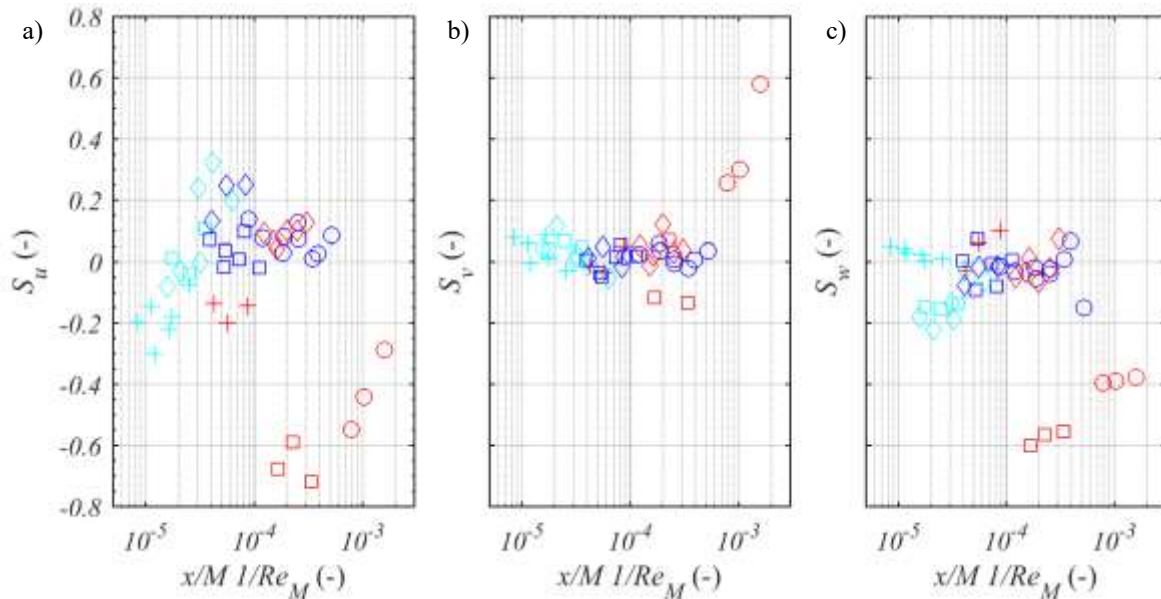


Figure 3.12 Skewness of velocity components for all grids and velocities. Colours after distance (Table 3.4).

The skewness of all components is plotted in Figure 3.12. Although a different behaviour is observed for the different grids, the skewness tends to become zero for $x/M > 10$. The stream-wise component only seems affected by the distance, as data taken at $x/M < 10$ shows to gradually converge towards zero. For grid #1, $S_u < 0$ indicates an enhanced production of vorticity characteristic of a point in an oscillating or unstable shear layer. Arguably, this occurs due to the large mesh size, which in turn produces a non-uniform velocity cross-profile (Isaza et al., 2014). Data taken at $x \geq 9.1$ m differs from $S_u = 0$. However, this only occurs for grids #2 and #3. Arguably, the lower β of grids #1 and #4 allows the near-field region characteristics to persist. This would also explain the negative values of S_u for grids #2 and #3 at $x/M < 10$. The other components show a more pronounced gaussian behaviour, but $S_{ii} \neq 0$ is observed after the expansion for grids #2 and #3.

The kurtosis (or flatness) of the flow is shown in Figure 3.13 for all components. The behaviour is more gaussian than for skewness, although after the expansion the data differs from $K_u = 3$ for grids #2 and #3 after the expansion. K_v and K_w , unlike the skewness case, differ more than K_u for all ranges of data. These results are consistent with the anisotropy of the flow: the expansion stretches the vortices and it affects the isotropy of turbulence. Another possible explanation for the deviation from the normal

distribution can be explained by a lack of flow homogeneity due to the particular grid arrangement. A lack in homogeneity causes the velocity field to be strained and it is believed this effect is also registered in the statistics (Mydlarski and Warhaft, 2006). The non-uniformity of the mean flow can be roughly assessed from Figure 3.7 b), where the change in the centreline value is plotted against distance. However, the uniformity of grid turbulence is a topic which would deserve a more thorough investigation (Carbó Molina et al., 2017).

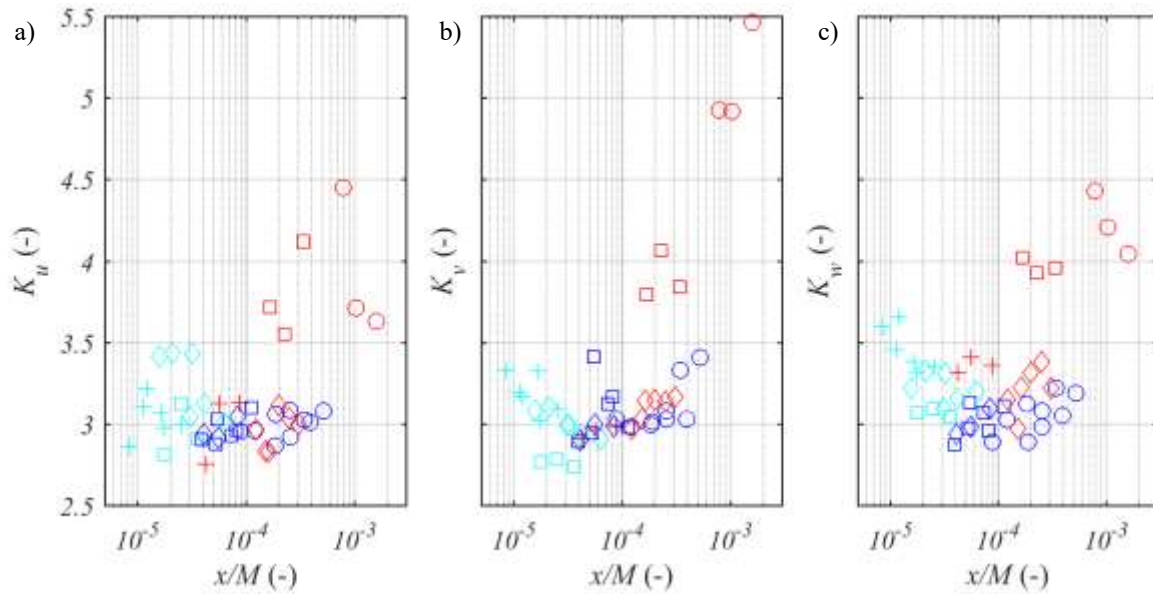


Figure 3.13 Kurtosis of velocity components for all grids and velocities. Colours after distance (Table 3.4).

3.3.4. Independently varied statistics

The use of a set of grids combined with an expansion section allows atmospheric-like highly isotropic turbulence to be reproduced, i.e. a flow field having $I_u \sim 10 \div 15\%$ and $L_u \sim 25 \div 30$ cm. The study on the turbulence decay, which has been proposed in Section 3.1, can be used to plot a turbulence intensity versus integral length scale diagram. This defines a design chart, which is useful when choosing the needed turbulence characteristics. In Figure 3.14 a), a simple empirical relation is proposed to fit the data, which might be useful to design an experimental setup combined with an expansion. The proposed model is based on the summation of two power laws in the form of $f(x) = Ax^{-p} + Bx^{+n}$, where the negative power law is obtained from the least square fits of I_u and L_u , shown in Figure 3.4. A combination of the fits which holds for all grids is $I_u = 0.025(L_u/M)^{-3/2}$, which is plotted in Figure 3.14 a). This curve

is not able to model the effect of the expansion. Therefore, a second positive power law is summed to the fit of the data, and the following formula has been derived:

$$I_u = A \left[\left(\beta \frac{b}{M} \right)^2 \left(\frac{L_u}{M} \right)^{-2} + \frac{B}{x_L} \left(\frac{L_u}{M} \right)^\alpha \right] \quad (15),$$

where $A=0.6$ and $B=1.5$ are two fitting constants, $\beta b/M = b/M(1-b/M)^2$ is a parameter based on the porosity of the grid, $x_L = 4/M$ is the expansion mesh distance, and $\alpha=1.45$ is the ratio of the expansion outlet and inlet cross section area $(2.5 \times 1.8)/(2 \times 1.5)$. Equation 12 is plotted in Figure 3.14 a) along with the least square fit of the data. With this simple model, the turbulence statistics found at the outlet of the expansion can be accurately estimated for grids #2, #3 and #4, while a significant mismatch is noticeable for grid #1, as expectable from previous results. The model is able to only estimate statistics straight at the outlet of the expansion section. For larger distances, no further conclusions can be made with this dataset. Equation 12 is then valid for $x_L > 10$ and for $\beta > 0.5$ only.

The fit proposed in Equation 12 is used to plot a dimensional design chart in Figure 3.14 b). The measured data is also plotted. Several alignments are found and plotted in the graph, where statistics can be varied independently of one another. In Figure 3.14 b), multiple points of interest are shown, where integral length scales up to $33cm$ can be reached and a turbulence intensity of $15-16\%$ can be achieved. The use of an expansion test section has an important role in obtaining such a variation in the statistics, and it might allow for constant I_u and varying L_u to be obtained using a single grid, as it is particularly evident for grids #3 grid #2. However, grid #4 does not show the same behaviour, and turbulence intensity monotonically decreases due to the lower porosity. Although it behaves differently, grid #1 is also shown together with its least square fit. It seems that turbulence intensity can be substantially increased placing the grid at $x_L < 10$, which in turn does not affect substantially the quality of the flow field.

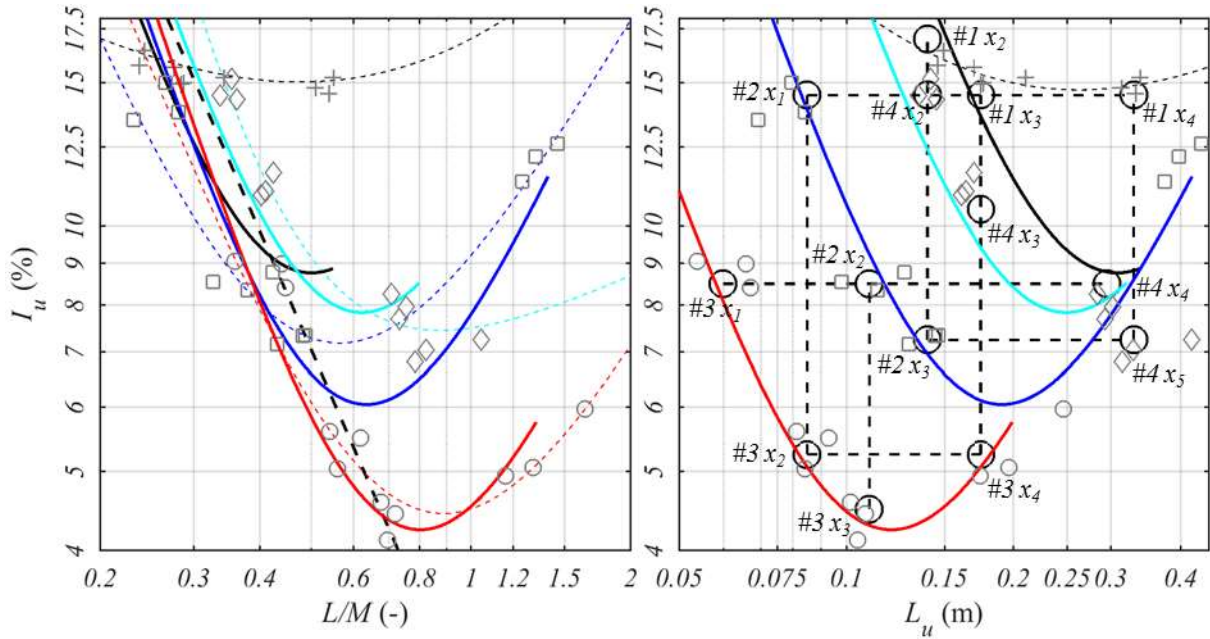


Figure 3.14 Turbulence Intensity versus Integral Length Scale of turbulence in a) non-dimensional, and b) dimensional form. Least square fit of all data (- -; - -; - -; - -; for grids #1, #2, #3 and #4, respectively), and of data at $x \leq 4$ m (\bullet) is plotted together with Equation 12 (\bullet -; \bullet -; \bullet -; \bullet -; for grids #1, #2, #3 and #4, respectively). Circles and dashed black lines in b) refer to Table 3.5.

The statistics varied independently in Figure 3.14 need to show similar turbulence characteristics to be useful for wind tunnel tests. The Power Spectral Density (PSD) of the velocity measurements E_u is useful for this purpose. The spectra are estimated using the Welch overlapped segment FFT averaging technique. To reduce noise at higher frequencies, a Hanning window is used to split the signal into segments of length 0.6042 s, which is $1/100$ th of the total realisation length of $u(t)$. The segments are overlapped by 50% . The number of Discrete Fourier Transform (DFT) used in the PSD estimate is given by the greater of 2^8 or the first exponent of power of 2^n greater than the length of the overlapped segment, i.e. $1/2 \cdot 0.6042$ s, which yields 151.05 Hz. This allows for a frequency step size of 3.33 Hz to be reached. A correction to exclude potential large scales from the wind tunnel was not necessary, as the turbulent flow characteristics in the empty wind tunnel test section are respectively: $L_u=0.013$ m, $\lambda_u=0.004$ m with $I_u=1.03\%$, $I_v=0.4\%$, $I_w=0.32\%$ and $U=16.3$ m/s. The estimated PSD is fitted to the von Kármán formulation given in Equation 6, to give a comparison with atmospheric turbulence.

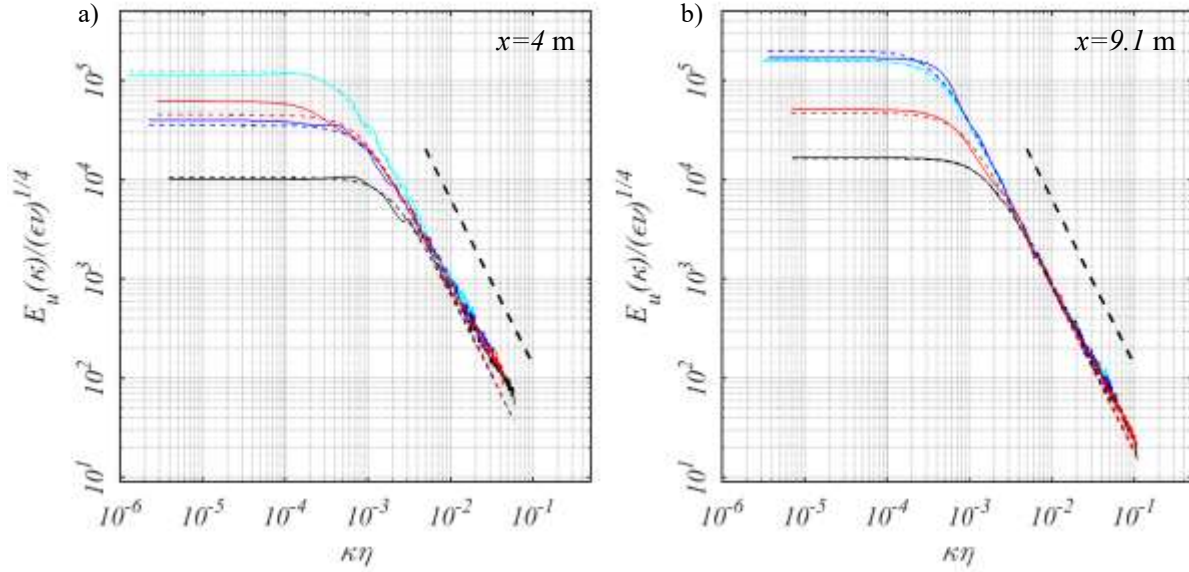


Figure 3.15 Wave number spectrum a) at the inlet of the expansion $x=4$ m, and b) at the outlet $x=9.1$ m; Continuous line for grid #1 (—), #2 (—), #3 (—), and #4 (—); dashed line for von Kármán fitting; (—) -5/3 power law.

The longitudinal wave number spectrum, non-dimensionalised using ε and η , is plotted in Figure 3.15 for measurements at the inlet (a) and at the outlet (b) of the expansion. This plot emphasizes the vicinity of the measurements with the -5/3 power law for the inertial subrange of the spectrum. For comparison, the von Kármán fit is plotted with dashed lines. All grids show a close match with the -5/3 law, consistently with previous results from literature (Isaza et al., 2014). This behaviour suggests that the isotropy and development of the energy cascade of the chosen experimental setup is not affected by the distance from the grid. A closer look might detect a slightly larger deviation from the -5/3 law for data measured at $x \leq 4$ m, which could be interpreted as a contradiction to findings shown in Figure 11. However, this might depend on the low sampling rate used in the experiments (Roach, 1987).

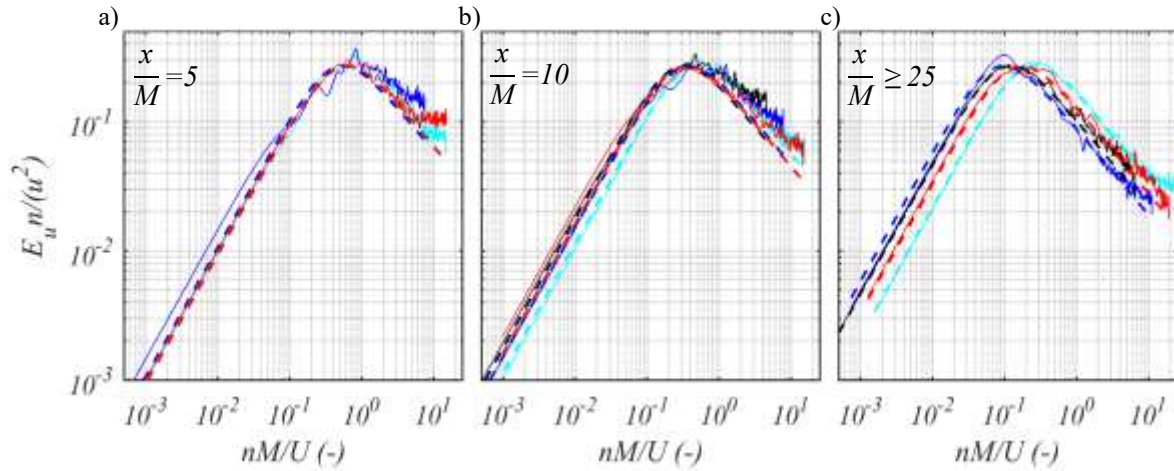


Figure 3.16. Power Spectral Density of turbulence for positions a) $x/M=5$, b) $x/M=10$ and c) $x/M>25$ and wind speed $u_{rot}=15\text{m/s}$. Continuous line for grid #1 —, #2 —, #3 —, and #4 —; dashed line for von Kármán fitting.

Nevertheless, the turbulence field is sufficiently developed and broad-banded for all distances, abnormal peaks in the spectra are absent, suggesting the absence of a residual effect of the bar wakes, even for small mesh distances, i.e. at $x/M\sim 5$.

The evolution of the spectra with the mesh distance is reported in Figure 3.16. The spectra are non-dimensionalised using $E_u n / \bar{u}^2$ and nM/U and plotted at (a) $x/M=5$, (b) $x/M=10$ and (c) $x/M>25$ for all grids. Grid #1 is plotted at slightly different distances: (a) $x/M=5$, (b) $x/M=6.5$, and (c) $x/M=15$. Grid #2 is the only one in the setup, which deviates from the von Kármán fit more evidently at the low frequency end of the spectrum. Nevertheless, neither x/M or the expansion test section appear to affect the deviation of the statistics from theory. The PSD of the three components of velocity u , v and w is plotted in Figure 3.17 at $x=9.1\text{ m}$. The vicinity to the von Kármán fit is analogous to that shown in Figure 3.16 and Figure 3.15.

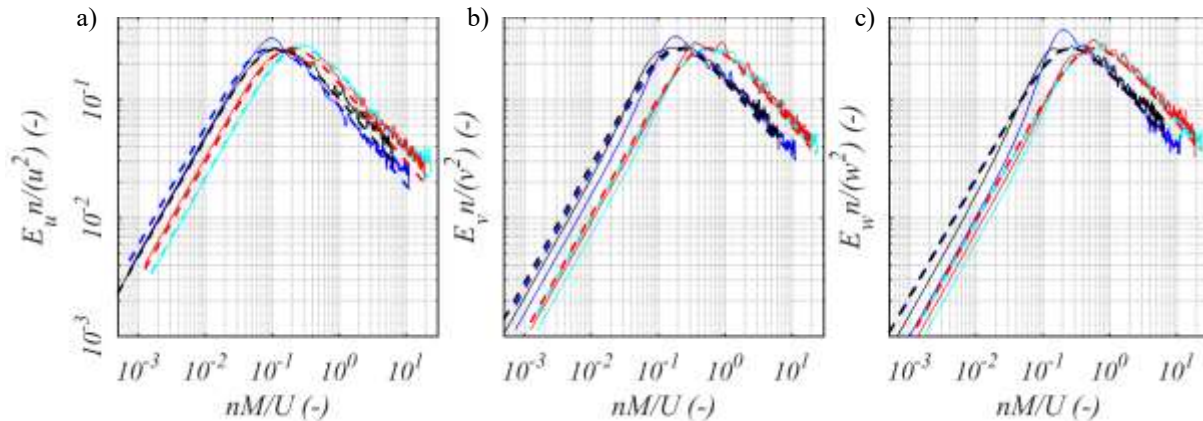


Figure 3.17 Non-dimensional PSD of all velocity components at $x=9.1\text{m}$ and for $u_r = 15\text{m/s}$; Continuous line for grid #1 —, #2 —, #3 —, and #4 —; dashed line for von Kármán fitting.

The results confirm that the spectra maintain the properties of isotropy and uniformity as they are shown to have the same shape and easily fit with the von Kármán formulation. In Figure 3.18, the spectra are reported for statistics varied separately. Constant integral length scale associate with (a), (b), (c), and (d) plots, while constant turbulence intensity associate with (e), (f), (g), and (h). In the case of L_u , the maximum position of the spectra is located at the same frequency for a given scale, while for I_u the spectra are roughly overlapped at lower frequencies.

Table 3.5 Independently varied turbulence intensity and integral length scale, with relevant grid and position.

	Constant Integral Length Scale					Constant Turbulence Intensity			
Grid	#3(x ₂)	#3(x ₃)	#2(x ₃)	#3(x ₄)	#4(x ₅)	#3(x ₂)	#2(x ₃)	#3(x ₁)	#2(x ₁)
#(pos.)	#3(x ₂)	#3(x ₃)	#4(x ₂)	#4(x ₃)	#1(x ₄)	#3(x ₄)	#4(x ₅)	#2(x ₂)	#4(x ₂)
Figure 3.14b	#2(x ₁)	#2(x ₂)	#1(x ₂)	#1(x ₃)				#4(x ₄)	#1(x ₃)
Figure 3.18									
Legend	a)	Not shown	b)	c)	d)	e)	f)	g)	h)
Figure 3.18	—; —;		—; —; —;	—; —; —;	—; —;	—; —;	—; —;	—; —; —;	—; —; —;
	—;		—; —;	—; —;	—;	—;	—;	—; —;	—; —;
	—;		—;	—;	—;	—;	—;	—;	—;
L_u (m)	0.085	0.11	0.145	0.175	0.33	0.09	0.165	0.065	0.08
						0.175	0.33	0.11	0.135
								0.29	0.175
									0.33
I_u (%)	5.5	4.5	7.25	5.0	7.0	5.25	7.25	8.5	14.75
	15	8.3	14.5	11.0	14.75				
			15.7	14.75					

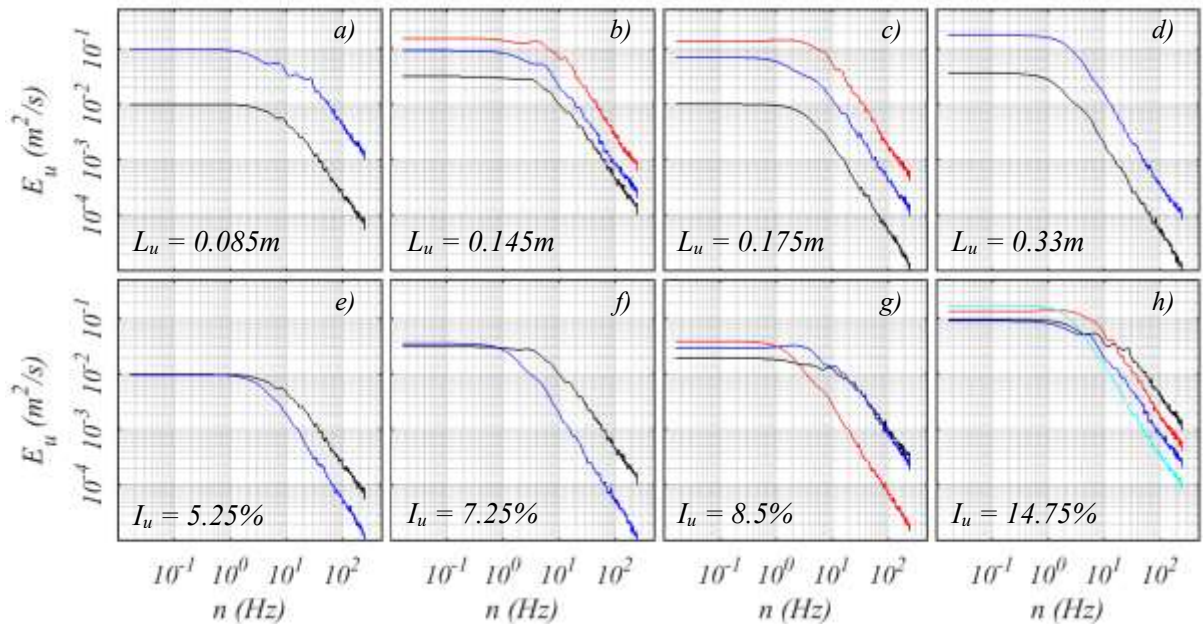


Figure 3.18. Power Spectral Density of velocity for constant integral length scale (a, b, c, d) and turbulence intensity (e, f, g, h); Colours as reported in Table 3.5.

3.4. Conclusions

The effect of an expansion test section on the turbulence characteristics of grid generated turbulence has been addressed in this study. To the knowledge of the authors, such a setup has not been discussed in literature. Results of measurements of the turbulent flow taken downstream of the expansion suggest following conclusions:

- A decrease of the mean velocity downstream of the expansion occurs due to the Venturi effect.
- Due to the change in the mean velocity, the turbulence intensity downstream of the expansion recovers to upstream values, instead of decaying proportionally to the distance.
- The stretching of vortices in the expansion also acts on the integral length scale, which is approximately doubled from what is normally encountered in literature.
- The flow behaviour changes from a pure isotropic one, to a slightly axisymmetric one.
- For lower porosity, the turbulence decay deviates less markedly from literature.
- The Taylor microscale is insensitive to the presence of the expansion, as dissipation remains the main phenomenon involved in the turbulence decay.
- Velocity Skewness and Kurtosis deviate from the normal distribution due to the expansion for lower grid drags for higher porosity.
- The energy spectra fit well to the von Kármán formulation downstream of the expansion, although a limited effect on the slope of the inertial sub-range is noticeable.

The possibility of separately varying both turbulence intensity and integral length scale has also been discussed with reference to the quality of the turbulent field. The flow field is acceptably close to the theoretical behaviour of homogeneous and isotropic turbulence throughout the measurements. The following conclusions can be made regarding grid generated turbulence as measured in this study:

- The near-field region is located at distances less than $x/M < 5$, as for $x/M \sim 5$ the flow is found to be fully developed and dissipation only drives the decay of turbulence.
- The flow field is broadly Gaussian. This feature persists with distance and Reynolds number. However, some form of anisotropy occurs for values at $x/M < 10$, which confirms that

uniformity is a difficult property of the flow field to be achieved. This is a feature worth further investigation.

- Flow field statistics varied independently have shown similar behaviour against isotropy, gaussianity or the turbulence decay. The expansion is of great help in achieving a turbulent flow field with large integral length scale combined with high turbulence intensity, which otherwise would require closeness of measurements to grids with large bar size, i.e. to take measurements in the near-field region of the flow, where dissipation is not the main driver of turbulence decay.

Some limitations of grid turbulence generation can be overcome by modifying the cross section of the wind tunnel. The turbulent flow field is easily fitted to the von Kármán formulation for all distances, grids and combinations considered. Therefore, this technique is suggested to reproduce atmospheric turbulence conditions for the study of the effect of free stream turbulence found in the built environment for a variety of aerodynamic applications, such as urban wind energy.

Chapter 4

Turbulence environment over a typical high-rise building

Results from Chapter 4 are compiled from preliminary research presented at a number of Conferences and published in their Proceedings (Vita et al., 2017a, 2017b, 2018b). These works are here amended and reproduced with the permission of all co-authors.

In the previous Chapter 3, the limitations of wind tunnel testing in terms of turbulence characteristics to be reproduced at the inlet of a physical simulation have been investigated, finding a good correspondence between the turbulence behaviour of the wind tunnel and what is generally acknowledged for atmospheric turbulent flows. This Chapter provides an investigation on the turbulent flow above a suitable location in the built environment to install an urban wind turbine, i.e. a high-rise building. Turbulence characteristics as computed in Chapter 3 are here assessed for several locations above the roof region of the high-rise building. Both numerical and physical simulations are implemented to compare the performance of both techniques in providing reliable results.

This study shows that far from the roof surface, a turbulence intensity of $>10\%$ is expected with large length scales $\sim 200\text{m}$, hence showing the limitations of grid generated turbulence in terms of the scaling of wind turbine aerofoil models to be representative of a suitable turbulent inflow. Closer to the roof turbulence intensity increases further while length scale decreases, with values up to $\sim 30\%$ and $\sim 5\text{ m}$, which is perfectly compatible with values found in grid turbulence.

4.1. Urban Wind Energy, High rise Buildings and the built environment

In Chapter 3, the capability of wind tunnel testing in generating suitable statistics of a turbulent inflow has been explored and a suitable methodology proposed to reach turbulence intensities ranging from 5% up to 15%, with an integral length scale from 0.08 to 0.33 m. It has been ensured that the flow maintained high quality characteristics in terms of isotropy and uniformity for all tested conditions (Vita et al., 2018a). The introduction of turbulence at the inlet of wind tunnel tests has the primary scope of simulating flow conditions found in real conditions. In this case, those correspond to turbulence characteristics found in a location in the built environment suitable for the positioning of a wind turbine. Such locations include those areas where a favourable combination of accelerated mean flow and low turbulence intensity take place, such as on isolated high-rise buildings. Being isolated, the flow at the rooftop of high-rise buildings is not disturbed by surrounding obstacles, while the wind naturally accelerates around its sides and top, due to the blockage to the wind flow.

The positioning of wind turbines within the urban environment is undoubtedly the core issue with Urban Wind Energy, together with non-technical issues (such as the visual appearance of devices or their integration in the urban fabric), and social acceptance. Wind turbines are normally classified against their geometry and technology, however this comes from the inflow they are going to face during their service life (for example offshore wind turbines are geometrically different from onshore ones). This can be well translated to define a new type of WT, meaning the Building Augmented Wind Turbine (BAWT, also Integrated or Environment: BIWT, BWET, or BWT). The building must be interpreted not only as a support for WTs, but also as a way of enhancing wind energy harvesting, by locally diverting and concentrating the wind flow. This can be put into practice in many ways (Figure 4.1). The mutual positioning of BAWTs within the built environment encompasses a number of typical situations:

- i) WTs mounted on top of buildings (Figure 4.1 b-i), which represent the large majority of the applications;
- ii) WTs mounted on the façade of buildings (Figure 4.1 b-ii);
- iii) WTs which are integrated within the building itself using its shape as a local catalyser for the inflow wind (Figure 4.1 b-iii) (Grant et al., 2008; Stankovic et al., 2009);

- iv) WTs mounted in the vicinity of buildings (Figure 4.1 b-iv), which might include bigger WTs (Oppenheim et al., 2004) and can be transposed to the case of complex terrain onshore wind energy (Kozmar et al., 2016).

To the knowledge of the author, no convincing research strategy has been developed to investigate the performance of different positioning strategies, and this list serves rather as a definition for a broad family of devices, which have been placed many times ineffectively in the built environment. However, to obtain the expected performance of a device from its location, as it is done for traditional wind farms (Porté-Agel et al., 2014), might be useful for future applications extending the meaning of this technology further to the localised electricity production. Being wind energy a resource harvested on large areas of land, the concept of Distributed generation might be interestingly combined with small devices (Ackermann et al., 2001). UWE and BAWT can be accounted as a first attempt of Distributed Wind Turbines (DWT). Energy generation with DWTs could represent the final scope of current urban wind energy applications: to multiply the number of devices, with an efficient positioning, in order to provide a reliable share of energy at the consumption site (Lund and Østergaard, 2000).

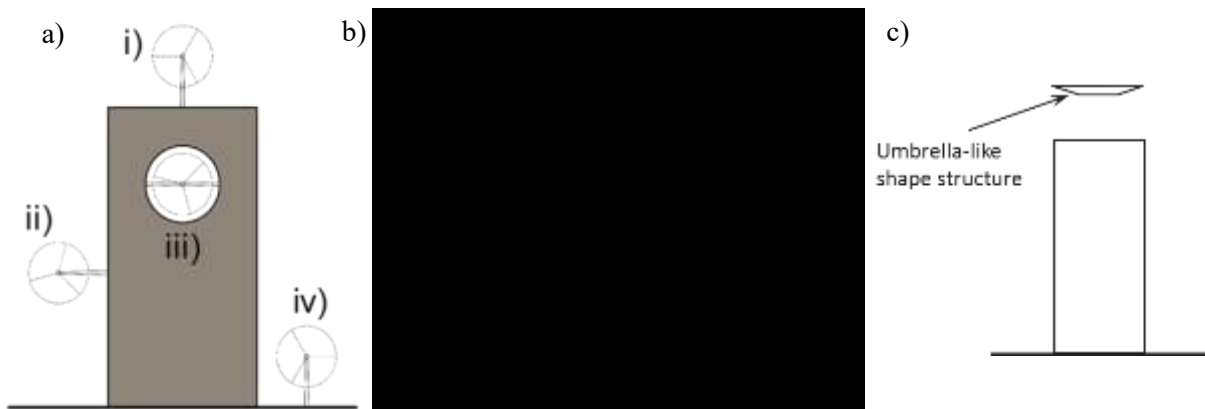


Figure 4.1. a,b) WT and buildings: i) on rooftop, ii) on façade, iii) integrated, iv) in vicinity; c) flow enhancer (Hemida, 2014).

A brief review of a number of significant works focusing on the understanding of building aerodynamics for wind energy purposes is now given, to introduce the scope of the present chapter. In literature a more detailed introduction to Urban Wind Energy as an independent niche of Wind Energy can be found in addition to information reported in this section (Stankovic et al., 2009; Stathopoulos and Alrawashdeh, 2019).

As broadly detailed in chapter 2, the motivation for research in urban wind energy comes from the fact that applications have so far resulted in fiasco. This does not affect the small wind energy market, which is constantly growing showing that a part of the population is willing to invest in a technology at its earliest stages, while several hundreds of thousands of jobs still exist (Gsänger and Pitteloud, 2015). There are several reasons why applications result in failure. Some simply produce only a derisory amount of energy, while others have exorbitant maintenance costs, or lack safety, produce noise, or more importantly there is no connection to an electrical grid, which causes electrical failure if the energy produced is not used. But the main reason for the failure of wind energy comes from the limited knowledge of the flow environment devices are facing throughout their service life, which in turn depends on the shape of the building(s) wind turbines are placed on (or around) (Dayan, 2006).

In literature, two main locations are recognised as suitable for the positioning of wind turbines, which attract the almost whole totality of publications about this topic: street canyons and high-rise buildings (Stathopoulos et al., 2018). Indeed, these locations might experience significant acceleration of the flow combined with a reduction in the turbulence intensity, conditions suitable for wind energy to be harvested more efficiently using available converters as designed at present (Stathopoulos and Alrawashdeh, 2019).

The large majority of investigations focuses on the assessment of the flow pattern, trying to locate spots with optimal augmentation of the mean flow, giving an assessment of the levels of turbulence to be avoided. Recent research on building aerodynamics has specifically developed a niche focusing on the surrounding flow pattern to locate wind energy harvesting opportunities (Toja-Silva et al., 2018).

Almost the whole totality of studies on the flow around high-rise buildings focuses on the assessment of the re-circulation zone above the roof of a given high-rise building, in isolated or juxtaposed configurations. All results agree in confirming velocity augmentation and enhancement of turbulence intensity are the leading features of the flow pattern (Abohela et al., 2013; Ayhan and Sağlam, 2012; Lu and Ip, 2009).

A rather limited amount of research has focused on the optimisation of the building shape to integrate BAWT with building architecture (Mertens, 2006; Stankovic et al., 2009). This has shown to be viable in a handful of applications, such as the Bahrain World Trade Centre (Stathopoulos et al., 2018). Other

works propose instead to enhance the energy yield by slightly improving the shape of the rooftop by building a collector directing the wind to the turbines to optimise the inflow (Hemida, 2014).

Other studies have instead focused on the identification of the rooftop shape which most suits urban wind energy harvesting (Abohela et al., 2013; Toja-Silva et al., 2015b). Results show that the shape of the roof is crucial in affecting parameters such as the region with higher turbulence intensity not suited for urban wind energy positioning. In particular, Figure 4.2 shows that a limit surface can be found which can be used as reference for the positioning of wind turbines with given characteristics by defining a turbulence intensity limit (Toja-Silva et al., 2015b). It was found that having a curved roof enhanced the possibilities for wind energy harvesting. However, the criteria chosen for defining the optimal location are not universally agreed, and therefore the setting of a priori conditions might not be enough to guarantee a shift in the technology in the near future nor prompting the public to trust the technology more. Furthermore the choice of the investigation methods is also important, e.g. RANS is known to have strong limitations in reproducing accurately the turbulence intensity of a flow (Hemida and Krajnović, 2010).

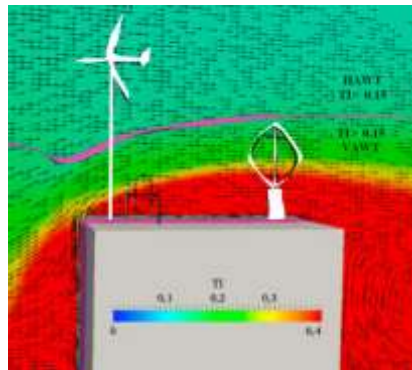


Figure 4.2. Choice of the most suitable typology of wind turbine based on the computation of regions of the flow having given characteristics (Toja-Silva et al., 2015b)

Moreover, finding the optimal configuration for a roof shape to yield higher energy performance might not be a feasible strategy to foster wind energy, because of the role of non-technical issues, such as aesthetical, architectural, and perception problems (Hamza, 2015).

Another sample of studies focuses on the choice of the best suited wind turbine for an urban configuration (Balduzzi et al., 2012). Vertical Axis Wind Turbines (VAWT) are recognised as the most viable choice, due to their response to urban highly turbulent flows. However, it has been confirmed

that Horizontal Axis Wind Turbines (HAWT) placed in the same location and having same rated power, are able to yield more energy than VAWTs over a significantly large time-span with variable wind conditions (Pagnini et al., 2015). The choice of the optimal match among available typologies for a given site might indeed help to understand how to use the technology in a more efficient way. However, the basic physical mechanisms under which site-specific flows impact performance is still left unexplained in these studies.

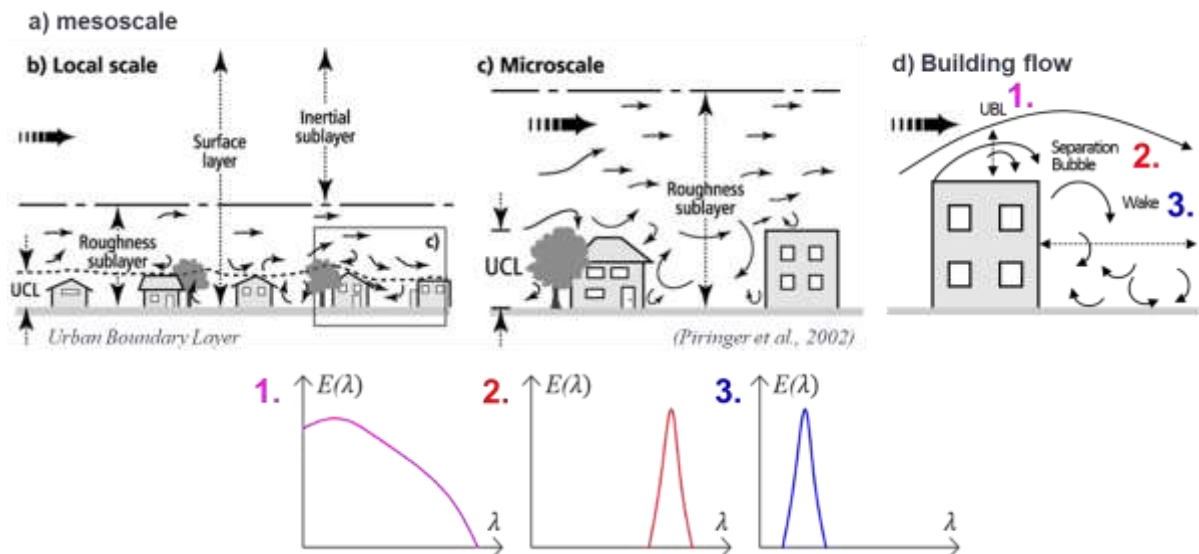


Figure 4.3. (Top) the different scales of the urban boundary layer (adapted from Piringer et al., 2007); (bottom) different typologies of turbulence around buildings (Haan and Kareem, 2009)

In literature, high turbulence is normally associated with problems (Burton et al., 2011). Figure 4.3 shows the genesis of turbulence structures within the urban environment, its different scales, and the different typologies of turbulence, which might occur (Haan and Kareem, 2009; Piringer et al., 2007):

- Atmospheric turbulence (referred to as 1 in Figure 4.3);
- Shear Layer turbulence within separation bubbles and recirculation zones (2);
- Signature turbulence in the wake of buildings (3).

Whether VAWT or HAWT are used, their superior or lesser efficiency is biased by a generalised lack of understanding of the turbulence effects on the aerodynamics of wind turbines (Vita et al., 2016). It is not clear whether signature turbulence coming from a wake of a building is more detrimental than atmospheric turbulence, or viceversa. Therefore, the customary attitude toward turbulence is to avoid it whatsoever. Few reference, cite locations with turbulence intensities higher than 0.15, as being

harmful for the performance of devices (Dekker and Pierik, 1998). In particular, the fatigue limit state (Mouzakis et al., 1999) and the power output (Sunderland et al., 2013) are usually looked at. However, indications on the effects of turbulence on the aerodynamic performance are almost undisclosed in literature (Sørensen, 2011). These works confirm the importance of understanding the wind pattern, the possibility of enhancing the wind energy resource and the choice of the proper wind turbine for use.

Street canyons might represent another location of interest for wind energy aerodynamicists. Adjacent high-rise buildings might be designed to enhance street canyon effects to harvest energy (Khayrullina et al., 2013).

This rather brief review of relevant literature pictures a challenging panorama when investigating the positioning of wind turbines in the built environment. Poor knowledge about the flow pattern around buildings does not allow a scientific positioning strategy similar to traditional wind farms, while it is also unclear how wind turbines respond to highly turbulent flows. In particular, before advancing the knowledge further, more results are crucially needed on the following issues:

- v) the aerodynamic response of wind turbines under turbulent flow structures;
- vi) the flow pattern around buildings and the relevant turbulence characteristics;
- vii) possible ways of enhancing wind energy harvesting using buildings and their shape;
- viii) social acceptance issues and the much required mediation with non-technical issues.

The aim of this chapter is to investigate the flow above the roof of an isolated high-rise building to assess the turbulence characteristics a hypothetical wind turbines might face during its service life. In particular the following objectives of the research are implemented in this chapter:

- ix) The assessment of turbulence intensity and length scales on a high-rise building, as in previous experimental tests (Hemida et al., 2015), providing a validation test-case.
- x) The adequacy of steady-state RANS simulation to predict the experimental results;
- xi) The adequacy of higher-fidelity CFD LES data to predict advanced flow statistics.

In Section 4.2 the experimental and numerical methodology are detailed, with reference to previous chapters for the post-processing of velocity statistics. In Section 4.3 the experimental results providing the validation test-case are briefly reported and discussed, with reference to the mean flow and statistical

moments. In Section 4.4, experimental results are compared with numerical RANS and LES to assess the adequacy of the various techniques in predicting the flow pattern. In Section 4.5, a discussion on energy spectra and length scales is also provided, assessing the influence of the inflow on the development of flow statistics.

4.2. Methodology

4.2.1. Experimental Setup at Ruhr Universität Bochum

The validation test-case for the numerical models performed in this research is provided by a previous experiment (Hemida et al., 2014; Šarkić Glumac et al., 2018). A series of wind tunnel experiments has been carried out at the Atmospheric Boundary Layer (ABL) Wind Tunnel Lab of the Ruhr-Universität Bochum (RUB), within the scope of the COST-Action TU1304 WINERCOST. The RUB wind tunnel has a cross section of $1.6\text{ m} \times 1.8\text{ m}$ and a length of 9.4 m , in an open tunnel configuration with fan downstream of the test section.

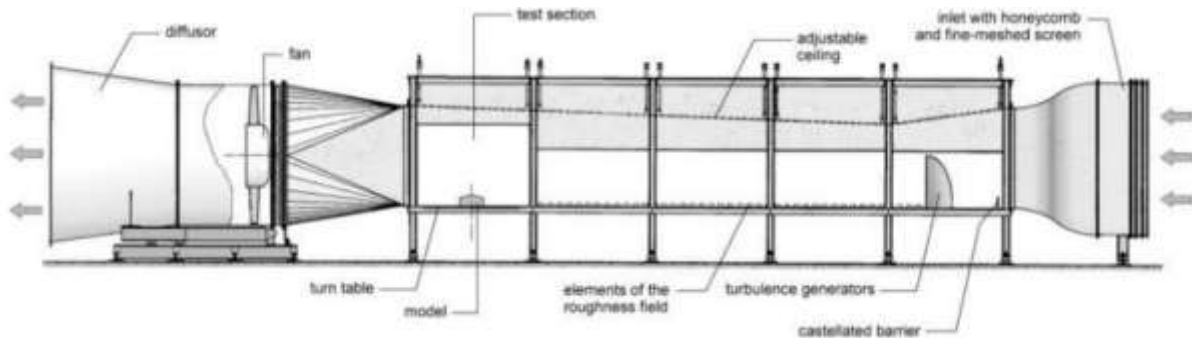


Figure 4.4. Wind Tunnel of the Ruhr-University Bochum

Figure 4.4 shows that the ABL is simulated thanks to a castellated barrier, turbulence generator fins, and roughness cubes (from 3.6 cm to 1.6 cm) working as roughness elements capable of generating a broad variety of boundary layer inlets. The high-rise building model has a $1:300$ scale, with a height-to-width ratio of $H/D=3$, where $H=400\text{ mm}$ and $D=133.3\text{ mm}$. This is equivalent to a 120 m high-rise building, with sides of 40 m .



Figure 4.5. Photo of the wind tunnel with the model mounted on a turning table

Figure 4.5 a) shows the model mounted on the rotating test table of the wind tunnel. Measurements of the flow pattern were taken above the rooftop, using hot-wire anemometry (HWA) of the miniature X wire probe of 11 DANTEC (55P61) kind (Figure 4.5 b and c) placed at different height and locations as schematised in Figure 4.6 b). HWA do not account for reversed flow, and results have been interpreted accordingly to detect any separation. Measurements have been taken to assure a good assessment of the turbulence intensity. The velocity components in the y and z directions, u and w , have been measured for $z/D > 0.1$. Time histories of each signal have been obtained using a length window of $131s$, and all results are referred to the width of the model $D=133.3mm$ and the reference velocity $u_{ref}=u(z=H)=15.85m/s$ (Figure 4.6).

The surface pressure has been measured as well, with 64 pressure taps placed on the rooftop and on the sides of the model HRB. This is treated in detail in Šarkić Glumac, Hemida and Höffer, (2018) and not further discussed in this chapter.

The inlet profile of mean velocity and turbulence intensity are shown in Figure 4.6a. Figure 4.6b shows the Positions considered in the experiment. In this chapter only results for Pos. 1 and 2. These values provide a very useful validation dataset, as the flow field is normally disregarded in studies about building aerodynamics in favour of the surface pressure field, which is more commonly considered and discussed in detail (Baniotopoulos et al., 2011).

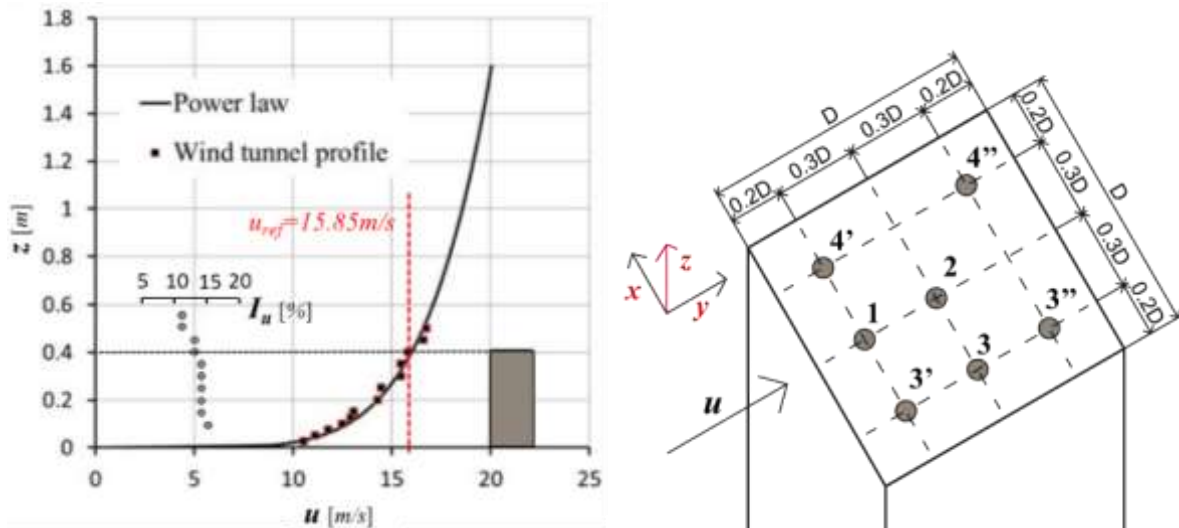


Figure 4.6. Wind-tunnel velocity profile ahead of the model

4.2.2. Numerical setup

Large Eddy Simulation (LES) is used for the numerical simulation of the isolated high-rise building. A turbulent inlet is introduced to generate fluctuating turbulence statistics. Precursor domain simulation is the technique of choice for the generation of inlet turbulence. The upstream part of the wind tunnel, which is responsible of the development of the ABL in the experiment, is modelled in the geometry. This approach accounts as a sort of virtual wind tunnel to be modelled. However, a great amount of caution is needed for computational accuracy, as with such large domains and strict mesh requirements, the convergence of the simulation as well as their cost is at stack (Lund et al., 1998).

In order to understand the effect of a turbulent inlet in the accuracy of results, two domains have been tested in the present chapter, as shown in Figure 4.7.

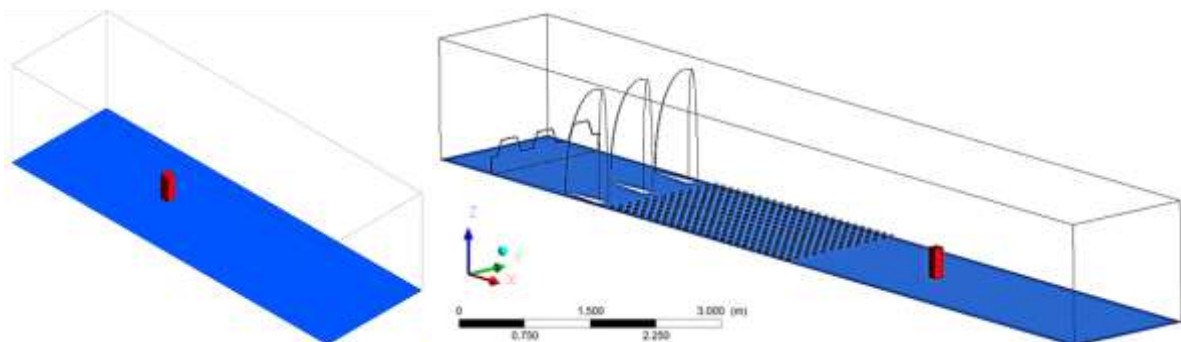


Figure 4.7. a) Fluctuating and b) steady inlet domains for LES.

A steady state RANS (Reynolds Averaged Navier-Stokes) simulation has also been implemented using the $k-\omega$ SST turbulence model, to obtain a comparison with lower-fidelity methods and their adequacy

in reproducing the turbulence environment on top of high-rise buildings. In fact the RANS approach has shown good viability for the estimation of the averaged fields and it is heavily used in urban wind energy (Stathopoulos and Alrawashdeh, 2019), however, its performance is hindered by the modelling of fluctuating statistics (Blocken et al., 2016; Ozmen et al., 2016).

A block structured mesh has been constructed (Figure 4.13), having $y^+ \sim 1$ and choosing the blocking strategy in order to limit the along-flow size of the elements to respect the CFL condition which imposes $Co < 1$. This has brought to the choice of a time step of $\Delta t = 5e^{-5}$ for the LES model presented. The Smagorinsky-Lilly model has been chosen as Sub-Grid Scale model (SGS), with the use of the van Driest damping function, as implemented in the OpenFOAM® software v.2.3.1. A damping function, such as the one formulated by Van Driest $l_{sgs} = C_{sgs} \Delta \left(1 - e^{-y^+/A^+}\right)$, where $A^+ = 26$, lowers the value of the model constant C_{sgs} or C_s in those regions of the flow where viscosity effects become preponderant. In fact, the Smagorinsky model uses a fixed constant to take into account the SGS effects, potentially yielding an unphysical behaviour. The eddy viscosity reads $\nu_{sgs} = (C_{sgs} \Delta)^2 |\tilde{S}| = (C_{sgs} \Delta)^2 \sqrt{2\tilde{S}_{ij}\tilde{S}_{ij}}$ where the Smagorinsky model constant has been set to $C_s = 0.17$ according to indications from the literature (Pope, 2000).

4.3. Results

4.3.1. Experimental validation testcase

The measurements of the velocity around the models show (as expected) that near the surface the flow is reversed, because of a separation bubble.

Figure 4.8 shows the mean velocity as measured with HWA. The horizontal and vertical components are respectively shown for positions 1 and 2. The reference velocity U_{ref} is from the inlet wind profile at the same height of the high-rise building model. Results show that the horizontal velocity increases by a factor of $\sim 30\%$ in both positions at about $z/D \sim 0.3$, at the centre of the roof (Pos.2). This is just above the shear layer between the separation region and the upstream flow, which is in agreement with previous experiments (Hemida, 2014).. However, the increase is noticeable for a broader region above the rooftop for position 2, where the separation bubble is thicker. In particular, the increase in the

velocity occurs at $y/D \sim 0.15$ for position 1, while the same increase occurs at $y/D \sim 0.2$ for position 2. The vertical component shows a pronounced magnitude in position 1, where at $y/D \sim 0.22$ a significant $\sim 50\%$ of the reference velocity can be noticed. This indicates that wind turbines placed at the edge of high-rise experience highly yawed flow. At position 2 the vertical component is negligible, which shows vicinity to the core of the separation bubble.

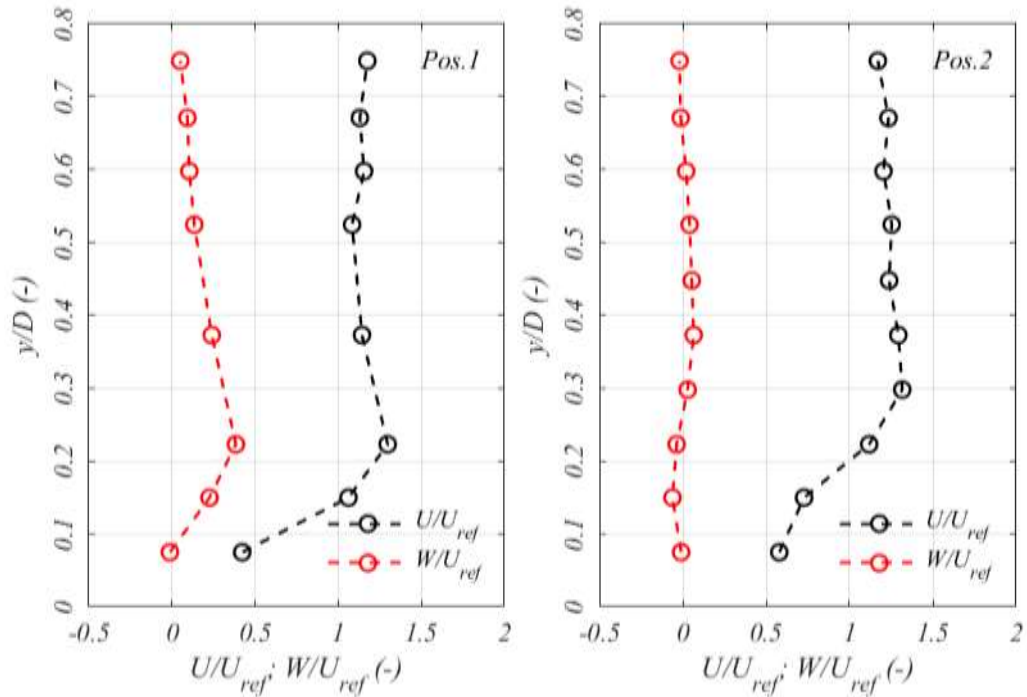


Figure 4.8. Velocity vectors, I_u and I_w as measured at pos. 1 and 2.

Numerical results might come useful in interpreting Figure 4.8. Figure 4.9b shows the flow pattern around the high-rise building model with a fluctuating inlet. The separation bubble can be noticed at the top of the building, with a broad region of sheared flow showing the difference in the height of the increased velocity magnitude.

Figure 4.9 shows the relative error between the reference velocity and the velocity measured on top of the model. It can be noticed how the flow stays steadily accelerated for both positions for a significant height above the model at around $\sim 20\%$ increment. Close to the surface a strong decrement is instead seen as expected.

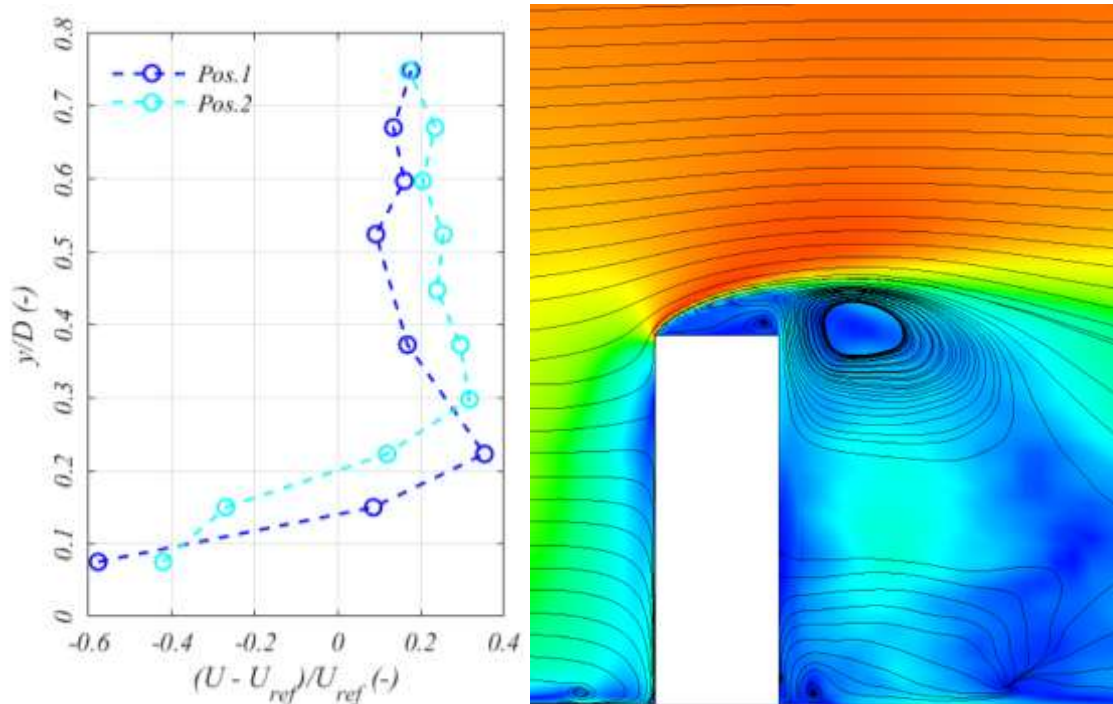


Figure 4.9. Mean velocity respectively at position 1 a) and 2 b), with experimental results (line for k - ω , dashed for les); c) streamlines of averaged velocity field for les model.

Figure 4.10 shows the horizontal and vertical turbulence intensity. Above $z/D \sim 0.3$, turbulence intensity declines to about 0.1 for both u and w , matching the one present in the upstream flow. This value is the lowest of the dataset above the rooftop, at a height consistent for both vertical and horizontal components, and it is quite close to limitations normally posed in literature of 15%. At a height of $y/D \sim 0.25$ and ~ 0.4 $TI \sim 15\%$, which would ideally require a 16m mast over the rooftop for a wind turbine to avoid the region with high turbulence. This also suggests that the building affects turbulence intensity up to a height of about one third of its width. Figure 4.10 also gives some information about the isotropy of the flow. For $y/D > 0.2$, $I_u \sim I_w$, meaning that the turbulence is rather uniform and isotropic and close to grid turbulence as reproduced easily in wind tunnels. However, such behaviour is not shown at lower heights, where the horizontal component is significantly higher than the vertical one. This anisotropy has indeed an effect in the behaviour and aerodynamic response of devices placed in its stream and at present there is no convincing technique to reproduce this rate of anisotropy in the wind tunnel without a significant and expensive amount of trial and error, so unfeasible for practitioners investigating the response of wind turbines.

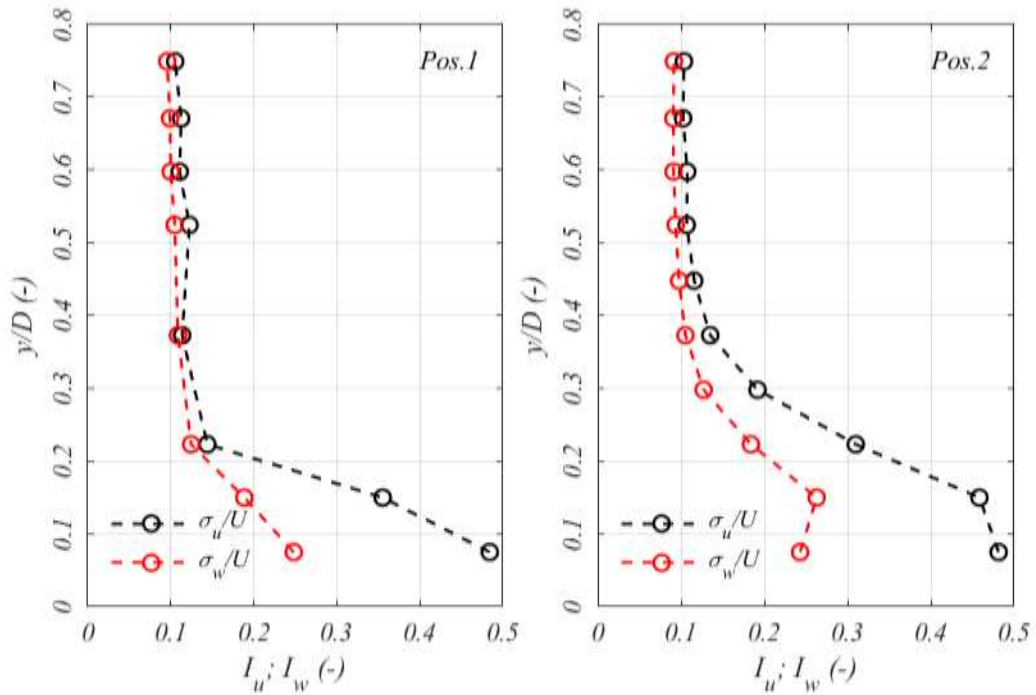


Figure 4.10. Horizontal and Vertical Turbulence intensity for Position (left) 1 and (right) 2.

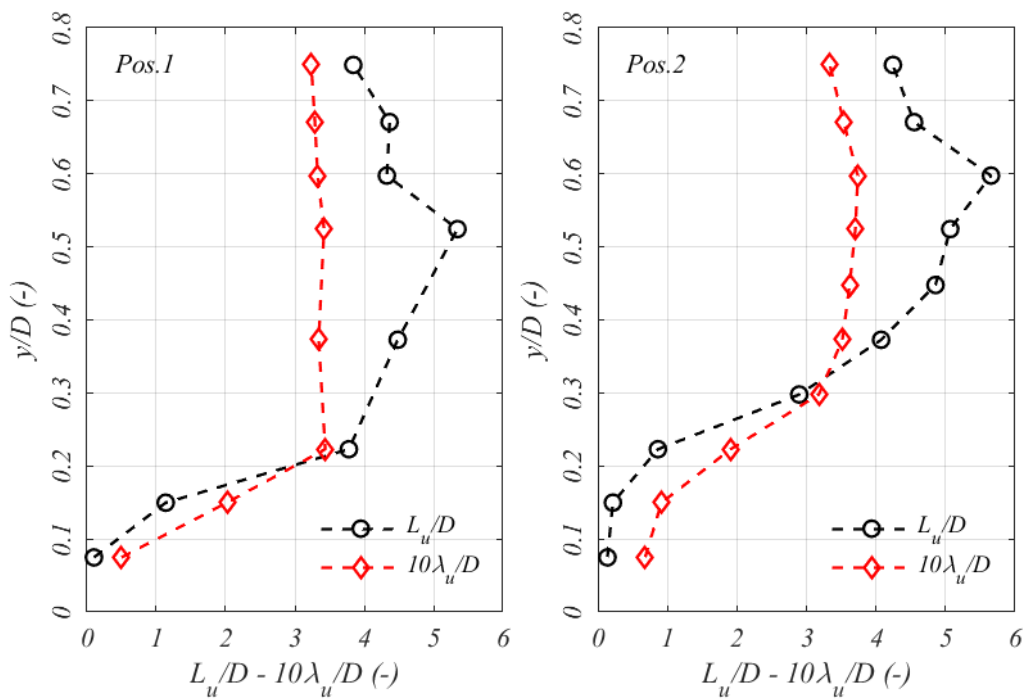


Figure 4.11. Integral and Taylor-s length scale of turbulence for Position (left) 1 and (right) 2. The Taylor-s microscale is plotted with a factor of 10.

Figure 4.11 shows the integral and Taylor’s length scale of turbulence. At position 1 the length scale is growing up to an height of $y/D \sim 0.2$ to then keep growing with a different but slower rate up to a maximum point at $y/D \sim 0.55$ to then decrease for higher heights. Figure 4.12 might explain the maximum in the integral length scale’s plot. At $y/D \sim 0.55$ the probe is in a region of the flow with high

shear stresses, which might explain the larger length scale measured. The Taylor's length scale shows an interesting behaviour. In fact, consistently with the integral length scale, a steady growth is noticeable up to a height of ~ 0.22 , to then keep a constant value throughout the rest of the height as measured. This suggests that at dissipation scale the turbulence environment has more or less the same characteristics regardless of the height outside of the separation bubble. At Position 2, the behaviour is analogous, with a larger extent of the separation bubble and a slightly different behaviour of the Taylor's scale, which shows a maximum in the same location as the integral length scale in this case.

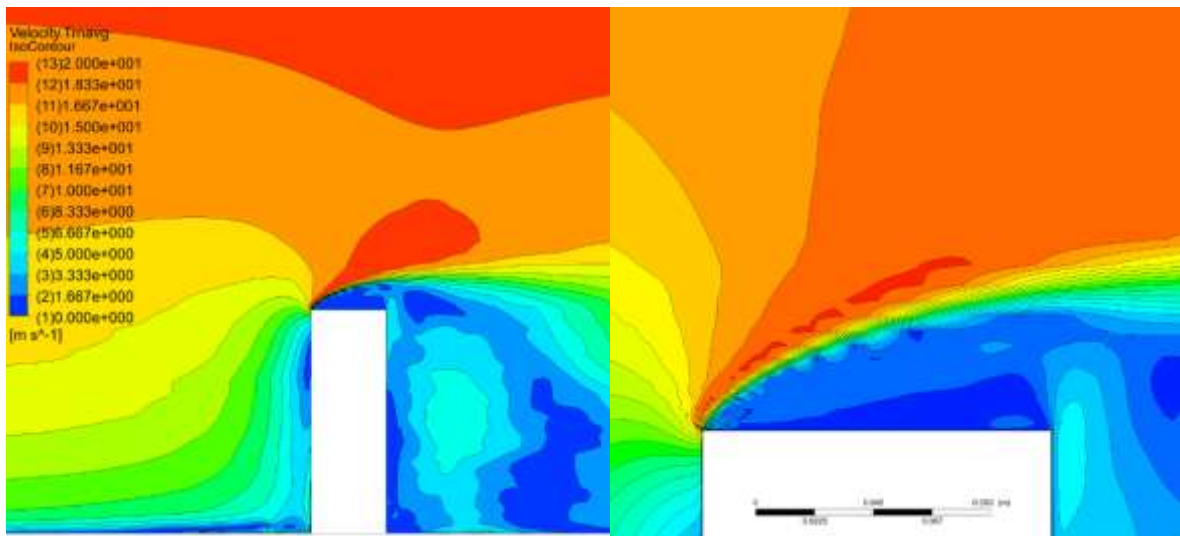


Figure 4.12. Iso-contours of the mean velocity field for the LES simulation.

4.3.2. Numerical flow pattern

Figure 4.13 shows the flow pattern around the high-rise building in the case of no inlet turbulence. This case is shown as the coherent structures of the instantaneous flow are more evident and recognisable. Horseshoe vortices are recognisable at the ground of the building, in particular two vorticities are present at $x/D \sim 1$ and $x/D \sim 0.2$ respectively. The separation is evident from the presence of leading edge vortices which affect the shear layer between the separation bubble and the free-stream flow. The leading edge vorticity evolves into vortex shedding with periodic behaviour, as regions with same Q -invariant are present at a spacing of $\sim 0.2D$. In the wake of the building the vorticity curls up into hairpin vortices which enhance the mixing with the free stream. For this reason the wake funnels and stretches towards the ground. Some vorticity is dragged downstream of the building with no apparent stretching at $x/D \sim 5$, where the development of the wake is entirely driven by the free stream flow. LES captures

quite accurately this behaviour in agreement with the literature and this can be attributed to the superior quality of the mesh shown in Figure 4.13b. In Figure 4.13c the Q-invariant for the turbulent inlet case is shown, with the vertical structures more chaotic around the building but suggesting a similar behaviour as in undisturbed case.

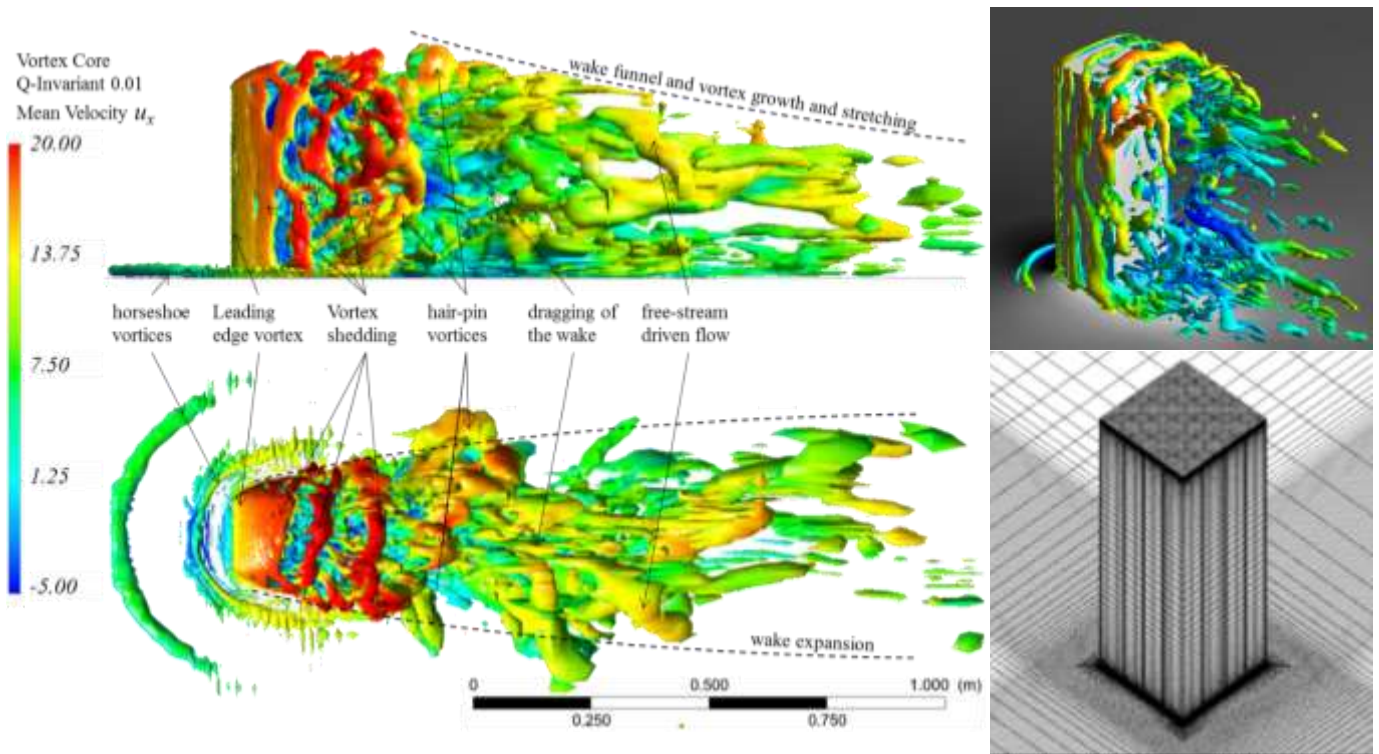


Figure 4.13. a), b) Vortex core visualisation (Q invariant $1/s^2$), with flow pattern identification; c) vortex core visualisation (swirling strength $1/s$) and d) structured block grid of the high-rise building model.

Figure 4.14 shows the flow pattern in all computations for the steady and fluctuating inlet cases and for the LES and RANS simulations. As regards the RANS cases, the vortical structures are more regular and symmetric, with a region of vorticity around the base of the building (more evident for the steady inlet). As for the turbulent inlet case, a large region of vorticity is present downstream of the building, which indicates an interaction between the separated flow region in the wake with the free-stream flow structures. In fact, a large vortex originating from the inlet spires is present in the top-right corner of the view. The LES flow is analogous to Figure 4.13, with a region of vorticity at the ground of the building, vortices around the separation bubble characterised by vortex shedding and large curved vortices in the wake of the building stretched and dragged downstream thanks to the free-stream flow. However, these structures are disrupted earlier than the steady inlet case in smaller structures, indicating that the wake might be much smaller in extension. Nevertheless the presence of a recognisable vortex

shedding indicates that close to the separation bubble the main flow mechanism is governed by the leading edge vorticity rather than the typology of the inlet.

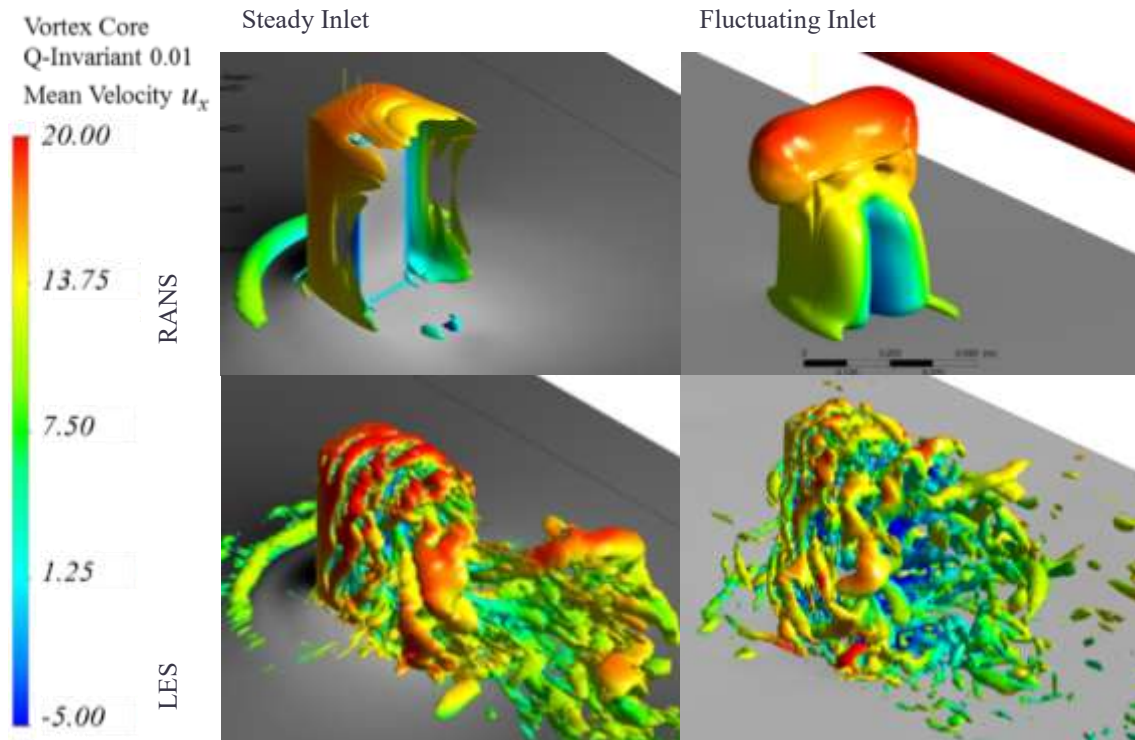


Figure 4.14. Flow pattern in terms of velocity-invariant $Q=0.1$ in the case of (left) steady and (right) fluctuating inlet for the (top) RANS and (bottom) LES cases.

4.3.3. RANS and LES results

Results are compared for the turbulence characteristics over the vertical profile over Position 1 and 2. RANS is traditionally used in industry to evaluate the turbulent flow around a bluff body. This approach is followed by recent works on the wind energy availability above high-rises (Toja-Silva et al., 2018, 2015a). Figure 4.15 shows that the performance of RANS and LES is comparable, with RANS being actually closer to the experimental results. Both techniques seem not to capture correctly the accelerated region of the flow, but this could also depend on the definition of U_{ref} , which is based on wind tunnel measurements. It is difficult to measure the wind profile produced by the CFD elongated domain without performing a simulation without the model inside and therefore the value from the wind tunnel test is used. Results also show that the separation bubble is ill captured in the wind tunnel tests, as no reversed flow is registered, which is not the case for RANS and LES, which report a similar extent of the separation bubble. The steady inlet condition shows no evident differences with the other case for

position 1, while for position 2 the extent of the separation bubble is around $\sim 50\%$ larger. This shows how turbulence in the inflow contracts the separation bubble hence delaying separation and reattachment. It is therefore important to reproduce the turbulent environment around a high-rise building to assess the mean wind potential above it.

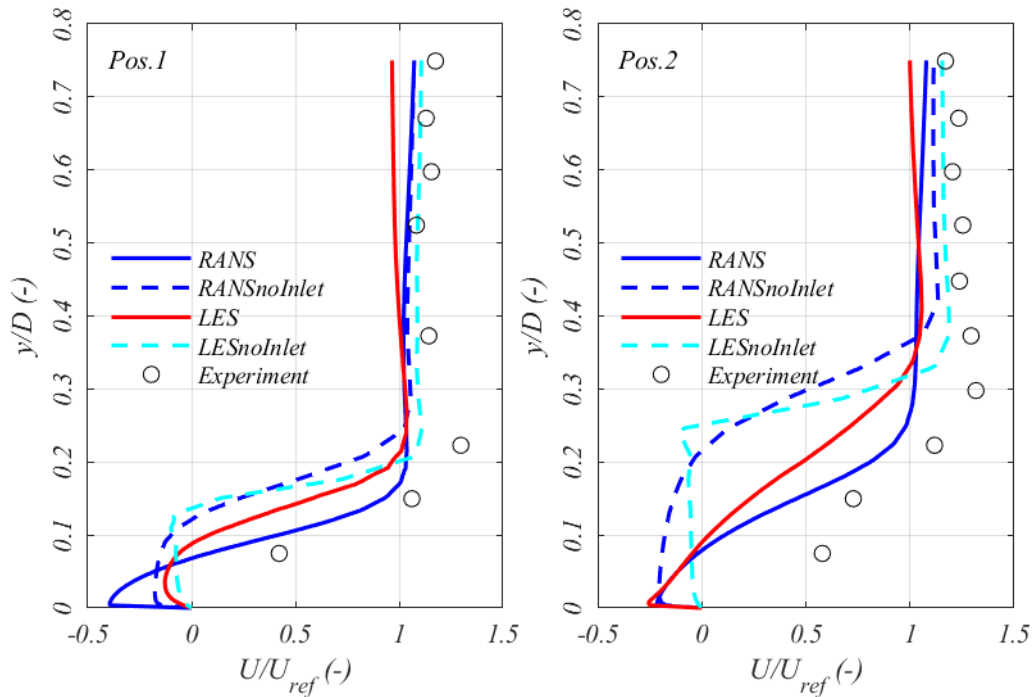


Figure 4.15. Horizontal mean velocity for Position 1 and 2.

Continuous line for turbulent inlet, dashed for steady and comparison with experimental results..

Figure 4.16 and Figure 4.17 show respectively the horizontal and vertical turbulence intensities. Turbulence intensities from RANS are calculated from the turbulent kinetic energy using the hypothesis of isotropy of the turbulent scales, and therefore is only reported for the horizontal velocity. Figure 4.16 confirms the necessity of introducing turbulence in the inlet as both RANS and LES underestimate turbulence by $>60\%$. As for the turbulent inlet case the prediction is very close to the experimental case for both RANS and LES. RANS over-estimates turbulence intensity for $z/D > 0.2$ at $\sim 30\%$ (three times of what predicted with experiments). This depends on the possible shift in the estimation of wakes of roughness elements, spikes and barriers used to develop the boundary layer in the turbulent inlet case. LES shows a close match at position 1, while at position 2 turbulence at the separation bubble is over-predicted by $\sim 80\%$. This might depend on the definition of the turbulence intensity based on U_{ref} , rather

than a mismatch in the physical mechanisms involved, as the position of the maximum turbulence intensity at $z/D \sim 0.2$ is analogous for both LES and experimental cases, while the RANS is at $z/D \sim 0.15$.

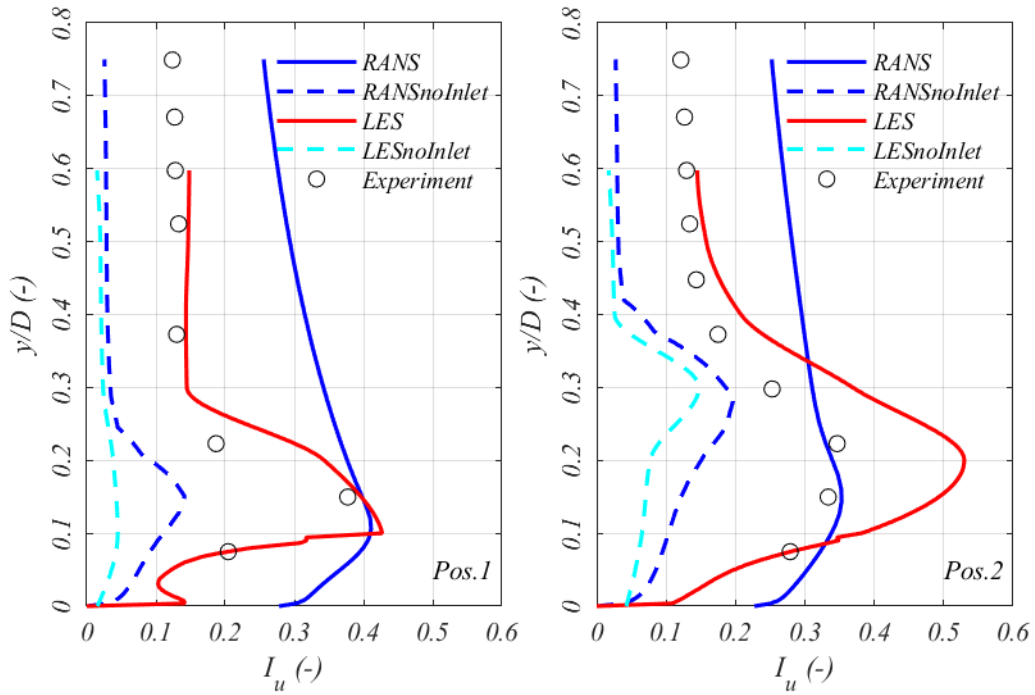


Figure 4.16. Horizontal turbulence intensity for Positions 1 and 2.

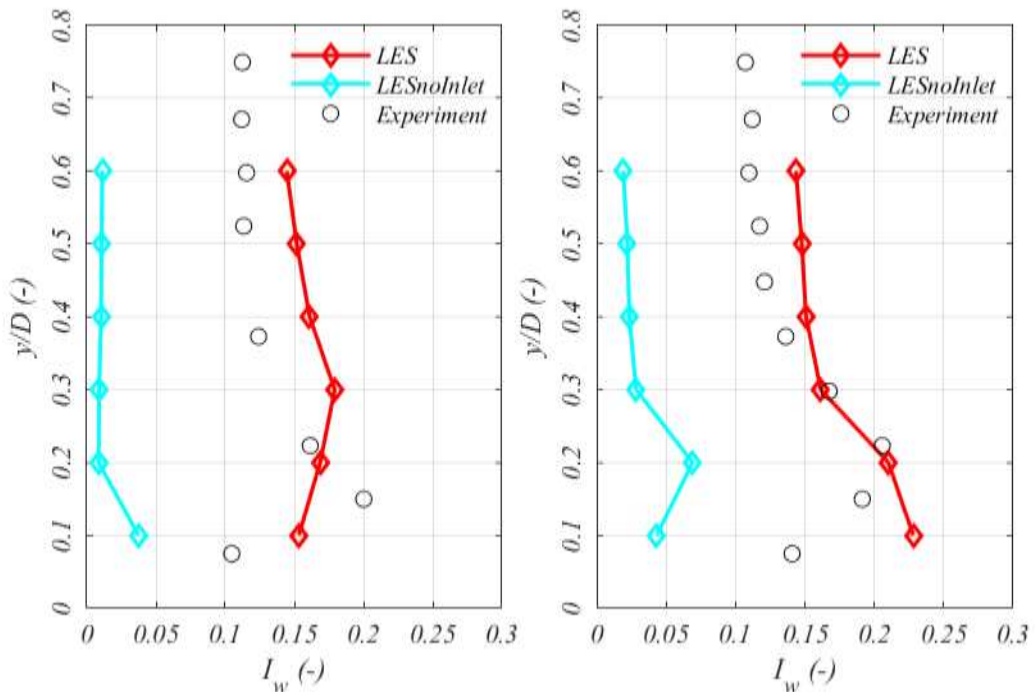


Figure 4.17. Vertical turbulence intensity for Positions 1 and 2.

Figure 4.17 shows how LES is also performant in the prediction of the vertical turbulence, with an over-prediction of I_w for $z/D \sim 0.2$ in position 2. The turbulence intensity is also over-predicted by $\sim 20\%$ for

$z/D > 0.3$. This might depend on the refinement of the mesh in the y direction of the model. While a discussion on the anisotropy of turbulence might be done using results from Figure 4.16 and Figure 4.17, there are other methods, which use all flow components and yield a more accurate interpretation, as done in Chapter 3. Figure 4.18 shows the velocity invariants for Position 1 and 2. At position 1 the flow is highly isotropic close to the wall, while the anisotropy increases for $z/D > 0.4$. At position 2 as the separation bubble thickens, the flow is more anisotropic for $z/D > 0.2$. LES seems to over-predict anisotropy, and this is in line with previous findings on the turbulence intensity, with a possible mesh dependence of the transversal properties of the flow. LES shows its great flexibility in reproducing a great range of characteristics of the turbulent flow provided that sufficiently detailed turbulence is provided at the inlet.

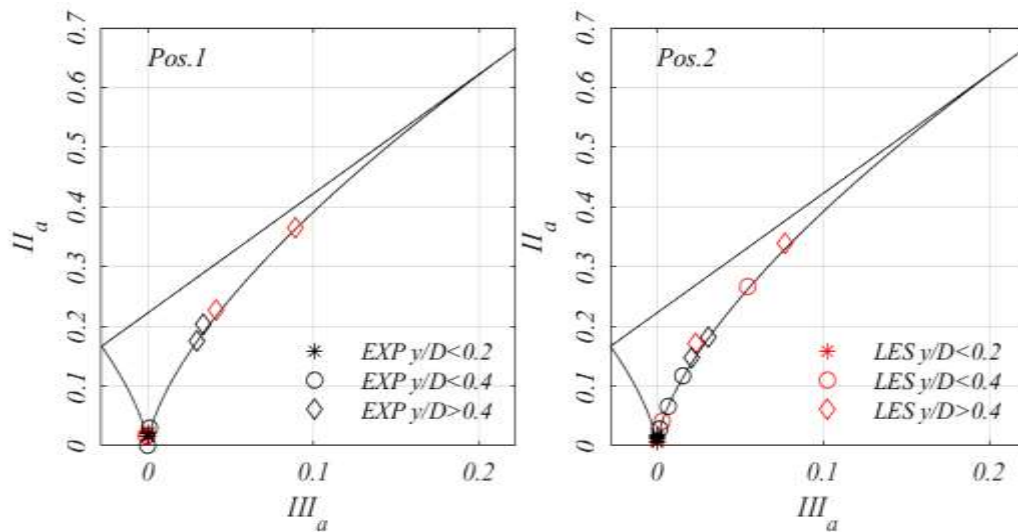


Figure 4.18. Velocity invariants for the assessment of flow anisotropy. Results for experimental setup and LES with turbulent inlet conditions.

The next results report on the frequency analysis and turbulence length scales of the model. To interpret results a diversion on the characteristics of the time-histories considered is due. In order to post-process LES, the time-histories needed trimming as the first flow-through-times are needed to eliminate any unwanted trends in the data. However, the cost-effectiveness of a LES aimed at solving most of the scales in the flow, especially close to walls, requests the comparison between the longer duration signal of the experiment and the $\sim 5s$ signal of the LES ($\sim 1s$ for the steady inlet LES due to problems with convergence). Figure 4.19 shows the time-histories for Position 1 at $x/D = 0.3$ overlapped. While the stationarity of the signal might result in accurate lower order statistical moments, for higher order

statistics the accuracy (or the lack of it) might depend on the short sample time used. Figure 4.19 also shows that while the LES and experimental signal is similar, with non-stationary peaks and turbulence, the steady inlet LES is rather smooth, which again confirms the need of turbulent inlet boundary conditions to enhance accuracy.

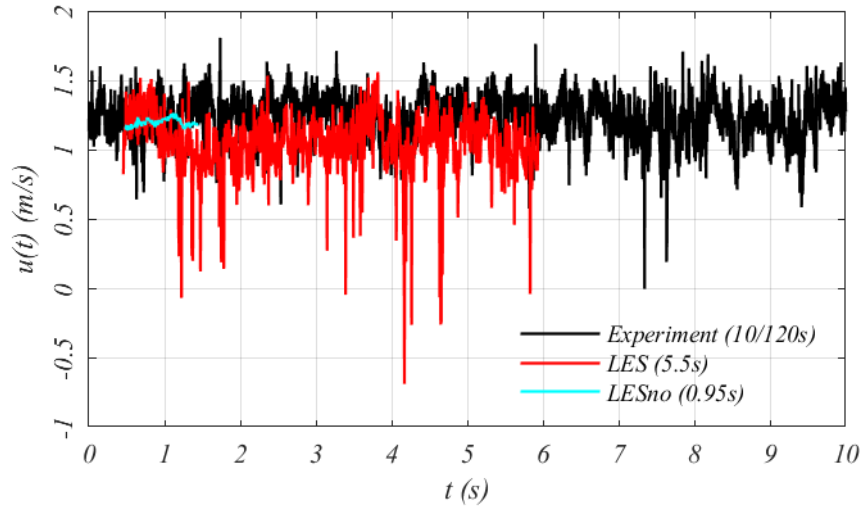


Figure 4.19. Time histories for Position 1 at $z/D=0.3$ for experimental, LES and no inlet LES cases.

Figure 4.20 shows the power spectral densities for both positions at two heights, $z/D=0.1$ and $z/D=0.6$. Close to the roofless and Les no inlet results match, indicating that the turbulence is affected mostly by the leading edge separation. At $nD/U_{ref} \sim 0.2$ a light vortex shedding frequency is captured by LES, in disagreement with the experiment. However, the experimental results might be affected by the incapacity of HWA in capturing reversed flow. At $z/D=0.6$ LES and experimental results are very close for both positions, while no inlet LES fails in capturing the behaviour. This shows the importance of the turbulent inlet conditions in the freestream and the fact that a longer sample time might be needed in the absence of turbulence, prompting a reflection on the cost-effectiveness of simulations requiring the generation of turbulence at the inlet. LES spectra experience a sharp fall at $nD/U_{ref} > 1$ where the filtering of turbulence due to the spatial refinement of the mesh takes place. Nevertheless the mesh is of high quality as a portion of the sub-inertial range is actually captured correctly by LES.

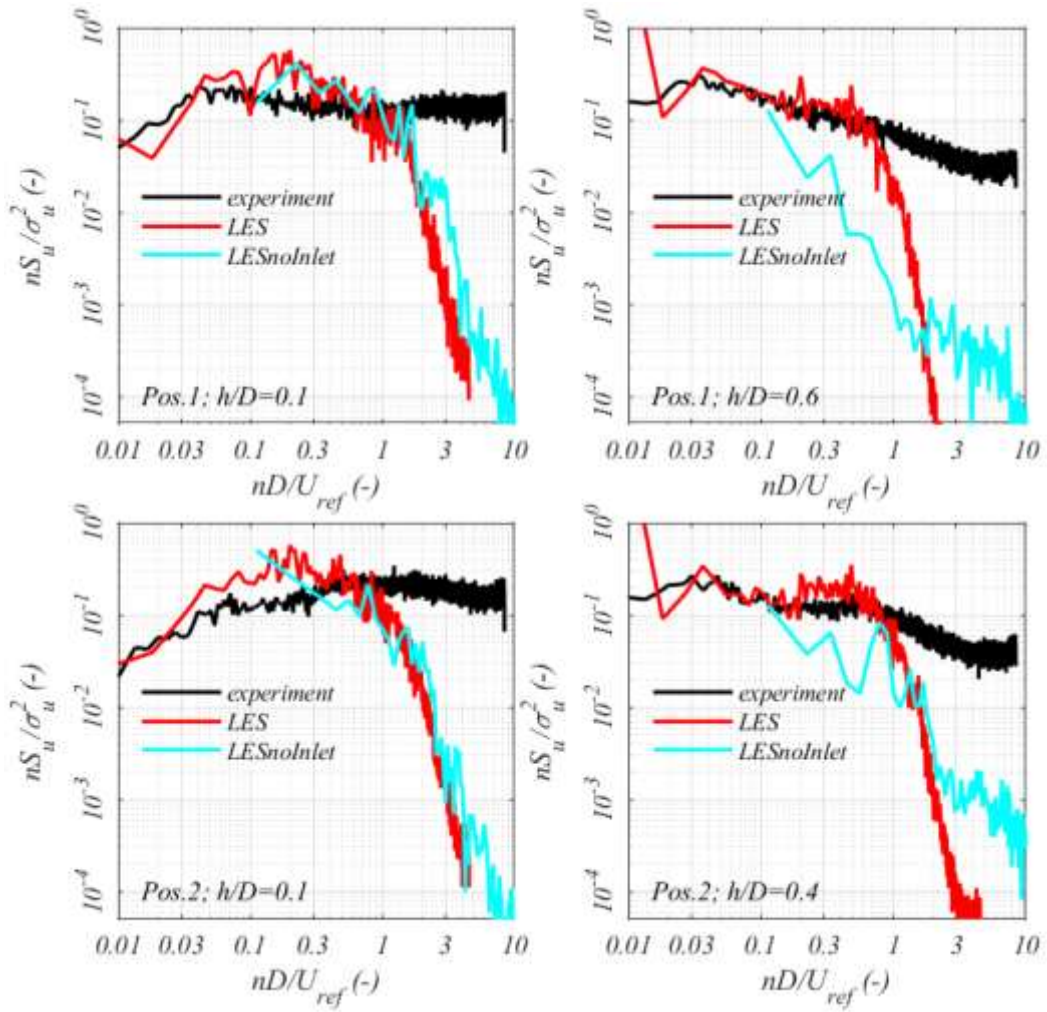


Figure 4.20. Non-dimensional Power Spectral Density for Positions 1 and 2 at two height $z/D=0.1$ and 0.6 .

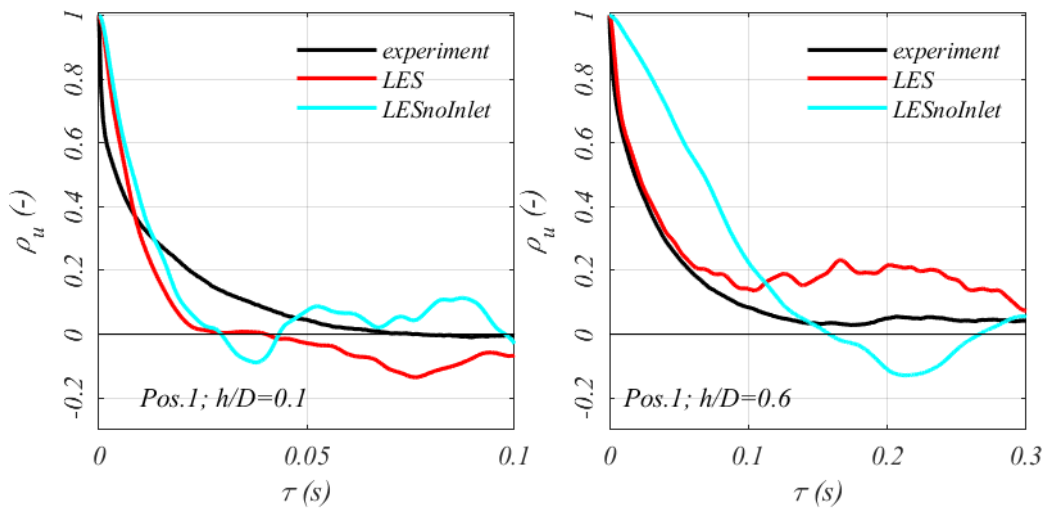


Figure 4.21. autocorrelation coefficient for Position 1 at two heights $z/D=0.1$ and 0.6 .

The integral length scale of turbulence is calculated using the autocorrelation coefficient shown in Figure 4.21. The same conclusions for Figure 4.20 can be drawn, as close to the ground LES results do

not match experimental ones, while at $z/D \sim 0.6$ the presence of inlet turbulence is responsible for the good match with experimental data. The effect of the short sample time can be seen, as LES data do not cross the abscissa in a similar way of the experimental ones.

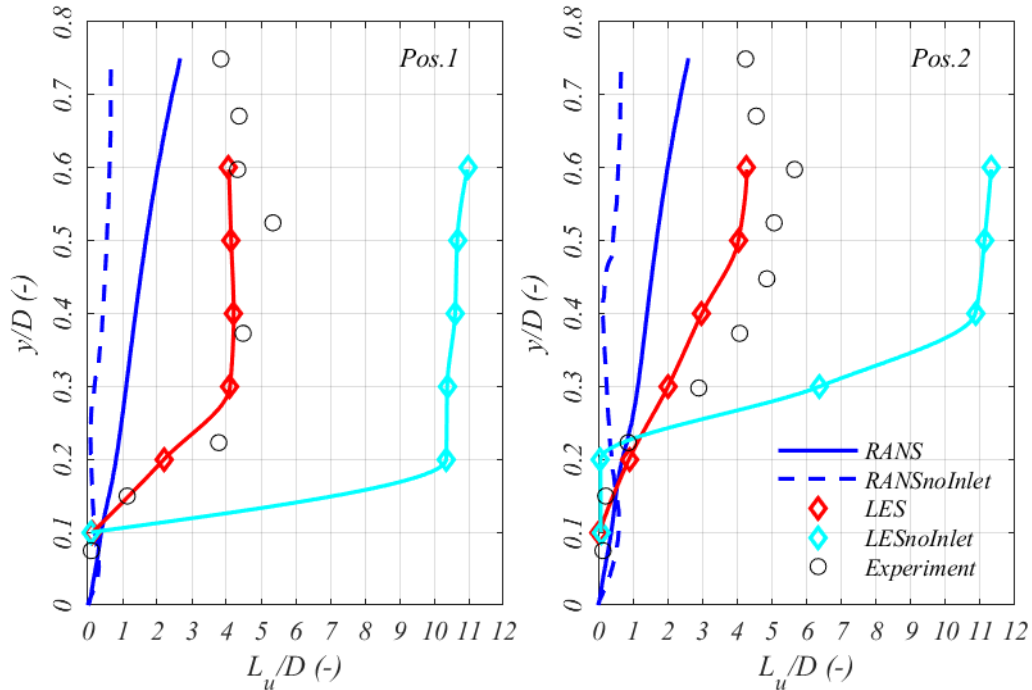


Figure 4.22. Integral length scale of turbulence for Positions 1 and 2.

Figure 4.22 shows the horizontal integral length scale of turbulence at Positions 1 and 2. RANS length scale is calculated from the turbulent kinetic energy and the dissipation rate, and it is evident how it is not possible to have an estimation of the length scale from this simplified method. However, results show that in case of no inlet the length scale is smaller than with turbulence. This is not in agreement with results from LES, where in case of no inlet the length scale is greatly over-estimated for $z/D > 0.2$. LES results show a good match with experimental data, with the exception of the peak in length scale as shown in Figure 4.11 in the presence of the shear layer. Arguably, this mismatch might depend on the performance of HWA in highly sheared flow regions. At position 2 LES slightly underestimates the length scale by $\sim 20\%$. And this might be connected to the over-estimation of the turbulence intensity inside the separation bubble, which might be solved either increasing the refinement of the mesh or the sample time. Figure 4.23 shows the prediction of the Taylor micro-scale of turbulence done from the energy spectra in a similar way as in Chapter 3. Again, a very good match with the experimental results is evident, with LES over-predicting the microscale slightly for $z/D > 0.3$. A microscale of $\sim 15\text{m}$ is

predicted with an integral length scale of $\sim 150\text{m}$, which is consistent with previous findings about the urban boundary layer (Antoniou et al., 1992; Emeis, 2013; Piringer et al., 2007).

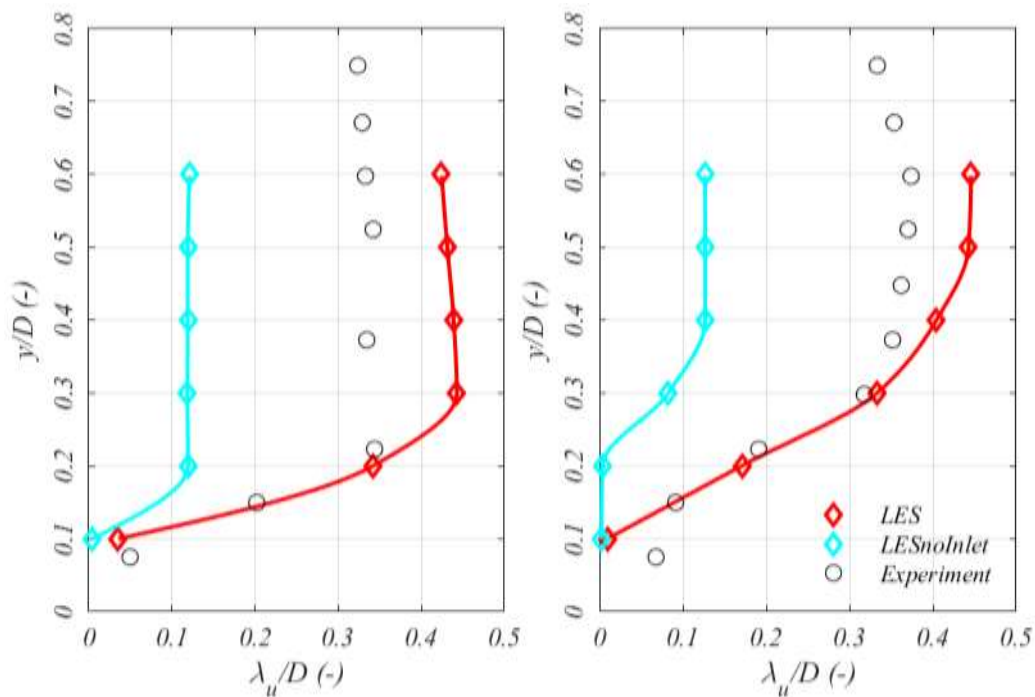


Figure 4.23. Taylor's microscale of turbulence for Positions (left) 1 and (right) 2.

4.4. Discussion and Conclusion

This chapter shows the limitedness of RANS in giving any information on the turbulence characteristics in the flow field. The mean velocity prediction shows a good match with those regions of the flow where there is no interaction with the freestream flow, such as close to leading edge and in the presence of vortex shedding, however the turbulence intensity is strongly under-predicted, which is counterfeiting with the current positioning requirements of wind turbines based on the turbulence intensity. The necessity of a suitable inlet boundary condition is also evident. LES greatly outperform RANS when a turbulent inlet is provided, and arguably it competes if not overcomes experimental techniques as well. The flow above the roof of a highrise building can be divided into three distinct regions:

- i) A region close to the wall where turbulence is exclusively affected by the building itself. In this region the mean velocity is reversed and low in magnitude, while the turbulence intensity is at its highest. The integral length scale is also smaller than the characteristic

size of the high-rise building. In this region experimental results from HWA might be misleading due to the insensitiveness to reversed flow conditions which characterise the flow field.

- ii) A region of highly sheared flow, which is well managed by LES. The velocity in this region is high combined with relatively low turbulence intensity. The position and extent of this region varies greatly with turbulence in the freestream and it challenges experimental HWA.
- iii) A region of accelerated flow highly influenced by the free stream. Turbulence is analogous to the inlet turbulence, having integral and microscales comparable to atmospheric boundary layer values, while the mean velocity is higher, accelerated due to the presence of the building. This region is well-predicted by HWA and LES.

In a significant region of the flow above the high-rise building flow conditions do not match traditional values found for the atmospheric boundary layer. In this region usually wind turbines are placed, as to avoid it expensive substructures might be necessary which are not (yet) justifiable from the energy efficiency of wind turbines. In the region spanning $\sim 0.3D$ from the roof the flow is most certainly reversed, highly turbulent, and low in velocity and it makes sense to avoid this region altogether to have any gain from wind energy harvesting. However, the extent of this region is heavily affected by the freestream turbulence. More results are needed to characterise this region in dependence of the surroundings and the shape of the building itself using techniques capable of predicting turbulence rather than mean velocity. This preliminary results show the need of a high-fidelity approach for the modelling of the turbulence pattern around building for wind energy harvesting.

In this dataset the minimum turbulence intensity is $\sim 10\%$. It is therefore to be supposed that laminar flow conditions never occur in the urban boundary layer and that the design approach for small wind turbines must include a methodology to reproduce turbulence intensity at the inlet. As regards the integral length scale, these are to be considered larger than the device by a factor of ~ 10 . However, it is unclear how surrounding buildings and roughness might influence this result, and it is indeed possible

that the length scale would be smaller, hence prompting doubts on the validity of the negligibility of turbulence effects in the design of devices due to the large size of vortices.

In this chapter, the flow pattern around a building has been modelled and validated using both the RANS and the LES approach, showing a significant difference in the accuracy of results. However, the quality of a LES strongly depends on the presence of the inlet turbulence conditions, which prompts to state that actually turbulence above the roof of a high-rise building is significantly affected by the surrounding turbulent flow.

A brief critical literature review has been made, showing the necessity of more studies about the physical phenomena involving the interaction of turbulence with bluff bodies, especially for practical applications involving the urban environment.

These results will be used as a reference for the next chapter to understand better the role of said surrounding flow conditions. The final aim is to understand the possibility of extending the wind tunnel scope to reproduce the effect of large length scale turbulence on small wind turbines.

Chapter 5

Turbulence Environment around high-rise buildings in the University of Birmingham Campus

Urban Wind is of growing concern as cities grow denser, buildings taller, and urban dwelling increases. In particular, wind safety or the positioning of devices for wind energy harvesting in the built environment represent a challenge for planners and practitioners. A multitude of configurations can be found in the built environment, but high-rise building of around three-times the height of surrounded building, represent a diffused setup, which is considered promising for the harvesting of wind energy, while it might create safety issues to pedestrians at their base.

This chapter aims at understanding if the turbulent flow patterns found for Chapter 4 for an isolated high-rise building are applicable to realistic urban configurations, such as the University of Birmingham Campus where two high-rise buildings are present.

Results confirm that LES is capable of predicting mean velocity and turbulence intensity accurately, while the prediction of the integral length scale is deeply affected by the turbulence characteristics of the inflow, or rather the ability of introducing turbulent inlet boundary conditions in LES. Results also show how the configuration found for an isolated high-rise ($L_u \sim 150-200\text{m}$ with $I_u \sim 10\%$) are not necessarily found in a realistic configuration. In this case, $L_u \sim 20\text{ m}$ with $I_u \sim 20\%$ seems to picture an environment where the effect of the integral length scale might not be negligible due to its supposed relative size with the wind turbine, while confirming that grid turbulence studied in Chapter 3 might be a sensible way of generating such an inflow in wind tunnel testing.

5.1. Numerical simulation of realistic built environments

As discussed in detail in Chapter 2, Urban Wind Energy (UWE) is a branch of wind energy which has shown poor success, questioning not only the sensibility of harvesting wind in the urban environment, but also hampering the public image of the whole wind energy sector. Key to a good positioning strategy is the prediction of the flow in the urban environment. However, simulations specifically tailored to assess the wind energy resource have only been conducted in a handful of studies, all reviewed in a recent paper (Toja-Silva et al., 2018). The totality of reviewed works uses RANS to predict the mean velocity and the turbulent kinetic energy to assess the wind energy resource. The majority of studies focuses on parametrising the shape of the building to maximise mean wind speed and minimise turbulence, without addressing the validation of results or attempting to deepen the knowledge on how turbulence is generated from the building and how turbulent coherent structures interact with obstacles. To the knowledge of the author only a single study has specifically modelled urban winds for wind energy harvesting purposes using Large Eddy Simulation (LES), or rather a technique capable of modelling more statistics than RANS (Millward-Hopkins et al., 2012).

However, LES has been used successfully in research about pedestrian level winds (PLW), which is a branch of urban wind research acquiring growing concern. PLW research is traditionally concerned with comfort (Blocken et al., 2016; Lawson and Penwarden, 1976; Melbourne, 1978; Stathopoulos, 2006), while in extreme weather conditions, also the safety of pedestrians and other users (e.g. cyclists) is of interest (Baker, 2015). In fact, inaccurate prediction of the effects of new developments on the PLW velocity field can cause injuries and even death (BBC, 2017).

The correct prediction of the unsteady nature of the flow in the built environment is key for both PLW and UWE. In particular, an accurate assessment of the turbulence characteristics is important as pedestrians respond to the variability of the flow field rather than its mean characteristics (Bottema, 2000).

The state-of-the-art techniques for the specific assessment of urban winds have been thoroughly reviewed in a recent significant work (Blocken et al., 2016). Wind tunnel modelling validated with limited field test measurements remains the foundation of urban winds assessment (Stathopoulos 2006;

Blocken et al. 2016). Due to the scaling of the geometry, wind tunnel measurements have some limitations. In particular close to walls and surfaces, it is difficult to obtain but a coarse number of measurement positions, while the uneven directionality of the flow field, the low wind velocities, and the reduced distance between probes and geometry-s surfaces might affect the sensor performance, impacting the assessment of wind comfort/safety (Kubota et al., 2008; Tominaga et al., 2004; Tsang et al., 2012). Furthermore, the omission of thermal and stratification effects might also represent a challenging limitation inside the urban plume, where thermal effects are known to modify the atmosphere physics (Kanda, 2007). Over the last two decades, the use of numerical techniques has been suggested, with growing conviction, as a possible way to overcome said experimental limitations (Blocken, 2015). The large majority of numerical works uses the steady formulation of the RANS equations. Indeed, very good agreement can be achieved upon validation with experimentally obtained mean velocities U ($|U_{CFD}/U_{EXP}| \sim 10\%$). In particular, a better performance is obtained in high-speed regions of the flow field (Blocken et al., 2016; Yoshie et al., 2007). This is arguably the reason why most of the recent literature on urban winds research considers low-fidelity numerical simulations to be sufficiently accurate to gain information on the flow field (Blocken, 2018). The large amount of RANS applications allowed for Best practice guidelines (BPG) to be developed for low-fidelity CFD techniques applied to urban winds (Franke et al., 2011). BPG provide indications, which are gradually being included in standards and regulatory bodies (Blocken, 2018). Indications on the computational setup (i.e. meshing characteristics, the choice of suitable boundary conditions, the level of geometric detail, the suitable sizing of the computational domain), are provided together with indications on how to punctually assess the accuracy of simulations and the validation with relevant metrics, hence supporting the growing trust to the use of CFD for urban winds. Nonetheless, validation with wind tunnel testing is still an indispensable part of the assessment of flow conditions by means of CFD (Stathopoulos, 2002), and it cannot be omitted.

A variety of turbulence models, mostly based on the definition of an eddy-viscosity solved by means of one- or two-equations (Pope, 2002), is used for RANS. Although differences exist on the performance of every turbulence model, the performance does not vary remarkably in the prediction of urban winds, and therefore there is no definition of a most suitable turbulence model, as long as BPG

are implemented (as pointed out by Blocken, Stathopoulos and van Beeck (2016) and Blocken (2018)). However, the validation of RANS models with available wind tunnel tests might strongly vary with the considered location, as RANS tends to overestimate separation lengths which in turn yields lower velocities in the wake of obstacles (Yoshie et al., 2007). The validation of results must be then appropriately setup, i.e. it has to be done in those areas of interest for which the CFD simulation is specifically tailored (Toparlar et al., 2017). However, this might prove difficult for urban winds due to the unfavourable combination of the small scale of wind tunnel geometries with the unsteady recirculating flow (Šarkić Glumac et al., 2018). Therefore, the validation of many CFD applications made with reference to the boundary layer development above specific locations or alignments, e.g. above the building heights or at the inlet, might very possibly not be evidence of the quality of urban winds assessment. This is especially worrisome if the most convenient use of CFD is made: extending the experimental scope beyond its physical limitations (e.g. varying wind or geometry characteristics). This poses the necessity of defining new metrics for the comparison of CFD results with alike experimental results (Franke et al., 2011).

The issue of whether it could be the case to switch to high-fidelity techniques in urban winds research is considered a secondary one, given the good amount of information which can be extrapolated with the mean velocity (Blocken, 2018). This is a reasonable argument if the mean velocity only is considered. For fluctuating winds, high-fidelity techniques, such as LES, are unmatched by low-fidelity ones in terms of accuracy (Sagaut, 2006). In fact, a still limited but growing number of works uses LES for urban wind research, corroborating the growing confidence in the validity and reliability of results towards design applications (Tamura, 2008; Zhiyin, 2015). However, of the limited amount of works implementing LES for a realistic urban geometry, only very few have addressed the PLW flow. The large majority of LES applications assesses wind conditions around simplified geometries such as isolated buildings (Liu et al., 2017; Tominaga et al., 2004) or simplified arrays of buildings (Abd Razak et al., 2013; Ikeda et al., 2015; Ikegaya et al., 2017; Merlier et al., 2018; Millward-Hopkins et al., 2012; Shen et al., 2017; Toliás et al., 2018). Most of these works compare the performance of different methods in describing different statistics of the flow field. Simplified configurations are useful to extrapolate trends and behaviour to be generalised for more realistic setups. The normal practice of

modelling an isolated building might indeed provide a very simple approach for parametric studies to be then included in a more comprehensive simulation, even considering the rather defective description of the inflow (Liu et al., 2019; Zhang et al., 2018). Work on simplified arrays of buildings with a variety of parameters might provide a thorough account for the effect of easily computable parameters such as the building aspect ratio or the canopy height (Abd Razak et al., 2013; Ikegaya et al., 2017). Obtained high-fidelity data can be used over a long time to get more and more insights on urban winds physics, as done effectively in Ikeda et al. (2015), where not only bulk statistics, but also the gustiness of the flow field is considered. However, the increase of accuracy towards the unsteadiness of the flow field requires more comprehensive validation techniques. Tolia *et al.* (2018) stress that the lack of a validation strategy tailored to the problem at stake is the main obstacle for LES to be practically feasible in urban flow research. Or rather, the validation of a numerical model for a specific statistic in a specific location is not a guarantee of the accuracy of the overall simulation (Hertwig et al., 2017). To this regard the wind tunnel model Michelstadt (Harms et al., 2013) represents an important step towards the development of LES BPG for the prediction of unsteady urban flows.

Most of the research on simplified geometries puts much effort on the possibility of introducing a suitable turbulent inlet to correct for the spatial limitedness of the computational domain (Tominaga et al., 2004). Notwithstanding the potential and high complexity of the choice of such methodology, it is not clear how an inlet profile matching mean velocity and turbulence intensity is a guarantee on the description of the fluctuating flow behaviour at pedestrian level (Vasaturo et al., 2018). Moreover, recent works indicate that the flow field across the domain might be divided into a far-from-buildings region showing a strong sensitivity to the inlet profile, and a through-buildings region where the behaviour seems rather insensitive (Ricci et al., 2018).

The possibility of providing an accurate turbulent inlet and of generalising findings for simplified geometries, does not negate the necessity of providing a detailed geometric modelling of the test case. He and Song (1999) are among the first authors to apply LES to a real urban configuration to assess urban winds. Their results show the unsteady behaviour of the flow field, claiming the competitiveness of numerical simulation with wind tunnel testing, although no systematic validation is provided. A number of more recent studies focuses on the implementation of real scanned geometries in large grids

and how to effectively parallelise the solver (LES-PALM method, developed by Raasch and Schröter (2001)). These works show the inherent difficulty of urban winds for the solver of choice, as the rather small region of interest where a high resolution of the mesh is required, clashes with the overall mean size of the cells, increasing the cost of the all simulation (Letzel et al., 2012). Wang, Xu and Ng (2018) use LES-PALM to assess performance at PLW to reconstruct the urban geometry from satellite raw images, showing that a rather rough reconstruction can still provide suitable results if the inlet profile of choice is accurate. Adamek *et al.* (2017) show the potential of LES in understanding the behaviour of the flow field as more buildings are in place over the years. Also for this study, a qualitative description of the instantaneous and mean flow pattern is given with limited experimental validation. However, the computational setup shows the ease of simulation a large portion of the city providing high-quality results.

Jacob and Sagaut (2018) provide a comparison of the available wind comfort criteria with an actual computation of the gust velocity using LES with the Lattice Boltzmann Method around a large built up area. The authors conclude that LES should be the technique of choice for urban winds. LES is able to describe accurately the physical phenomena, providing data with general validity to improve wind comfort criteria. Wind fluctuations of interest are shown to be non-Gaussian in nature and therefore not predicted correctly by only giving account of mean velocity and standard deviation.

Most of the referenced works focus on the comparison of several CFD techniques. Besides SRANS and traditional LES, also hybrid RANS-LES methods can be implemented for urban winds. Hybrid methods are composed by the Detached Eddy Simulation (DES) and the Wall Modelled LES (WM-LES). DES is a technique to decrease the cost of LES simulation by the individuation of RANS regions in the flow field by means of a blend function, which activates close to walls (Spalart, 2009). If properly tuned, DES can be as accurate as LES with a far smaller grid size. However, many modifications to the original SA model have been proposed to account for the extreme sensitivity of the model to the grid, and indeed the amount of work necessary to fine-tune the mesh might be off-putting and leading to actual LES grids to be used. WM-LES on the contrary has no blending function, as the wall function is only applied at the first cell close to the wall (Piomelli, 2008). This models prove very efficient as results coincides with LES for high quality grids, while the accuracy of complex flow features such as separation is

entirely dependent on the performance of the wall function (Shur et al., 2008). Being very analogous to traditional LES for urban wind, WM-LES is implemented in successful studies with no distinction from LES in terms of the scientific field (Gousseau et al., 2011).

Table 5.1 Review of research implementing LES for pedestrian level wind and pedestrian comfort.

Study	Model SGS	Geometry	Domain size $L \times W \times H$	Grid size Resolution
(Liu et al., 2017)	DES LES Smag.	Isolated building	$H = 50\text{ m}$ $13.5H \times 11.5H \times 6H$	2.6-5.6 mln -
(Tominaga et al., 2004)	LES Smag.	Isolated building	$B = 0.08\text{ m}$ $21B \times 14B \times 11.5B$	0.1 mln $B/9$
(Shen et al., 2017)	LES Smag.	Simplified urban pattern	$900 \times 900 \times 150\text{ m}^3$	4.6 mln -
(Abd Razak et al., 2013)	LES PALM	Simplified buildings array	$L = 25\text{ m}$ $9.5L \times 9.5L \times 4L$ $3L \times 3L \times 4L$	~1400 mln $L/64$
(Ikegaya et al., 2017)	LES PALM	Simplified buildings array	$L = 25\text{ m}$ $9.5L \times 9.5L \times 4L$ $3L \times 3L \times 4L$	~1400 mln $L/64$
(Ikeda et al., 2015)	LES PALM	Simplified buildings array	$L = 25\text{ m}$ $4L \times 4L \times 4L$	~1400 mln $L/64$
(Millward-Hopkins et al., 2012)	LES Smag.	Simplified buildings array	$H = 0.01\text{ m}$ $16H \times 16H \times 10H$	2.3 mln $H/16$
(Merlier et al., 2018)	LBM-LES Smag.	Simplified buildings array	$H = 0.12\text{ m}$ $L = 10H$ $2.5L \times 1.6L \times 8.3L$	41 mln $H/48$
(Tolias et al., 2018)	LES Smag.	Idealised Michel-Stadt	$1670 \times 900 \times 147\text{ m}^3$	0.7-28 mln 6.6-1.2 m
(Dadioti and Rees, 2017)	DES SA model	Realistic Leicester	$2.2 \times 1.3 \times 0.3\text{ km}^3$	24 mln -
(He and Song, 1999)	LES Smag.	Realistic Taipei	$700 \times 700\text{ m}^2$	- -
(Adamek et al., 2017)	LES Smag.	Realistic Toronto	$B = 610\text{ m}$ $H = 285\text{ m}$ $7B \times 4B \times 3H$	1.1 mln $H/50 - H/10$
(Jacob and Sagaut, 2018)	LBM-LES Smag.	Realistic Tokyo	$4.6 \times 5 \times 1.5\text{ km}^3$	22-136 mln 2-32 m
(Gousseau et al., 2011)	WM-LES dyn.Smog.	Realistic Montreal	$1000 \times 425 \times 330\text{ m}^3$ $1150 \times 460 \times 330\text{ m}^3$	4.8-5.2 mln 1-3 m
(Wang et al., 2018)	LES PALM	Realistic Hong Kong	$1.2 \times 1.2\text{ m}^2$	- 2 m
(Letzel et al., 2012)	LES PALM	Realistic Hong Kong	$400 \times 400 \times 400\text{ m}^3$	720-1600 mln 2.5 m
Present work	WM-LES WALE	Realistic Birmingham	$600 \times 600\text{ m}^2$	17 mln ~5 m

The deficiencies associated with DES, in particular towards the grid requirements might explain the almost total absence of DES applications for PLW. From this brief survey, it might be concluded that WM-LES and DES are superior to RANS in terms of accuracy.

An overview of simplified and realistic urban models implementing LES is given in Table 1, with indications about the geometry and grid size. Although some indications towards an urban LES framework have been attempted (Franke et al., 2004), more novel works should flank the listed ones towards the definition of BPG in LES for urban wind. The trickiest aspect of such a framework remains to balance the gained accuracy with the prohibitive verification and validation requirements (XING, 2015), which usually discourage users from implementing high-fidelity analyses. In this regards, authors are tempted to coarsen the mesh far from the area of interest. In fact, coarsening the grid means using it as a filter without any control on the cut-off frequency, hence the effect on results can be disastrous if a proper validation strategy is not sought for (Hanjalic, 2005). The challenge of the computational cost vs the gain in the accuracy remains the most important one, as most authors agree that a solid mean velocity field is still more reliable than a full fluctuating one, but less accurate (Blocken, 2018).

The review of LES works given in this paragraph shows the concern of most research with the flow pattern around buildings. Although the majority of works focuses on the mean velocity field and/or its standard deviation, some recent works point to the direction that a more reliable description of the unsteadiness is needed to progress in urban winds research. The success of RANS as a tool for describing the mean flow field should not lead to assumptions on the flow unsteadiness and its relation to the mean velocity, i.e. its statistical behaviour.

This chapter aims at assessing the flow pattern above high-rise buildings in a realistic urban configuration. A comparison with available wind tunnel and full-scale data is also presented. Results will contribute to Chapter 4 findings on the turbulence characteristics on flow regions suited for the positioning of wind turbines in the built environment. The adequacy of CFD low- and high-fidelity techniques is of particular interest in the debate about the choice of a suitable technique, which guarantees cost-effectiveness and sufficient accuracy in terms of reproducing rapidly changing flow fields and potential scale effects. Available techniques for the physical and numerical simulation of

urban winds in realistic urban configurations are introduced in Section 5.2. The physical and numerical simulation methodology used in this study are synthesized in Section 5.3. Relevant results and discussion are presented in Section 5.4 and conclusions are given in Section 5.5.

5.2. Background

Among the available methods to assess urban winds, a distinction can be made between low-fidelity (LF) and high-fidelity (HF) techniques. Due to the limitations in the setup (such as the achievable spatial resolution of measurements, and the accuracy of the output in terms of the fluctuating wind velocity), LF techniques can only give limited account of the flow field, whereas HF techniques do not suffer from these limitations. LF techniques are the industry-standard for the assessment of pedestrian distress and the design of mitigation measures. These might therefore be affected by a large degree of uncertainty as the available picture is limited - accuracy is, to an extent, sacrificed for practicality and cost in the choice of methods. Although available to the industry for a number of applications (Baker, 2007), HF techniques are not implemented as standard to estimate pedestrian distress. One reason for this may be the higher complexity of HF setups, which can cause macroscopic errors which impair the performance of HF against LF methods (Hanjalic, 2005). Another issue is the difficulty in providing a full scale field test case for the validation of such simulations (Jacob and Sagaut, 2018). Consequently, HF techniques have been implemented to only a very limited extent in urban winds research, but have shown improved accuracy over LF methods for fluctuating flow fields (Blocken et al., 2016).

Table 5.2 summarises LF and HF techniques, and comments are given on the worthiness and shortcomings of each technique. Physical and numerical simulations techniques are both referred to and compared to full-scale testing. Full-scale field tests are also mentioned in Table 5.2 as practitioners might be tasked in conducting a full-scale experimental campaign to monitor existing conditions. However, such-tests are not possible at the design stage, may be very complex to set up due to practical, regulatory and interferential issues, and are generally short-term. This final point means that the test period may not coincide with high wind periods, resulting in data of limited usefulness. These reasons explain the paucity of PLW research that validates physical and numerical simulations against full-scale test data.

Table 5.2. Classification of techniques for wind velocity measurement. Techniques implemented in the present study are marked *. **The capability of varying flow conditions comes with an intrinsic high complexity.

	<i>LF</i>	<i>HF</i>	<i>Advantages</i>	<i>Disadvantages</i>
<i>Experimental Full Scale Test</i>	-	<ul style="list-style-type: none"> • Sonic Anem.* • LiDar 	<ul style="list-style-type: none"> • Real wind and geometry conditions 	<ul style="list-style-type: none"> • Not available at the design stage • Complex and costly campaign • Variability of wind conditions • Coarseness MP • Random factors presence
<i>Experimental Wind Tunnel Test</i>	<ul style="list-style-type: none"> • IP* • HWA* • Omni-probe • Sand erosion 	<ul style="list-style-type: none"> • PIV • LDA 	<ul style="list-style-type: none"> • Detailing of geometry • Variability of wind conditions** • Quick results • Well established 	<ul style="list-style-type: none"> • Scaled models only • Directionality of flow • Positioning of probes • Coarseness MP
<i>Numerical Test</i>	<ul style="list-style-type: none"> • 3D (S)RANS* 	<ul style="list-style-type: none"> • (DES) • (hybrid)LES* 	<ul style="list-style-type: none"> • Detailing of geometry • Variability of wind (HF)** • Fineness MP • Quick results (LF) • Well established 	<ul style="list-style-type: none"> • Complexity and costs (HF) • Physics modelling (LF) • Validation

5.2.1. Physical Simulation

By far the most common technique for urban winds assessment is physical simulation through wind tunnel testing. The simplest way of assessing the flow field is to introduce a single or multiple physical probes in those areas of interest. When considering Pedestrian Level Wind comfort the direction of the wind is generally unimportant and wind speeds (rather than velocities) are typically measured, with Irwin probes (IP) almost exclusively used (Wu and Stathopoulos, 1993).

Hot-wire anemometers (HWAs) are commonly used in wind tunnels experiments to assess fluctuating flow characteristics in urban winds, both at pedestrian level and for urban wind energy. HWAs give more accurate measurements of the fluctuating energy than IPs and, if correctly positioned, can provide a very high-precision for a wide range of flow fields (Stainback and Nagabushana, 1993). However, HWAs are still classified as LF in Table 5.2 because measurements can only be obtained in a non-simultaneous way in discrete positions. In general, the wire is heated up to a temperature above the ambient temperature and current required to maintain a constant temperature is a function of the wind speed at the wire (Durgin, 1992; Blocken et al., 2016). The major advantages of hotwire anemometers

include their very high frequency-response and capability for high spatial resolution due to their small dimensions. Nonetheless, it is worth mentioning that in order to provide an average speed over the wire length, it is often required to position the hot wire anemometer in a vertical manner in the wind tunnel. In such case, it can be reasonably anticipated that the accuracy of hot wire measurement might be somewhat affected by the angular changes in the velocity vector normal to the wire axis (Durgin, 1992; Castro, 1992). Furthermore, many researchers indicated that the use of hotwire anemometer is limited to flows of low and moderate turbulence intensities. It is shown that at high turbulent intensities, hotwire anemometer will rectify the negative wind and result in a higher mean wind speed and lower standard deviation about the average wire (Durgin, 1992; Blocken et al., 2016).

5.2.2. Numerical Simulation

In parallel with physical simulation, a simple approach, which is increasing in popularity (particularly in the earliest architectural design stages) is numerical simulation (Computational Fluid Dynamics, CFD). Numerical simulations allow a realistic geometry to be setup in full scale, with results easily available for the whole flow field and without the disturbance of inserting a physical measurement probe that can be a serious limit to physical simulations implementing scaled geometries. Having the possibility of visualising the flow field is a great advantage as conjectures on results might be done in an easier way. It is also helpful in interpreting the experimental results, explaining patterns in the behaviour or coarseness in the data. The industrial standard is to use three-dimensional Steady Reynolds Averaged Navier-Stokes (RANS). However, RANS only allows for the mean velocity U and (to a limited extent) its standard deviation σ_u to be predicted. Analyses provide very good accuracy if best practice guidelines are implemented (Blocken et al., 2016). Alternative numerical methods can overcome the major limitations of RANS and provide HF approaches. HF methods essentially include the Large Eddy Simulation (LES) family, which includes the hybrid RANS-LES methods, e.g. Detached Eddy Simulation (DES). LES is known to describe very accurately the fluctuating flow behaviour if the mesh resolution is sufficiently high, i.e. it is able to resolve a large proportion of the turbulent energy production. Normally a very refined mesh at wall boundaries is required, although the mesh resolution might be coarsened in those flow regions where a highly isotropic behaviour is likely

to occur. These are normally where the turbulence characteristics as modelled by the sub-grid scale (SGS) models, which can also have varying complexity. DES has been used very rarely as the complexity of geometry makes the tweaking of the mesh to correct the drawbacks of the method very difficult. Wall-Modelled LES (WM-LES) is an alternative hybrid approach which allows for a great simplification of the meshing strategy. In WM-LES, the RANS model is not introduced with a blending function with all the complications entailed with DES. Instead, the RANS model is only automatically present at the first cell, and then swaps to LES independently of the nature of the flow field or the mesh resolution. In principle, a very coarse mesh resolution might be used in a similar way as SRANS, however practice shows that is still necessary to monitor the size of the mesh at the wall (Shur et al., 2008).

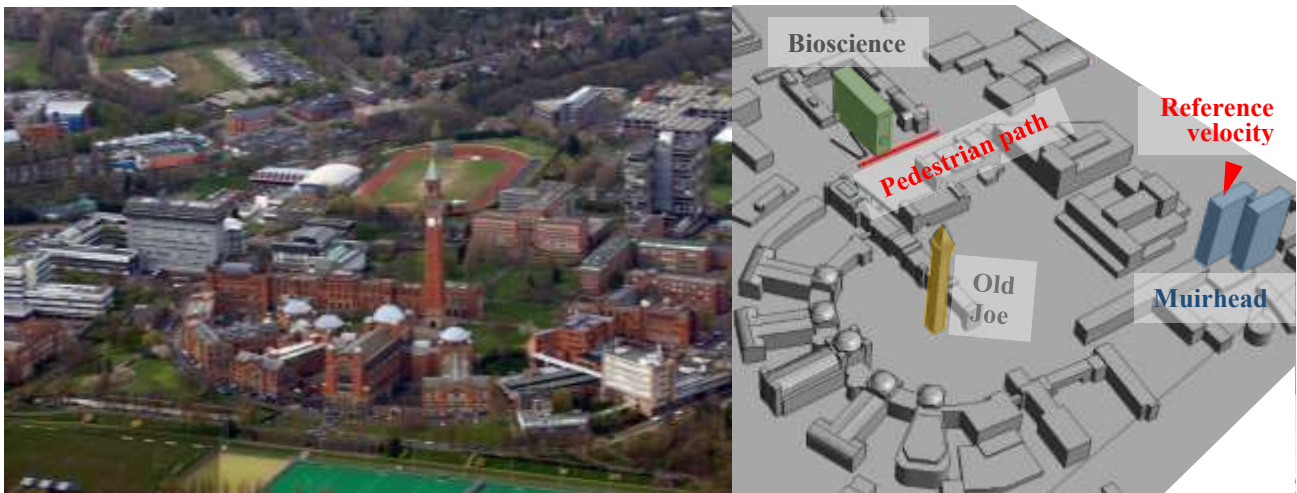


Figure 5.1. University of Birmingham Campus. (Left) aerial view as of 2015. (Right) view of geometry with landmarks and reference locations.

5.3. Methodology

In order to assess the turbulent flow environment around high-rise buildings in a realistic urban configuration, both physical and numerical simulations have been implemented with wind tunnel testing and CFD. In Section 5.3.1, the validation test-case is described. It consists of a full-scale field test conducted during an experimental campaign at the University of Birmingham (UoB) campus, with the campus being a good representation of high-rise buildings insisting on a typical urban environment. Figure 5.1 shows the UoB Campus as of 2015 compared to the numerical geometry with relevant landmarks labelled. In Section 5.3.2, the physical simulation is reported, with velocity measurements

done with hot-wire anemometry at pedestrian level and above the roof of high-rises. Profiles were not recorded at full scale. In Section 5.3.3 the numerical simulation of both pedestrian and roof level is described with the three computational domains implemented.

5.3.1. Full Scale Validation test-case

Storm Ophelia was a major disruptive wind event, which caused damage and injury in the United Kingdom and the Republic of Ireland, occurring on the 12th October 2017. For the investigation of Pedestrian Level Winds in full scale, those wind conditions represented an ideal test case to conduct this study. The storm blew from South-South-West (SSW, 203° from North).

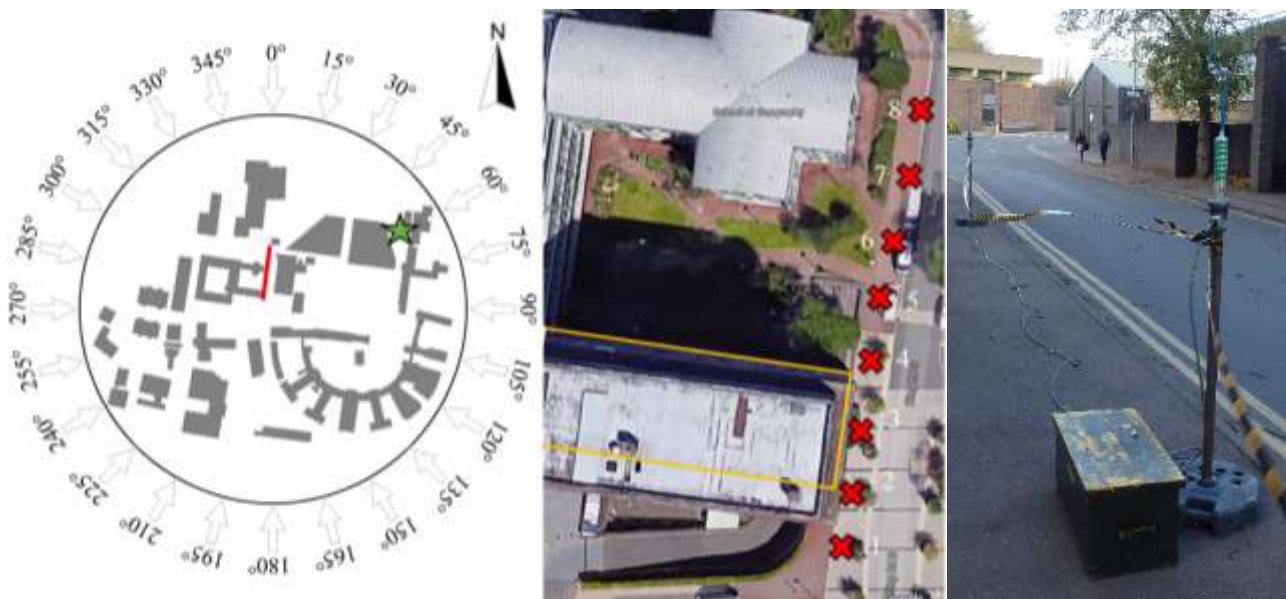


Figure 5.2. Full Scale Experiment. (Left) Map of UoB campus, with footpath alignment at the base of the BB and reference point position on top of the MT, with cardinal directions; (centre) Aerial view of footpath and position of 8 sonic anemometers; (Right) view of sonic anemometers as installed during the measurement campaign.

A reference anemometer (Gill WindMaster) is permanently installed on a 10m mast on the south-west corner of the roof of the 62m tall Muirhead Tower (MT), as marked in Figure 5.1 and Figure 5.2. Figure 5.2 shows the eight sonic anemometers used at pedestrian level, and their positions at particularly gusty area near the base of the UoB Biosciences building (BB). The anemometers were at a spacing of 9m, 5 m from the closest side of the building. All of these anemometers (a mixture of Gill WindMasters and Gill R3-50s) were configured to measure wind speeds at a height of 2 m above the ground, this being the standard height for Pedestrian Level Wind data. Both reference and pedestrian anemometers were

set to record three-dimensional velocity data at a sampling rate of 10 Hz. Obtained full-scale data were split into 10-minute segments, each containing 6000 individual measurement data. Unless otherwise specified, wind speed parameters given in this paper are 10-minute mean values taken over one of these segments. The raw velocity signals of full scale measurement data were low-pass-filtered using a 3rd order Butterworth filter with a cut-off frequency equivalent to 3 s or 0.33 Hz. High-pass filtering of the signals to remove potential white noise was not needed for the time sample considered (i.e. during the Storm Ophelia).

5.3.2. *Physical Simulation*

In wind tunnel tests, both reference, pedestrian level wind speeds, and above-roof wind velocity profiles have been measured at locations equivalent to those in the full-scale test using various measurement instruments. HWAs have been used to measure the incoming wind speed at pedestrian level, on top of the MT, and the Biosciences Building.

Overall setup and inlet flow

The physical simulation tests were carried out in the University of Birmingham ABL Wind Tunnel. This wind tunnel is of open-circuit type, with a 2×2 m square working cross-section with a 14 m-long fetch section. The maximum freestream wind speed is about 10 m/s. For wind tunnel simulation of ABL flow interaction with an urban area, it is necessary to model both the ABL flow and the immediate proximity of the area of concern (Isyumov and Davenport, 1976). The approaching flow conditions were produced using two triangle spires and an array of surface roughness blocks with two different heights (Figure 5.3). A 1:300 scale ABL flow was obtained with the resultant mean wind speed profile at the test section matching a power law profile with coefficient of 0.3, with a maximum turbulence intensity at ground level of about 30% (Figure 5.5). The power spectrum of wind speed measured at reference height upstream the model fits well with the von Kármán model (Figure 5.5). The wind tunnel was fitted with a circular 1:300 scale model (matching the ABL scale) of the relevant area of the UoB campus, equivalent to a radius of 300m at full-scale. The model was fixed on a turntable to allow setting of the angle of the incoming wind. The pedestrian-level anemometer positions were approximately at

the centre of the campus model, around the South-East corner of the Biosciences building which was positioned at the centre of the turntable.

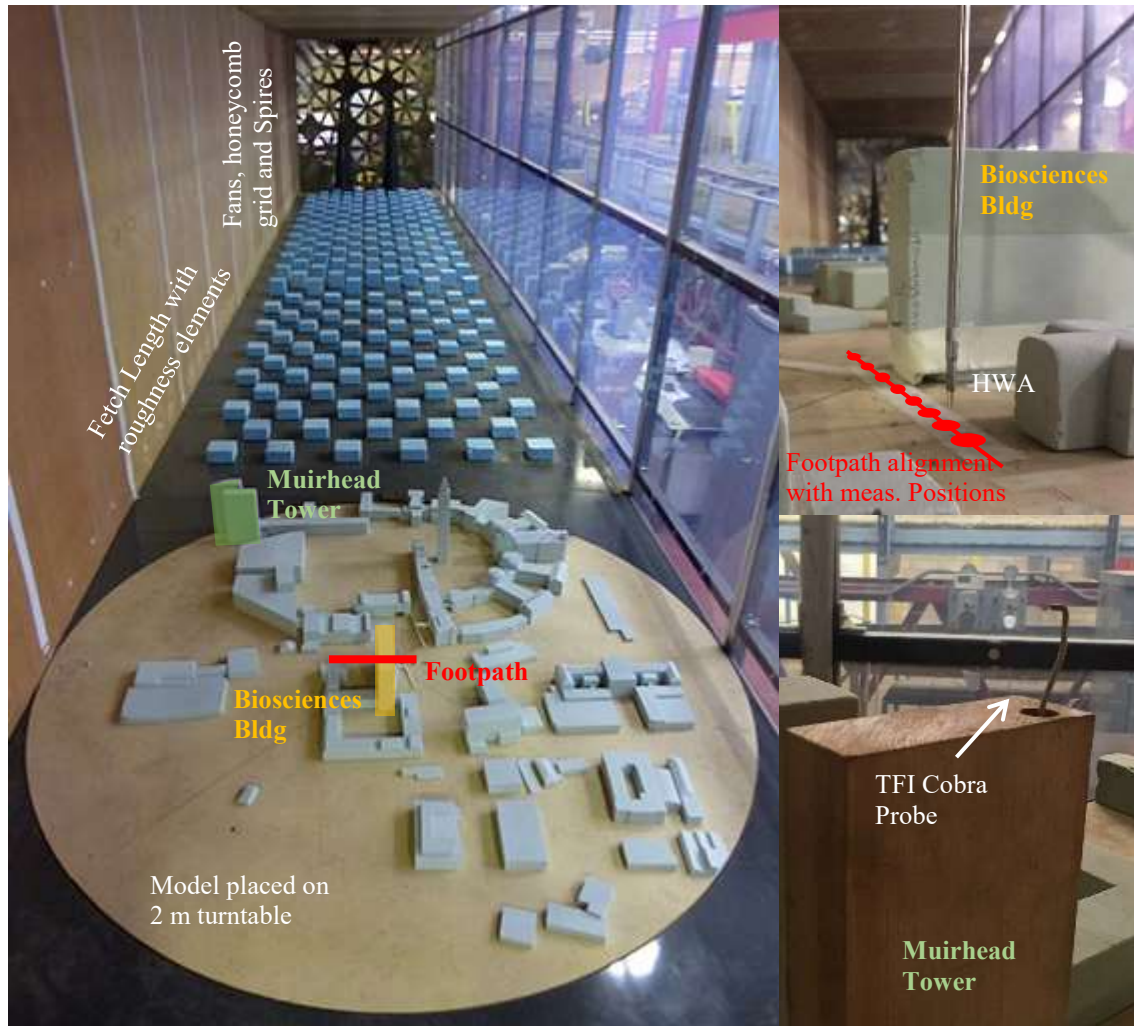


Figure 5.3. (Left) overview of wind tunnel test setup. (top) HWA placed according to 8 locations in full-scale. (Bottom) Cobra Probe for reference point measurement.

The reference wind speed was recorded using a Cobra probe, manufactured by Turbulent Flow Instrumentation (TFI) Ltd. This probe was fitted on the model Muirhead Tower in the same position and equivalent height as the anemometer at full-scale (Figure 5.3), thereby providing an equivalent reference velocity for mapping of the wind tunnel results onto the full-scale data. The probe measures 3-D velocity data, and was configured to record at a sampling rate of 250 Hz. The orientation of the Cobra probe head was adjusted to face the approaching flow, i.e. directly upstream into the wind tunnel. The same low-pass filtering technique as described for the full-scale field tests was used on the raw velocity signals.

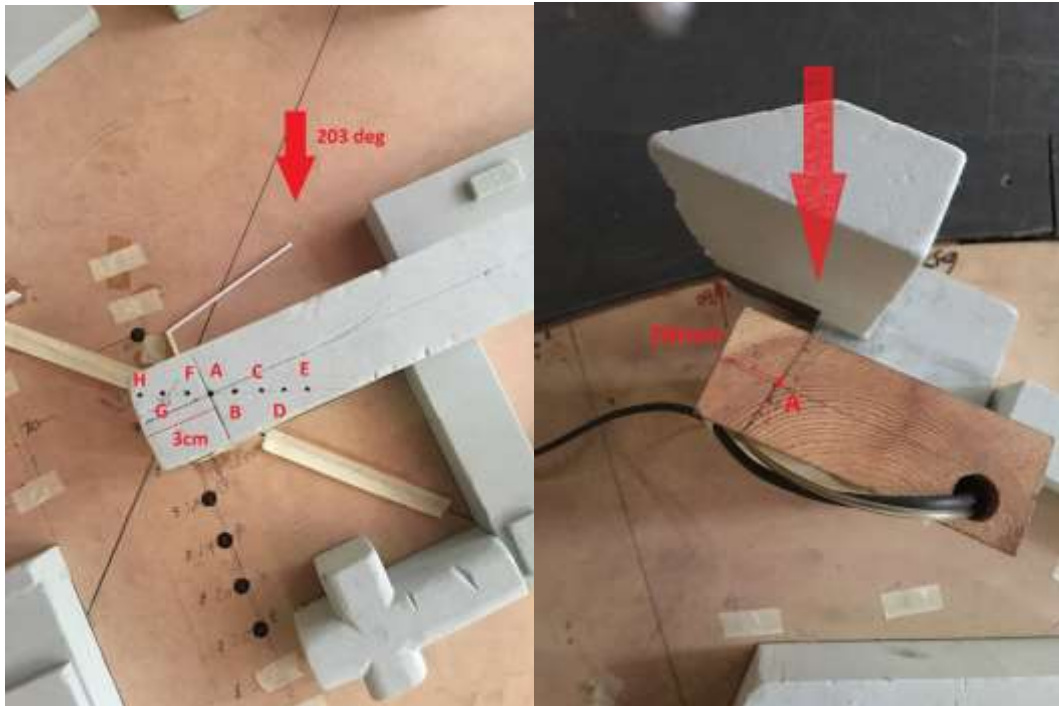


Figure 5.4. Detail of experimental setup with indication of wind direction for the storm Ophelia. (Left) Biosciences Building and (Right) Muirhead Tower.

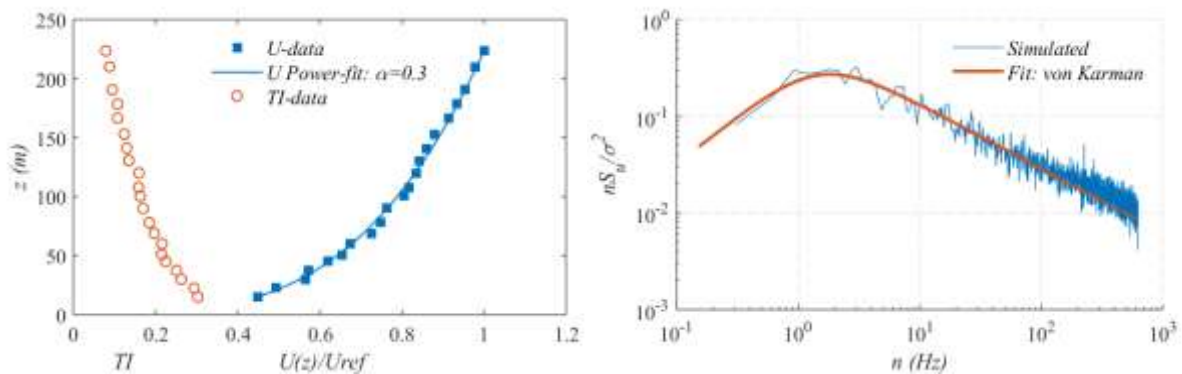


Figure 5.5. Properties of approaching atmospheric boundary layer (ABL) flow. (Left) vertical profiles of mean wind speed and turbulence intensity; (Right) power spectral density of wind speed measured at reference height upstream the model.

Hot Wire measurements

In addition to the Irwin probe measurements, wind speed measurements at pedestrian level were also carried out using a hot-wire anemometer at the same locations. The hotwire anemometer deployed in the current study was the Tri-axial probe (Dantec Dynamics, Ltd), which has three mutually perpendicular sensors. The sensors form an orthogonal system with an acceptance cone of 70.4° (Dantec Dynamics, 2015). The centre of the hotwire was positioned at a height equivalent to 2 m in full-scale

above the model surface, equivalent to approximately 2 m in full-scale. The sampling rate of the HWA was set to 1000 Hz in this study.

Wind speeds were recorded for sufficient time, corresponding to at least 1-hour in full-scale (ASCE, 2003). This is done in order to estimate statistically stable values of the target wind speed variables. As with the processing of the full-scale data, the outputs of the Cobra probe and hot-wire anemometer were high-pass filtered to eliminate unwanted noise from the data.

5.3.3. Numerical Simulation

A set of numerical simulations has been carried out using the commercial code Ansys CFX as available in the Linux High Performance Cluster “BlueBEAR” of the University of Birmingham. RANS and WM-LES were both implemented and their performance compared with HWA data from the physical simulations and the full scale data. Both numerical methods are detailed in the following.

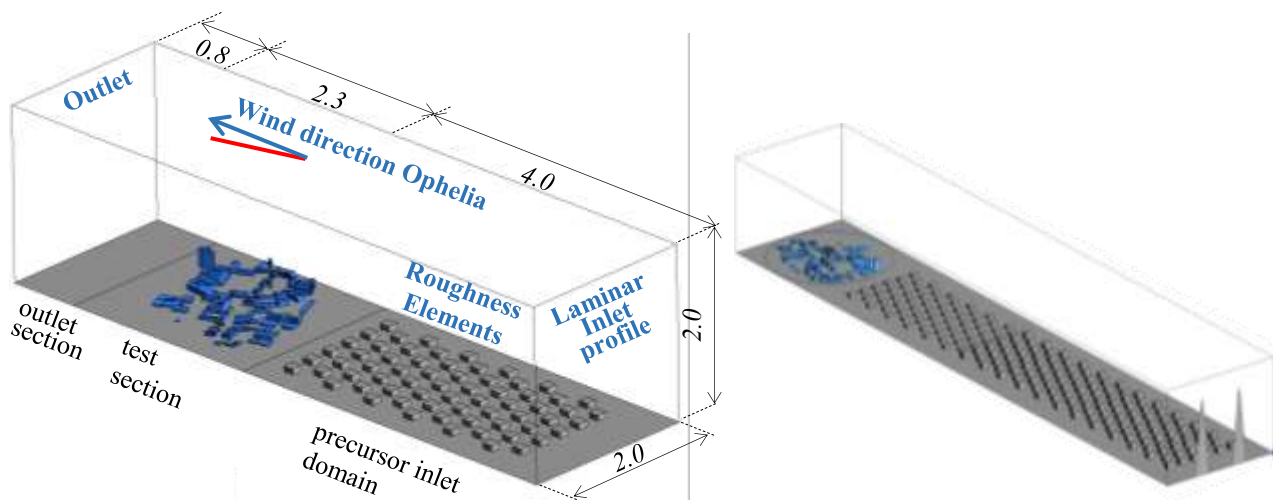


Figure 5.6. (Left) Wind tunnel domain.
(Right) Alternative computational domain: whole wind tunnel geometry.

Computational Domain and Grid, and Overall Setup

The numerical simulation setup replicated as faithfully as possible the physical simulation setup. This was due to the availability of a solid validation test case and the relevant scaled wind speed profile. A radius of 300 m of the UoB Campus was therefore modelled at a scale of 1:300, as for the wind tunnel test. The only difference between the physical and numerical domains was the level of detail of the geometry, which was slightly higher for the numerical case. This is done in order to improve the matching of full-scale conditions, and matches what would be used in standard industrial applications

(Blocken, 2015). Three computational domains have been built for the campus geometry, shown in Figure 5.1. Figure 5.6 shows on the left the first wind tunnel domain, replicating a portion of the wind tunnel test, where only the first 12 rows of the roughness elements are modelled. The wind tunnel test section is prolonged towards the outlet, to avoid blockage issues, which might occur numerically due to the vicinity of the geometry to the outlet surface. This domain was studied to reproduce partially turbulent inlet characteristics and has been implemented for both LES and RANS, in which case results are named RANSwc. On the right, the second domain reproduces the whole wind tunnel fetch length. This domain has only been implemented with RANS and discarded for LES, due to the lack of information on the flow around spires at the inlet of the wind tunnel section. Results are named RANSwt. A third domain has been studied which only replicated the test-section without any fetch length, in which case results are named RANSwtm.

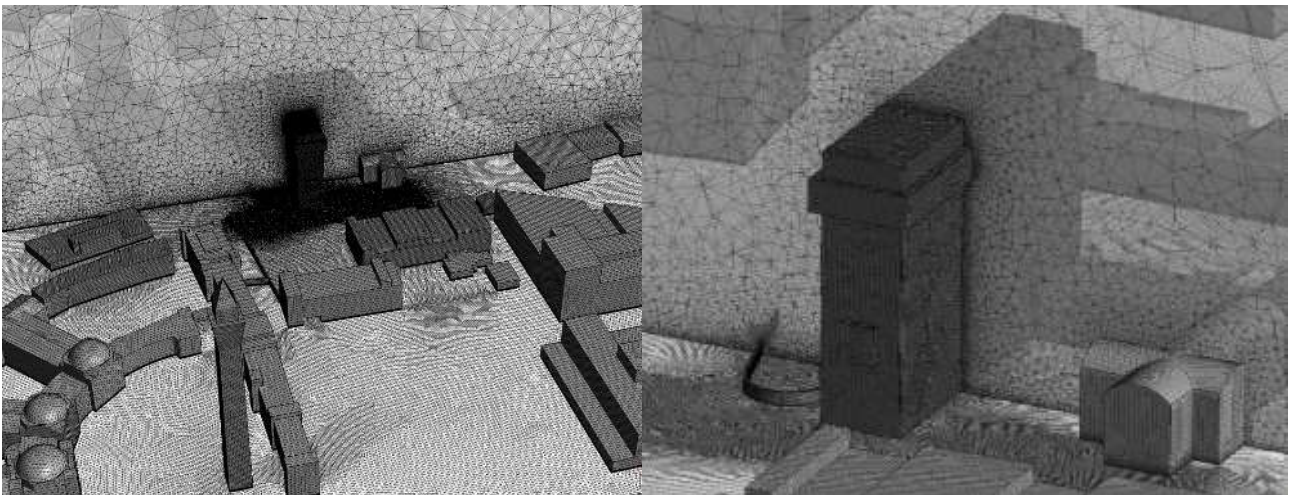


Figure 5.7. (Left) General view of the computational unstructured mesh, with refined topology along the footpath. (Right) Detail of mesh on the Biosciences Tower.

The computational grid is generated using Ansys IcemCFD. It consists of a hybrid unstructured tetraedrical grid. Figure 5.7 shows a view of the triangulated surface mesh over the Chancellor Court (on the left) at the UoB Campus, and a detail of the refined surface mesh over the Biosciences Building in proximity to the position of the pedestrian-level anemometers (on the right). The volume mesh is also shown in transparency, thanks to a plane sectioning the flow domain. The size of the volume cells varies greatly (Figure 5.7). In fact, the size increases from $\sim 2\text{-}5$ cm close to the ground to $\sim 0.1\text{-}0.5$ m in proximity of the roof of buildings. Further higher from buildings over the UoB campus and the wind

tunnel fetch length the cell size was increased up to $\sim 5\text{-}10$ m. This was done to limit the overall mesh size and pursue a cost effective simulation. Various preliminary SRANS simulation have been performed to ensure that the performance of adaptive wall-functions implemented by both RANS and WM-LES is guaranteed through the quality of the surface mesh. A boundary layer mesh composed of at least 7 prismatic layers was also introduced at walls to ensure the first cell lies within the Prandtl boundary sub-layer ($y^+ \sim 10$) and velocity gradients are resolved accurately.

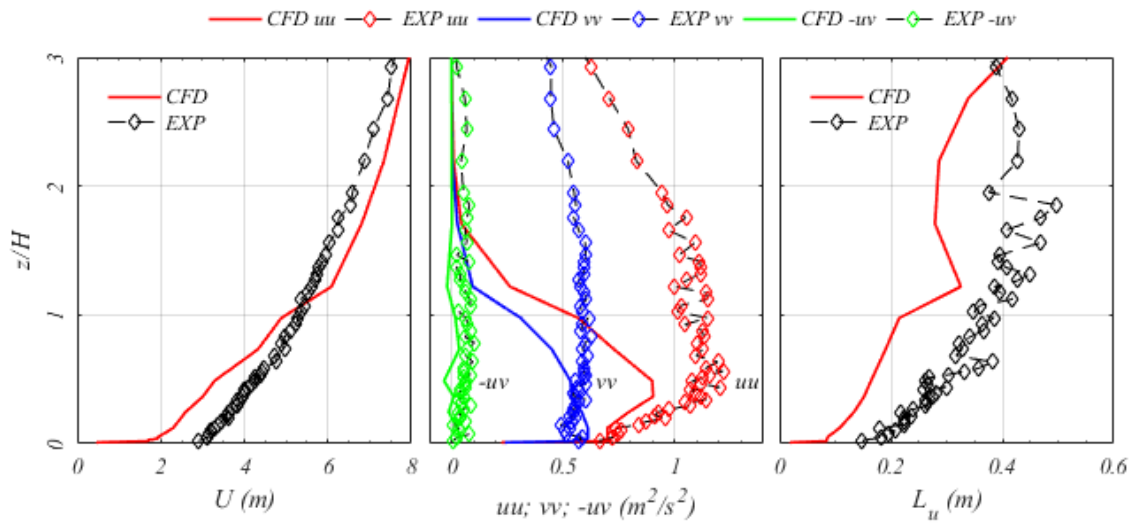


Figure 5.8 – Inlet velocity statistics downstream of precursor domain. a) Mean velocity; b) variance and covariance; c) integral length scale. H in this case is the height of the Muirhead tower

Turbulent inlet boundary condition

The computational domain replicates the wind tunnel setup with two differences. At the outlet surface, an extrusion is added to the domain to reduce the blockage of the model with the external boundary. At the inlet, the section is elongated to include a portion ($\sim 1/3$) of the roughness elements, which are used in the wind tunnel to generate the experimental inlet wind profile. The purpose for these elements is to create a precursor simulation by means of an added geometry to generate a turbulent inlet. The obtained inlet is shown in compared to the wind tunnel profile. The experimental vertical mean velocity profile as measured at the inlet of the test section is placed at the inlet boundary, while turbulence characteristics are generated with the geometry roughness. Figure 5.8 a) shows a deviation for the mean velocity profile. This is due to the wake that develops downstream of the roughness geometry. However, the effect of such a geometry is to have a rather good match at $z/D < 1$ for the velocity covariance. A

larger deviation from the experimental results is then noticeable for the integral length scale, however a limited number of roughness elements is able to generate, which still yields $L_u \sim 15H$, where $H=2$ m is the pedestrian reference height. Results shown in Section 3 seem to support the thesis that PLW is heavily affected by the immediate surrounding geometry, while being rather insensitive to the global wind profile.

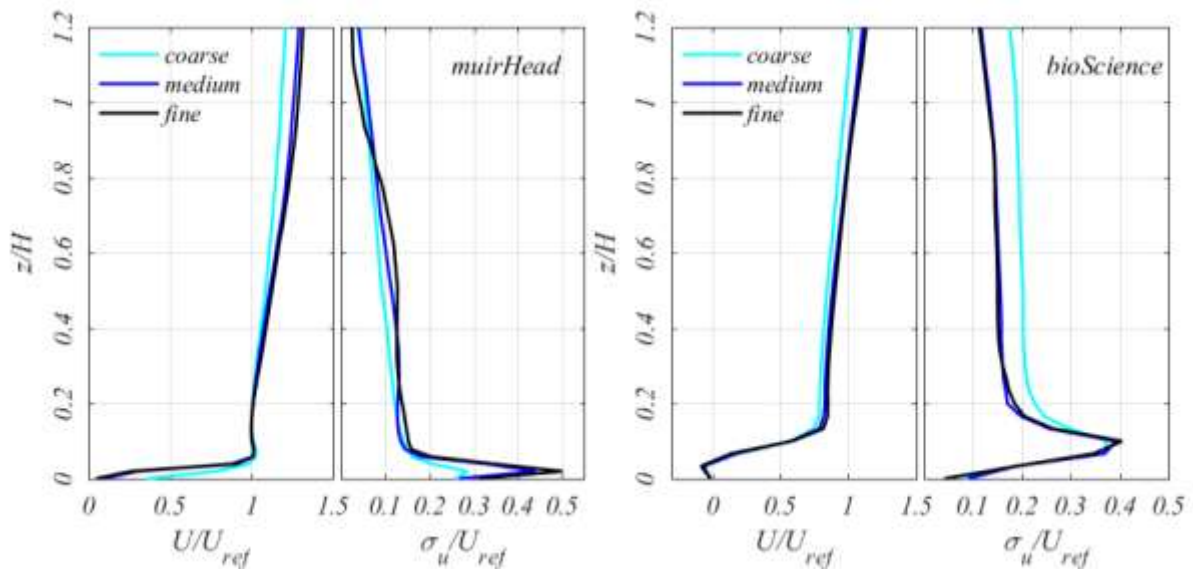


Figure 5.9. Mesh independency study a) Mean velocity; b) standard deviation; c) Integral length scale.

Mesh independence study

The quality of a LES largely depends on the quality of the computational grid. The computational grid should not affect results, although this condition theoretically only holds true in LES when $\Delta \sim \lambda_u$. For this reason the solver has been run on 3 computational grids and results on both the mean and fluctuating statistics are shown in Figure 5.9. The coarse grid shows a large deviation from the medium and fine grids, which provide analogous results for U and σ_u . The integral length scale L_u shows a more pronounced deviation of results. However, at $x/D=0$ the medium and fine mesh are consistent. This is the location of most interest in the dataset and a good prediction in this location reassures on the quality of the mesh.

Table 5.3 – Computational Setup and grid resolution details

Case	Grid	Cell size bioscience (m)	Cell size freestream (m)	Nr Cells b.l. pedestrian (m)	y+ pedestrian (-)	Cell size pedestrian (m)	Grid size ($\times 10^6$)	Turbulence model	SGS model	Time step Iterations*	CFL number (mean; max)
LESc	Coarse	0.05	0.5	7	~ 5	0.03	6.69	WM-LES	WALE	0.0005	3×10^{-4} ; 16
Rwtn	Medium (no turb. inlet)	0.03	0.2	7	~ 2	0.01	8.21	RANS	k- ω SST	* ~ 1000	-
LES	Medium	0.03	0.2	7	~ 2	0.01	16.9	WM-LES	WALE	0.0005	8×10^{-5} ; 12
Rwc	(cut)	0.03	0.2	7	~ 2	0.01	16.9	RANS	k- ω SST	* ~ 2000	-
Rwt	Medium (whole)	0.03	0.2	7	~ 2	0.01	21.1	RANS	k- ω SST	* ~ 2000	-
LESf	Fine	0.02	0.1	15	~ 2	0.01	27.9	WM-LES	WALE	0.0005	3×10^{-5} ; 6

The optimal coarseness of the mesh has been chosen thanks to a mesh independency study, reported in Figure 5.9. Three different grids have been created for the LES case with growing refinement. Figure 5.9 shows the mean and standard deviation velocity at the eight measurement positions. The coarsest mesh LESc deviates significantly from the medium and fine meshes LES and LESf. On the other hand, LES and LESf show an analogous and similar trend. For this reason, only results from the medium grid resolution LES are considered in the rest of the paper. Table 5.3 shows further details about the three independency grids together with the grid used for the RANSw case, built after the medium LES grid specifications.

The models were solved using 7 Haswell computational nodes, each having a RAM of 128 GB and a clock-time of 4.6 GHz over 20 processors. Simulations took from a minimum of ~ 2 -5 hours for the RANS cases to a maximum of ~ 10 -20 days for the LES cases.

RANS setup

Two RANS simulations have been carried out for the two domains shown in Figure 5.6 using the medium mesh resolution. The turbulence model of choice is the common k- ω SST, which has shown to be successful in predicting the position of the separation and the extension of wakes in bluff body aerodynamics (Blocken, 2014). The steady approach is implemented as an alternative to the unsteady

one (URANS), as the transient equation is only beneficial when alternating flow patterns such as vortex shedding are examined, which is not the case for urban winds (Blocken et al., 2016). The velocity introduced at the inlet is directly taken from the experimentally measured wind speed profile, while in the RANSw case a constant inlet of 15 m/s is introduced to allow a boundary layer to develop. At the outlet a Neumann boundary condition is used, while all other boundaries have a no-slip condition on the velocity and pressure gradient, as is current practice.

WM-LES setup

The recommendation for a state-of-the-art LES would require a mesh with $\Delta \sim \lambda_u$, where $\Delta = \sqrt[3]{dx dy dz}$ is the grid size (also called the cut-off length), and λ_u the dissipation length scale of turbulence. However, besides the difficult supposition of λ_u without preliminary data or simulations, this criterion generally leads to quasi-DNS (Direct Numerical Simulation) with an exponential increase in costs. For this reason, a much coarser mesh is chosen for a more economical simulation, as this is arguably more appealing for industrial practice.

This approach is usually not recommended in literature (Blocken, 2018; Hanjalic, 2005), as the increase in the complexity of the methodology comes with an intrinsic increase in the complexity of its setup which might lead to macroscopic mistakes. However, authors are very careful in giving a handbook on LES in literature, as the potential of the methodology is mostly unknown. Research has started pushing the boundaries of coarse LES, but more results are needed to draw robust conclusions to inform guidelines for, as already available for RANS (Blocken, 2015; Franke et al., 2011).

In cases where a validation test case is not available, it is advisable to invest more effort in the quality of the mesh and perform a standard LES, to make sure a greater number of turbulent scales is resolved. However, in this case, the reduction in the computational costs justifies the use of a coarser mesh. Nevertheless, extra effort in monitoring the convergence of statistics and the generation of suitable fluctuations at the inlet is an unavoidable requirement. In the present study, the quality of the grid at roof and pedestrian level is optimised with greater refinement than at other locations, and results therein are monitored for convergence. A sample time of $T_g = 15$ s was found to be a good compromise between quality and cost-effectiveness.

The inlet boundary condition requires special attention in LES simulations. The mean velocity profile as measured experimentally is introduced directly at the inlet boundary, in the same way as done for RANS. However, the turbulence necessary for LES is introduced using the roughness elements shown in Figure 5.6. This technique falls into the category of precursor simulation domain for the generation of inlet turbulence for LES (Tabor and Baba-Ahmadi, 2010). In the whole wind tunnel domain (used for RANS only), the mean velocity is calculated through the roughness, while in the LES case a portion of the wind tunnel fetch length is enough to create fluctuations capable of greatly increasing the quality of data in those locations of interest. This approach has proved very effective in increasing the accuracy of numerical data against full-scale tests (Chaudhari et al., 2016). Figure 5.8 (right) shows the inlet profile as measured experimentally and predicted with the LES simulation using the partial computational domain. The effect of the 12 rows of roughness element is visible in the mean flow development (Figure 5.8), however results in Section 5.4 show that this mismatch does not interfere with the validity of results.

The outlet boundary is analogous to RANS, while the boundary condition at the wall plays a significant role in coarse LES simulations.

Wall functions are implemented in the WM-LES model, which is a hybrid LES-RANS model where the RANS part is automatically applied at the first cell only. The ratio between LES and RANS uniquely depends on y^+ , i.e. if $y^+ \sim 1$ WM-LES coincides with standard LES. This model still requires a number of cells similar to traditional LES, but avoids all the limitations of the classical hybrid model Detached Eddy Simulation (DES) which may arise due to a too fine/coarse grid. More indications on the methodology as coded in Ansys CFX/Fluent are available in Shur *et al.* (2008). The Wall-Adaptive Lagrangian-Eulerian (WALE) sub-grid scale (SGS) model has been selected as it allows for a better output for the anisotropy at SGS with respect to the Smagorinsky-Lilly SGS model, without requiring additional computations as for the Germano SGS model (Nicoud and Ducros, 1999). WALE still requires the definition of a model constant, here put $C_w = 0.35$ as indicated in CFX guidelines. C_w regulates the amount of energy dissipated through the deviatoric part of the velocity tensor close to the wall, which plays a relatively small role when using wall functions as in WM-LES. The computational scheme is of overwhelming importance in LES. However, a good resolution of the mesh allows for a

rather stable simulation. In order to help convergence without losing accuracy the bounded central differencing scheme (CDS) as coded in CFX is used. The time step choice is also another delicate aspect. The Courant–Friedrichs–Lewy (CFL) condition for numerical convergence requires the Courant number $Co < 1$, where $Co = U\Delta t/\Delta x$, Δx , Δt and U are respectively the local cell size, the local through-flow time, and the local flow velocity. To ensure the stability of the solution, a time step of $dt = 0.0005$ s is therefore set up and the relevant Courant number is shown in Table 5.3.

Results in Section 5.4 refer to the medium grid size.

5.3.4. Processing of fluctuating wind speed data

In order to compare results from full-scale, physical and numerical simulations, the relevant scales need to be considered when post-processing. Not only the geometrical scale, which accounts to 1:300 for both the physical and numerical simulations, but also the velocity and time scales.

Table 5.4 Processing parameters for numerical (CFD), wind tunnel (EXP) and full scale (FUL) setups.

Case (scale)	Sample rate f_s (Hz)	Sample time T (s)	U_{ref} (m/s)	D (m)	Velocity scale	Time scale	3 s cut- off freq. (Hz)	nr. of 60s windows (-)
CFD (1:300)	2000	14	5.84	0.042	2.15	139.33	46.5	32
EXP (1:300)	1000	50	4.87	0.042	2.58	116.14	38.7	96
FUL (1:1)	10	9100	12.58	12.6	1	1	0.33	151

Table 5.4 shows the relevant time and velocity units taken as reference when post-processing the horizontal speed $q = \sqrt{u^2 + v^2}$ at pedestrian level, or the u and v velocity components above the roof. The raw velocity signals are low-pass-filtered using a 3rd order Butterworth filter with a cut-off frequency equivalent to 3 s (Table 5.4). Data are sampled over several sample times T (as shown in Table 5.4), however the stationarity of the statistics has been assured by mean of a visual inspection of the time-histories. The data are then scaled according to the relevant length D^{FUL}/D , velocity U_{ref}^{FUL}/U_{ref} or time scale $(D^{FUL}/D)/(U_{ref}^{FUL}/U_{ref})$, which is variable for each method and reported in Table 5.4. Numerical, wind tunnel and full scale data is referred to as respectively CFD, EXP and FUL in the rest of the paper.

5.4. Pedestrian Level Wind Results

In Figure 5.10, CFD results are compared to EXP and FUL ones at the eight measurement positions. Data is non-dimensionalised using U_{ref} as indicated in Table 5.4. U/U_{ref} is predicted within 20% absolute error bounds for almost the whole dataset. The prediction ability for the mean flow is similar for the two methods, although CFD compares better to EXP at lowest velocities. In agreement with Yoshie *et al.* (2007), the performance seems to slightly increase with higher mean velocities. The validation of higher order statistics is however more complex. Unlike U/U_{ref} , Figure 5.10 shows a better match with FUL data for σ_u/U_{ref} , while on the contrary the prediction is slightly better for the length scale ratio λ_u/L_u of the EXP data. In Figure 5.10 c) the maxima of three different moving average velocities are reported. Although EXP and FUL data compare similarly to CFD, a better match can be observed for u_{60s} , as CFD tends to systematically overestimate the maximum u_{10s} and u_{3s} .

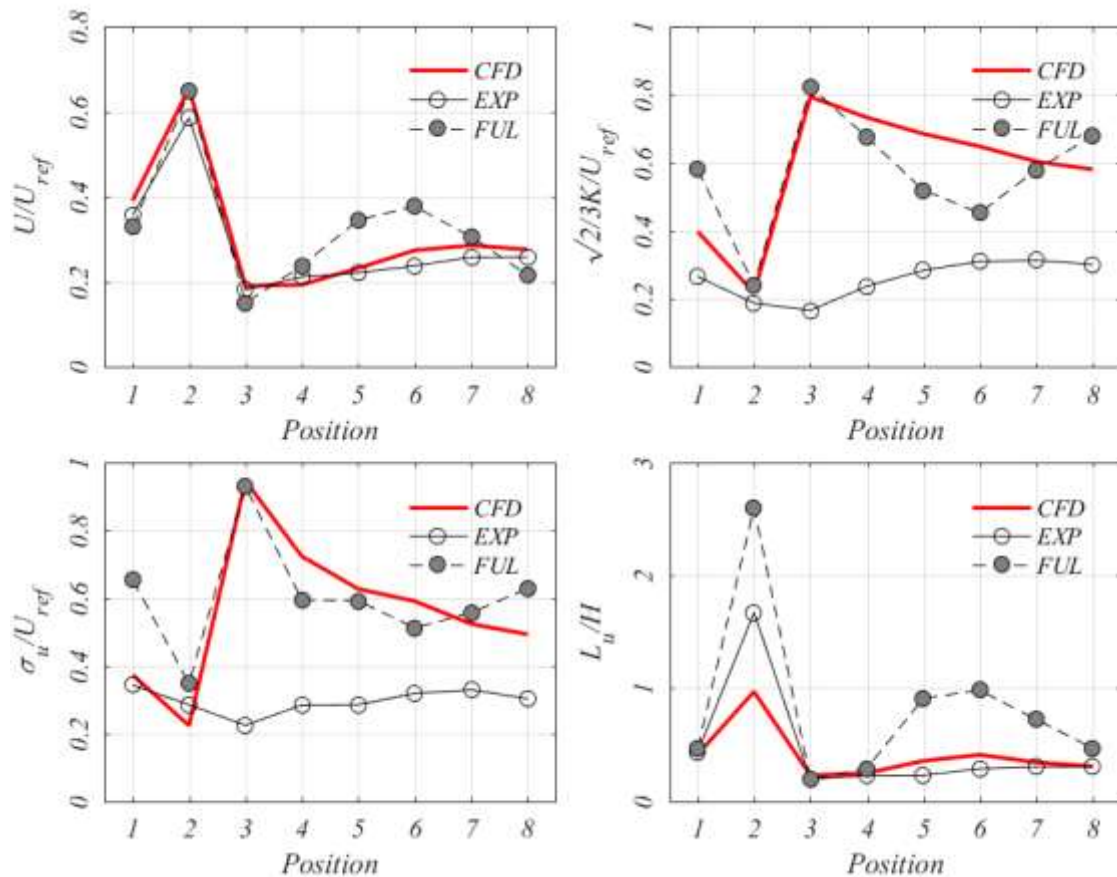


Figure 5.10. Mean, standard deviation, turbulent kinetic energy, and integral length scale along the 8 measurement positions on the pedestrian test route indicated in Figure 5.2. CFD results refer to LES and are compared to EXP and FUL data.

The reason for the mismatch between CFD and FUL/EXP data can be found looking at the flow pattern at pedestrian level, shown in Figure 5.11. The mean flow shows a large recirculation region which affect positions 4 to 8. In this region, $U/U_{ref} \sim 0.2$ with a turbulence intensity of $\sim 0.2 \div 0.25$ and an overall maximum velocity of $\sim 1 \div 1.3$. Positions 1 to 3 show each a specific behaviour. Position 1 is undisturbed by the presence of the bioscience tower, as the mean flow does not show particularly high values, while standard deviation and maximum velocity are in the highest range shown in Figure 5.10. Position 2 is right in front of the eastern corner of the bioscience tower, as the SSW wind is washed down the walls of the building and delivered to the footpath with velocities close to those at roof height.

The standard deviation is $\sim 0.1 \div 0.15$ the lowest in the dataset, while the maximum velocity is the highest. Position 3 shows the lowest maximum velocity and the highest standard deviation, due to the low mean velocity of ~ 0.4 . Figure 5.10 shows U/U_{ref} along the positions. In general, both EXP and CFD provide a good prediction of the mean velocity at the windiest location, however both CFD and EXP diverge from FUL inside the recirculation region downstream of the bioscience complex. In position 3 at $x/D \sim -0.5$, the EXP data yields a strong mismatch ($\sim 120\%$ over-prediction). This might depend on positioning issues of the hot-wire probes in what is the location with the largest shear strain of this dataset, right behind the corner of the bioscience tower, where the strong winds mix with the recirculation region in the wake of the tower. In Figure 5.12, the surface pressure on the bioscience tower and the surroundings is shown along with flow streamlines. The streamlines are generated so they cross the pedestrian alignment of interest. A region where the flow blows parallel to the bioscience is followed by a region of high recirculation as the surface pressure on the ground abruptly changes sign at approximately position 3, where the criticality in EXP data is found.

Figure 5.12 shows the flow pattern around the Biosciences Building. On the left, velocity streamlines are computed from the alignment of interest at pedestrian level, showing a quite complex flow environment. Wind from the Storm Ophelia hits the BB with a 203 degree. A large amount of mass flow rate is redirected towards the base of the building, in a downwash, which causes a jet to occur at the southern corner of the BB in correspondence with Position 2. A recirculation region on the

downstream side of the building forms due to the angle of the wind, which affects all remaining positions. The wake of the building can also be noticed on the right side of Figure 5.12.

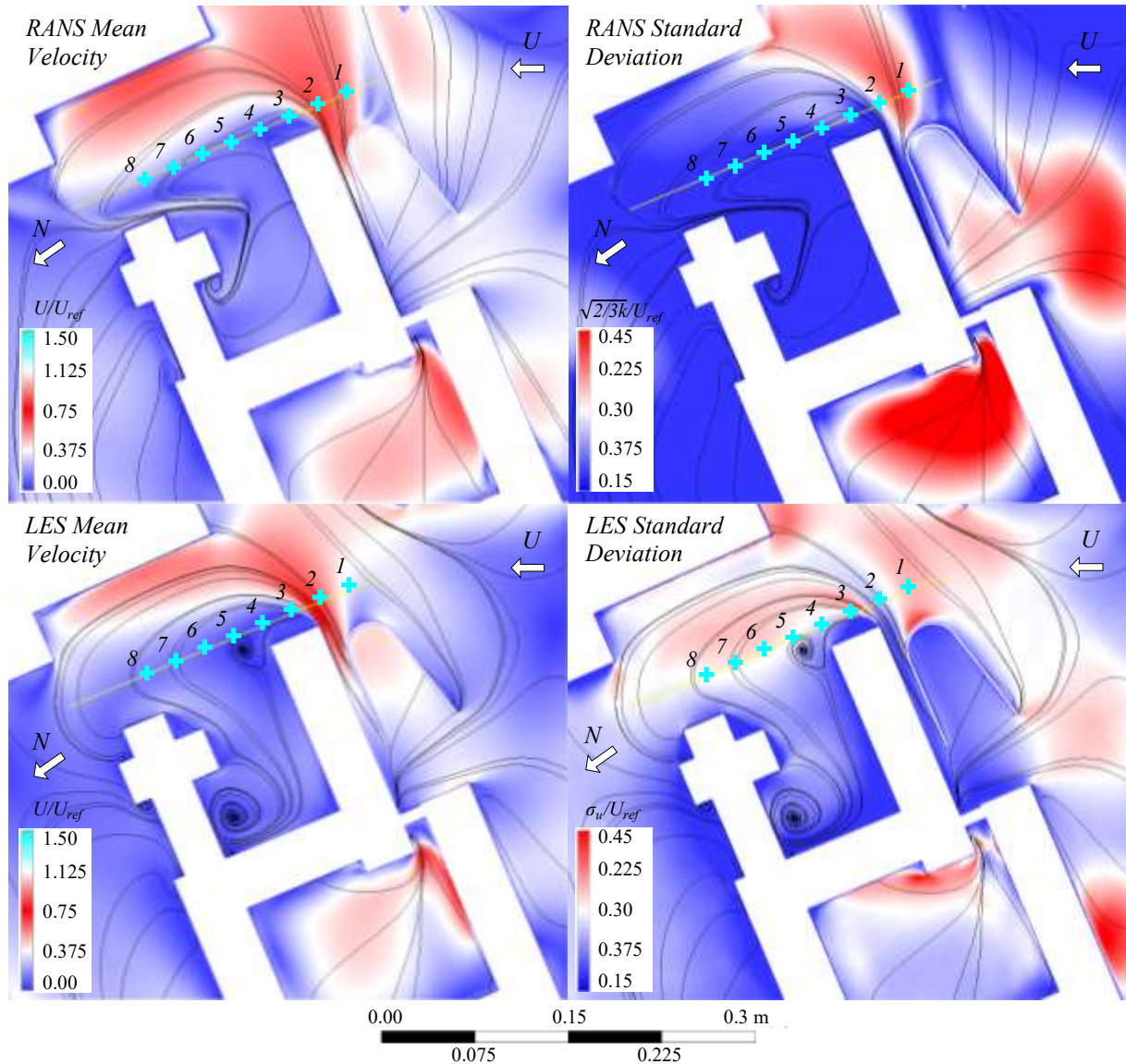


Figure 5.11. Mean and standard deviation field over the 8 measurement positions. (upper row) RANS case; (lower row) LES case. Black lines are mean velocity streamlines

Figure 5.10 shows both the standard deviation and the turbulent kinetic energy normalised with the reference velocity. CFD outperforms EXP especially in the recirculation region (positions 3 to 5 and 7 to 8). This might well depend on the difficulty in positioning hot-wire probes in recirculating regions and their directional performance in such strong varying flow fields. In recirculation regions the flow might indeed feature small mean velocities and large standard deviations which can cause even strong gustiness. Figure 5.10 also shows the integral length scale of turbulence, calculated as described in Chapter 3. The validation of the length scale is tricky as several factors have an influence. This is the

case for Position 2, where FUL results show a much larger value than EXP and CFD. As the rest of the dataset is consistent, alternative calculation methods are not implemented. However, results show clearly how in the recirculation region the integral length scale is comparable to the pedestrian height $L_u \sim H$, while in positions with strongly coherent flow structures, such as in position 1-2, $L_u \gg H$.

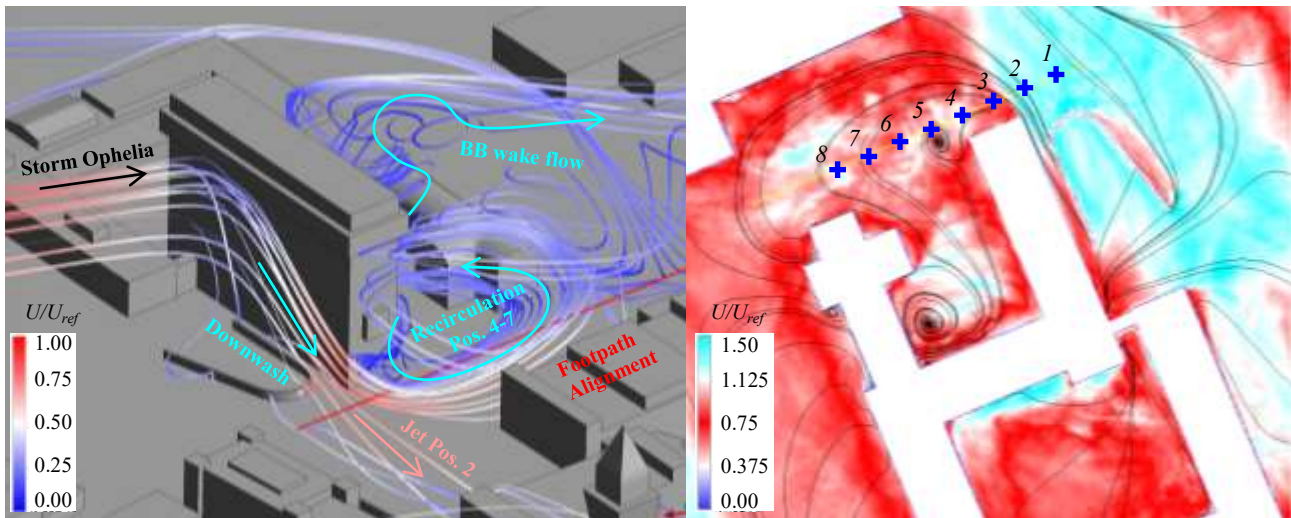


Figure 5.12 (left) Flow pattern along the footpath, showing the downwash at the BB southern façade with the jet nearby Position 2, the recirculation region which affects Positions 4-to-7 and the wake flow at the northern side. (right) 99th Percentile of the velocity magnitude.

Bulk statistics show the complexity of validating a numerical simulation at pedestrian level and the criticality in modelling higher order statistics for the fluctuating flow. Although the practitioners' standard is to rely on wind tunnel testing, the performance of numerical high-fidelity techniques is if not superior, comparable to experiments. Accurate wind tunnel measurements are complicated by the difficulty in accurate positioning of probes in areas of the flow field with sudden changes in direction and unsteadiness, which is well captured by CFD.

5.5. Rooftop level wind results

Figure 5.13 shows the velocity profiles for the Muirhead tower and the Biosciences Building. Both velocities in the horizontal and vertical directions are considered and compared with the experimental results. The LES predicts accurately both U and W , with a deviation from EXP results of less than $\sim 2\%$. For $z/H > 0.6$ results deviate by $\sim 10\%$ for the BB. This deviation might occur due to the positions of the models. In fact, the MT is facing directly the inflow from the wind tunnel, while the BB is right in the middle of the model and hence affected by the signature turbulence and wakes coming from surrounding

buildings. As for the RANS prediction, in the vertical direction results are comparable to LES in terms of accuracy. As for the horizontal velocity, Rwc under-predicts the behaviour by a factor of $\sim 10\%$. This might depend on the mismatch in the choice of U_{ref} and the profile over the Muirhead Tower. In fact, this position is heavily affected by the mismatch of inlet boundary conditions as shown in Figure 5.8, and therefore different velocities are found above the roof. Nevertheless, all RANS techniques are able to predict the trend of the wind profile. However, the Rwt shows that the aerodynamics is heavily affected by the inlet wind, even closer to the roof. This seems to contradict findings of Chapter 4, however a second LES simulation has not been performed in this case.

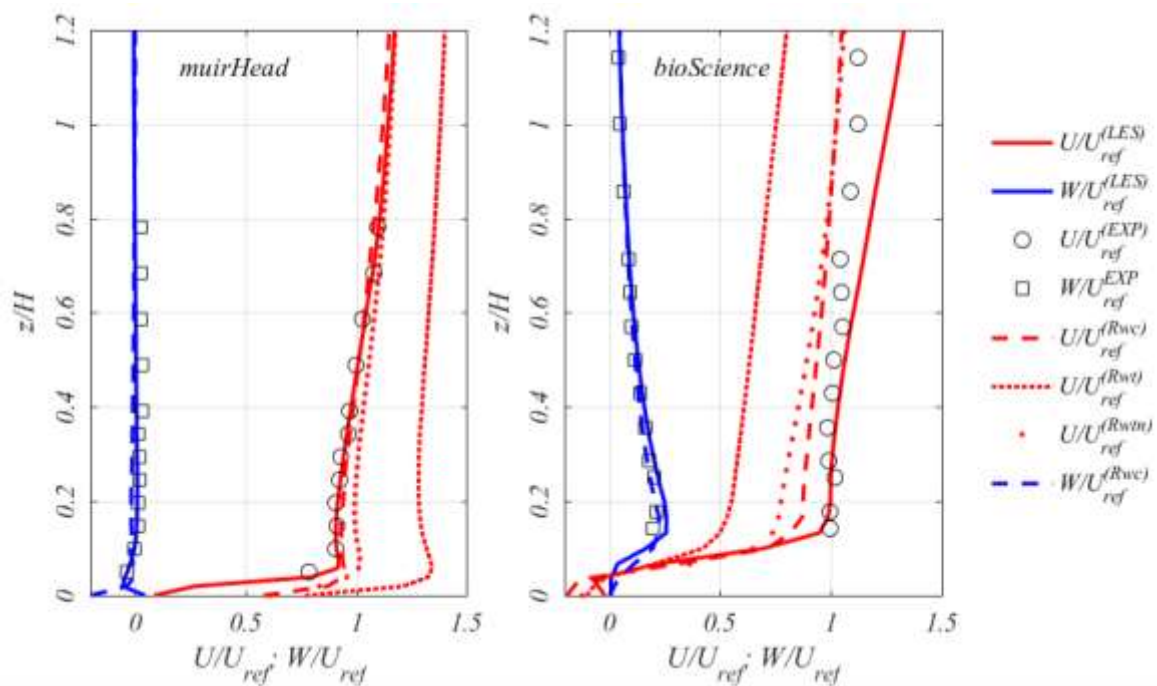


Figure 5.13. Mean horizontal and vertical velocity at the rooftop of the Muirhead tower (left) and Biosciences building (right).

Figure 5.14 shows the turbulence intensity for both horizontal and vertical velocities. All techniques underestimate the turbulence intensity, with LES showing an error of $\sim 40\%$, similar to Rwc, and other RANS models showing a mismatch larger than $\sim 60\%$. Both towers are affected, with the MT showing the larger mismatch. This also applies to the vertical direction. The mismatch can be attributed to the inlet turbulence of the cut wind tunnel domain. The portion of the fetch length modelled is enough to guarantee a match with the experimental wind conditions up to $z/H \sim 0.2$ from the ground, however at the roof height, a strong mismatch is present, affecting the turbulence intensity as predicted. The mismatch of the BB is less pronounced again due to the effects of the surrounding buildings.

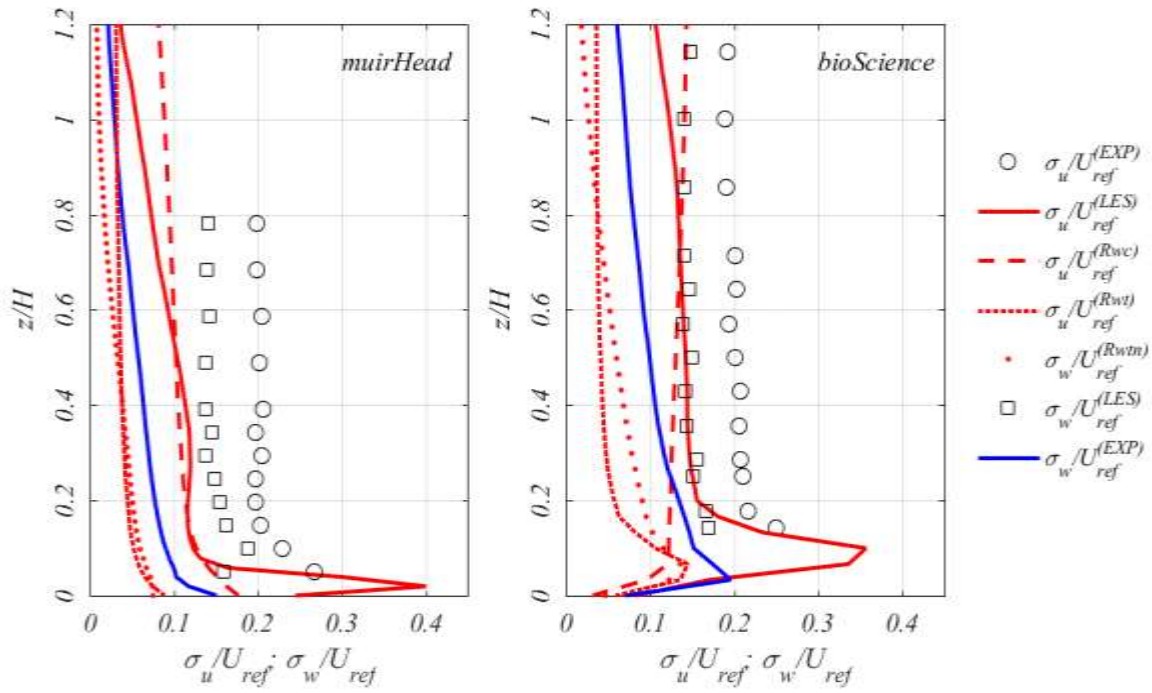


Figure 5.14. Horizontal and vertical standard deviation at the rooftop of the Muirhead tower (left) and Biosciences building (right).

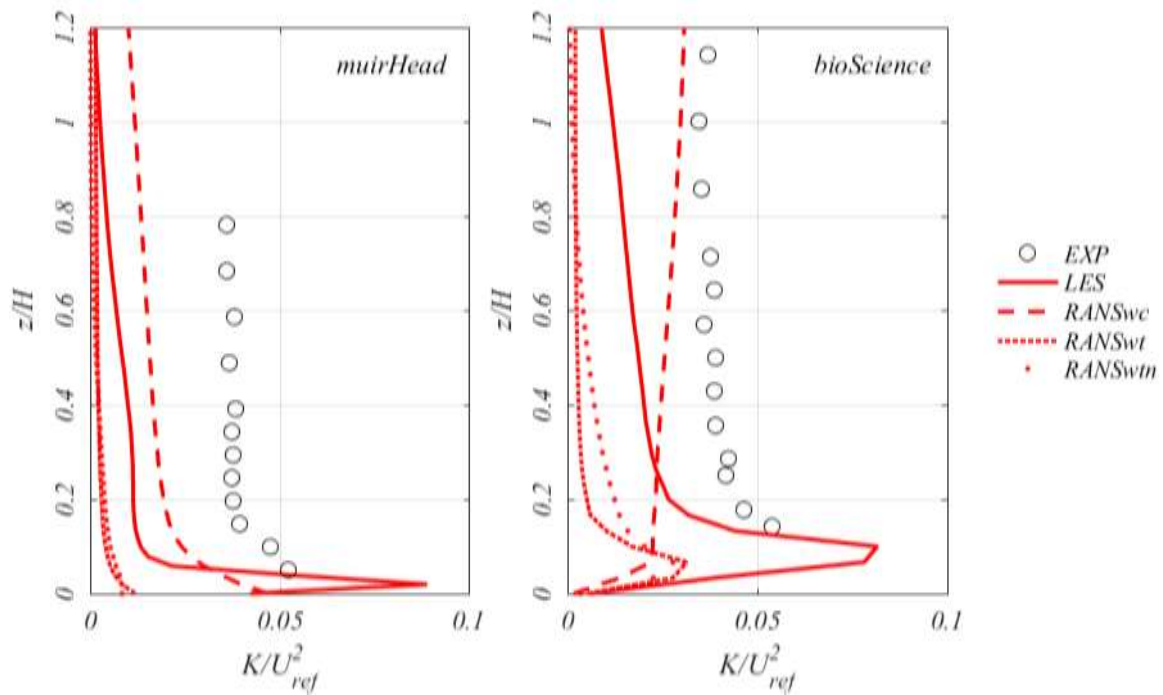


Figure 5.15. Turbulent Kinetic Energy at the rooftop of the Muirhead tower (left) and Biosciences building (right).

Figure 5.15 shows the turbulent kinetic energy as predicted in the LES and RANs cases. The mismatch is analogous to that shown in Figure 5.14. The RANSwc case seems to converge towards experimental values for $z/H > 1$ for the BB. This might be influenced by the proved tendency of RANS of over-

estimating turbulence in separated regions, like the urban plume which encompasses the BB. Both RANSwt and RANSwt_n strongly under-predict the turbulent energy at both sites, showing the importance of producing a suitable balance between the accuracy of the mean velocity inlet and its turbulence contents.

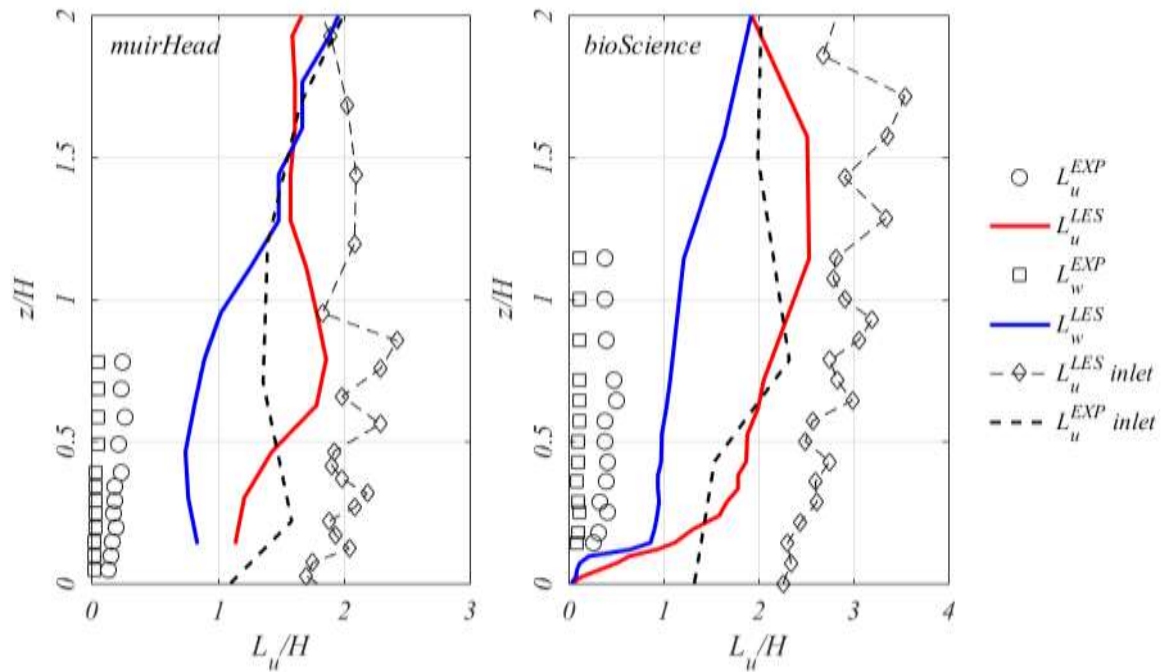


Figure 5.16. Integral length scale of turbulence at the rooftop of the Muirhead tower (left) and Biosciences building (right) compared with integral length scale as found at the inlet flow.

Figure 5.16 shows the integral length scale of turbulence. In both cases LES over-estimates the length scale by a factor of ~ 5 when compared to experimental values. Results are plotted alongside inlet integral length scale. Little difference with the inlet scales is present over the buildings. This means that the turbulence intensity deficit as shown in Figure 5.8 is responsible for a lack of interaction with the aerodynamics of high-rise buildings, which in turn causes the integral length scale to be analogous to that found for the inlet. Over the Biosciences Building, at $z/H < 0.1$ the match with experimental values is closer than at other heights, suggesting that the behaviour is commanded by the leading edge vortices only. The prediction of coherent structures above high-rises requires a careful modelling of the inflow in terms of turbulence characteristics. In fact, mean velocity is predicted accurately over the height of the geometry.

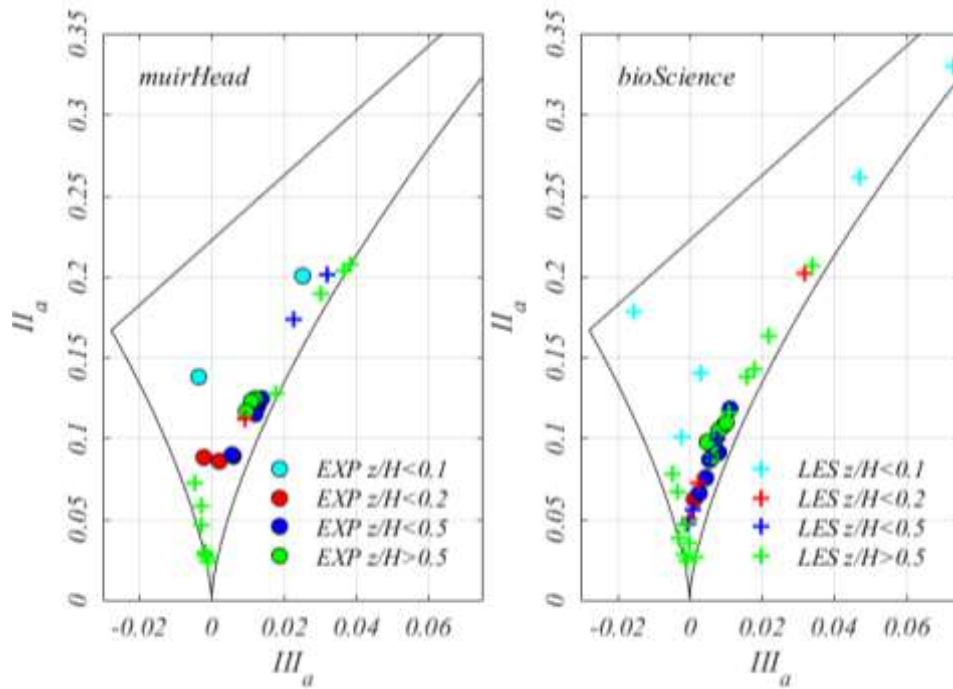


Figure 5.17. Anisotropy of velocity in terms of velocity invariants at the rooftop of the Muirhead tower (left) and Biosciences building (right)

Results shown in Figure 5.13, Figure 5.14, and Figure 5.16 might also suggest indications about the anisotropy of the flow field. Figure 5.17 shows the velocity invariant plots as introduced in Chapter 3 and 4. The role of the turbulent inflow is evident from the behaviour of LES as $z/H > 0.5$ yields a high isotropy, which is not found in the experimental case. At lower heights, the behaviour is inconsistent with findings of Chapter 4, where the flow becomes highly isotropic closer to walls. This depends on the directionality of the flow. In fact, in the realistic urban configuration of Chapter 5, the buildings are oriented randomly with the flow depending on the event of choice, the storm Ophelia. This affects the aerodynamic behaviour and the isotropy of turbulence as unlike the isolated high-rise building case; the geometry is not symmetric around an axis. Close to walls LES provides accurate estimation of the anisotropy, while further the behaviour is strongly affected by the mismatch in the turbulent inflow.

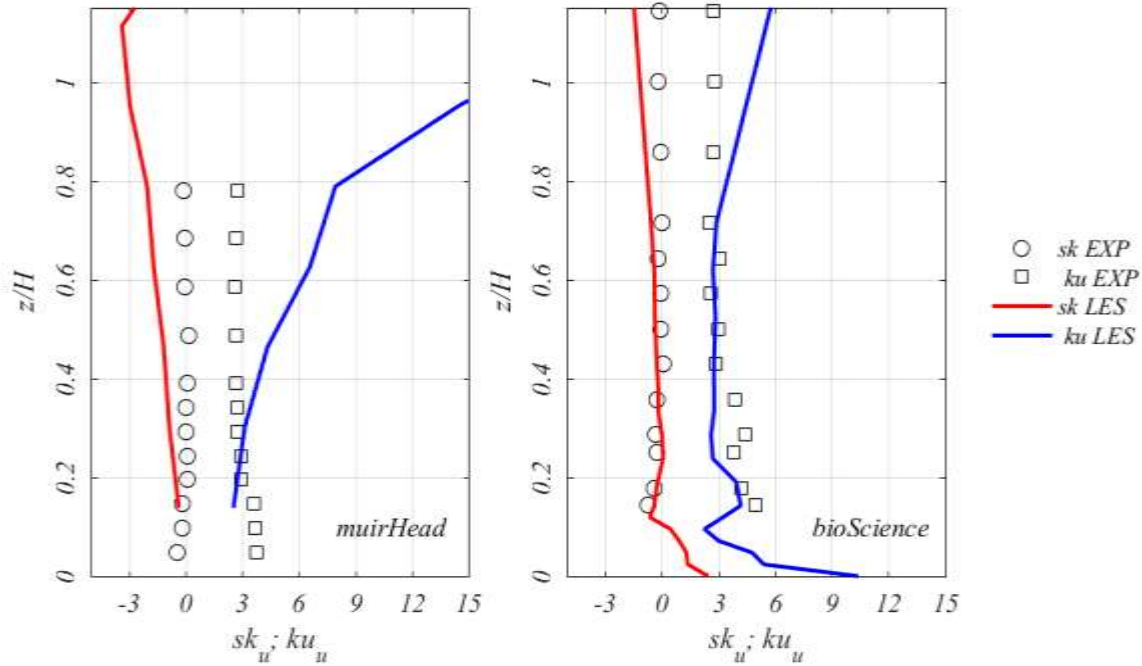


Figure 5.18. Skewness and kurtosis of horizontal velocity at the rooftop of the Muirhead tower (left) and Biosciences building (right)

Figure 5.18 shows higher order moments for the horizontal velocity. Besides the mismatch of turbulence characteristics, the prediction of LES is very accurate for the skewness for both towers, with a mismatch for the Muirhead tower above $z/H \sim 0.4$, where the flow is negatively skewed according to the LES predictions. As for the kurtosis, values are over-predicted for $z/H > 0.4$ for MT and $z/H > 0.8$ for BB. This might be interpreted with the coarseness of the mesh above the model, which has been developed to be cost-effective and with a refined mesh only in the vicinity of the buildings.

For the BB another issue might be noted around the behaviour of higher order moments close to the roof. In fact, kurtosis becomes strongly positive, while skewness is positive. This is indicative of the highly vorticity of the behaviour inside the separation bubble, which experiences bursting and vorticity which causes high velocities to be more likely than slow ones in a region with low mean velocity.

This behaviour can be better understood briefly looking at the estimation of the gust speed calculated using the moving average of the velocity signal using two windows of 3s and 60s respectively. The signals are post-processed according to indication given in Table 5.4. The maxima of the moving average signal is shown in Figure 5.19 for both the velocity profiles over the two high-rise buildings and the pedestrian route of Figure 5.11.

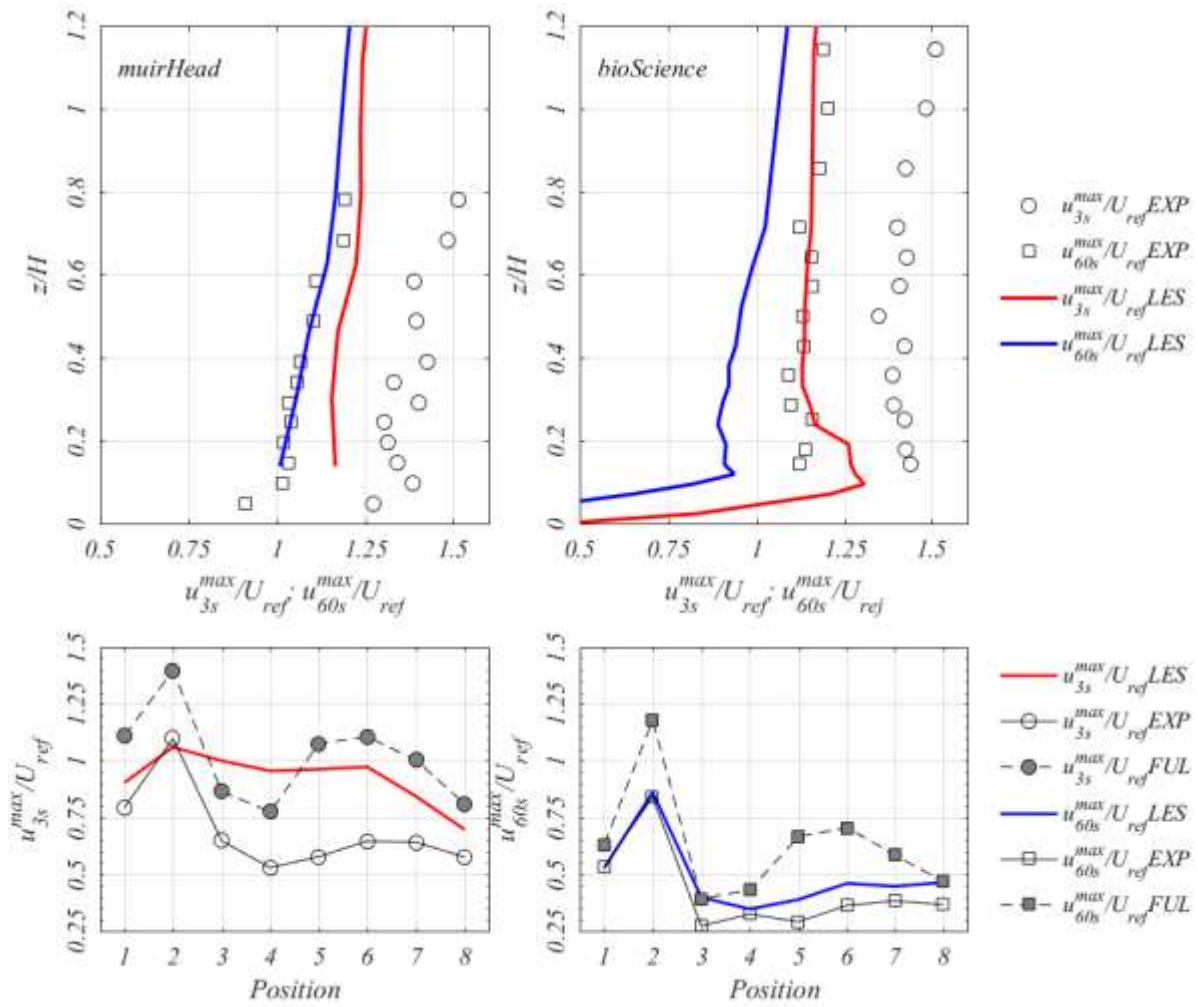


Figure 5.19. Gust wind speed at the rooftop of the Muirhead tower (top-left) and Biosciences building (top-right) and along the pedestrian route (bottom).

5.6. Discussion and Conclusions

This Chapter provides an insight on the adequacy of wind tunnel testing and numerical simulations to assess the flow around high-rise buildings suited for positioning of wind turbines. As high-rises are placed in a realistic urban configuration, several factors affect the flow pattern in contrast with the case studied in Chapter 4 of an isolated high-rise building:

- The randomness of the wind conditions implies a random angle of attack and asymmetry of the geometry of the high-rise building;
- The roughness distribution around the high-rise, which varies greatly depending on the immediate surroundings of the building and the built environment around;

Results show that conclusions on the turbulence environment are difficult to draw. The length scale generally is large, however the behaviour shows the connection between turbulence intensity and scales, which largely depends on the interaction with the turbulent inlet, i.e. the surrounding environment.

When turbulence intensity is enhanced in the inlet, turbulence length scales are governed by the building, and their size reduces dramatically ($\sim 20\text{m}$ compared to $150\text{-}200\text{m}$ of the inflow). When turbulent inflow is not high $\text{TI} < 5\%$ then the length scales above the high-rise have a size comparable to that of the inflow, with only a small region of the flow where the scales are heavily affected by the aerodynamics of the building. The interaction between inlet scales as predicted numerically and the buildings might also be an effect of the meshing strategy, which balances the cost of the simulation with the size of the mesh, resulting in a cell-size of $\sim 10\text{m}$ in the freestream region above the UoB campus. Modelling the correct inlet turbulence is therefore deemed necessary to have a correct assessment of the flow pattern above the buildings.

The pedestrian level winds are more accurate as the coarseness of the mesh is reduced close to the ground and the processes that affect performance are weakly influenced by turbulence in the inflow, and determined by the building aerodynamics.

The numerical setup prompts a further observation. The unstructured coarse grid used for this study is normally a risky choice for LES, as a broad band of frequencies is demanded to the SGS model of choice. However, refining the mesh in those regions of interest, as in the present study, paying attention to the y^+ value and the convergence of results and provided a good validation test-case is available, shows how the local features of the flow field in the urban environment are mostly insensitive to the surrounding flow field, or the turbulent inflow at pedestrian level. This could open up the possibility of implementing coarse high-fidelity simulations to aid wind tunnel tests in increasing the prediction accuracy of PLW, which is shown to be at best similar to LES in this work. Vice versa such a conclusion cannot be made about the roof-level flow on high-rise buildings, which is heavily influenced by the turbulence at the inlet. Although the mesh resolution might contribute greatly to the accuracy, it remains to be seen whether refining might be avoided with a careful modelling of the turbulent inlet structures at the inflow.

Chapter 5 has prompted a reflection on the behaviour of the flow above the roof of high-rise buildings if the positioning of wind turbines is looked at. The mere match of the mean velocity inlet profile is not a guarantee for a careful prediction of turbulence statistics, in particular the integral length scale. It remains unclear whether the coarseness of WM-LES contributes to the lack in accuracy for the integral turbulence length scales, as a deficit in the inlet turbulence intensity at roof level is present which might affect results to a greater extent. As for the positioning of wind turbines, experimental data confirms that turbulence intensities greater than 20% are to be expected in a region above the high-rise building as high as the building itself, prompting doubts on findings of Chapter 4 or literature (Abohela et al., 2013; Toja-Silva et al., 2018) that RANS is suitable to assess the turbulent environment and state limits on the positioning of wind turbines based on turbulence intensity.

Results also confirms that LES is suitable to model a wide range of statistics and competes with wind tunnel testing in accuracy, if a correct balance between the cost-effectiveness of simulations and the provision of suitable inlet turbulence characteristics.

Chapter 6

The effect of integral length scale of turbulence on a wind turbine aerofoil

A significant amount of this chapter has been partly presented in the WES2018 Conference (Vita, Hemida and Baniotopoulos, 2018). Some content is reproduced in Chapter 6 with the permission of the co-authors. In this Chapter, the effect of turbulence intensity and of integral length scale of a turbulent inflow is tested on a wind turbine aerofoil using physical simulation. The turbulent inflow is treated in detail in Chapter 3. For the first time in literature, an aerofoil is tested against a realistic turbulent inlet and the separate effect of turbulence characteristics is considered. The most important finding of this study is that an effect of turbulence on the aerodynamic performance is present even at the largest integral length scales $L/c \sim 3$. This questions the negligibility of turbulence in the atmospheric and built environment when designing a wind turbine and it might explain the lack in performance for urban wind energy.

6.1. Effect of turbulence on bluff bodies and wind energy converters

6.1.1. Motivation (background wind energy deals with turbulence)

The performance of wind turbines (WT) is heavily affected by the installation site. In the built environment, site conditions involve strong signature turbulence, either coming from the wake of obstacles, arising from thermal effects due to the urban heat island, or due to the separated flow pattern in the proximity of buildings. All these configurations have some turbulence characteristics, which can be described with flow parameters such as the mean velocity U , and the aforementioned turbulence intensity I_u and length scale L_u . In Chapter 2, passive grid turbulence has been implemented to generate a variety of turbulent inflows having turbulence intensity I_u and integral length scales L_u , which could be varied independently. The aim of the work was to reach a combination of high turbulence intensity $I_u \sim 15\%$ having a sufficiently large length scale $L_u \sim 30$ cm. Such a combination is necessary to be of any relevance to the urban wind environment, as shown later in Chapter 4 and 5.

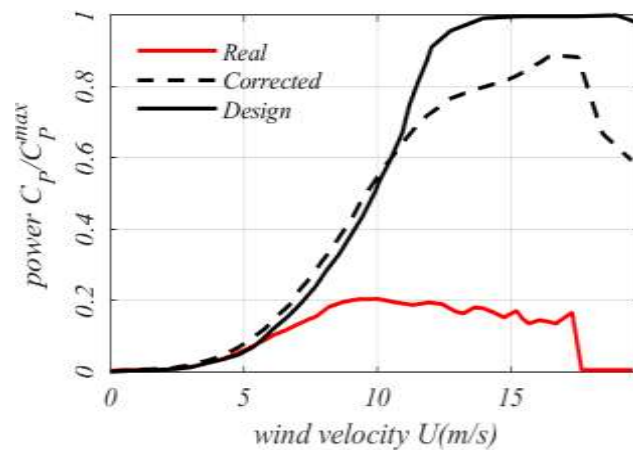


Figure 6.1. Power coefficient of a HAWT as measured, predicted and designed (Pagnini et al., 2015)

A recent study demonstrates convincingly how the performance of Wind Turbines placed in the Urban Environment correlates directly with the enhanced turbulence present in the urban wind inflow (Pagnini et al., 2015). This study is particularly emblematic for urban wind energy as the authors were prone to investigate the amount of power produced by an HAWT and a VAWT placed in the same location, but instead they noticed that it is not really the technology type, which correlates with the power produced, but rather the free stream atmospheric turbulence of the wind. Figure 2.1 shows how turbulence is responsible for a reduction of the available power output of $\sim 80\%$, while available methods to correct

the power curve for the effect of turbulence are ineffective in predicting this reduction (Sunderland et al., 2013).

FST is always present in the ABL, having different characteristics depending on the site of interest. Thus, a wind turbine rotor is to interact with turbulence for its whole service life (Emeis, 2014; Kaimal et al., 1976). WTs placed in unconventional locations such as the urban environment are expected to be significantly affected in their performance by enhanced turbulence (Arnfield, 2003). In fact, its effects are evident in the power output (Milan et al., 2013; St Martin et al., 2016; Sunderland et al., 2013), the structural loading (Frandsen, 2007; Kelly et al., 2014), the development of aeroelastic instabilities (Hansen, 2007), or also fatigue limit state (Toft et al., 2016). All these studies agree that turbulence affects performance and it should be taken into account when considering the positioning of a wind turbine. However, Bak (2007) stresses out how the rotor aerodynamics, i.e. its response to the unsteady atmospheric inflow, is the key feature to address the optimisation of performance. Designing the rotor implies a thorough study on the pressure coefficient distribution along the blades for given flow conditions. Blade Element Momentum (BEM) theory is the industrial methodology to design wind turbine rotors and blades. The method applies simplifying hypotheses on the flow field, and the response output is conveniently corrected to adjust for unsteady conditions, mostly with empirical proven methods. An artificial velocity component called induced velocity w_i accounts for unsteady effects (Hansen et al., 2006). One of the simplifying hypotheses of BEM is the use of the 2D cross-section of blades, i.e. aerofoils, and the distribution of their polars along the blade-span. 2D aerofoil data mostly rely on wind tunnel testing with different velocity inlets and angles of attack, and rare research has been conducted on the evaluation of any effect of turbulence (Tangler, 2002). An interpretation on the effect of FST on wind turbines is therefore to be directly attributed to the behaviour of aerofoils, which is a topic only scarcely addressed in bluff body aerodynamics research.

6.1.2. *Effect of turbulence on bluff bodies*

The interaction of wind turbines and Free Stream Turbulence (FST) is part of the broader topic of bluff body aerodynamics. As briefly addressed in Chapter 1, FST in the inflow is known to have a rather appreciable impact on the aerodynamic performance (Laneville et al., 1975). A recent study confirms

that turbulence strongly affects separation bubbles and vortex shedding frequencies. Inlet turbulence should be by no means neglected when assessing aerodynamic phenomena such as vortex shedding (Mannini et al., 2017). Two basic mechanisms can be identified under which turbulence affects the flow around the bluff body:

- The triggering of transition in the boundary or shear layers;
- Enhanced mixing and entrainment, which increases the thickness of the detached shear layer, resulting in a delayed separation or early reattachment.

The typology of the bluff body may play an important role in the effect of turbulence. However, it has been recognised that a different role is played by the energy carried by the different scales of turbulence in the flow field. Small scales are supposedly responsible for the mechanism ii), while the largest one acts on the overall feature of the flow pattern, such as the wake recovery or the vortex shedding if present (Bearman and Morel, 1983; Nakamura et al., 1988). Arguably, the length scale acts as a trigger of turbulence effect if the integral length scale has a size comparable to the thickness of the boundary or shear layer (Haan et al., 1998)

$$L_u \cong \delta \quad (6.1).$$

Other works have argued that the length scale may also act as a constraint to the effect of turbulence, preventing it, if the length scale is large (Kistler and Vrebalovich, 2006; Ohya, 2004), or rather

$$L_u \gg D \quad (6.2),$$

being D the characteristic length of the bluff body. However, authors are clear in stating that this is more a suggested tendency of results, rather than proven knowledge. In fact, the strong difficulties in providing a controlled turbulent inlet in wind tunnel testing prevents from stating the separate effect of turbulence intensity and integral length scale on bluff body aerodynamics (Bearman and Morel, 1983; Taylor, 1935). Nevertheless, in dealing with the Atmospheric Boundary Layer (ABL), it is common practice to neglect FST as a governing parameter (Simiu and Scanlan, 1986), as (6.2) is normally verified. It is then acceptable to consider large turbulent coherent structures as a fluctuation of the mean flow (Buresti, 2012).

6.1.3. *Effect of turbulence on wind turbine aerofoils*

In Chapter 1, the survey of the literature about the effect of turbulence on wind turbine aerodynamics indicates a direct causal relation between performance and aerofoil aerodynamics. Aerofoils are specifically designed to increase lift while keeping drag to a minimum. An aerofoil is an elongated aerodynamic body (as counterposed to bluff body) having a rounded leading edge (LE) and a sharp trailing edge (TE). The maximum distance between LE and TE is called chord c and is the characteristic length of aerofoils. The angle of attack α between the chord line and the horizontal is the main parameter for the performance of aerofoils. A performant aerofoil is able to increase α while increasing lift, and keeping drag to a minimum. However, a critical angle of attack exists when lift drops, a condition known as stall. The stall mechanism constitute the 2D aerofoil data used in BEM. Other variables affecting aerofoil performance include the Reynolds regime, and the aerofoil surface finish. In aerofoil aerodynamics it is customary to improve performance by acting on the local flow features at LE or TE, for example by trimming the boundary layer by imposing transition with a roughness strip (Buresti, 2012). In parallel with bluff bodies, also aerofoils show response to turbulent inflows. Early studies on the effect of FST on aerofoils confirm that turbulence strongly relates to the performance of aerofoils in terms of maximum lift, stall angle and the presence of a separation bubble (at low flow regimes) (Hoffmann, 1991; Huang and Lee, 1999). In particular, an increase in turbulence intensity enhances the performance of aerofoils, causing a beneficial delay in stall, increasing maximum lift and aerodynamic performance, defined as the ratio between lift and drag. The increased transport of momentum for the boundary layer, acts in a similar way as in bluff bodies to prevent an adverse pressure gradient to cause separation (Burton et al., 2011). Early studies normally focus on a very limited range of turbulence intensities $I_u < 1\%$, as it was of interest whether wind tunnel turbulence backgrounds would affect results. More recently, some studies have been available to specifically address wind turbine blades and the atmospheric turbulence. As BEM only considers the low frequency content of the turbulence spectrum at the inlet of wind turbines, the research question is whether high-frequency energy is able to modify the performance. Aerofoils show insensitiveness to turbulent structures at the inflow (Buresti, 2012), at low angles of attack, i.e. when the flow is attached. As the blade stalls, the effect of turbulence is consistent with early findings of a delayed stall and increase transport of momentum. However, such

an effect is negligible in large length scale turbulence, as stated by Miley (1982). Relevant works are listed together with the experimental setup and the turbulence characteristics used to investigate the effect of FST in Table 6.1. Most of the studies do not provide a clear description of the flow field used in the experiments, as the integral length scale is mostly disregarded, being the intensity the parameter of choice in all studies. However, it is also clear that a clear consensus on the response of aerofoils under atmospheric turbulence is not available and all authors in the mentioned studies auspicate further experiments. Sicot, Aubrun, *et al.* (2006) and Amandolèse and Széchényi (2004) show that turbulence affect the stall mechanism in a stronger way than respectively rotation or oscillations. However, the former is neglected in BEM calculations, while the latter is corrected and accounted for. Maldonado *et al.* (2015) acknowledge the difficulty in studying the effect of turbulence having a length scale larger than the chord length, while stressing how indeed the performance of the rotor increases due to turbulence at the expense of the increased demand to the blade structure due to the increase in drag. Nevertheless it is unclear whether these conclusions hold in real atmospheric turbulence. Swalwell, Sheridan and Melbourne (2004) notice a monotonic trend between the delay in stall and increase in performance with the turbulence intensity for different thicknesses of aerofoils and Reynolds flow regimes.

Table 6.1. Experiments on effect of turbulent inflow on WT blades.
PG/AG Active/Passive grid, pt pressure taps

<i>Authors/year</i>	<i>chord c [m]</i>	<i>grid type</i>	<i>t. int. TI [-]</i>	<i>len. sc. L/c</i>	<i>measures</i>	<i>Notes</i>
<i>Present Study</i>	0.125	PG	0.05- 0.15	0.40- 2.80	40 pt	<i>independently varied</i>
<i>(Amandolèse and Széchényi, 2004)</i>	0.5	PG	0.075	-	25 pt	<i>oscillating aerofoil</i>
<i>(Devinant et al., 2002)</i>	0.3	PG	0.16	-	43 pt	-
<i>(Kosasih and Saleh Hudin, 2016)</i>	0.15	PG	0.29*	-	power	<i>Rot. Blade *close to grid</i>
<i>(Li et al., 2016)</i>	0.14	PG	0.139	-	46 pt	<i>Low Re custom. blade</i>
<i>(Seddighi and Soltani, 2007)</i>	0.25	PG	0.4*	-	64 pt	<i>pt placed at 20deg angle</i>
<i>(Sicot et al., 2006b)</i>	0.3-0.07	PG	0.16	-	43 pt; PIV*	<i>*small blade for PIV</i>
<i>(Sicot et al., 2008)</i>	0.07	PG	0.12	0.88	26 pt	<i>Rotating blade</i>
<i>(Swalwell and Sheridan, 2001)</i>	0.125	PG	0.07	0.56	28 pt	<i>thin aerofoil</i>
<i>(Swalwell et al., 2004)</i>	0.125	PG	0.13	1.30	28 pt	<i>thick aerofoil</i>
<i>(Maldonado et al., 2015)</i>	0.25	AG	0.061	0.60	32 pt	<i>Rough blade</i>
<i>(Wang et al., 2014)</i>	0.1	AG	0.06	0.25	LDA	<i>Low Re</i>

This Chapter uses the passive grid turbulence as studied in Chapter 2 to investigate the separate effect of turbulence intensity and integral length scale on a wind turbine aerofoil at three angles of attack. To the author's knowledge, this is the first time a bluff body or stalled aerofoil is given evidence towards its interaction with independently varied turbulence statistics. The experiment also provides a variability of length scales, namely $L_u/c \sim 2.8$, which is normally not reachable in wind tunnel testing. Combining this characteristics with $I_u \sim 15\%$. Highly qualitative grid generated turbulence is used to show the physical mechanism under which wind turbine aerofoils are affected by free-stream atmospheric turbulence. Section 3.2 shows the experimental methodology and calculation strategy. In Section 3.3, results are presented in terms of the measured surface pressure and related force coefficients. Proper orthogonal decomposition is used to highlight the flow features and identify differences on the modes of fluctuations in the flow field. Section 3.4 proposes a discussion on the possible physical mechanism using Pope's model spectrum, highlighting production, inertial and dissipation terms in the energy spectra. Conclusions are presented in Section 3.5.

6.2. Methodology

6.2.1. Experimental setup: the DU96w180 aerofoil model

The tests have been carried out in the tested in the Wind Tunnel Lab of the University of Liège (Belgium). The model aerofoil has been 3D printed with Selective Laser Sintering (SLS). This technique was chosen as the pressure taps have been modelled in 3D and printed together with the aerofoil geometry. SLS has been used for the mid-span section of the aerofoil, while the rest of the 1.25 m total span consisted of mountable sections printed with the Fused Deposition Modelling (FDM).



Figure 6.2 – Experimental setup at the university of Liège.

Figure 6.2 shows the model in position in the wind tunnel. The model is fitted with a steel bar to hold it together and it is fixed to an aluminium frame screwed to the wind tunnel floor.

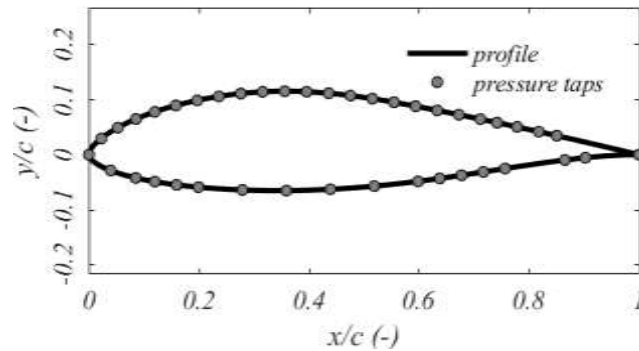


Figure 6.3. The DU 96w180 aerofoil and the position of the pressure taps.

The model is fitted with 40 pressure taps (PT) having a diameter of 0.6 mm. The need of minimising the chord while having a sufficiently high resolution required the embedding of the PTs in the 3D printing of the mid-span section. A monolith is thus built, which hosts the PTs and a 2 cm section of the tubing, which is then fitted with recesses to glue the 1 m long pressure tubing in order to avoid any disturbance to the signal. The tubing is connected to a Dynamic Pressure Measurement System (DPMS, from the company Turbulent Flow Instrumentation), able to measure up to 128 PTs in the range 0-2500 Pa. Figure 6.3 shows the position of the PTs along the aerofoil. The upper section of the aerofoil, called ‘suction’ side, presents 24 taps, while the lower section is called ‘pressure’ side and has the remaining 16 taps, with a larger spacing. A pressure tap has been placed in correspondence of the leading edge, while the value of the pressure at the trailing edge is estimated by extrapolating from closest taps.

The wind turbine aerofoil of choice for the test is the DU 96w180, designed at the Delft University of Technology (Timmer and van Rooij, 2003), shown in Figure 6.3 along with the position of the pressure taps. This aerofoil has been specifically designed for small-scale wind turbines, as it allows for a smooth stall mechanism and it is optimised against noise, while it allows for a sufficient structural stiffness due to its thickness of $0.18c$. The chord of the model is 0.125 m. This value has been chosen in order to achieve a compromise between the possibility of fitting the model with pressure taps and the ability to test large length scale turbulence $L_w/c \sim 2$. In fact, preliminary estimations reported in chapter 2 suggested $L_w \sim 20-25$ cm are reachable with passive grid generated turbulence. This chord length allows for

Reynolds numbers up to $Re \sim 120'000$ being reachable, which is consistent with a small wind turbine operating in the urban environment. The main parameter to be varied throughout the experiment is the angle of attack α (Fig. 1). The angles are chosen so they can be representative of the stall mechanism: pre-stalled 4 deg; post-stalled 14 deg; and full-stalled 24 deg. In the pre-stalled condition, the flow is attached to the aerofoil and a partial limited separation can be observed as α grows. 4 deg has been specifically chosen as the flow is fully attached until the trailing edge. As separation occurs, the lift coefficient c_L increases up to a maximum value $c_{L,max}$, which occurs at $\alpha \sim 10$ deg. c_L does not suddenly drop for this kind of aerofoils, and a post-stall region can be defined $10 < \alpha < 20$ deg, where c_L slowly decays. For $\alpha > 20$ deg, c_L starts to increase again, following a flat plate-like pattern.

6.2.1. *Experimental setup: the inflow*

The novelty of this study is to test separately the effect of turbulence intensity and integral length scale, by controlling the variability of turbulent characteristics in the inflow. The experimental setup of Chapter 3, implementing 4 passive grids and 5 distances, has been developed specifically to obtain a broad variation of the statistics to obtain turbulence combinations having analogous characteristics. This setup has never been achieved using passive grids before this study. In particular the configuration where for a given turbulence intensity several length scales are obtained.

Table 6.2 and Table 3.5 show that 9 Turbulence Intensity vs Integral Length Scale combinations in total could be achieved. In four cases, named LS1-LS4, the turbulence intensity is kept constant to assess the effect of varying the integral length scale. In the other five cases, TI1-TI5, the integral length scale of turbulence is kept constant to evaluate the negligibility of turbulence intensity effects.

Table 6.2 and Table 3.5 also report the power spectral density for the inlet configurations. In the case of LS1-LS4, the low-frequency ends of the spectra overlap, while in TI1-TI5 the maximum occurs at the same frequency for all spectra, which is consistent with the wanted turbulence statistics. More details are given in Chapter 3, where a slightly different grouping of statistics has been performed due to the need of testing the effect of the expansion test section on the statistics.

Table 6.2. Independently varied turbulence intensity and integral length scale, with relevant grid and position with Power Spectral Density of velocity for constant integral length scale (a, b, c, d) and turbulence intensity.

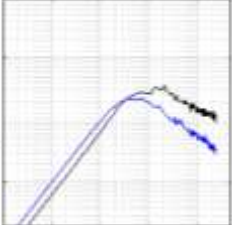
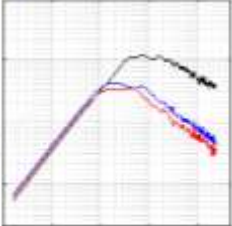
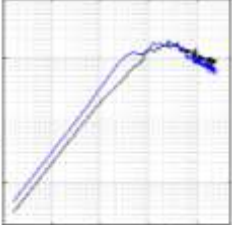
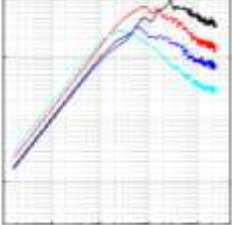
	Spectra	Grid# (dist.)	L_u (m)	L_w/c	I_u (%)
Constant Turbulence Intensity		#3 (4 m) —;	0.11	0.88	5.00
		#3 (9 m) —;	0.175	1.40	
		#2 (4 m) —;	0.145	1.16	7.25
		#4 (9 m) —;	0.29	2.32	
#4 (12 m) —;	0.33	2.64			
	#3 (1.5 m) —;	0.065	1.16	8.50	
#2 (3 m) —;	0.11	2.32			
	#2 (1.5 m) —;	0.08	0.64	14.75	
#4 (3 m) —;	0.135	1.08			
#1 (4 m) —;	0.175	1.40			
#1 (9 m) —;	0.33	2.64			

Table 6.3. Independently varied turbulence intensity and integral length scale, with relevant grid and position.

		Spectra	Grid# (dist.)	L_u (m)	L_u/c	I_u (%)
Constant Integral Length Scale	TI1		#3 (4 m) —; #2 (3 m) —;	0.07	0.56	8.50 14.75
	TI2		#2 (4 m) —; #4 (3 m) —;	0.11	0.88	5.00 8.50
	TI3		#3 (9 m) —; #4 (4 m) —;	0.145	1.16	7.25 14.75
	TI4		#3 (9 m) —; #4 (4 m) —; #1 (4 m) —;	0.175	1.4	5.00 11.00 14.75
	TI5		#3 (9 m) —; #4 (4 m) —;	0.33	2.64	6.50 14.75

6.2.2. Statistical Moments and Proper orthogonal decomposition

The analysis of fluctuating pressure fields may take advantage of various techniques with increasing complexity to highlight the physical behaviour (Carassale and Marré Brunenghi, 2011). In bluff body aerodynamics, the physical behaviour is normally investigated with statistical moments, mainly mean and standard deviation, rarely higher order moments such as skewness and kurtosis. Moreover, the power spectral density (PSD) gives an insight on the time-probabilistic structure of a signal, detecting peak frequencies in the data (e.g. vortex shedding frequency). However, it might be complicated to study the PSD for a whole dataset, and normally the PSD is plotted for a subset or a relevant statistics (such as the force coefficient). Both statistical moments and PSD focus on the time probabilistic properties. In the present study, a set of inlet characteristics with given statistics acts on the flow pattern around the aerofoil, modifying its statistical behaviour. Therefore, also the spatial probabilistic properties might be worth studying, especially to underline different patterns in the different setups. The detection of similarities and differences in the dataset as well as the distinction of separate concurrent phenomena is, after all, the purpose of research in bluff body aerodynamics (Roshko, 1993). The proper orthogonal decomposition (POD, or principal component analysis, PCA) provides a mathematical tool to find typical or repeated spatial and temporal patterns in the data, separating their effect and allowing for the identification of their supposed physical cause (Berkooz et al., 1993; Holmes, 1990; Tamura et al., 1999). However, the mathematical constraints that come with POD might actually even fail in identifying concurring physical behaviours (Baker, 2000). Nevertheless, this technique is chosen for this dataset for its simplicity and for the possibility of generating a reduced order model (ROM) providing the starting point for a more thorough study, which goes beyond the scope of this chapter.

In POD, for a statistical pressure field with N spatial and $M=T/\Delta t$ time-components $p^{(I \times N)}(t^{(I \times M)})$, a modal decomposition might be found, which is represented by the linear combination

$$p(t) = \bar{p} + \sum_{j=1}^N a_j(t) \psi_j \quad (6.3).$$

where $\psi_j^{(I \times N)}$ is the j -th generalised space coordinate or POD mode, $a_j^{(I \times M)}(t)$ is the j -th generalised time coordinate, or POD coefficient. The pressure components are arranged in a matrix $P^{(M \times N)}$. The covariance matrix $Z^{(N \times N)}$ is then computed

$$Z = P^T P \quad (6.4).$$

and the eigenvalue problem is solved to compute the generalised space and time coordinates

$$Z \varphi_j = \lambda_j \varphi_j \quad (6.5).$$

where φ_j is the j -th eigenvector of the eigenvalue problem and λ_j the eigenvalue. Both the POD modes ψ_j and coefficients $a_j(t)$ can be constructed from the eigenvectors, respectively

$$\psi_j = \frac{\sum_{i=1}^N \varphi_j^{(i)} p_j}{\left\| \sum_{i=1}^N \varphi_j^{(i)} p_j \right\|}; \quad a_j(t) = \psi_j p_j \quad (6.6).$$

where $\varphi_j^{(i)}$ is the i -th component of j -th eigenvector, and $z_j^{(I \times N)}$ the j -th column of the P matrix. It is easy to show that the correlation between two coefficients $a_j(t)$ and $a_i(t)$ is zero and therefore

$$a_j^2(t) = \lambda_j \quad (6.7).$$

which shows that the eigenvalues can be used to estimate the energy ratio contained in the ROM.

Figure 6.4 shows that for the present dataset $\sim 90\%$ of the energy is contained in the first 4 modes, while the remaining 36 contain $\sim 10\%$ and for this reason they are discarded in the rest of the chapter.

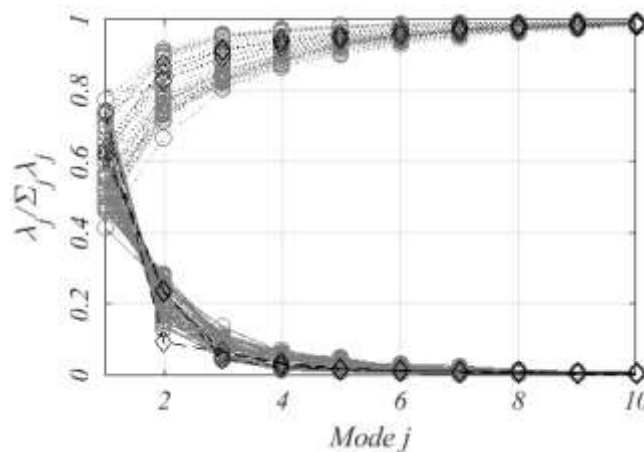


Figure 6.4. Energy Ratio of the Proper Orthogonal Decomposition

6.3. Results: Reynolds effects and stall mechanism

Although this study is not aimed at the stall mechanism specifically, one of the turbulent setups has been used to assess the presence of possible Reynolds effects. In fact, the mean velocity downstream of grids varies depending on the solidity of the grid and the distance to it, as specified in Chapter 2.

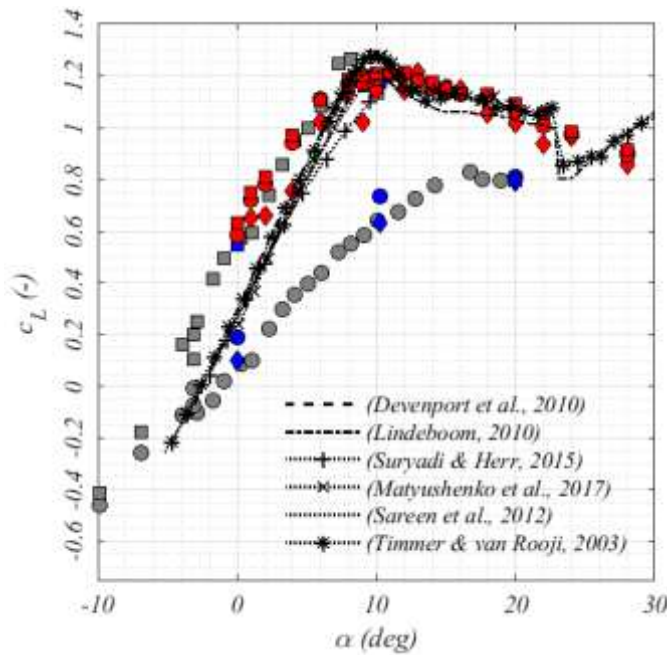


Figure 6.5. Stall Mechanism and comparison with experimental data from literature.

Table 6.4. Reynolds number ranges for the datasets presented in Figure 6.5.

sym	grid	U_r (m/s)	U (m/s)	Re $U c/v$
◆	#3	5	2.6	2.1×10^4
●	#3	10	7.5	6.0×10^4
■	#3	15	12	10.0×10^4
◆	-	5	4.6	4.0×10^4
●	-	8	7.8	6.7×10^4
●	-	10	9.5	7.9×10^4
■	-	12	11.8	10.0×10^4
■	-	15	14.5	12.0×10^4

Figure 6.5 shows the mean lift coefficient against the angle of attack for a variety of configurations as specified in Table 6.4. The Reynolds number of the experimental dataset varies from 21000 to 120000. Such range is limited to small wind turbines in full scale and therefore relevant to urban wind energy (Rezaeiha et al., 2018). Figure 6.5 compares the present dataset with results available from literature for much higher Reynolds ranges varying from 1 to 3×10^6 (Devenport et al., 2010; Lindeboom, 2010; Matyushenko et al., 2017; Sareen et al., 2012; Suryadi and Herr, 2015; Timmer and van Rooij, 2003). A strong Reynolds effect is noticeable in the absence of turbulence when $\alpha < 20$ deg. However, when $Re \sim 1 \times 10^5$, such an effect disappears as c_L is analogous to the experimental data from literature (Freudenreich et al., 2004). In the turbulent case, the Reynolds effect is completely absent, and therefore the mean velocity is not adjusted to match exactly the whole dataset: as shown in Chapter 2 turbulence

characteristics are insensitive to the mean velocity. Figure 6.5 suggests that in the presence of turbulence, an aerofoil behaves similarly to a bluff body with respect to Reynolds effects even in the attached flow region. This means that under a turbulent inlet the aerodynamic performance could be investigated regardless of Reynolds effects. Unfortunately, this study has not been designed to shed light on Reynolds effects under a turbulent inflow. However, it could provide a motivation for future studies as if results might be confirmed then a new generation of turbulence-friendly aerofoil might be designed hence overcoming the diffused opinion that turbulence harms wind energy.

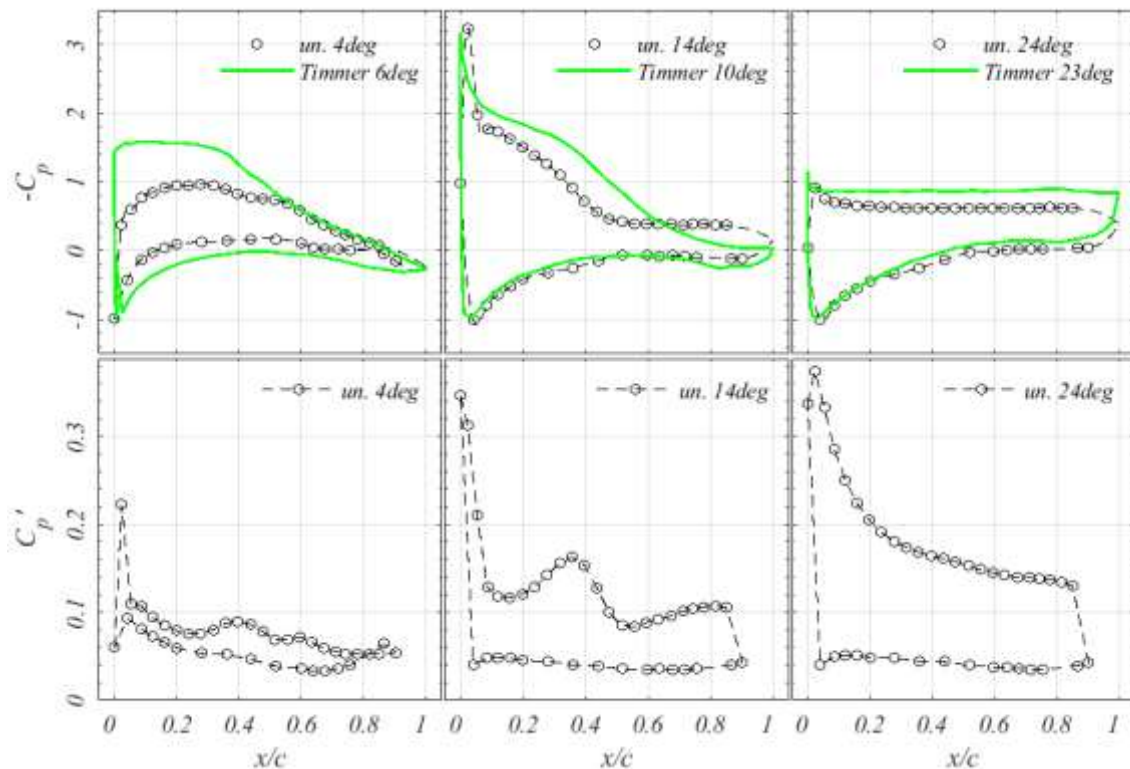


Figure 6.6. Undisturbed case. (Top) Mean surface Pressure Coefficient for 3 Angles of attack used in this study, compared with results from (Timmer, 2010; Timmer and van Rooij, 2003).

(Bottom) Standard deviation of surface pressure coefficient

6.4. Undisturbed case

Figure 6.6 shows the effect of the angle of attack for the chosen aerofoil in undisturbed flow conditions. The present experimental dataset is compared with pressure coefficient distributions as available in literature for $Re \sim 3 \times 10^6$ (Timmer, 2010; Timmer and van Rooij, 2003). The mean pressure c_p is shown together with its standard deviation c_p' . Results in the present dataset compare quite well to results in literature. For $\alpha = 4$ deg, the c_p shows a monotonic trend which indicates the absence of separation. The

local maximum at $x/c \sim 0.55$ might occur due to a separation bubble which spans the distance between the two local maxima of c'_p , i.e. $0.4 < x/c < 0.6$. The formation of separation bubbles might occur at low angles of attack, if the boundary layer is not tripped as in this case, and this pattern might explain the slight deviation of the stall mechanism at low angles of attack shown in Figure 6.5. When $\alpha = 14$ deg, a more pronounced local maximum can be observed at $x/c \sim 0.35$. As α increases, the possible separation bubble which might occur moves upstream as the adverse pressure gradients of the flow become more pronounced. This is the condition when the maximum lift is reached. For $x/c > 0.5$, c_p shows a plateau which might indicate a region of separated flow. Such a plateau runs throughout the chord length in the case of $\alpha = 24$ deg, with no local maxima for c'_p , indicating the post-stall behaviour. A peak in the pressure coefficient can be observed at $x/c \sim 0.02$ for 14 and 24 deg, close to the stagnation point. Also c'_p shows a peak for all cases, but at the next pressure tap at $x/c \sim 0.05$. This is due to the fluctuating flow downstream of the stagnation region.

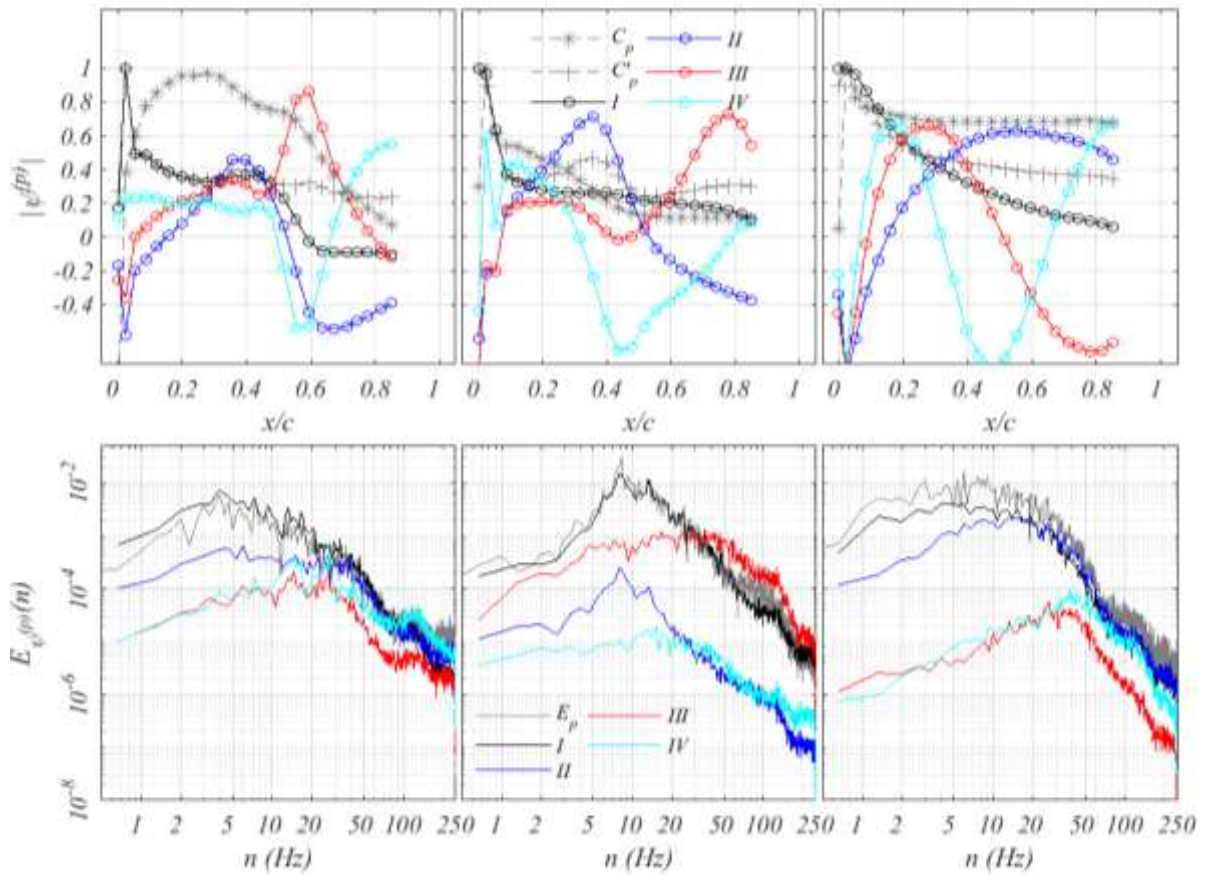


Figure 6.7. (Top) Proper Orthogonal Decomposition of the undisturbed case, spatial generalised modes. (Bottom) energy spectra of the time generalised coordinates. Comparison with undisturbed case

In order to underline the physical mechanism of stall for this aerofoil, proper orthogonal decomposition is carried out and shown in Figure 6.7. 4 out of 40 spatial generalised modes $\psi^{(p)}$ are shown along with normalised mean pressure and standard deviation. Also the energy spectra for the time generalised coordinate is shown for the three angles of attack. It is evident that most of the energy is represented by the first mode only, which shows a peak close to the leading edge, gradually degrading towards the trailing edge. This peak is sharper for low angles of attacks. The shape of the first mode resembles closely the standard deviation. Mode II is the reattachment mode, as its maximum corresponds to the position of the separation bubble if present. This mode always resembles the first mode in terms of the frequency distribution. Modes III and IV are more difficult to interpret, maybe because this is a lift device. Nevertheless a peak in the frequency at ~ 21 Hz is noticeable, which is not visible in the energy spectrum of the recomposed signal. Such a peak might highlight the natural frequency of the model, which showed some vibrations during testing. However, the energy present in these last two signals is negligible, and it might be assumed that these modes do not highlight any particular physical behaviour.

6.5. Effect of turbulence in attached flow conditions

In literature, aerofoils are considered immune from turbulence effects as they are more often implemented with attached flow conditions. When the flow is attached turbulence is more likely to trigger early transition, rather than enhance mixing with the boundary/shear layer. This holds especially when an adverse pressure gradient is absent. This is the case for the present experiment at $\alpha=4$ deg. Both Figure 6.8 and Figure 6.12 do not indicate that turbulence is affecting the pressure distribution. This is also the case for the pressure side of the aerofoil, where the flow is attached and virtually no variation in the pressure distribution is noticeable due to turbulence in the inflow. This matches results from literature for aerofoils in attached flow conditions (Amandolèse and Széchényi, 2004; Hoffmann, 1991; Maldonado et al., 2015). For this reason, the 4 deg angle of attack configuration is not discussed any further in this chapter, and results are just shown in the Figures Figure 6.8 to Figure 6.15 for reference. For the same reason also results about the pressure side of the aerofoil are omitted, as an adverse pressure is absent in this region of the aerofoil and pressure measurements show that turbulence does not affect the distribution on the pressure side.

6.6. Effect of turbulence intensity on surface pressure

This Section reports on statistical moments for the pressure time histories for the cases T11 to T15, where the integral length scale L_u is kept constant to study the effect of turbulence intensity I_u (

Table 6.2). Although reference is made only to the suction side, results on the pressure side are included in Figure 6.8 for the mean pressure coefficient c_p . Figure 6.9 shows the standard deviation c'_p , while Figure 6.10 and Figure 6.11 show respectively the skewness Sk_p and the kurtosis Ku_p of the pressure coefficient. Of the *five* shown cases, *three* configurations are discussed, depending on the ratio L_u/c .

6.6.1. Small length scale $L_u/c < 0.6$

It is common opinion that a small integral length scale is more effective in triggering an effect on statistics, as the turbulent inflow is easily entrained in the aerofoil boundary layer. In fact, this is not what is noticeable in the present study. Figure 6.8 shows no noticeable effect for c_p at 4 and 14 deg angles. At $\alpha=24$ deg, stall delay takes place and an increased peak in c_p is noticed close to the leading edge for higher I_u . c'_p is affected by I_u close to the leading edge, however the effect disappears for $x/c > 0.5$ due to the small L_u . No effect is noticeable in c'_p for $I_u < 10\%$.

6.6.2. Length scale close to chord length $0.8 < L_u/c < 1.4$

As $L_u \sim c$ a clearer pattern on the effect of I_u is noticeable. Turbulence significantly delays separation, as c_p shows an increased peak at the leading edge in all reported cases. The amplitude of this peak is directly correlated with I_u . For $I_u < 10\%$, the effect of turbulence is negligible, as no significant peak close to the leading edge is noticeable in c_p . However, this is not the case for c'_p , as an effect can be noticed for $I_u > 5\%$, and a direct coincidence between turbulence intensity and pressure standard deviation can be stipulated. For $x/c > 0.5$ if there is an effect all values tend to collapse on a curve, regardless of turbulence intensity. The higher moments Sk_p and Ku_p recover to normal values for all turbulence intensities, regardless of the value. Skewness does not normalise close to leading edge if $I_u < 8\%$. The higher the angle of attack, the lower the skewness goes, while the higher the turbulence the more constant skewness and kurtosis tend to behave in the chord-wise direction.

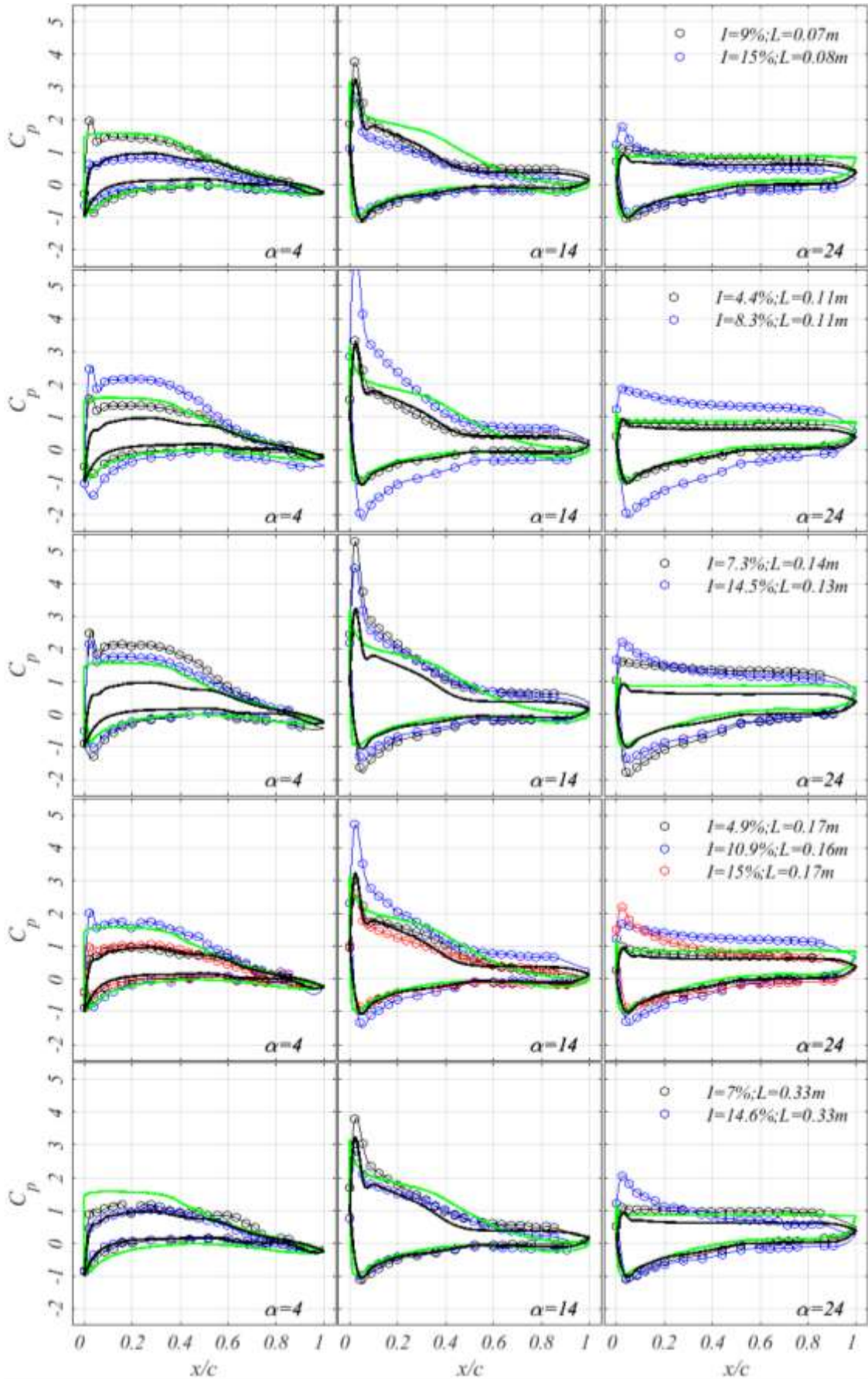


Figure 6.8. Mean pressure coefficient on the aerofoil. Compared with undisturbed case and results from Timmer.

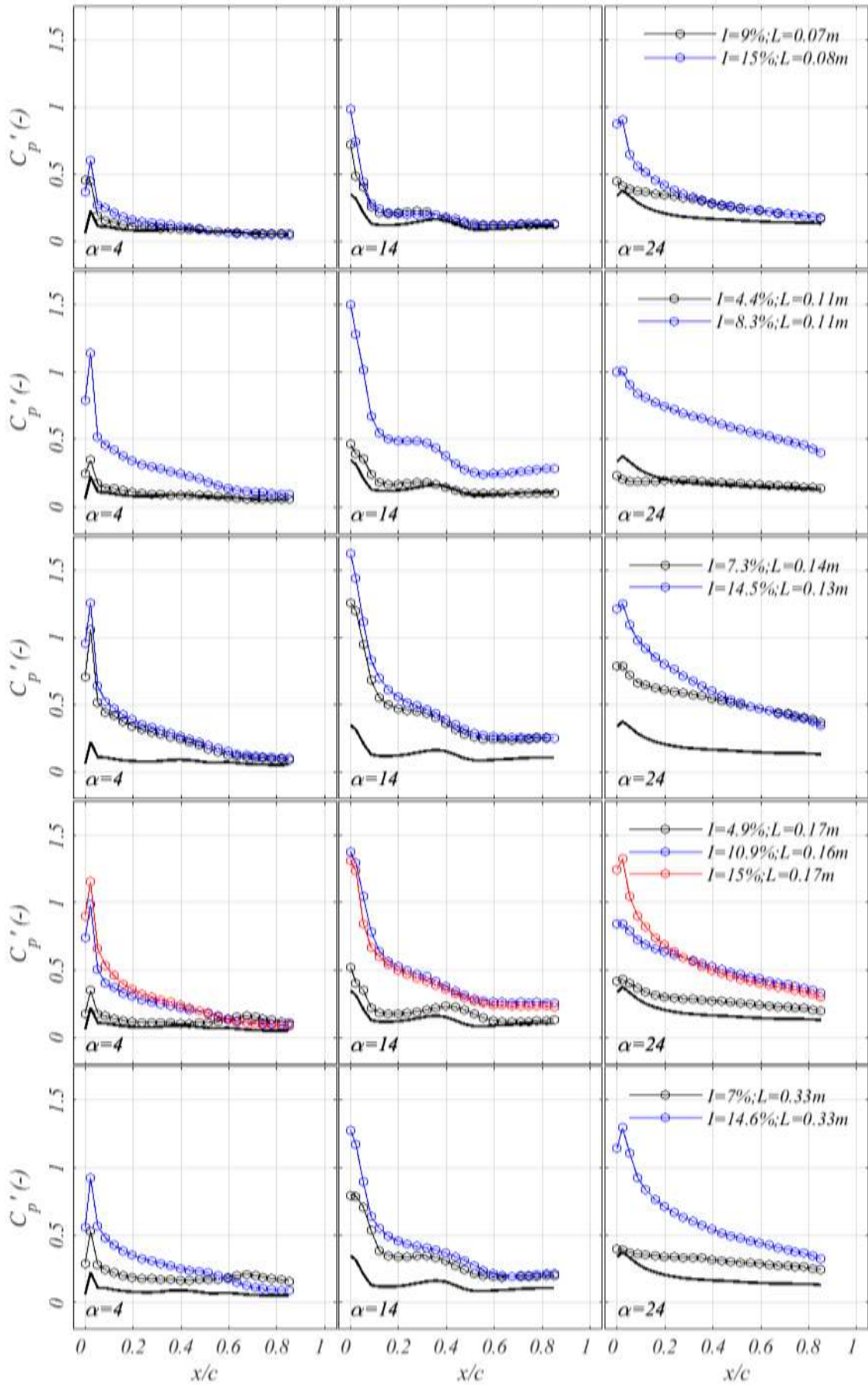


Figure 6.9. Standard deviation of pressure coefficient

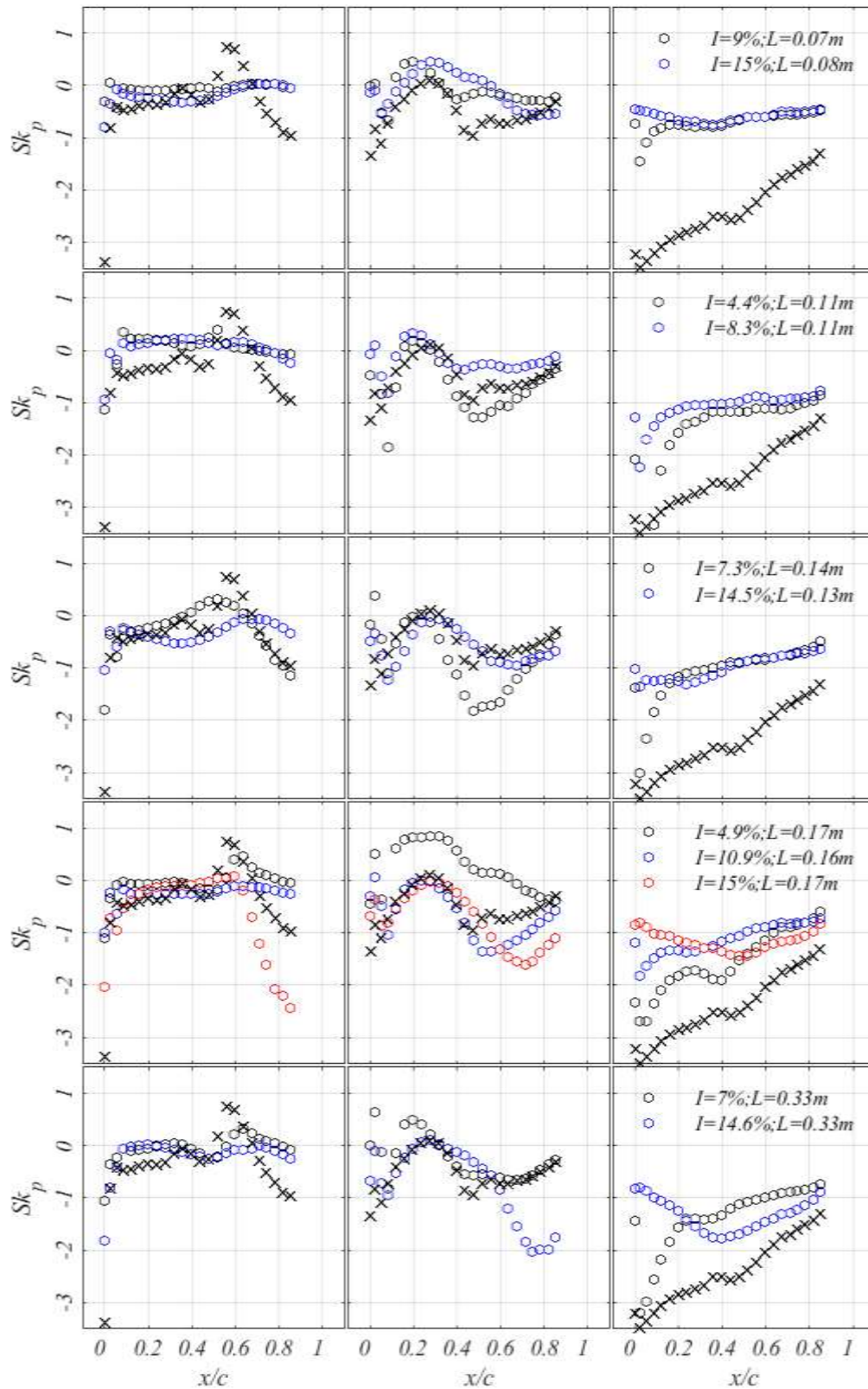


Figure 6.10 skewness of pressure coefficient

6.6.1. Large Length Scale $L_u > 2.6$

Contrary to indications in literature, the effect of turbulence is still present for $L_u \sim 3c$. No significant deviation is noticeable with the case $L_u = 0.17$ m and separation is still delayed if $I_u > 10\%$.

However, c'_p is enhanced in TI3 for $I_u \sim 7.5\%$, while for the same I_u an effect is not present for TI5. This might indicate that indeed L_u might affect the critical intensity under which effects of turbulence start to take place. Turbulence intensity is still able to normalise higher moments, although to a lesser extent, indicating that the entrainment of the flow in the boundary layer is less efficient for large L_u .

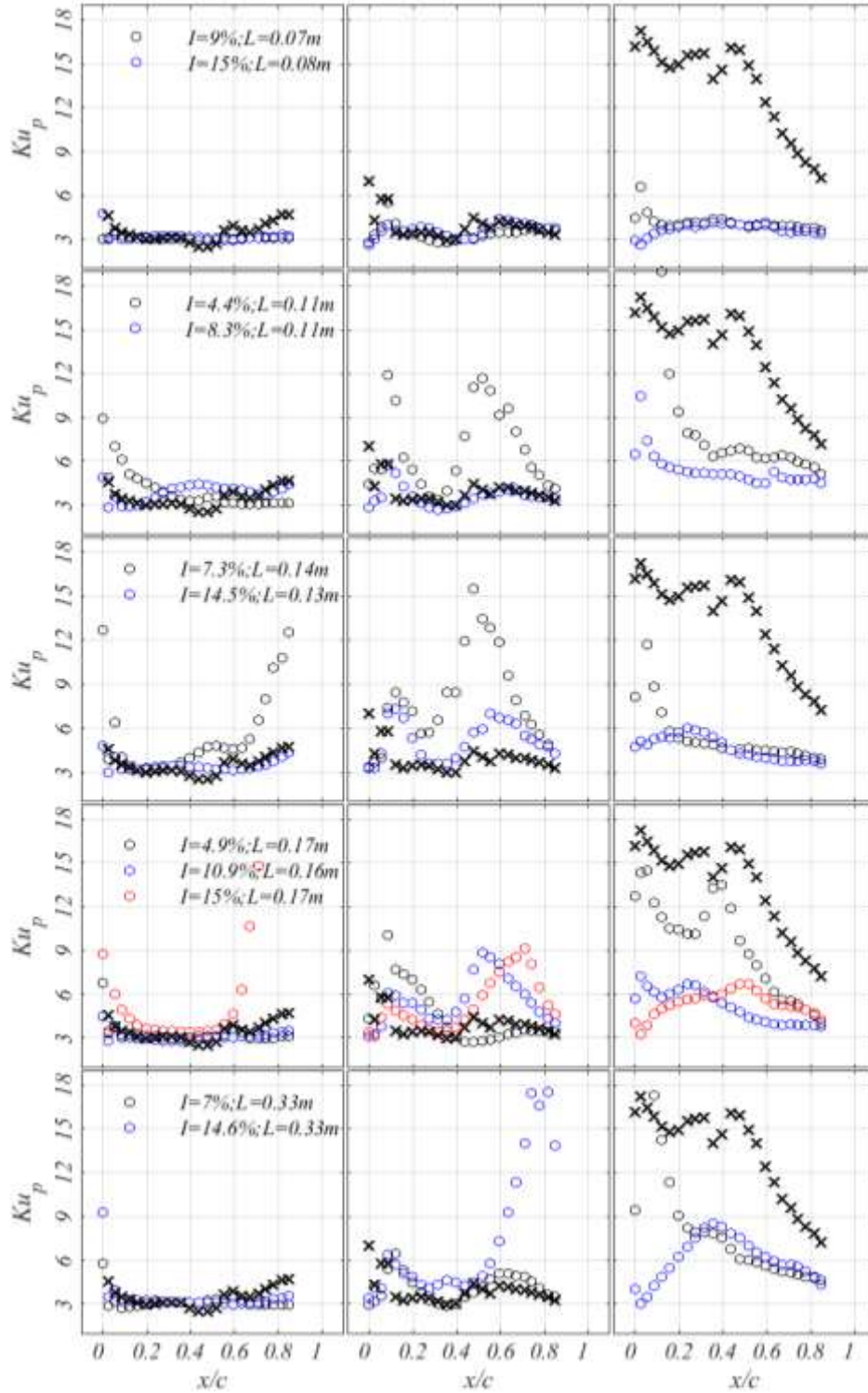


Figure 6.11. kurtosis of pressure coefficient

6.7. Effect of integral length scale on surface pressure

This Section reports on statistical moments for the pressure time histories for the cases LS1 to LS4, where I_u is kept constant to study the effect of L_u (Table 3.5). Figure 6.12 shows c_p , Figure 6.13 shows c'_p , while Figure 6.14 and Figure 6.15. Figure 6.11 show respectively Sk_p and Ku_p , as in the previous.

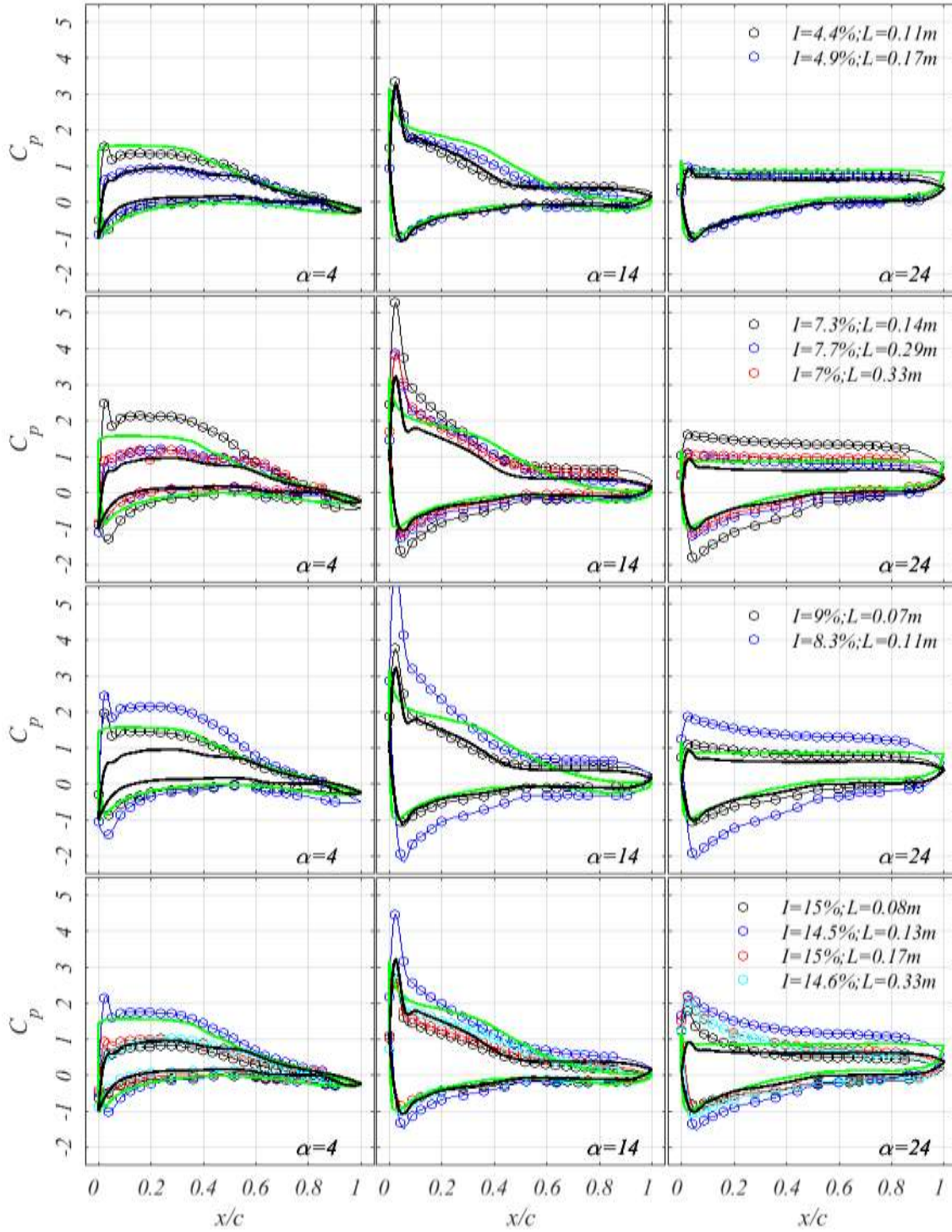


Figure 6.12. Mean pressure coefficient c_p for the three angles of attack and LS1-4.

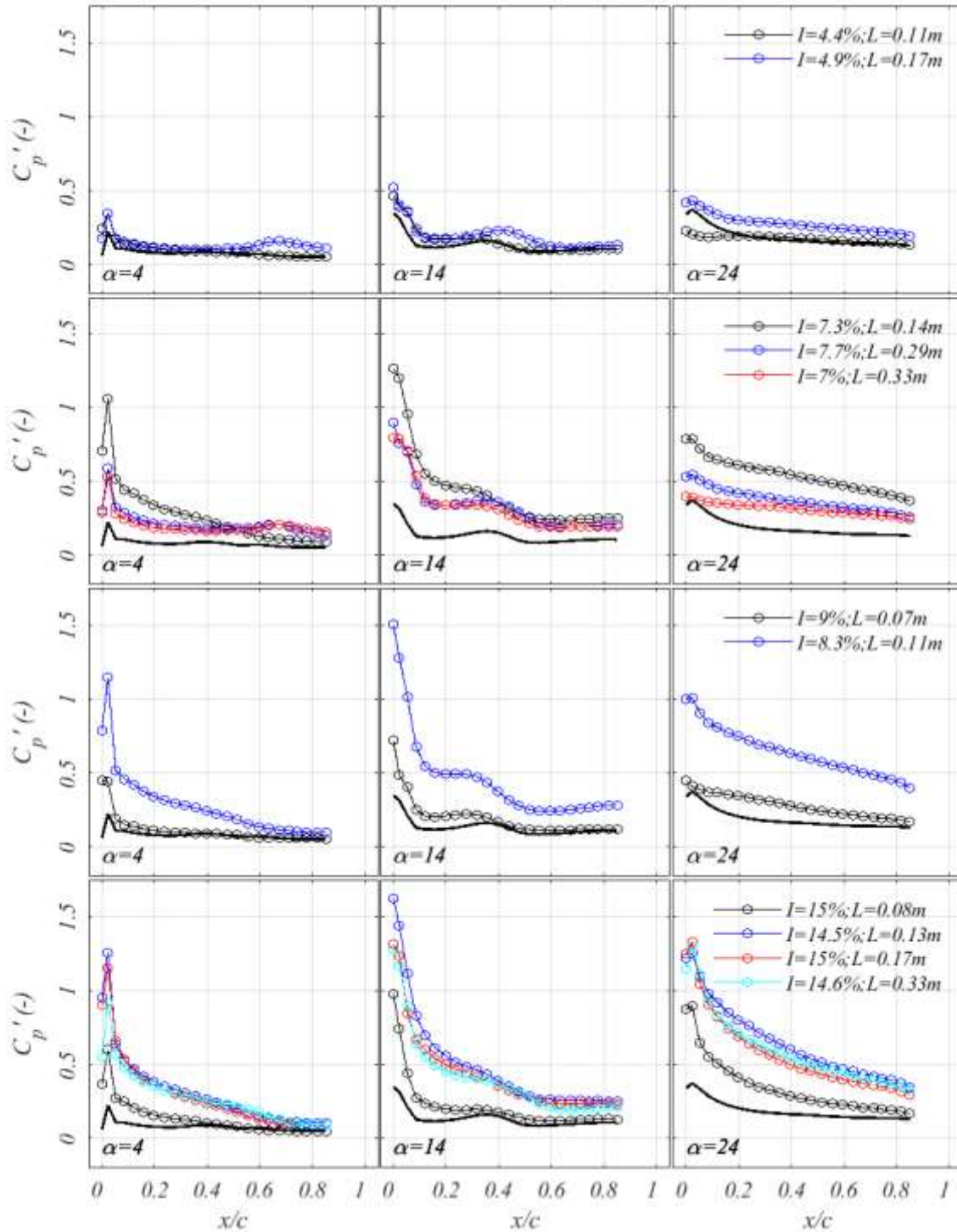


Figure 6.13. Standard deviation for the three angles of attack and LSI-4

6.7.1. Low Turbulence Intensity $I_u < 5\%$ (LS1)

When $I_u < 5\%$ no appreciable difference with the undisturbed case is noticeable in \bar{c}_p or c_p' for all angles of attack. However, both Sk_p and Ku_p show a tendency to recover towards normal values in the turbulent case, as in the whole dataset, and this tendency is stronger for $\alpha = 24$. Consistent to findings shown in

the previous section, L_u affects the higher moments, and results are closer to the undisturbed case for larger length scales.

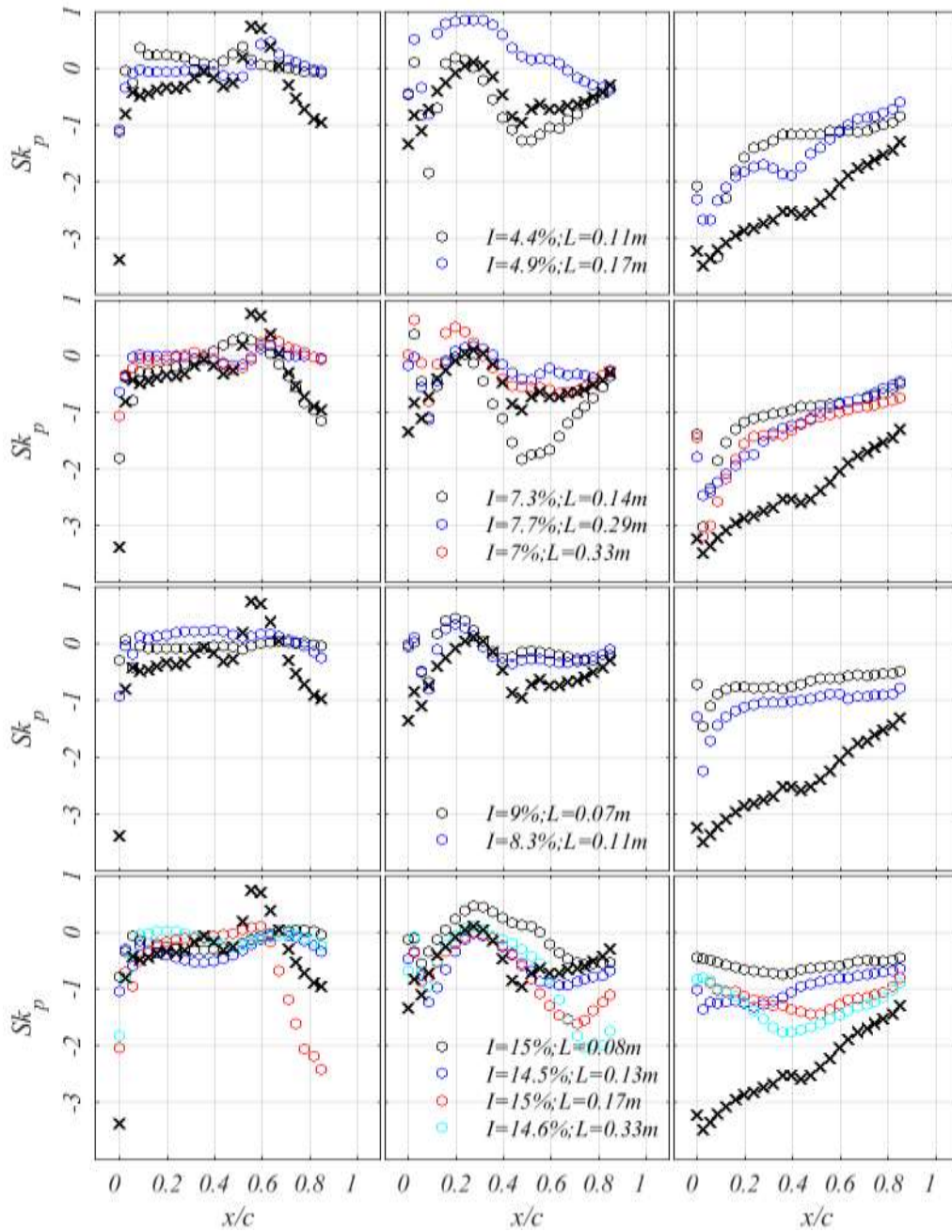


Figure 6.14. Skewness for the three angles of attack and LS1-4

6.7.2. Medium Turbulence Intensity $7 < I_u < 10$ %

As I_u increases, L_u does not seem to affect c_p . As for c'_p , a smaller L_u seems to enhance fluctuations of the surface pressure, although this effect is not monotonic as for $L_u/c < 1$ fluctuations are also damped. As for the higher moments, the same conclusions as in the previous subsection are found, a larger length scale hinders the normalising of skewness and kurtosis.

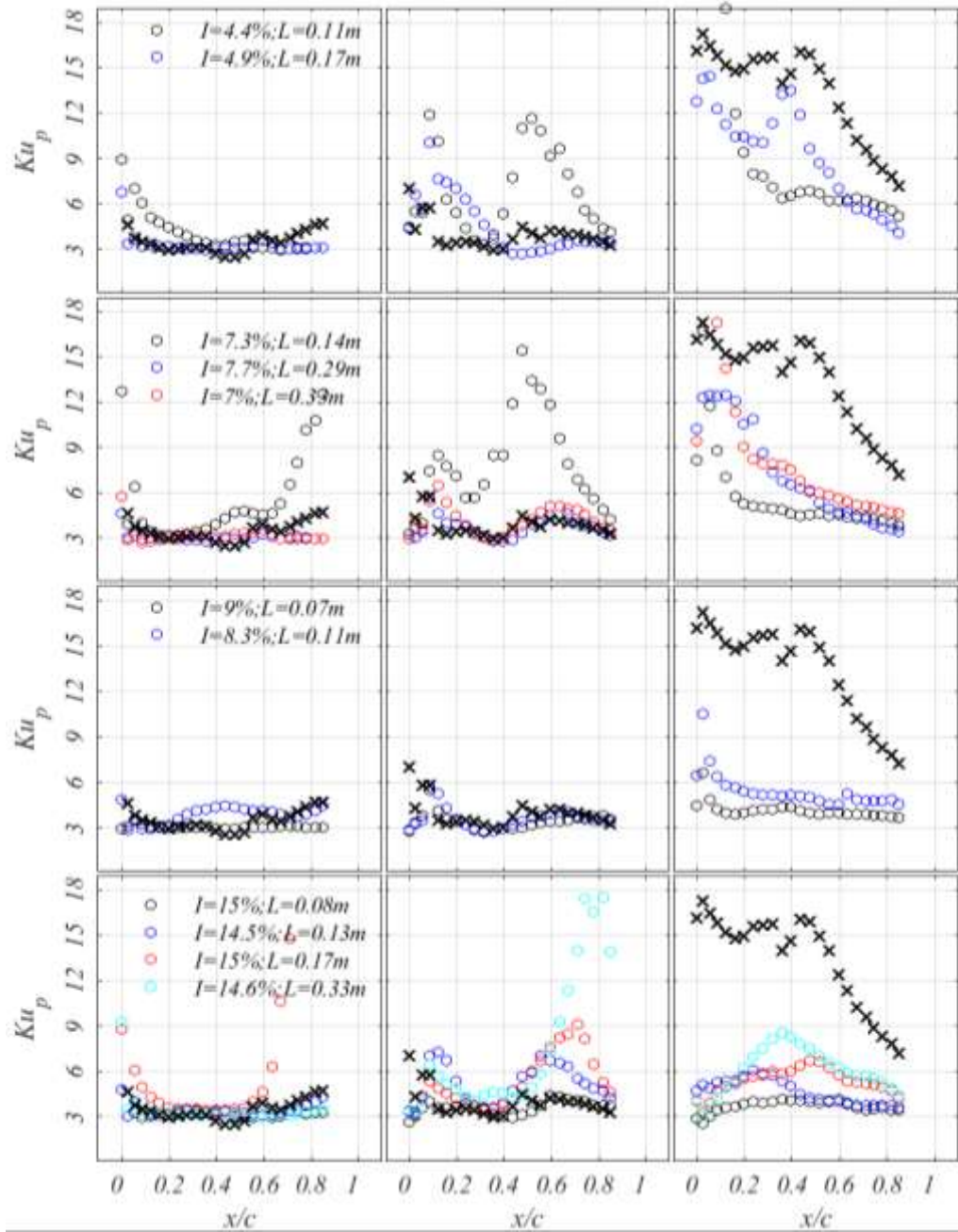


Figure 6.15. Kurtosis for the three angles of attack and LSI-4

6.7.3. High Turbulence Intensity $I_u > 14\%$

A very strong stall delay is noticeable for $I_u > 14\%$, but the length scale seems to play a rather small role, as its variability does not show a significant effect on c_p , although the effect may seem to increase for larger length scales. The effect of the length scale on c'_p seems to now disappear, as for $L_u > 0.1$ m the same increased fluctuations in the pressure field can be observed. For $L_u < 0.1$ m, this effect is weakened, showing that L_u acts as a trigger to the effect of turbulence.

As for the higher moments, a distinct effect of the length scale is noticeable, as the normalising effect increases monotonically with a decreasing length scale.

6.8. Separation point position

The analysis of the statistical moments can be enhanced with the computation of a common parameter, which can be easily checked against his interaction with turbulence, such as the separation position. In absence of measurements about the boundary layer profile over the aerofoil or its skin friction, as in the present case, it is not possible to give an accurate estimate of the separation position. However, a necessary and not sufficient condition for separation is the negligibility of the chord-wise pressure derivative $dc_p/dx \sim 0$. The Stratford separation criterion is based on the derivative and it imposes a condition on the arrangement of the turbulent boundary layer around the body at separation by comparing it to that of a flat plate (Cebeci et al., 1972; Stratford, 1959). It states:

$$x_S \equiv c_p \sqrt{x \frac{dc_p}{dx} (10^{-6} Re_x)^{-1/10}} \sim 0.4-0.5 \quad (6.8).$$

where $Re_x = xU/v$, and 0.4-0.5 is a threshold based on the von-Karman constant $\kappa = 0.41$.

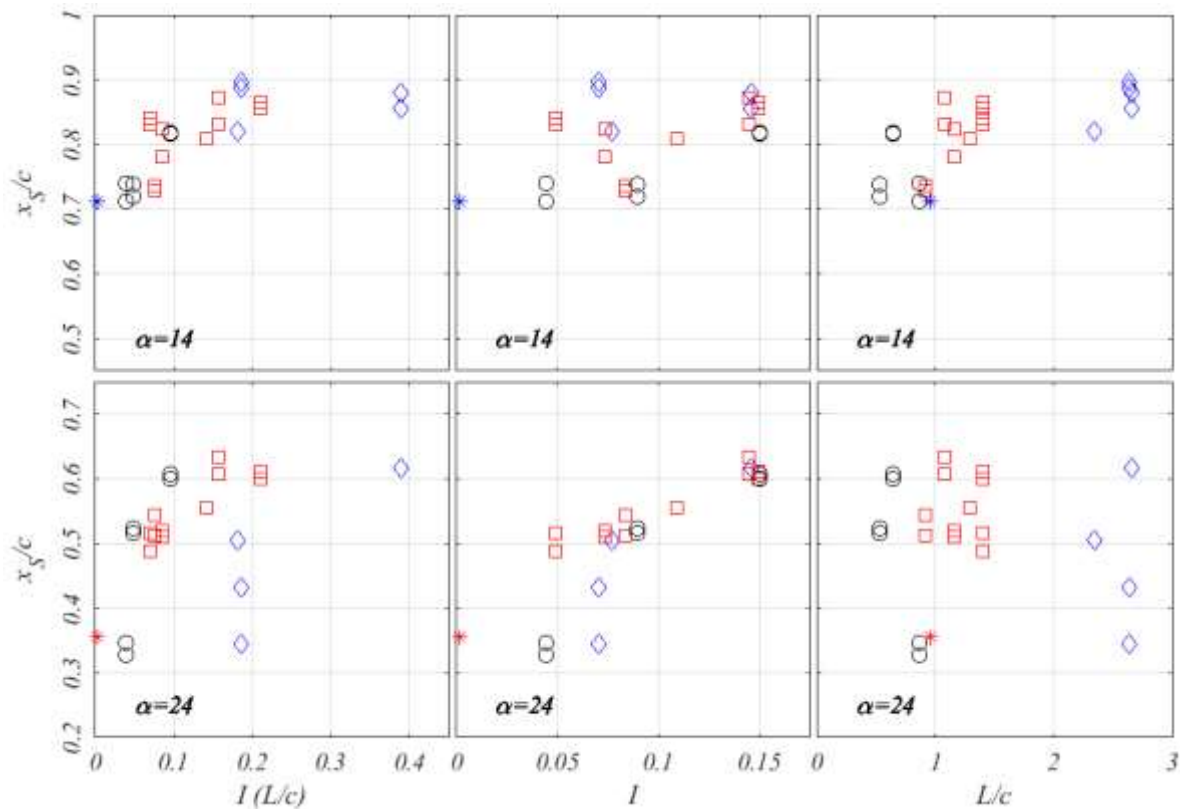


Figure 6.16. Effect of turbulence on Separation Point x_S for 4 and 24 deg. Results marked as in Table 6.5.

Figure 6.16 shows the separation point as found with (6.8 for 14 and 24 deg. Results are marked according to the legend reported in Table 6.5. For the 14 deg configuration, both L_u and I_u seem to have a similar effect, and for this reason the turbulence parameter is introduced as it better fits the data

$$I_u (L_u/c)^n \quad (6.9),$$

where n is an exponent normally taken as unitary (Bearman and Morel, 1983).

Table 6.5. Legend for Separation Points (Figure 6.16) and Force coefficients (Figure 6.17 and following).

Symbol	Case
◇	$L_u/c > 2.6$
□	$0.8 < L_u/c < 1.4$
○	$L_u/c < 0.6$

Results show that separation is delayed from $x_s/c \sim 0.7$ to ~ 0.9 and this effect seems to be triggered by the turbulence intensity and enhanced by the length scale, as separation increases monotonically. When $L_u/c > 2.3$, the effect seems to reach an asymptote. When $\alpha = 24$ deg, separation is also delayed from ~ 0.35 up to ~ 0.6 , however the effect seems uncorrelated with the length scale, while it grows proportionally to the turbulence intensity. The turbulence parameter shows that for $L_u/c > 2.3$, stall delay might not be influenced strictly by turbulence intensity, as other mechanisms might occur with a growing adverse pressure gradient. From Figure 6.16, a critical turbulence intensity might be defined as

$$I_{u,c} \sim 7\% \quad (6.10),$$

when the effect of turbulence steadily delays separation, regardless of L_u/c . If $I_u < 7\%$, the effect of turbulence is also affected by the length scale and only present when $L_u \sim c$.

6.9. Force coefficients

The force coefficients are calculated by integration over the aerofoil surface of the pressure coefficient. The coefficient of Lift c_L , Drag c_D and Moment c_M are defined respectively based on the vertical and horizontal direction, and the resultant around a pole taken at $x = c/4$ as customary in aeronautics. Strictly speaking c_D should be referred to as form drag, as the skin friction coefficient is not included in its calculation. Pressure time histories are integrated to obtain forces time histories, whose statistical moments are considered in the following for the 14 and 24 deg configurations.

6.9.1. Post-stall $\alpha=14$ deg

Figure 6.17 shows the variability of force coefficients against the turbulence parameter for $\alpha=14$ deg. Data is marked according to Table 6.5. c_L shows a dual behaviour as most of the data is aligned to the undisturbed case. However, as $L_u \sim c$, the effect of turbulence is enhanced, decreasing as $I L/c$ increases. c_D seems instead to have a linear relation with $I L/c$. In literature, turbulence is normally associated with an increase in Drag (Milan et al., 2013). However, the form drag shown in Figure 6.17 drops as long as turbulence is present to then increase monotonically as the turbulence parameter increases. c_M shows a similar behaviour to c_L , with a dual response to turbulence enhanced if $L_u \sim c$.

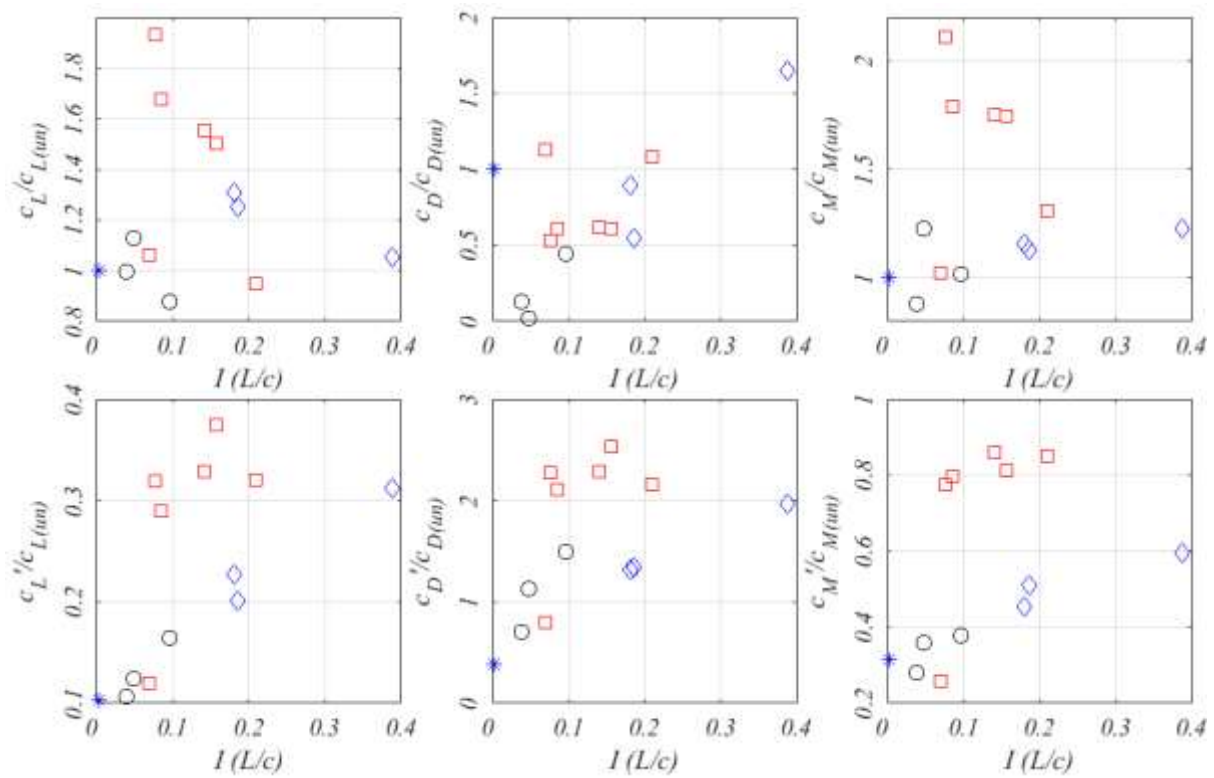


Figure 6.17. Normalised force coefficients for $\alpha=14$ deg against turbulence parameter $I(L/c)$.

Figure 6.17 also shows the standard deviation of the force coefficients, normalised against the undisturbed force coefficients. The effect of turbulence is here more recognisable as a linear relation can be observed with $I(L/c)$ for the whole dataset, with the exception of data taken when $L_u \sim c$, which show an enhanced standard deviation.

Figure 6.18 shows the probability density distribution for all turbulent cases, compared with the undisturbed case. In all cases, turbulence normalises the distribution, consistently with results on pressure distribution statistical moments.

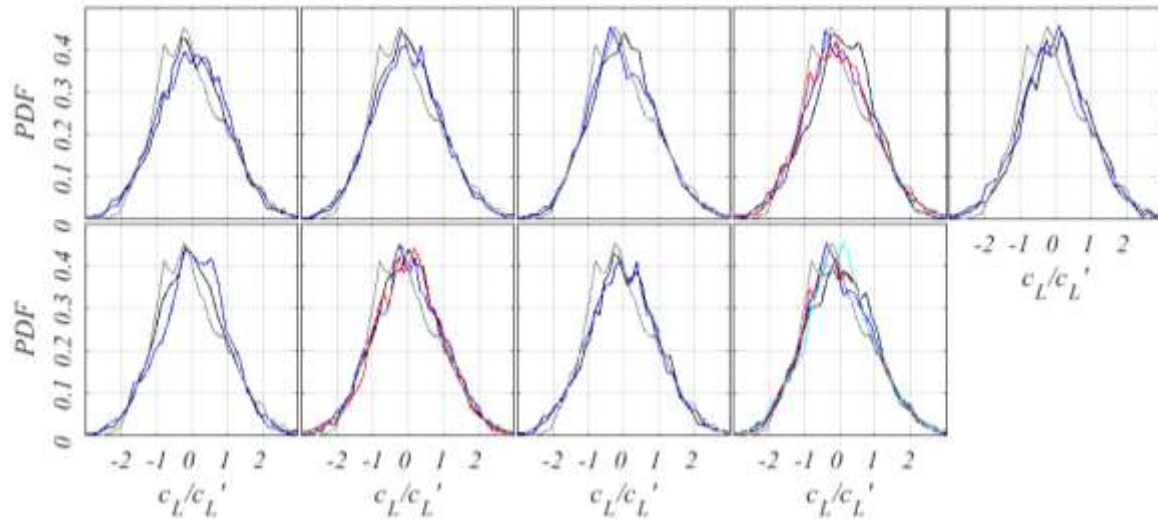


Figure 6.18. Probability Density Function of Lift coefficient for cases as in Table 6.2 and Table 3.5.

6.9.2. Full-stall $\alpha=24$ deg

Figure 6.19 shows the force coefficients for the 24 deg configuration. All the force coefficients show a dual behaviour, where the effect of turbulence is either absent or enhanced. c_L is however constantly increasing with $I(L/c)$ showing the beneficial effect of turbulence in delaying stall. When $L_u \sim c$, the same behaviour occurring for 14 deg is noticeable, a steep increase in lift after at $I(L/c) \sim 0.08$, with a linear decrease until the alignment valid for all other L_u/c is intersected.

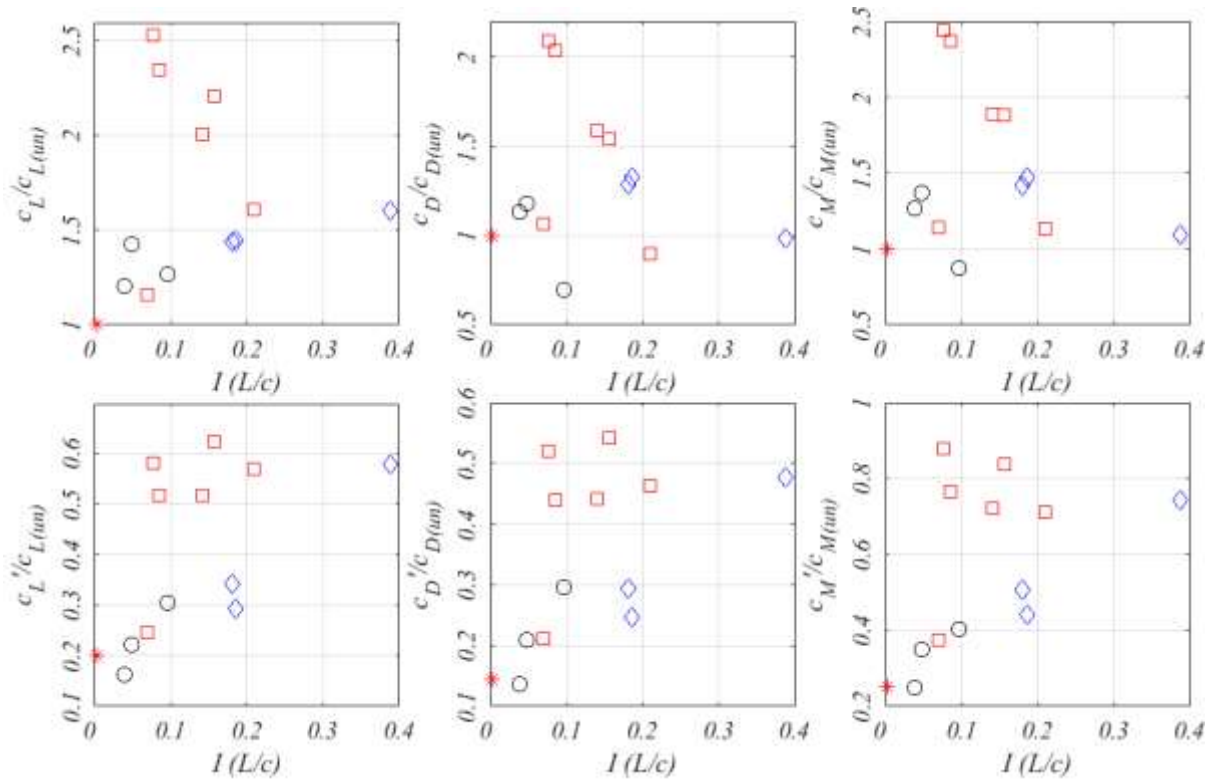


Figure 6.19. Normalised mean and standard deviation of force coefficients against turbulence parameter $I(L/c)$.

The same behaviour can be observed for c_D and c_M , which however do not show a particular trend for cases other than $L_u \sim c$. The force standard deviation follows a pattern similar to 14 deg, where a steep increase in fluctuations occurs and a more pronounced increase is noticeable for $L_u \sim c$ in all cases.

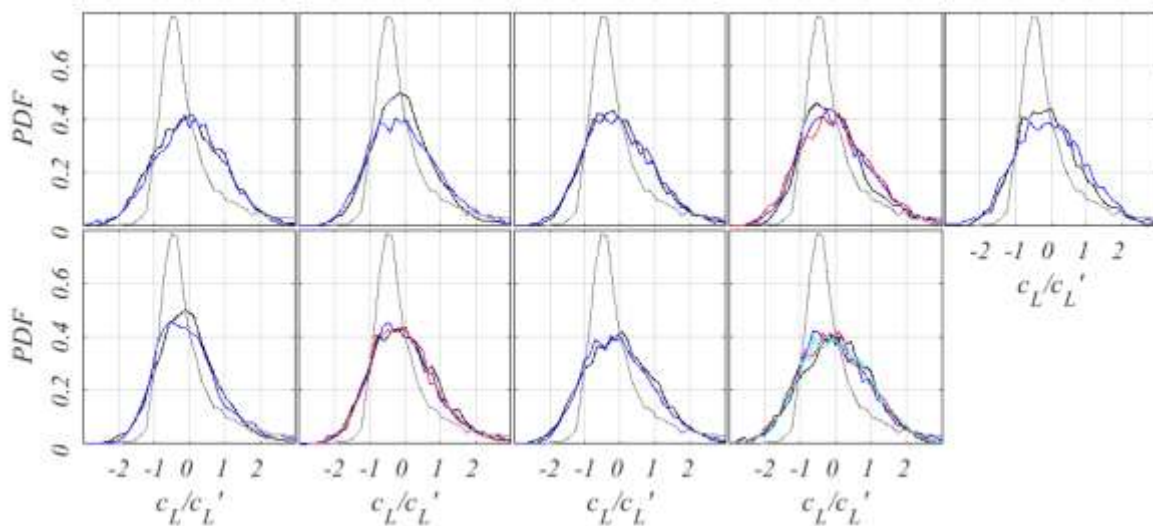


Figure 6.20. Probability Density Function of Lift coefficient for cases as in Table 6.2 and Table 3.5.

Figure 6.20 shows the PDFs of the lift coefficient for all cases. The effect of turbulence normalises the distribution in all cases, although a slightly negative skewness is noticeable especially for low

turbulence intensities (LS1, LS2). This agrees to observations made for the higher order statistical moments made in the previous sections.

6.10. Proper Orthogonal Decomposition

In this section, POD is applied to identify patterns in the pressure field. The first 4 POD modes, are shown in Figure 6.21 for the cases T11-5. Although a physical interpretation is difficult to give, in general the first mode (first row of the figure) closely resembles the standard deviation (Figure 6.9), as the strong fluctuation peak at the leading edge gradually reduces towards the trailing edge. Of all configurations, the black lines represent data having the lowest turbulence intensities. For this data, the first mode deviates from the undisturbed configuration, possibly suggesting a different physical mechanism, where the maximum is not at the leading edge but further downstream at around $x/c \sim 0.3$. The second mode is instead consistent in shape for all cases, with a minimum point moving towards the leading edge as turbulence intensity increases.

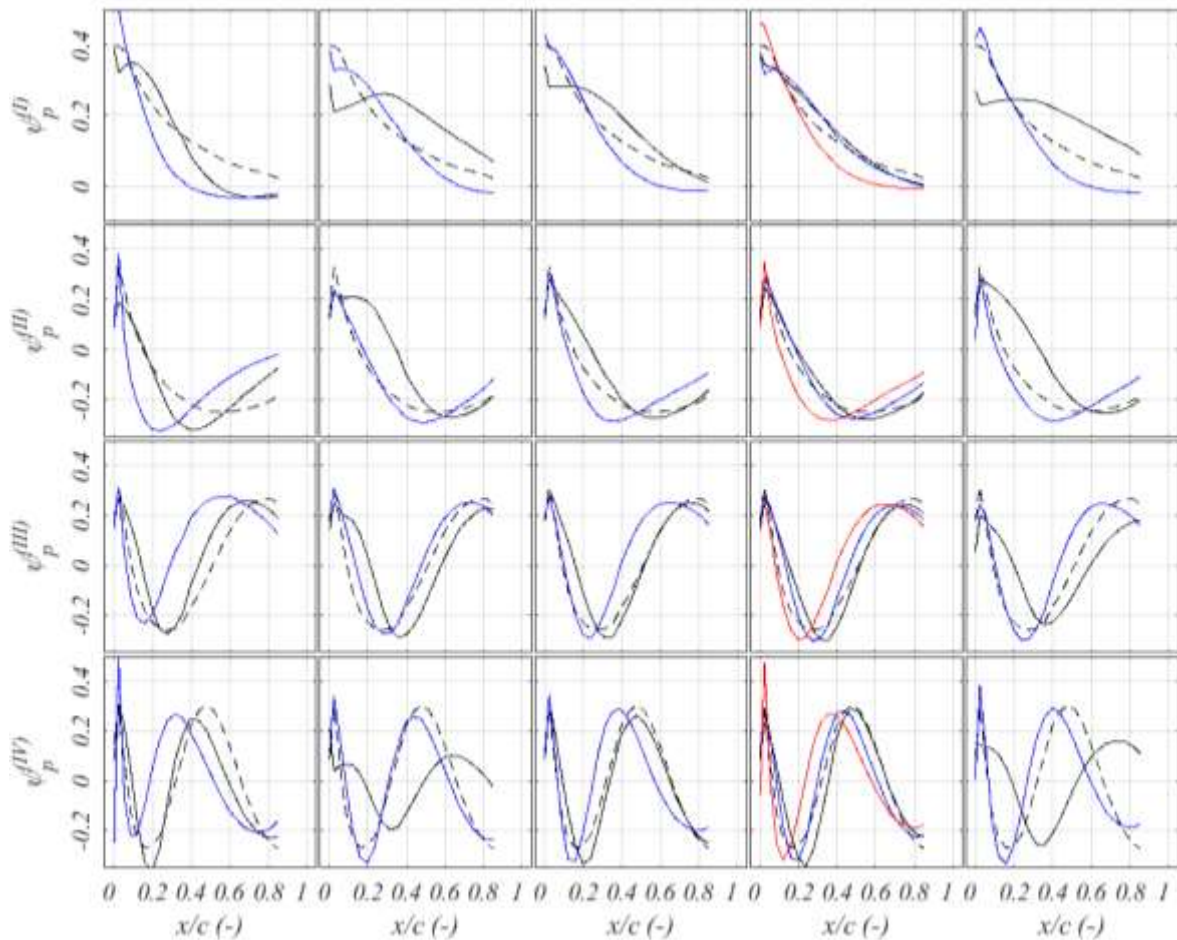


Figure 6.21. First 4 POD modes (rows) for T11-5 (columns). Colors as in

Table 6.2.

This point might represent the fluctuations due to the entrainment of turbulence. It is however quite difficult to assign a physical meaning to maxima of the third and fourth mode, and a more sensible approach is to recombine the ROM signal to highlight physical mechanisms otherwise hidden by noise at high frequency and low energy.

Likewise, Figure 6.22 shows the first 4 POD modes for cases LS1 to LS4. The length scale seems to affect the first mode when $L_w/c < 1$, while in all other cases the first modes coincide. As for the second mode, the minimum close to the trailing edge seems to move further downstream with increasing length scale, suggesting that the flow might be more energetic due to the entrainment of turbulence, however these far-fetched interpretations show how POD might be more suited to remove noise from the data and to prepare it for further analysis rather than shedding lights on the physical mechanisms involving the flow field.

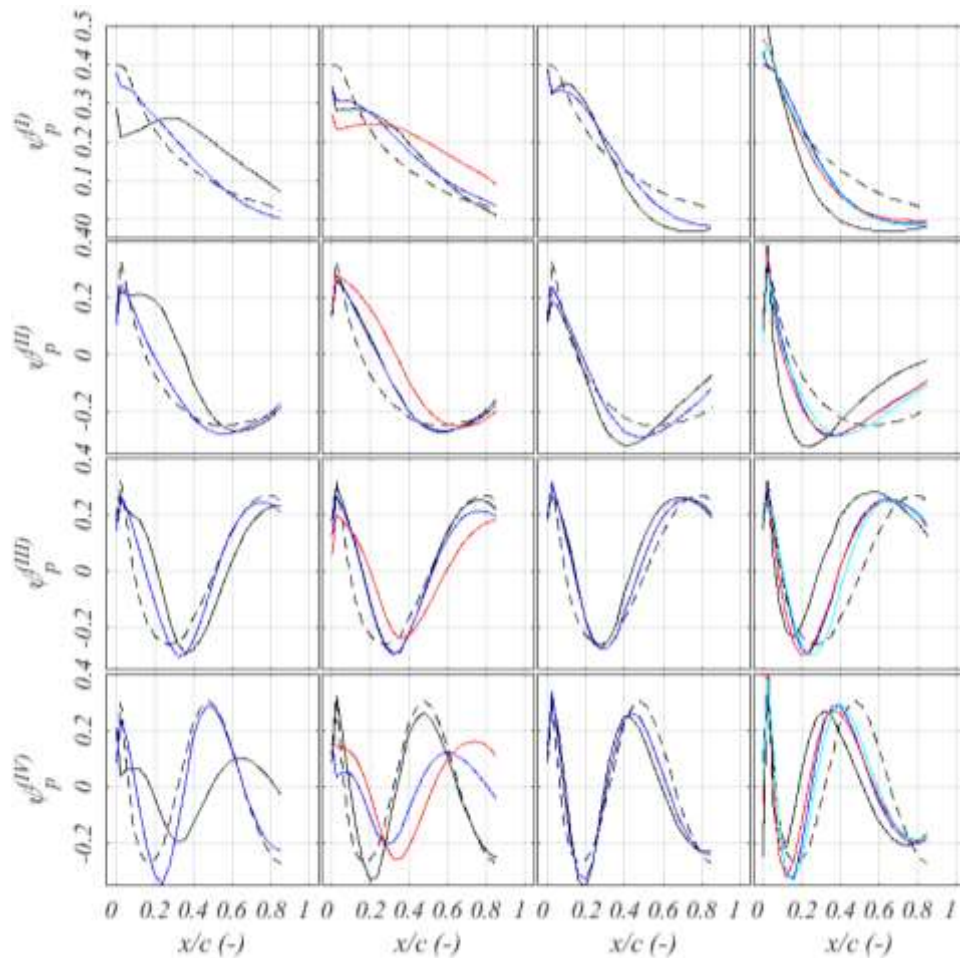


Figure 6.22. First 4 POD modes (rows) for LS1-4 (columns). Colors as in Table 3.5.

6.11. Conclusions

In this chapter, novel results on the separate effect of turbulence intensity and length scale have been discussed with reference to statistical moments of the pressure distributions, separation length variation and force coefficient. Results confirm for the first time how an enhanced turbulent inflow is able to modify the aerodynamic performance even if the integral length scale is around three times larger than the characteristic size of the aerofoil. This setup is analogous to turbulent flow conditions a hypothetical small wind turbine would find in the urban environment in the vicinity of a building roof top or ground level. The following conclusions can be made on the results:

- L_u acts as a trigger of turbulence effect, dampening or enhancing the effect, provided that a sufficiently high I_u is present in the inflow;
- When $L_u > c$, the effect of turbulence is present, and it goes stronger proportionally with the parameter $I(L/c)$, which better correlates with results;
- When $L_u < c$, the effect of turbulence is much weaker even for high turbulence intensities;
- Turbulence effects might be neglected when $I_u < 5\%$ if c_p or c'_p are looked at;
- Turbulence always affects higher order moments, normalising statistics in all cases (especially kurtosis) suggesting that turbulence helps the stationarity of the behaviour;
- First three POD modes are weakly unaffected by the presence of turbulence, suggesting that the aerofoil still behaves as a lift generating device.
- When $L_u < c$, POD modes show the highest variation compared to the undisturbed case. This suggests a deeper interaction with the boundary layer of the aerofoil, modifying its behaviour.

These results provide first evidence to question the legitimacy of the negligibility of turbulence effects assumption, when calculating the aerodynamic forces of an aerofoil in a large-scale turbulence inflow, as results show an effect of turbulence is present despite the large length scale of turbulence. The setup developed in Chapter 3, might be indeed analogous to a realistic urban configuration as investigated in Chapter 5, however a careful assessment of the wind resource is required when installing small wind turbines in the urban environment.

Chapter 7

The effect of large integral length scale of turbulence on a wind turbine aerofoil using LES

In this Chapter, a methodology is briefly introduced, which is proposed to extend the scope of wind tunnel testing as explored in Chapter 3 in relation to the turbulent inflow and Chapter 6 in relation to the wind turbine aerofoil. Turbulence characteristics which can be obtained in physical simulations are limited from the integral length scale achievable in wind tunnel testing, which depends on the size of the wind tunnel itself and it roughly scales to $\sim L/5$ where L is the minor size of the wind tunnel test-section. Large Eddy Simulation represents a performant instrument to overcome said limitations and provide a superior representation of conditions found in the atmospheric environment, as shown in Chapters 4 and 5. LES is known to perform well when modelling turbulence decay and production, provided that the mesh is sufficiently refined. This study provides indications on how to build the mesh and set up the simulation to guarantee cost-effectiveness while not losing in accuracy. Results reported here are preliminary in nature, as many methodologies exist which could be suitable for the modelling of inlet turbulence, which cannot be considered in the limited scope of this thesis. However, the precursor domain simulation is implemented and results show that using LES an extension of the wind tunnel testing limitations is possible to achieve higher $L/c \sim 10-20$.

7.1. Generation of inlet turbulence in Large Eddy Simulation

The successful analysis of the effects of turbulence on wind turbine aerofoils requires the reproduction of turbulence characteristics as found in the built environment. Chapter 4 and Chapter 5 show two possible configurations and in a way contradict each other in the sense that only large integral length scales are found in the built environment. In fact, the presence of surrounding buildings in realistic conditions might account for length scales comparable to the size of wind turbine converters and their blades. In particular, this means a turbulent flow, which might range from $L_u \sim 0.5-1.0$ m to $L_u \sim 100-150$ m. What is of extreme importance is that turbulence intensity tends to be higher than what thought in urban wind energy positioning research, spanning a range from $\sim 10\%$ at very low ambient turbulence wind conditions to $\sim 20-30\%$ in realistic flow conditions. Clearly, wind tunnel testing provides limited capabilities to reproduce such a large range of values for the investigation of a realistic turbulent inlet on wind turbine converters. Using the rather complex setup of Chapter 3, only scales up to ~ 2.8 times the chord length of the aerofoil blade could be achieved only thanks to the non-conventional features of the wind tunnel. In that case, a turbulence intensity of $\sim 15\%$ was achieved. CFD might provide a useful tool to complement wind tunnel testing extending its scope to generate a larger extent of turbulence characteristics with the generation of turbulent inlet within large-eddy simulations (LES). Previous chapters are in agreement with findings in literature that LES is highly capable of resolving a large range of turbulent eddies, their temporal and spatial correlations, and account for nonlinearities, unsteadiness and non-stationarity (Tamura, 2008; Zhiyin, 2015). However, the specification of inlet turbulence in LES is currently under heavy scrutiny from researchers trying to understand whether it might be suitable to replicate exactly a turbulent inlet as found in nature and eventually get closer to the scope of the virtual wind tunnel (Stathopoulos, 2002).

Typically, inlet turbulent generation techniques for LES consist of two philosophies:

- Precursor turbulence - generation from a wall boundary or a porous region of the domain.
- Synthetic turbulence – generation from an analytical algorithm that creates numerical noise with specific statistics at the inlet boundary.

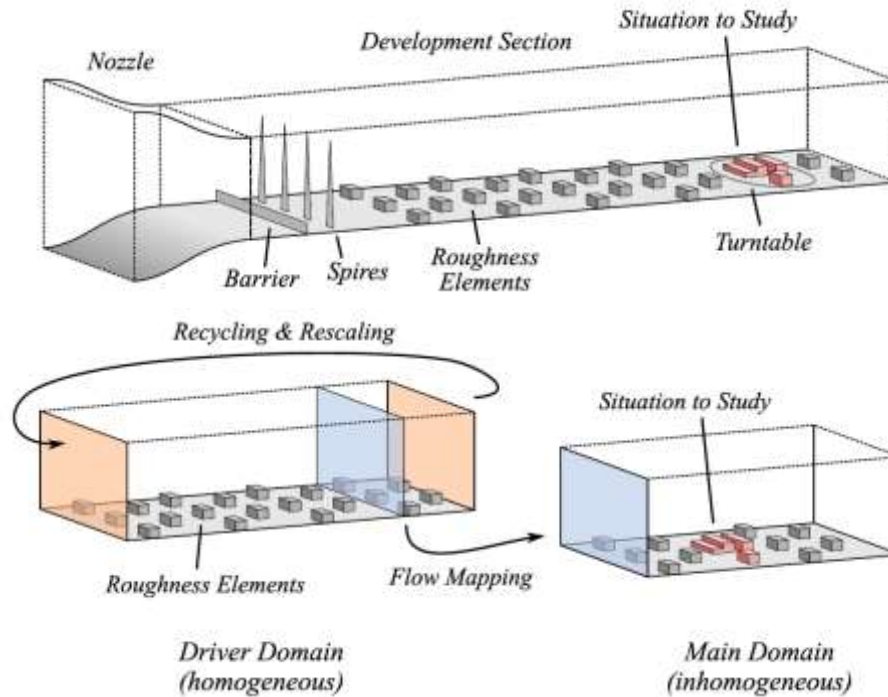


Figure 7.1 Precursor turbulence generation techniques, (top) virtual wind tunnel, (bottom) double recycling/rescaling domain method, with flow mapping at the inlet of the geometry of interest (Immer, 2016).

Figure 7.1 shows two of the possible precursor turbulence generation techniques. Whether inlet turbulence is computed alongside with the model or calculated separately to then be fed into the domain to study, this technique requires the presence of a physical wall to create turbulence (Chaudhari, 2014; Tabor and Baba-Ahmadi, 2010). As for applications, precursor turbulence is normally considered expensive and inefficient in terms of computational cost, as the introduction of a large portion of additional domain is required. However, this technique allows the turbulence to develop naturally, making no assumptions about its behaviour. To get the inlet flow to behave according to specified flow characteristics, body forces or porosity might be introduced to have some flexibility on turbulent statistics (Tabor and Baba-Ahmadi, 2010). The technique is therefore simple and accurate and the mesh can be optimised in the development section or driver domain to reduce the overall costs (Immer, 2016). This methodology is not exempt of numerical issues, and several works have been published to increase the efficiency of the method (Chung and Sung, 1997), or to store data computed in the driver domain into the main domain more efficiently, as shown in Figure 7.1 (De Villiers, 2006).

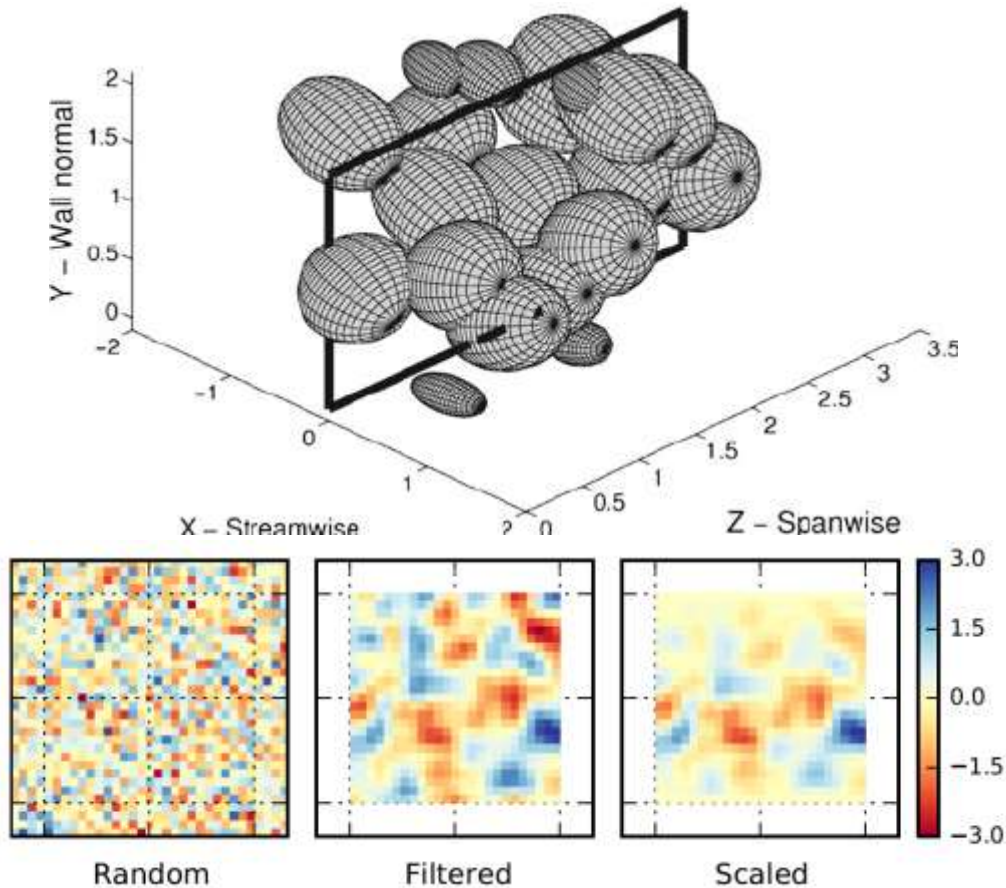


Figure 7.2. Synthetic turbulence generation, (top) Synthetic Eddy Method approach of synthetic vortex mapping (Jarrin et al., 2006; Poletto et al., 2013); (bottom) Digital noise Filtering Method of introducing a random white noise, filter it to achieve wanted turbulence statistics and scale it according to the model geometry (Immer, 2016; Klein et al., 2003)

Figure 7.2 summarises the philosophy behind the two most common synthetic turbulence generation techniques: synthetic eddy generation and digital noise filtering. These methods are most commonly implemented when investigating freely decaying homogeneous isotropic turbulence in a periodic boundary domain, and rarely used to actually generate an inlet for an engineering application (Jarrin et al., 2006). The reason for the limited number of applications is twofold. On one hand guidelines to set and validate models are missing, and on the other the implementation of analytical expressions is somewhat critical in the accuracy in replicating the physical behaviour (Immer, 2016; Tabor and Baba-Ahmadi, 2010). One critical condition to respect is the divergence free one, which is a much debated issue in inlet turbulence generation (Kim et al., 2013). Two techniques are however mature enough to be considered as feasible in their applicability to the generation of homogeneous and isotropic turbulence, shown in Figure 7.2. The synthetic eddy method, generates a field of discrete coherent structures with a specific topology and anisotropy controlled by a random algorithm, which is then

swapped in time by a plane which introduces the relevant fluctuations to the domain (Jarrin et al., 2006; Poletto et al., 2013). This technique, as implemented in OpenFOAM, requires the definition of Reynolds stresses and integral length scales to replicate turbulence statistics as those found in Chapter 3, 4 or 5. Figure 7.2 also shows the digital noise filtering techniques. A random noise is generated as initial condition, which is then filtered to match specified autocorrelation functions. Fluctuations are then superimposed to a mean flow and appropriately scaled. However, these fluctuations are not correlated in space and therefore they normally dissipate quickly if the flow is not manipulated to respect the continuity and divergence free conditions, which provide a more realistic representation of flow fields (Tabor and Baba-Ahmadi, 2010). Much work has been carried out to investigate the possibility and progress the technique to transform a random field into a realistic turbulent inflow (Davidson, 2008; Fathali et al., 2008; Saarinen et al., 2016; Smirnov et al., 2001). However, the formulation shown in Figure 7.2 has been recently used successfully to implement a realistic urban flow field (Immer, 2016; Klein et al., 2003), and it will be used as a continuation to this research to investigate the possibility of editing guidelines for the use of inlet generation techniques to model the urban flow.

In this chapter, an uncommon precursor turbulence generation technique is implemented (Blackmore et al., 2013). The concept behind this alternative to precursor simulations using a driver domain is directly related to the concept of grid generated turbulence. A solid region is individuated in the inlet surface of the domain resembling the bars of one of the configurations shown in chapter 3. Turbulence is generated thanks to the shear between the solid region and the inlet flow, in a similar way as in grid generated turbulence in wind tunnel testing. This technique allows for a simpler setup than common precursor domain, while retaining the same advantages of turbulence produced and dissipated physically, hence of high quality.

The aim of this chapter is to extend the scope of wind tunnel testing with a methodology framework where experiments are interlaced with Large Eddy Simulation. In fact, the main limitation of wind tunnel testing is the ratio of integral length scale with the characteristics size of the model. In this chapter, this limitation is overcome by reducing the size of chord of the model by five times.

7.2. Methodology

The experimental setup of Chapter 6 is reproduced using CFD. The computational domain comprises of a portion of the wind tunnel domain in correspondence to the centre of the test-section measuring 0.9×0.9 m. The passive grid configuration used in the numerical simulation is the one reported in Table 7.1, which reports details of the turbulent flow downstream of the grid and the distance x/M considered to position the aerofoil to test the effect of turbulence. The configuration is chosen due to the high quality of the turbulence downstream of the grid combined with a turbulence intensity compatible with findings from Chapter 4.

Table 7.1 Configuration of the grid geometry reproduced in the numerical simulation with turbulence statistics at $x/M=10$ ($x/M=6.5$ for grid #1) and $U_r=15$ m/s.

Grid	b [m]	M [m]	M/b [-]	β [-]	C_d [-]	x/M [-]	I_u [%]	L_u/c [-]	λ_u/c [-]	I_u/I_v ~1	L_u/L_v ~2	λ_u/λ_v ~ $\sqrt{2}$
#2	0.063	0.30	4.76	0.62	0.97	10	8.35	0.92	0.34	1.14	2.13	1.320

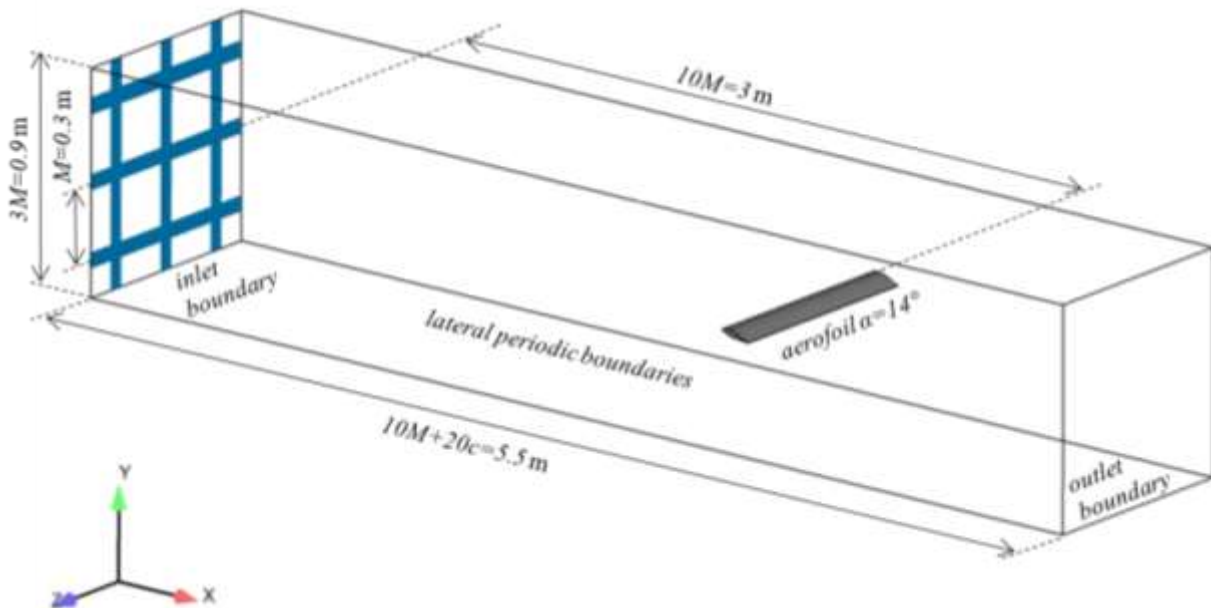


Figure 7.3. Computational domain with inlet surface and solid region and distance from the aerofoil model.

The turbulent flow is reproduced with a precursor simulation where turbulence is generated with solid boundary at the inlet surface of the domain, as proposed in a recent study (Blackmore et al., 2013). This technique uses a virtual passive grid to generate turbulence in the same way as in the wind tunnel, and therefore avoiding the limitations of synthetic turbulence or other precursor simulations techniques for its simple implementation. The computational domain is shown in Figure 7.3. The inlet boundary is

divided into a fluid region where a uniform inlet velocity of 20 m/s has been set up, and a solid region where a wall boundary has been set up implementing Spalding wall function for LES to allow for a coarse mesh (Blocken et al., 2007). This choice allows for a much coarser mesh around the solid surface at the inlet, unlike what has been done in previous research (Blackmore et al., 2013). The WALE SGS model has been used in OpenFOAM v5.0 with a bounded central difference scheme and the PISO solution algorithm.

Figure 7.4 shows the mesh topology for the aerofoil. A C-Grid is combined with an H-Grid with a particular effort in guaranteeing the orthogonality between the surface of the aerofoil and the boundary layer cells. A mesh independence study has been carried out and it was found out that this increases the accuracy of results and allows a coarser mesh to be implemented. RANS technique has been used on a variety of domains and simulations to find the optimal combination for the mesh refinement and topology.

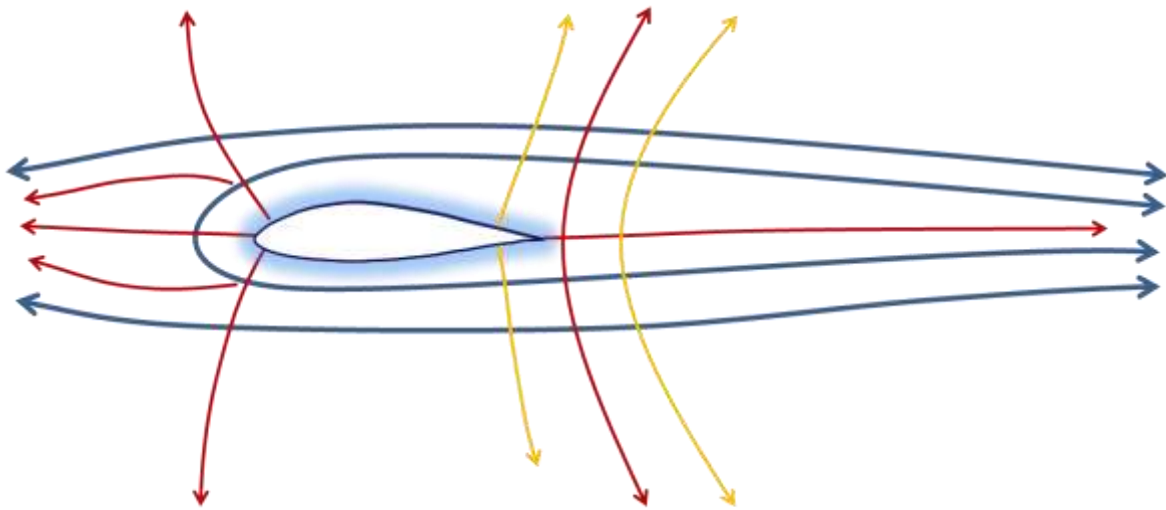


Figure 7.4. Schematic of the structured hexahedral mesh topology around the aerofoil.

Figure 7.5 shows the effect of the blockage due to the domain size. Results are computed using RANS with the $k-\omega$ SST model implementing adaptive wall functions. No significant differences in the results have been found by using the standard or the Low-Re formulation of the wall-functions. Simulations have been carried out using openFoam v.3.0.1 with a 2D model of the Du96w180 aerofoil at 4 degrees for the angle of attack. The computational scheme of choice is the 2nd order bound scheme with a weakly relaxed SIMPLE solution algorithm. Lateral boundary conditions have been set up to Symmetry.

Figure 7.6 shows the effect of the mesh refinement on the pressure coefficient. Refinement is varied in terms of the y^+ and number of cells in the boundary layer. A close experimental match is shown for all levels of refinement, and therefore the coarsest mesh resolution is chosen, with $y = 0.01$ mm at the wall, 75 cells in the boundary level, and 789 cells around the development of the aerofoil.

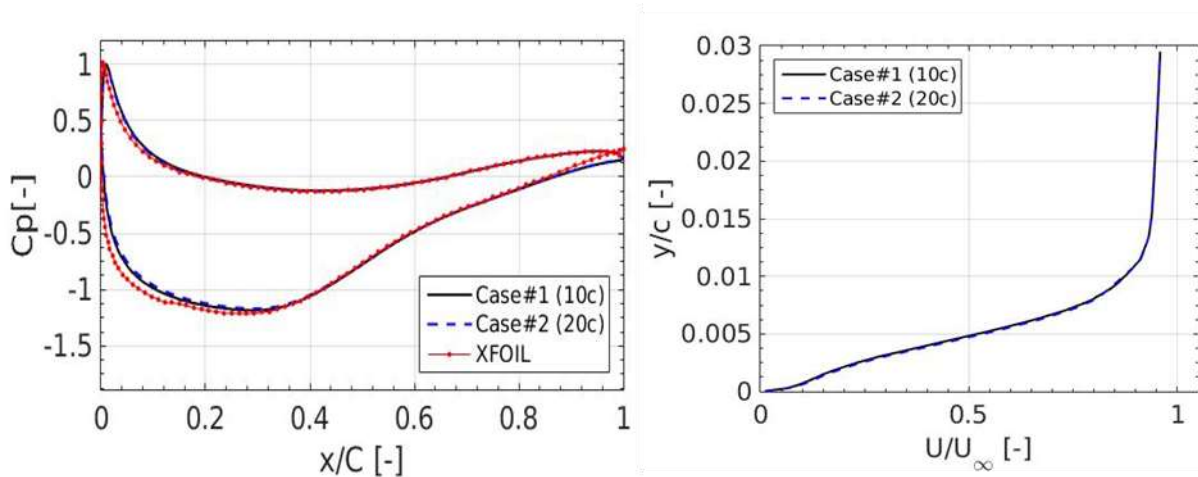


Figure 7.5. Effect of domain size on mean pressure and boundary layer thickness at $0.99c$.

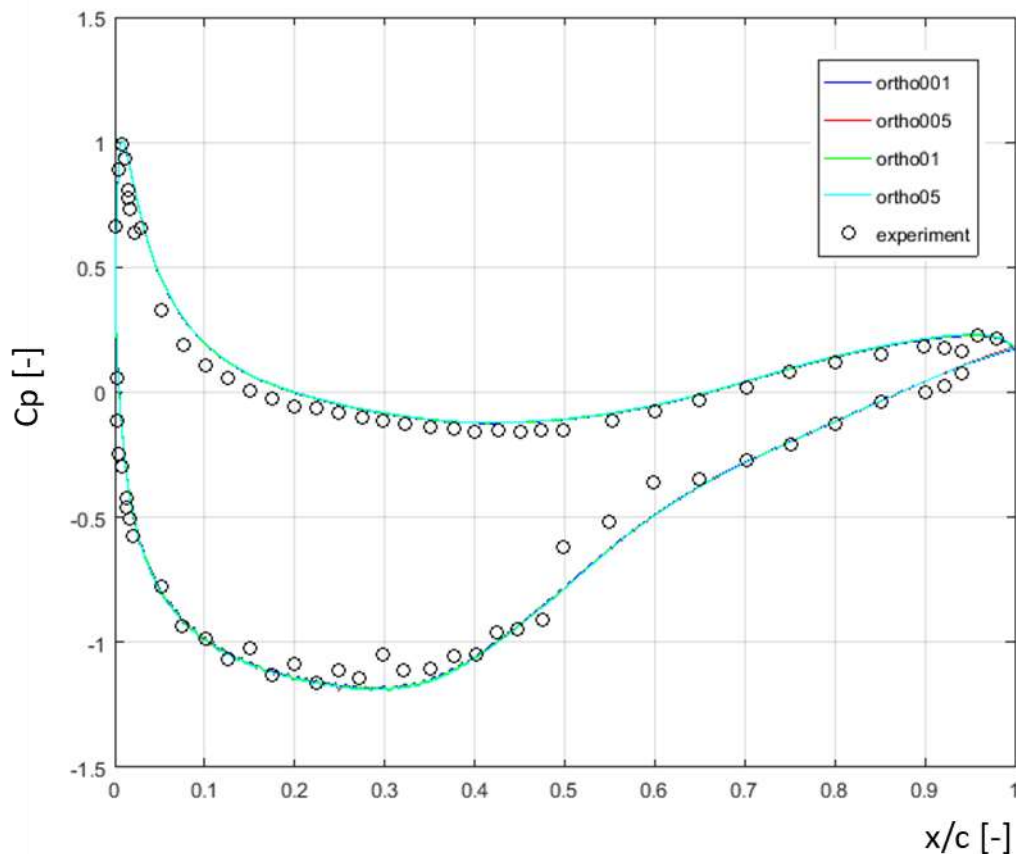


Figure 7.6. Effect of orthogonal mesh refinement on surface pressure coefficient.

The mesh is shown in Figure 7.7. A region of uniform mesh with a spacing of 0.03 m is present straight after the virtual grid. This resolution has been chosen with reference to results in literature as it provides

a compromise between resolution, accuracy, and costs (Blackmore et al., 2013). From $x/M \sim 8$, a structured block mesh is implemented to guarantee a $y^+ \sim 0.3$ and a uniform growth around the aerofoil in the y direction of ~ 1.05 . In this way a sufficiently high resolution is obtained to model the interaction of the turbulent structures in the inflow with the boundary layer of the aerofoil. The aerofoil is the DU96w180 as implemented in Chapter 6, with a chord of $c=0.125$ m, in which case the geometry is referred to as C125.

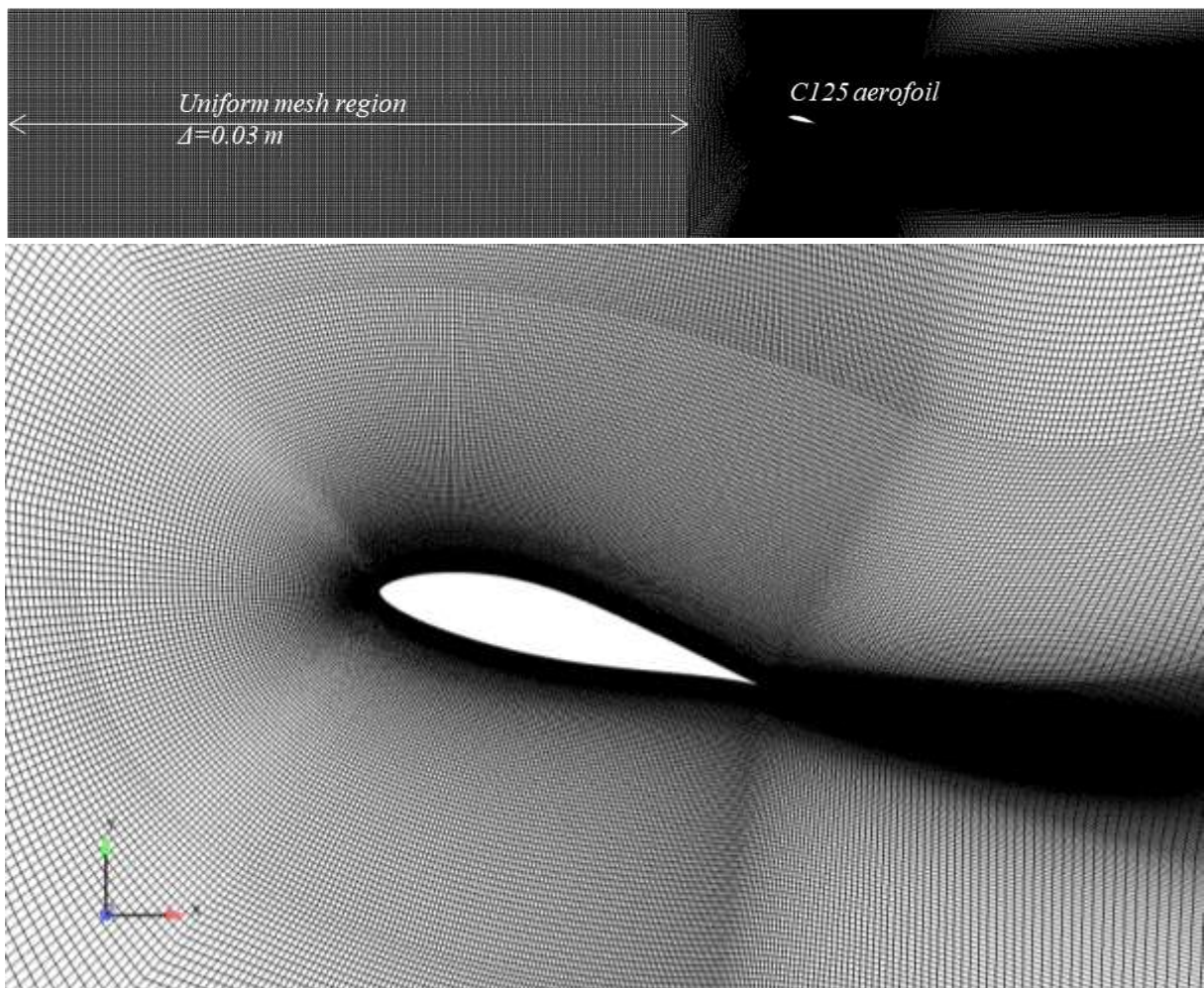


Figure 7.7. Structural hexahedral mesh for the aerofoil with chord $c=0.125$ m. (top) side view and (bottom) view of the topology around the aerofoil boundary layer.

The scope of the experimental setup has been extended thanks to the numerical setup by implementing a second model aerofoil having $c=0.025$ m and referred to as C25 in the rest of this Chapter. However, in the z direction a change in the resolution of the mesh was needed to reach $z^+ \sim 50$. At the top of Figure 7.8, the top view of the mesh shows the refined region at the middle of the test section to adjust for z^+ .

The bottom of Figure 7.8 shows instead a side view of the different topology of the structured blockmesh.

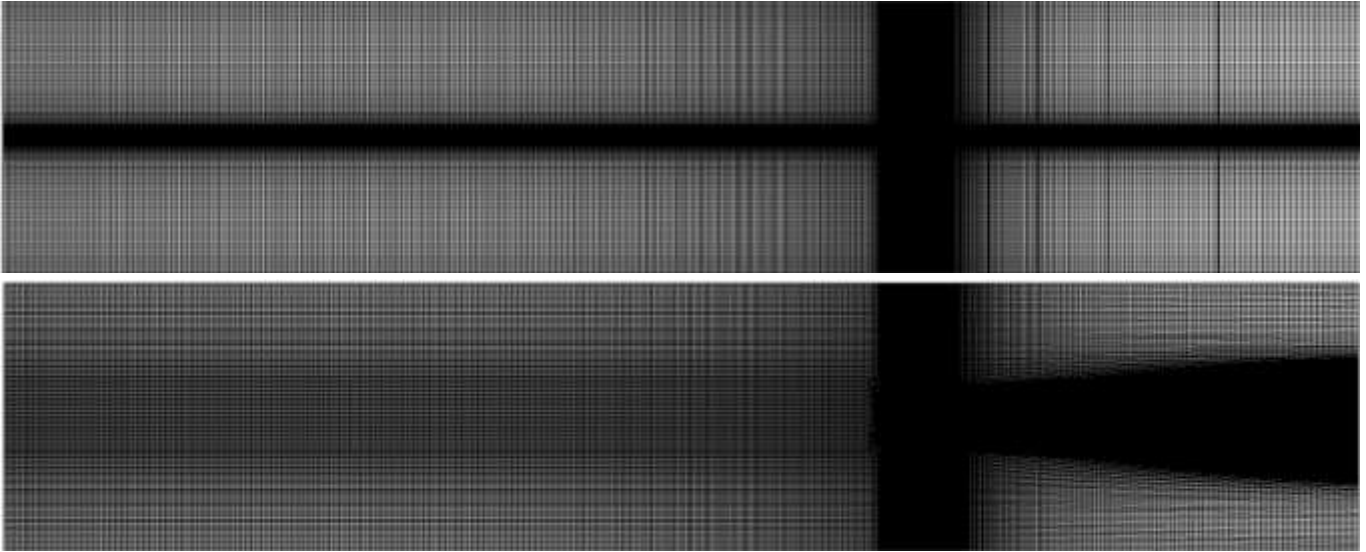


Figure 7.8. Structured hexahedral mesh for the aerofoil having chord $c=0.05$ m. (bottom) side and (top) top view.

The aerofoil in the shorter chord case was discretised in order to have the same number of cells around the surface of the aerofoil, while keeping y^+ and the growth rate similar to the large chord case, at respectively ~ 0.3 and ~ 1.05 . Figure 7.9 shows the topology of the mesh around the aerofoil.

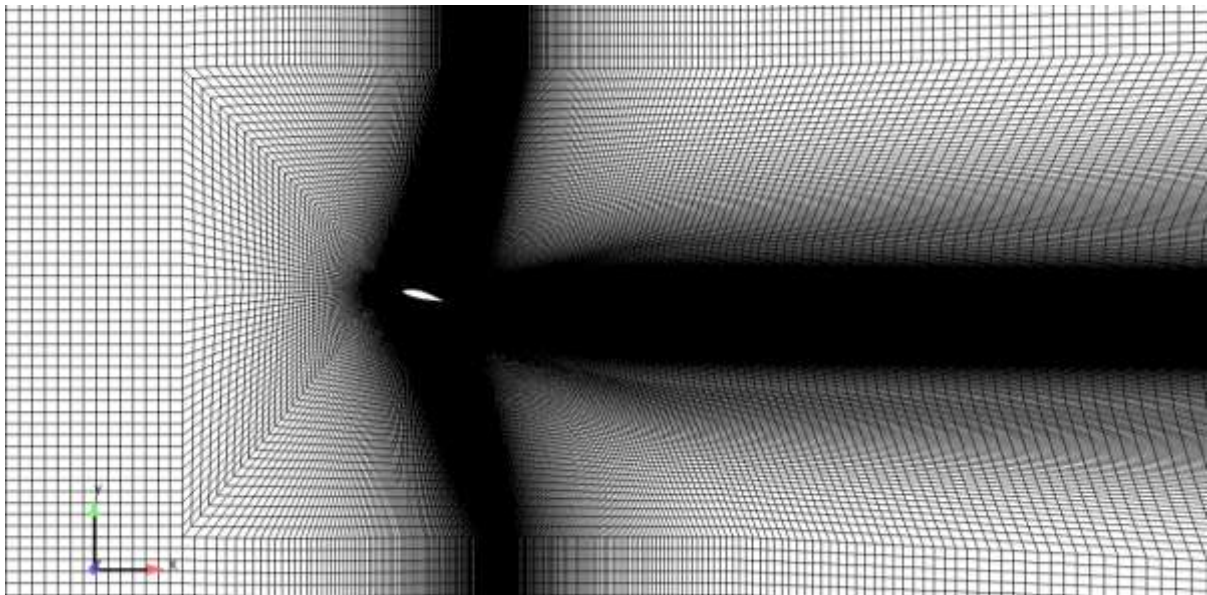


Figure 7.9. Topology of the computational mesh around the aerofoil with short chord length

Figure 7.10 show the y^+ value for both geometries, which is analogous, reassuring on the equivalence of the meshing conception for the two geometries.

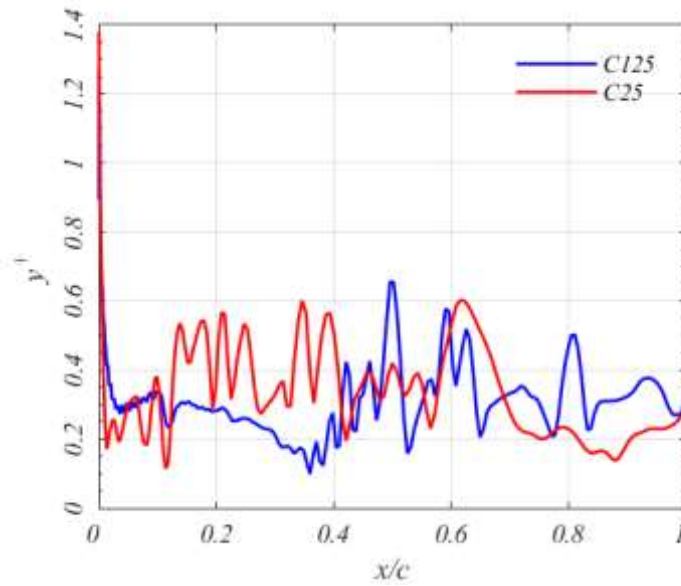


Figure 7.10. y^+ instantaneous value along the suction side of both C125 and C25 aerofoil models.

7.3. Preliminary results and discussion

In this section, preliminary results included in this chapter are briefly presented and discussed. Inlet statistics, the flow pattern, and surface pressure coefficients are presented in parallel with what has been introduced in the previous chapter. A brief discussion on the possible effect of very large length scale turbulence is then attempted to show the potential of the methodological framework provided in this thesis to increase the knowledge about bluff body aerodynamics in atmospheric turbulent flows.

7.3.1. Inlet statistics

Inlet statistics relevant to the numerical precursor domain simulation are hereafter compared to the experimental setup developed in Chapter 3. In particular results are referred to Grid #2 at a distance of $10M$, which corresponds to 3 m between the inlet boundary layer surface and the leading edge of both models C125 and C25.

Figure 7.11 shows the mean velocity distribution along the length on the computational domain. The two computational domains show a $\sim 5\%$ average difference, which most certainly might depend on the refinement of the cells along the mean line of the computational domain for the C25 geometry. This problem could be overcome by choosing a more improved meshing strategy, i.e. implementing non-conformal blocking to overcome the different meshing requirements necessary to respect the condition $z^+ \sim 20-50$, which is particularly demanding in conformal meshing strategies as the present simulation.

Results are compared with the experimental case, showing a good match. However, as discussed in chapter 3, the experimental mean velocity shows a negative trend, while the numerical one a slightly positive one. As confirmed in recent research, this might depend on the detailing of the experimental passive grid, which might configure a wake or a jet behaviour depending on the positioning of bars close to the walls of the wind tunnel (Carbó Molina et al., 2017). At $x \sim 3$ m, the disruption in the mean flow in correspondence with the aerofoil is noticeable with a significant drop in the mean velocity, which recovers fast in the wake, confirming that inlet turbulence has an important role in the behaviour of the wake of bluff bodies.

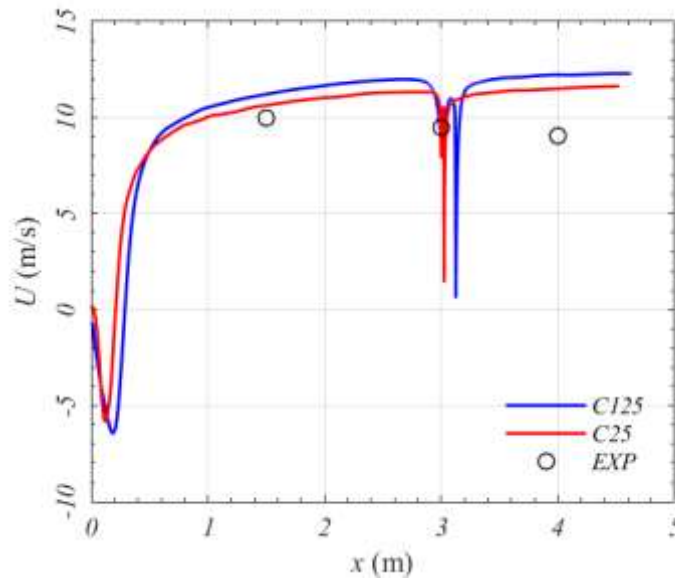


Figure 7.11. Mean velocity along the computational domain, compared with experimental results.

Figure 7.12 shows the turbulence intensity decay, as calculated using the mean velocity found at $x \sim 3$ m. The decay rate is analogous to experimental results, confirming that the mesh refinement is sufficient not to induce any numerical decay on the data. A dumping of the turbulence intensity closer to the solid grid is noticed, with a relative error of $\sim 35\%$ with wind tunnel data. This is likely depend on local flow features rather than a too coarse mesh, as at $x/M \sim 5$ grid turbulence is still heavily affected by local disturbances and imperfections. In fact, at $x/M \sim 10-15$ results are analogous. As regards the transversal component I_v results show a high degree of isotropy, as $I_v \sim I_u$.

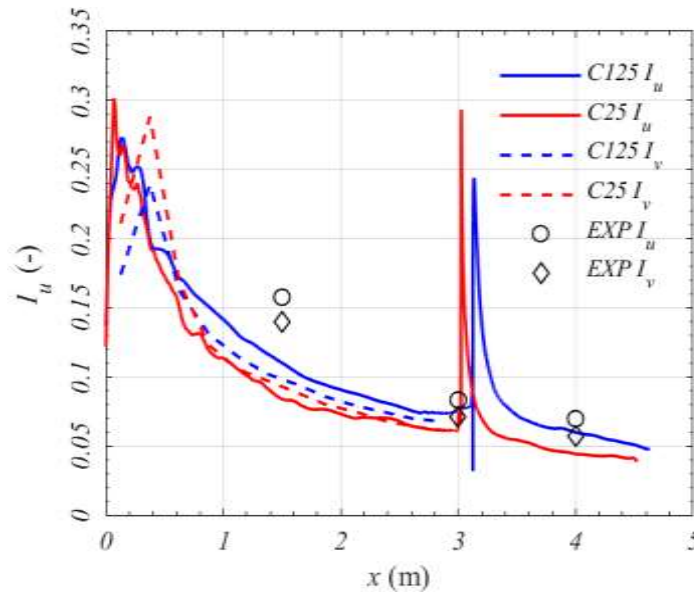


Figure 7.12. Turbulence intensity decay along the computational domain, compared with experimental results, for both the along wind and across wind directions.

A possible effect of the refined region of C25 is noticeable in Figure 7.13, which shows the integral length scale decay for both the longitudinal and transversal velocities. While results show a high degree of match between the C125 and the EXP case, the C25 domain tends to underestimate the integral length scale by $\sim 30\%$. In the transversal direction the performance is slightly better for C25, and a close match with EXP results is available. This confirms the need of a different meshing strategy, which would also benefit the optimisation of computational resources by adapting the mesh topology appropriately.

Results for the C125 and C25 domains are only available up to $x \sim 2.8$ m, due to the disturbance of the aerofoil. This could explain the why the last point in Figure 7.13 tends to drop rather than increase as indicated by experimental results. Nevertheless, the decay rate is correctly captured by both C25 and C125, showing the good level of refinement of both meshes.

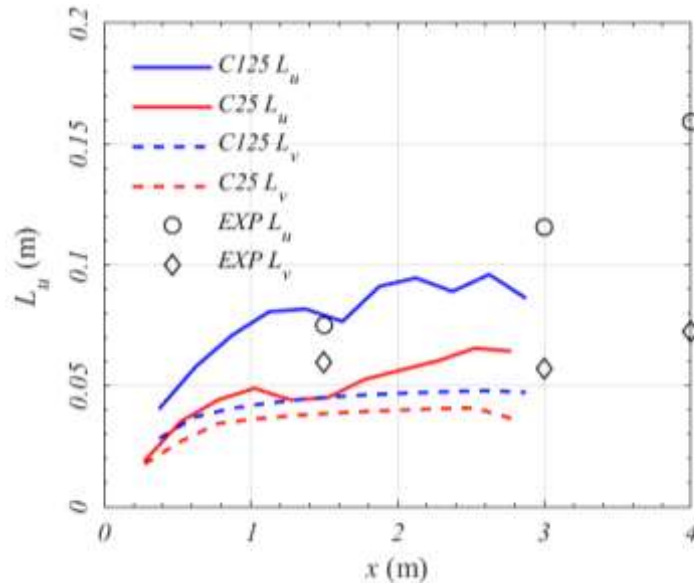


Figure 7.13. Longitudinal and Transversal integral length scale decay, compared with experimental results.

Figure 7.14 proves that at $x \sim 2.8$ m, the flow is influenced by the aerofoil, which deviates it. Velocity invariants computed from the three components of velocity are plotted alongside experimental results, showing a high degree of isotropy, which is essentially matched by both C25 and C125 domains. This might suggest that the meshing strategy might not be the issue for the underestimation of L_u noticed for C25. In fact, the sample time could be deemed responsible as the autocorrelation function precision varies with the sampling time, which might not be enough in the case of C25.

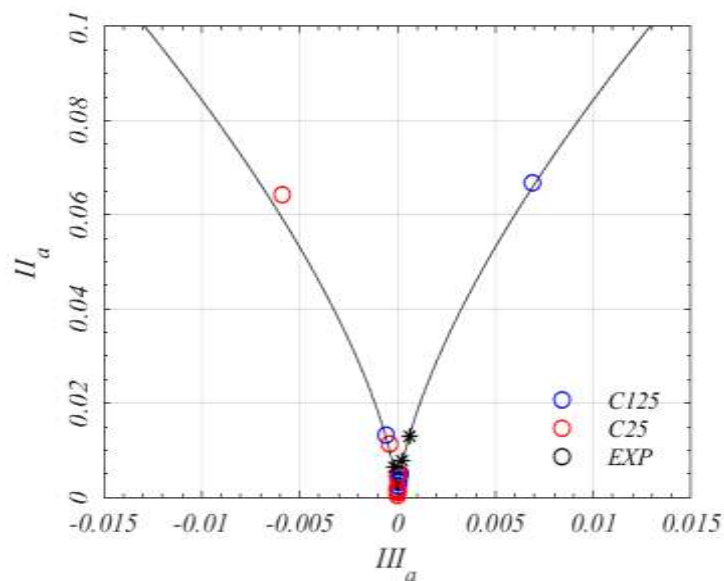


Figure 7.14. Velocity Invariants for C125, C25 and EXP.

Figure 7.15 confirms the high degree of precision in reproducing the unsteadiness in the flow and its non-stationary behaviour as results for the skewness and kurtosis are essentially unaffected by the refinement in the mesh.

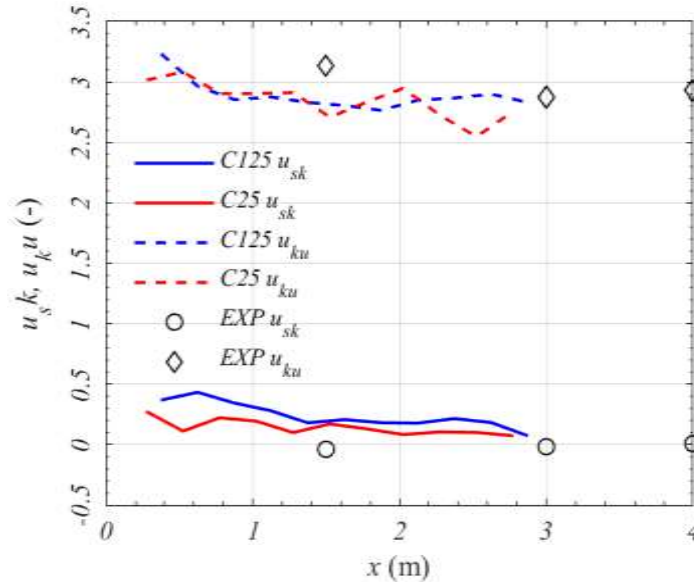


Figure 7.15. Velocity Skewness and kurtosis compared with experimental results.

Figure 7.16 compares energy spectra with the experimental counterpart. Results are compared in dimensional term as to understand whether the nature of turbulence produced in both simulation is analogous to draw conclusions on the results. Figure 7.16 seems to confirm the mismatch in terms of integral length scale for C25, while C125 closely replicates experimental findings. In the high-frequency range, the behaviour of the energy spectra confirms that a significant part of the sub-inertial range is reproduced (up to $n \sim 100$ Hz), which is enough to estimate the dissipation rate as done in Chapter 3. This advanced analysis is postponed to further research, as it lies outside of the scope of this Chapter. Nevertheless, Figure 7.16 confirms the possibility of implementing a coarse simulation for the study of atmospheric flows and extend wind tunnel scopes, without losing in accuracy. It is also shown the need of guidelines on LES used for engineering applications, for instance the role of the sample rate as well as the minimum meshing requirements to obtain a suitable energy spectrum of use, as achieved in this case.

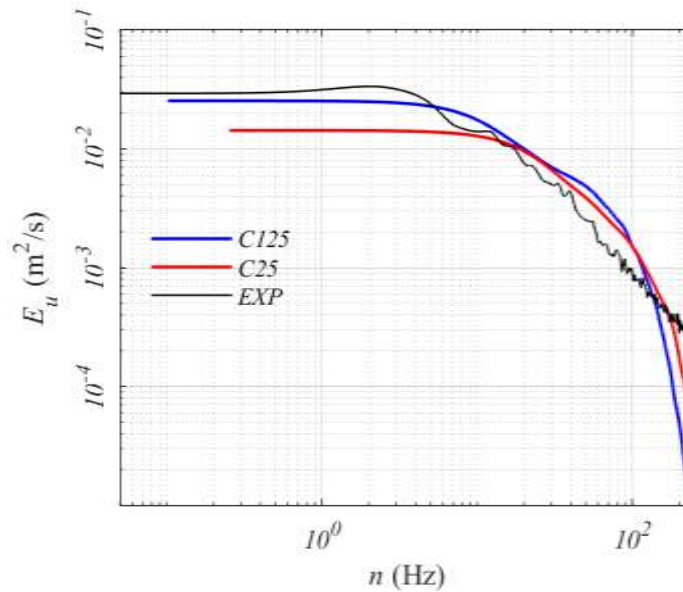


Figure 7.16. Energy Spectra compared with experiments.

The chosen precursor method shows how it is indeed possible to achieve noteworthy correspondence with experimental results without requiring a cost-intensive simulation, provided that an improved simulation setup is optimised when modifying the ratio between the inlet flow and the body itself.

7.3.2. Flow pattern

Figure 7.17 shows the flow pattern for both C125 and C25 models. Qualitatively, results are analogous as the flow patterns could be overlapped. A region spanning $\sim 3M$ is present at the inlet where the jets blocked by the solid inlet boundary do not interact. Then a region spanning $\sim 2-3M$ shows the jets merging and widening. At $x/M \sim 5-6$ the flow is very turbulent (brighter colour in Figure 7.17), with the jets become undistinguishable. This minimum reference distance is important in terms of atmospheric flows, as it allows for the highest turbulence intensities to be reached. In correspondence with the aerofoil, Figure 7.17 does not show particular difference in the flow pattern, although the colour scale of the two cases is the same.

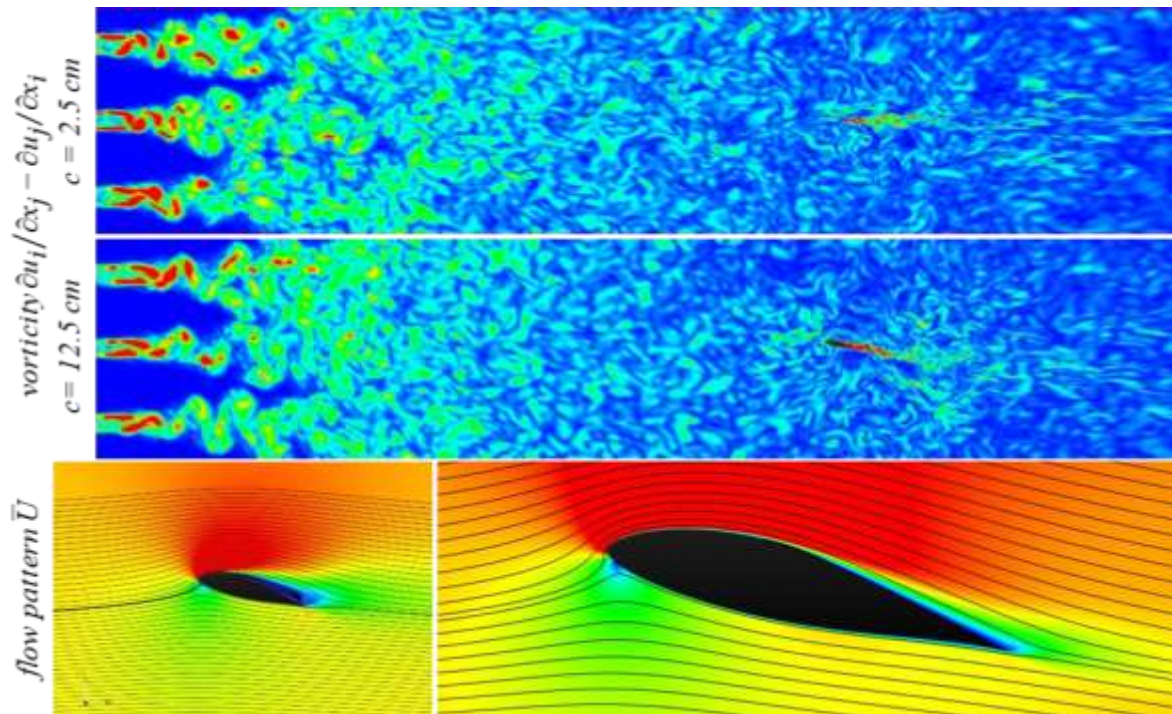


Figure 7.17. (top) vorticity of C25 (above) and C25 (below). (bottom) dimensional mean velocity for C25 (left) and C125 (right), with streamlines showing the flow pattern.

The bottom of Figure 7.17 shows the mean velocity around both aerofoils. The flow is heavily accelerated above the suction side and slowed down below the pressure side in both cases. However, a large separation region can be noticed in C25, which is not the case for C125. Given results presented in the previous part of this Chapter it is unlikely that this depends on the mesh refinement or the small difference in turbulence intensity depending on it. However, as experimental results have never been attempted for such a ratio between a bluff body and integral length scale of turbulence, it is difficult to state whether these differences account for an effect of the much larger integral length scale. If that is the case, from Figure 7.17 it can be said that a large integral length scale is responsible for a recovery of the separation occurring in the undisturbed case, minimising the effect of the turbulence intensity. Nevertheless, looking at results in Chapter 6, this configuration only reaches $I_u \sim 7.5\%$, which does not show dramatic changes in the surface pressure as with a higher intensity $I_u \sim 15\%$. However, this requires the positioning of the aerofoil closer to the grid, and this chapter shows that the quality of the flow field is sufficient to do so in the next steps of this research.

7.3.3. Pressure coefficient

Figure 7.18 shows the mean pressure coefficient and its standard deviation as computed in C125 and C25 and measured in Chapter 6. For comparison also the undisturbed experimental setup is plotted. Results confirm a systematic difference in the mean pressure coefficient on the pressure side of the aerofoil, with both C125 and C25 missing the plateau noticeable in the experimental case for both the turbulent and undisturbed case. This would indicate a delay in separation, hence an increase in lift. However, the experimental case picked for assessing the performance of LES in reproducing the behaviour does not show significant differences in terms of flow pattern with the undisturbed case, as both mean pressure coefficients can be overlapped. This choice has been done consciously, as to highlight the possible role of SGS and a fine mesh in overestimating the effect of turbulence. More simulations and more meshes need to be tested in order to assess the role of the computational setup and the inlet turbulence. The right of Figure 7.18 shows the standard deviation of the pressure coefficient. The role of the turbulence length scales seems to enhance the fluctuations around the aerofoil, somewhat confirming findings of Chapter 6 that an increase in length scale enhances the effect of turbulence rather than hampering it. However, this simulation needs to be propped up with an experiment and more turbulent inlet to fully understand the role of large integral length scales.

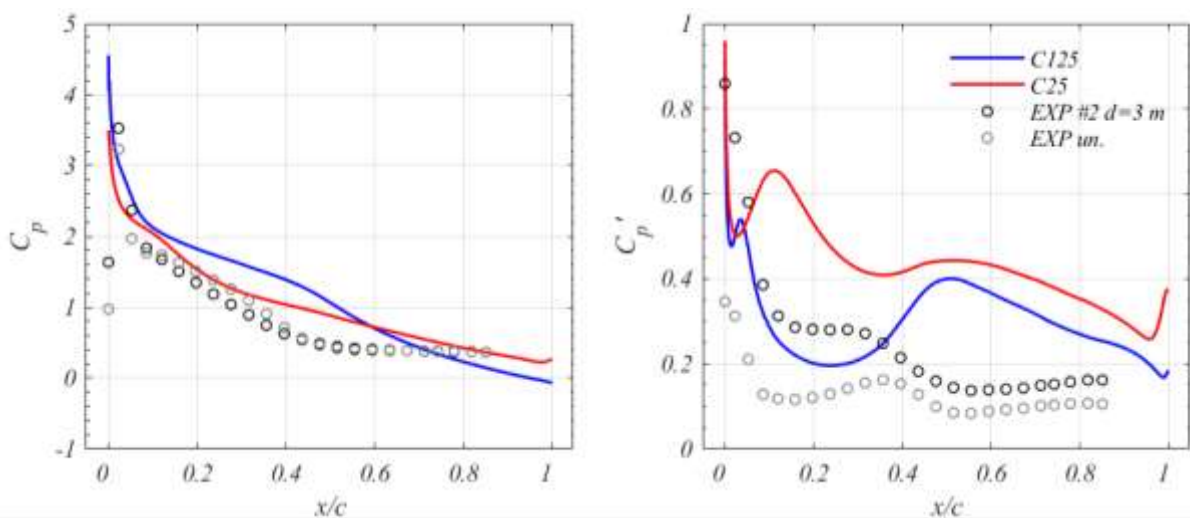


Figure 7.18. Surface pressure coefficient at the suction side for C25 and C125, compared with the experimental case and the undisturbed experimental case.

Moreover, the angle of attack chosen might not be enough to highlight the dramatic effect of turbulence on the separation delay as shown in Chapter 6, and indeed more noticeable for $\alpha=24$ deg. More research is then needed to highlight this effect and recognise a pattern towards a possible physical mechanism which might trigger the effect of shield it.

7.4. Conclusions and take out points

In this Chapter, only a brief report on the outcome of preliminary research exploring the possible extension of the scope of wind tunnel testing using CFD has been given. While results are not of much use regarding the correspondence with experimental results as presented in Chapter 6, this chapter confirms the possibility of implementing coarse LES to generate a suitable high quality and close-matching with reality turbulence inflow to extend wind tunnel experiments. A way of doing this, as done in the present chapter, might be to reduce the size of the bluff body of interest keeping the turbulent inlet fixed. In order to achieve this, guidelines on the correct implementation of LES, in terms of sample rate and mesh refinement, might be needed to avoid numerical effects on the results. Present results show possibly how a too fine mesh might cause numerical effects responsible of over-estimating the effect of turbulence in a case where this effect should be not dramatic.

The numerical research on the effect of large integral length scale of turbulence on wind turbine aerofoils needs to be expanded from the present limited scope, e.g. with more turbulent statistics, more angles of attack, or more aerofoils, to be able to draw significant conclusions. However this chapter confirms the success of the methodological framework as introduced in Chapter 1, and it reassures on the quality of LES towards being likened to experimental results once the numerical setup is optimised.

Chapter 8

Conclusions

These conclusions summarise conclusions given in the previous chapters, where a detailed discussion on the implication of results has been presented specifically for the objective at stake. A statement is given on how each objective has been fulfilled in the thesis. The original research contributions of the work are also listed together with indications on the possible next steps of the research.

This work originates from the scope of the “Aeolus4future” Marie Skłodowska-Curie Innovative Training Network, aimed at addressing the “efficient harvesting of wind energy”. The author of this work was in charge with Work Package 5, which aimed at improving the knowledge about the “efficient positioning of wind turbines in the built environment”. From the very first steps of the research, as specified in Chapter 1, it was clear how a categorical change in the way this problem has been addressed until that point was needed. This has been the motive at the core of this thesis.

This research provides an alternative in the definition of what constitutes a suitable turbulent flow as found in a relevant location within the atmospheric boundary layer. In literature, the problem of a wind turbine facing a turbulent flow is avoided by defining a generic or at best subjective limitation to the statistical properties that a turbulent flow should (or should not) possess in order to be considered harmless (or harmful). This has motivated the investigation on the characteristics of realistic flow conditions a wind turbine sustains during its service life. However, this uncovered a multitude of issues, which have been summarised with the twofold problem and the final partition of this thesis:

- The assessment of turbulent inflow conditions as found in built up locations;
- The assessment of the aerodynamic performance of wind turbines facing those conditions.

As reiterated in Chapter 1, this thesis has been able to address this twofold issue and combine it by exploring the capability of both wind tunnel testing and numerical simulations in cooperating to overcome each other’s limits. The crucial point of the research is to be able to finally elevate experimental and numerical results so they can be post-processed in a similar way, hence bringing them

at the same level of accuracy and/or trust. The work has been conducted following the twofold shape of the problem and each objective was carefully undertaken to prove or disprove assumptions as presented in Chapter 1.

Table 8.1 summarises objectives listed in Chapter 1 and the correspondent conclusions presented in every Chapter.

Table 8.1. Objectives and relevant outcome of the research

Objective	Outcome of the research
Literature review: effects of free-stream turbulence on bluff bodies and wind turbine aerodynamics.	Unclear whether turbulence intensity, integral length scales, or both concur in triggering the effect. Unclear legitimacy of neglecting the effect of turbulence due to large length scales
Capability of wind tunnel testing to vary inlet turbulence intensity and integral length scale separately.	Limited range of turbulence intensities and integral length scales combinations achievable. Great benefit of expansion test section in varying statistics. Very high quality of the flow in terms of anisotropy, homogeneity, gaussianity.
Capability of CFD to reproduce signature turbulence on an ideal location within the built environment.	Very accurate results indicate larger length scales ~20-100 m take place at high turbulence intensities ~10-15 % unlike what normally considered in experiments and at design stage. Turbulent flow conditions comparable to grid turbulence in terms of quality.
Capability of CFD to reproduce signature turbulence at different locations over a realistic urban geometry with a suitable experimental validation strategy.	Accuracy of CFD and wind tunnel testing is analogous when reproducing full-scale data even with very coarse meshing strategy, provided that atmospheric boundary layer turbulent flow is modelled at the inlet in terms of turbulent characteristics. Very large length scale ~100-200 m combined with enhanced turbulence intensities ~15-20 %
Effect of variability of integral length scale of turbulence on the aerodynamics of a model wind turbine aerofoil.	Turbulence length scales act as an enhancer of the effect of turbulence. The larger the scale, the stronger the effect, provided that a critical intensity is available, in this test >12 %
Capability of CFD to extend results obtained for the model wind turbine aerofoil and match turbulence characteristics as found in wind tunnel testing and precursor CFD to test the effect of realistic urban turbulence.	Accuracy and flexibility of CFD in reproducing turbulence characteristics of high order. Necessity of improved guidelines when simulating fluctuating behaviour. Possible residual effect of very large length scales.

Table 8.1 shows the comprehensiveness of results towards the establishment of a methodological framework which is specifically aimed at overcoming the limitations of wind tunnel testing to reproduce an inflow representative of the urban environment.

As already discussed in Chapter 1, this research contributes to

- i) the generation of turbulence having intensity and length scale varied separately in wind tunnel testing, using an expansion section placed downstream of a passive grid;
- ii) the investigation on the independent effect of TI and LS on the aerodynamics of a wind turbine aerofoil ($I \sim 15\%$ and $L/c \sim 2.7$);
- iii) the generation of realistic inlet turbulence using available turbulent inlet generation techniques to extend a wind tunnel experiment ($I \sim 15\%$ and $L/c \sim 15$);
- iv) the assessment with CFD and wind tunnel of the signature turbulence with reference to LS both on an isolated high-rise building and on a realistic urban configuration (University Campus);
- v) the post-processing and validation of large eddy simulation results with respect to high-order statistics, feature extraction methods (POD), and coherent structures;
- vi) the hypothesis of a possible a mechanism in which large length scale turbulence affects the aerodynamic behaviour.

8.1. Original Research Contribution

The final research contributions from this thesis regards primarily the assessment of suitable techniques to generate inlet turbulence in physical and numerical simulations of urban wind energy related research. A framework is established for the investigation of the independent effect of turbulence intensity and integral length scale of turbulence. This study contributes on an advancement of the understanding of the mechanism due to which turbulent structures of an inflow affect the aerodynamic performance. Results in this study might lead to further future research on the effect of turbulence found in the built environment on the aerodynamic behaviour of bluff bodies.

The main research contributions are listed as follows:

- i) the generation of turbulence having intensity and length scale varied separately in wind tunnel testing, using an expansion section placed downstream of a passive grid;
- ii) the investigation on the independent effect of TI and LS on the aerodynamics of a wind turbine aerofoil ($I \sim 15\%$ and $L/c \sim 2.7$);
- iii) the generation of realistic inlet turbulence using available turbulent inlet generation techniques to extend a wind tunnel experiment ($I \sim 15\%$ and $L/c \sim 15$);
- iv) the assessment with CFD and wind tunnel of the signature turbulence with reference to LS both on an isolated high-rise building and on a realistic urban configuration (University Campus);
- v) the post-processing and validation of large eddy simulation results with respect to high-order statistics, feature extraction methods (POD), and coherent structures;
- vi) the hypothesis of a possible a mechanism in which large length scale turbulence affects the aerodynamic behaviour.

8.2. Further steps of the research

Results from Chapters 6 and 7 are most certainly not sufficient to expand on the implications of a turbulent flow having large length scale and the subsequent aerodynamic behaviour of a wind turbine aerofoil and its related physical mechanism. However, it is clear from this research that the negligibility of atmospheric turbulence in the aerodynamic design of wind energy converters has no foundation on the basis that the integral length scale is larger than the body of interest. This thesis confirms that under a flow as found in the built environment, a large turbulence length scale enhances the effect of turbulence, provided that turbulence intensity reaches a sufficiently high, or critical, value.

In physical terms, the kinetic energy distribution of a large scale turbulent flow is mostly concentrated at frequencies corresponding to the integral length scales. These scales are not comparable with the scale of the boundary and shear layer existing around a bluff body. Nevertheless, some energy is available, and it spans smaller scales at much higher frequency, which this study proves are able to affect the behaviour of the boundary layer. The definition of a critical turbulence intensity $I_{u,cr}$, in the

same way as done in terms of Reynolds effects, might be the key to understand the interaction with a boundary layer and the definition of turbulence effects regimes.

It is also significant as evident from Figure 6.5, that Reynolds effects disappear in the presence of a turbulent inlet, although this study not specifically designed to prove this aspect does not shed light on whether this only occurs at small length scales or otherwise. Nevertheless, it is evident how turbulence affects the behaviour of the boundary layer to a greater extent than the mean velocity, and this justifies the need for more research to understand the implications of a turbulent flow having large length scale in engineering applications. Indeed as dramatically evident in Figure 6.1, turbulence is deemed responsible for a large decrease in the power output of a wind turbine ever placed in a location where turbulence might be present, and available methods to taken into account the low-frequency energy content in terms of fluctuating directionality due to large scale turbulence is clearly not enough to explain the tremendous lack in performance.

References

- Abd Razak, A., Hagishima, A., Ikegaya, N., Tanimoto, J., 2013. Analysis of airflow over building arrays for assessment of urban wind environment. *Build. Environ.* 59, 56–65.
- Abohela, I., Hamza, N., Dudek, S., 2013. Effect of roof shape, wind direction, building height and urban configuration on the energy yield and positioning of roof mounted wind turbines. *Renew. Energy* 50, 1106–1118.
- Ackermann, T., Andersson, G., Söder, L., 2001. Distributed generation: a definition. *Electr. Power Syst. Res.* 57, 195–204.
- Adamek, K., Vasan, N., Elshaer, A., English, E., Bitsuamlak, G., 2017. Pedestrian level wind assessment through city development: A study of the financial district in Toronto. *Sustain. Cities Soc.* 35, 178–190.
- Almohammadi, K.M., Ingham, D.B., Ma, L., Pourkashanian, M., 2015. Modeling dynamic stall of a straight blade vertical axis wind turbine. *J. Fluids Struct.* 57, 144–158.
- Amandolèse, X., Széchényi, E., 2004. Experimental study of the effect of turbulence on a section model blade oscillating in stall. *Wind Energy* 7, 267–282.
- Antoniou, I., Asimakopoulos, D., Fragoulis, A., Kotronaros, A., Lalas, D.P., Panourgias, I., 1992. Turbulence measurements on top of a steep hill. *J. Wind Eng. Ind. Aerodyn.* 39, 343–355.
- Antrobus, D., 2011. Smart green cities: from modernization to resilience? *Urban Res. Pract.* 4, 207–214.
- Arie, M., Kiya, M., Suzuki, Y., Hagino, M., Takahashi, K., 1981. Characteristics of Circular Cylinders in Turbulent Flows. *Bull. Japan Soc. Mech. Eng.* 24, 640–647.
- Arnfield, a. J., 2003. Two decades of urban climate research: A review of turbulence, exchanges of energy and water, and the urban heat island. *Int. J. Climatol.* 23, 1–26.
- Atkinson, B.W., 2003. Numerical modelling of urban heat-island intensity. *Boundary-Layer Meteorol.* 109, 285–310.
- Ayhan, D., Sağlam, Ş., 2012. A technical review of building-mounted wind power systems and a sample simulation model. *Renew. Sustain. Energy Rev.* 16, 1040–1049.
- Baines, W.D., Peterson, E.G., 1951. An investigation of flow through screens. *Trans. ASME* 73, 467–80.
- Bak, C., 2007. Sensitivity of Key Parameters in Aerodynamic Wind Turbine Rotor Design on Power and Energy Performance. *J. Phys. Conf. Ser.* 75, 012008.
- Baker, C., 2015. Risk analysis of pedestrian and vehicle safety in windy environments. *J. Wind Eng. Ind. Aerodyn.* 147, 283–290.
- Baker, C.J., 2000. Aspects of the use of proper orthogonal decomposition of surface pressure fields. *Wind Struct.* 3, 97–115.
- Baker, C.J., 2007. Wind engineering—Past, present and future. *J. Wind Eng. Ind. Aerodyn.* 95, 843–870.
- Balduzzi, F., Bianchini, A., Ferrari, L., 2012. Microeolic turbines in the built environment: Influence of the installation site on the potential energy yield. *Renew. Energy* 45, 163–174.
- Bandyopadhyay, S., 2019. The first step towards energy revolution. *Clean Technol. Environ. Policy* 21, 227–228.
- Banerjee, S., Krahl, R., Durst, F., Zenger, C., 2007. Presentation of anisotropy properties of turbulence, invariants versus eigenvalue approaches. *J. Turbul.* 8, N32.
- Baniotopoulos, C., Borri, C., 2015. Wind Energy Technology reconsideration to enhance the concept of smart

- cities. In: WORKSHOP Trends and Challenges for Wind Energy Harvesting. Coimbra, pp. 7–12.
- Baniotopoulos, C.C., Borri, C., Stathopoulos, T., 2011. Environmental Wind Engineering and Design of Wind Energy Structures. Springer-Verlag.
- Baniotopoulos, C.C., Stathopoulos, T., 2007. Wind Effects on Buildings and Design of Wind-Sensitive Structures. Springer-Verlag, Wien.
- Batchelor, G.K., 1953. The Theory of Homogeneous Turbulence. Cambridge University Press.
- BBC, 2017. Wind death in Leeds prompts tower safety fears [WWW Document]. URL <https://www.bbc.co.uk/news/uk-england-leeds-12717762>
- Bearman, P.W., Morel, T., 1983. Effect of free stream turbulence on the flow around bluff bodies. Prog. Aerosp. Sci. 20, 97–123.
- Bereketab, S., Wang, H.-W., Mish, P., Devenport, W.J., 2000. The Surface Pressure Response of a NACA 0015 Airfoil Immersed in Grid Turbulence. Volume 1; Characteristics of the Turbulence.
- Berkooz, G., Holmes, P., Lumley, J.L., 1993. The Proper Orthogonal Decomposition in the Analysis of Turbulent Flows. Annu. Rev. Fluid Mech. 25, 539–575.
- Bernhammer, L.O., van Kuik, G.A.M., De Breuker, R., 2016. Fatigue and extreme load reduction of wind turbine components using smart rotors. J. Wind Eng. Ind. Aerodyn. 154, 84–95.
- Blackmore, T., Batten, W.M.J., Bahaj, A.S., 2013. Inlet grid-generated turbulence for large-eddy simulations. Int. J. Comput. Fluid Dyn. 27, 307–315.
- Blazquez, J., Fuentes-Bracamontes, R., Bollino, C.A., Nezamuddin, N., 2018. The renewable energy policy Paradox. Renew. Sustain. Energy Rev. 82, 1–5.
- Blocken, B., 2014. 50 years of Computational Wind Engineering: Past, present and future. J. Wind Eng. Ind. Aerodyn. 129, 69–102.
- Blocken, B., 2015. Computational Fluid Dynamics for urban physics: Importance, scales, possibilities, limitations and ten tips and tricks towards accurate and reliable simulations. Build. Environ. 91, 219–245.
- Blocken, B., 2018. LES over RANS in building simulation for outdoor and indoor applications: A foregone conclusion? Build. Simul. 11, 821–870.
- Blocken, B., Stathopoulos, T., Carmeliet, J., 2007. CFD simulation of the atmospheric boundary layer: wall function problems. Atmos. Environ. 41, 238–252.
- Blocken, B., Stathopoulos, T., van Beeck, J.P.A.J., 2016. Pedestrian-level wind conditions around buildings: Review of wind-tunnel and CFD techniques and their accuracy for wind comfort assessment. Build. Environ. 100, 50–81.
- Bogdanov, D., Toktarova, A., Breyer, C., 2019. Transition towards 100% renewable power and heat supply for energy intensive economies and severe continental climate conditions: Case for Kazakhstan. Appl. Energy 253, 113606.
- Bogle, I., 2011. Integrating wind turbines in tall buildings. CTBUH J. 4, 30–33.
- Bottema, M., 2000. A method for optimisation of wind discomfort criteria. Build. Environ. 35, 1–18.
- Bradshaw, P., Pankhurst, R.C., 1964. The design of low-speed wind tunnels. Prog. Aerosp. Sci. 5, 1–69.
- Brzek, B., Torres-Nieves, S., Lebrón, J., Cal, R., Meneveau, C., Castillo, L., 2009. Effects of free-stream turbulence on rough surface turbulent boundary layers. J. Fluid Mech. 635, 207.
- Buresti, G., 2012. Elements of Fluid Dynamics. Imperial College Press, London.

- Burton, T., Sharpe, D., Jenkins, N., Bossanyi, E., 2011. *Wind Energy Handbook*. John Wiley & Sons, Ltd, New York.
- Cal, R.B., Lebr n, J., Castillo, L., Kang, H.S., Meneveau, C., 2010. Experimental study of the horizontally averaged flow structure in a model wind-turbine array boundary layer. *J. Renew. Sustain. Energy* 2, 013106.
- Carassale, L., Marré Brunenghi, M., 2011. Statistical analysis of wind-induced pressure fields: A methodological perspective. *J. Wind Eng. Ind. Aerodyn.* 99, 700–710.
- Carbó Molina, A., Bartoli, G., De Troyer, T., 2017. Wind Tunnel testing of small Vertical-Axis Wind Turbines in Turbulent Flows. In: *Procedia Engineering, X International Conference on Structural Dynamics, EUROODYN 2017*. Elsevier, Rome, pp. 3176–3181.
- Carrasco, J.M., Franquelo, L.G., Bialasiewicz, J.T., Galvan, E., PortilloGuisado, R.C., Prats, M.A.M., Leon, J.I., Moreno-Alfonso, N., 2006. Power-Electronic Systems for the Grid Integration of Renewable Energy Sources: A Survey. *IEEE Trans. Ind. Electron.* 53, 1002–1016.
- Cebeci, T., Mosinskis, G.J., Smith, A.M.O., 1972. Calculation of Separation Points in Incompressible Turbulent Flows. *J. Aircr.* 9, 618–624.
- Cekli, H.E., van de Water, W., 2010. Tailoring turbulence with an active grid. *Exp. Fluids* 49, 409–416.
- Chamorro, L.P., Porté-Agel, F., 2011. Turbulent Flow Inside and Above a Wind Farm: A Wind-Tunnel Study. *Energies* 4, 1916–1936.
- Chaudhari, A., 2014. Large-eddy simulation of wind flows over complex terrains for wind energy applications. Lappeenranta University of Technology.
- Chaudhari, A., Hellsten, A., Hämäläinen, J., 2016. Full-Scale Experimental Validation of Large-Eddy Simulation of Wind Flows over Complex Terrain: The Bolund Hill. *Adv. Meteorol.* 2016, 1–14.
- Chel, A., Kaushik, G., 2018. Renewable energy technologies for sustainable development of energy efficient building. *Alexandria Eng. J.* 57, 655–669.
- Christiansen, M.B., Hasager, C.B., 2005. Wake effects of large offshore wind farms identified from satellite SAR. *Remote Sens. Environ.* 98, 251–268.
- Chung, Y.M., Sung, H.J., 1997. Comparative Study of Inflow Conditions for Spatially Evolving Simulation. *AIAA J.* 35, 269–274.
- Comte-Bellot, G., Corrsin, S., 1966. The use of a contraction to improve the isotropy of grid-generated turbulence. *J. Fluid Mech.* 25, 657.
- Conan, B., 2012. Wind resource assessment in complex terrain by wind tunnel modelling. Orléans.
- Conan, B., Chaudhari, A., Aubrun, S., van Beeck, J., Hämäläinen, J., Hellsten, A., 2016. Experimental and Numerical Modelling of Flow over Complex Terrain: The Bolund Hill. *Boundary-Layer Meteorol.* 158, 183–208.
- Dabiri, J.O., Greer, J.R., Koseff, J.R., Moin, P., Peng, J., 2015. A new approach to wind energy: Opportunities and challenges. In: *AIP Conference Proceedings*. American Institute of Physics, pp. 51–57.
- Dadioti, R., Rees, S., 2017. Performance of Detached Eddy Simulation applied to Analysis of a University Campus Wind Environment. *Energy Procedia* 134, 366–375.
- David, M., 2017. Moving beyond the heuristic of creative destruction: Targeting exnovation with policy mixes for energy transitions. *Energy Res. Soc. Sci.* 33, 138–146.
- Davidson, D.J., 2019. Exnovating for a renewable energy transition. *Nat. Energy* 4, 254–256.

- Davidson, L., 2008. Hybrid LES-RANS: Inlet Boundary Conditions for Flows with Recirculation. In: *Advances in Hybrid RANS-LES Modelling*. Springer Berlin Heidelberg, Berlin, Heidelberg, pp. 55–66.
- Davidson, P.A., 2004. *Turbulence: An Introduction for Scientists and Engineers*. OUP Oxford.
- Dayan, E., 2006. Wind energy in buildings: Power generation from wind in the urban environment - where it is needed most. *Refocus* 7, 33–38.
- de Karman, T., Howarth, L., 1938. On the Statistical Theory of Isotropic Turbulence. *Proc. R. Soc. London A Math. Phys. Eng. Sci.* 164.
- De Villiers, E., 2006. *The Potential of Large Eddy Simulation for the Modeling of Wall Bounded Flows*. Imperial College London.
- Dekker, J.W.M., Pierik, J.T.G., 1998. *European Wind Turbine Standards II*.
- deLlano-Paz, F., Calvo-Silvosa, A., Iglesias Antelo, S., Soares, I., 2015. The European low-carbon mix for 2030: The role of renewable energy sources in an environmentally and socially efficient approach. *Renew. Sustain. Energy Rev.* 48, 49–61.
- Devenport, W., Burdisso, R.A., Camargo, H., Crede, E., Remillieux, M., Rasnick, M., Van Seeters, P., 2010. *Aeroacoustic Testing of Wind Turbine Airfoils: February 20, 2004 - February 19, 2008*. Blacksburg, Virginia.
- Devinant, P., Laverne, T., Hureau, J., 2002. Experimental study of wind-turbine airfoil aerodynamics in high turbulence. *J. Wind Eng. Ind. Aerodyn.* 90, 689–707.
- Devine-Wright, P., 2005. Beyond NIMBYism: towards an integrated framework for understanding public perceptions of wind energy. *Wind Energy* 8, 125–139.
- Díaz-González, F., Sumper, A., Gomis-Bellmunt, O., Villafañila-Robles, R., 2012. A review of energy storage technologies for wind power applications. *Renew. Sustain. Energy Rev.*
- Díaz, G., Coto, J., Gómez-Aleixandre, J., 2019. Optimal operation value of combined wind power and energy storage in multi-stage electricity markets. *Appl. Energy* 235, 1153–1168.
- Droste, A.M., Steeneveld, G.J., Holtslag, A.A.M., 2018. Introducing the urban wind island effect. *Environ. Res. Lett.* 13, 094007.
- Drysdale, D., Vad Mathiesen, B., Lund, H., 2019. From Carbon Calculators to Energy System Analysis in Cities. *Energies* 12, 2307.
- Emeis, S., 2013. *Wind Energy Meteorology. Atmospheric Physics for Wind Power Generation*, Springer-Verlag, Green Energy and Technology. Springer Berlin Heidelberg, Berlin, Heidelberg.
- Emeis, S., 2014. Current issues in wind energy meteorology. *Meteorol. Appl.* 21, 803–819.
- Essel, E.E., Tachie, M.F., 2015. Roughness effects on turbulent flow downstream of a backward facing step. *Flow, Turbul. Combust.* 94, 125–153.
- Estrella, R., Belgioioso, G., Grammatico, S., 2019. A shrinking-horizon, game-theoretic algorithm for distributed energy generation and storage in the smart grid with wind forecasting. *IFAC-PapersOnLine* 52, 126–131.
- Evans, B., Parks, J., Theobald, K., 2011. Urban wind power and the private sector: community benefits, social acceptance and public engagement. *J. Environ. Plan. Manag.* 54, 227–244.
- Evans, S.P., KC, A., Bradney, D.R., Urmee, T.P., Whale, J., Clausen, P.D., 2017. The suitability of the IEC 61400-2 wind model for small wind turbines operating in the built environment. *Renew. Energy Environ. Sustain.* 2, 31.

References

- Fathali, M., Klein, M., Broeckhoven, T., Lacor, C., Baelmans, M., 2008. Generation of turbulent inflow and initial conditions based on multi-correlated random fields. *Int. J. Numer. Methods Fluids* 57, 93–117.
- Fichaux, N., Frandsen, S., Sørensen, J.D., Eecen, P., Malamatenlos, C., Arteaga Gomez, J., Hemmelmann, J., van Kuik, G., Bulder, B., Rasmussen, F., Janssen, B., Fischer, T., Bossanyi, E., Courtney, M., Giebhardt, J., Barthelmie, R., Holmstrøm, O., 2011. UpWind - Design limits and solutions for very large wind turbines.
- Finley-Brook, M., Holloman, E., 2016. Empowering Energy Justice. *Int. J. Environ. Res. Public Health* 13, 926.
- Frandsen, S.T., 2007. Turbulence and turbulence-generated structural loading in wind turbine clusters.
- Franke, J., Hellsten, A., Schlunzen, K.H., Carissimo, B., 2011. The COST 732 Best Practice Guideline for CFD simulation of flows in the urban environment: a summary. *Int. J. Environ. Pollut.* 44, 419.
- Franke, J., Hirsch, C., Jensen, A.G., Krüs, H.W., Schatzmann, M., Westbury, P.S., Miles, S.D., Wisse, J.A., Wright, N.G., 2004. Recommendations on the use of CFD in wind engineering. In: van Beeck, J.P.A.J. (Ed.), COST Action C14, Impact of Wind and Storm on City Life Built Environment.
- Frenkiel, F.N., Klebanoff, P.S., Huang, T.T., 1979. Grid turbulence in air and water. *Phys. Fluids* 22, 1606.
- Freudenreich, K., Kaiser, K., Schaffarczyk, A.P., Winkler, H., Stahl, B., 2004. Reynolds Number and Roughness Effects on Thick Airfoils for Wind Turbines. *Wind Eng.* 28, 529–546.
- Fuglsang, P., Bak, C., Schepers, J.G., Bulder, B., Cockerill, T.T., Claiden, P., Olesen, a., van Rossen, R., 2002. Site-specific Design Optimization of Wind Turbines. *Wind Energy* 5, 261–279.
- Galvao, J.R., Moreira, L.M., Ascenso, R.M.T., Leitao, S.A., 2015. Energy systems models for efficiency towards Smart Cities. In: IEEE EUROCON 2015 - International Conference on Computer as a Tool (EUROCON). IEEE, pp. 1–6.
- Gartshore, I., 1984. Some effects of upstream turbulence on the unsteady lift forces imposed on prismatic two dimensional bodies. *J. Fluids Eng.*
- Gasch, R., Tvele, J., 2012. *Wind Power Plants: Fundamentals, Design, Construction and Operation*, 2nd ed. Springer-Verlag, Berlin, Heidelberg.
- George, W.K., 1992. The decay of homogeneous isotropic turbulence. *Phys. Fluids A Fluid Dyn.* 4, 1492–1509.
- George, W.K., 2012. Asymptotic Effect of Initial and Upstream Conditions on Turbulence. *J. Fluids Eng.* 134, 061203.
- Geyer, T.F., Sarradj, E., Hobracht, M., 2016. Noise generated by a leading edge in anisotropic turbulence. In: 45th International Congress on Noise Control Engineering (Inter.Noise 2016). Hamburg.
- Gilling, L., Sørensen, N.N., Davidson, L., 2009. Detached eddy simulations of an airfoil in turbulent inflow. In: 47th AIAA Aerospace Science Meeting Including The New Horizons Forum and Aerospace Exposition. pp. 1–13.
- Goldthau, A., Sovacool, B.K., 2012. The uniqueness of the energy security, justice, and governance problem. *Energy Policy* 41, 232–240.
- Gottschall, J., Peinke, J., 2007. Stochastic modelling of a wind turbine's power output with special respect to turbulent dynamics. *J. Phys. Conf. Ser.* 75, 012045.
- Gousseau, P., Blocken, B., Stathopoulos, T., van Heijst, G.J.F., 2011. CFD simulation of near-field pollutant dispersion on a high-resolution grid: A case study by LES and RANS for a building group in downtown Montreal. *Atmos. Environ.* 45, 428–438.
- Grant, A., Johnstone, C., Kelly, N., 2008. Urban wind energy conversion: The potential of ducted turbines. *Renew.*

- Energy 33, 1157–1163.
- Grauthoff, M., 1991. Utilization of wind energy in urban areas — Chance or utopian dream? *Energy Build.* 16, 517–523.
- Gross, A., Fasel, H.F., Friederich, T., Kloker, M.J., 2012. Numerical investigation of rotational augmentation for S822 wind turbine airfoil. *Wind Energy* 15, 983–1007.
- Grosspietsch, D., Saenger, M., Girod, B., 2019. Matching decentralized energy production and local consumption: A review of renewable energy systems with conversion and storage technologies. *Wiley Interdiscip. Rev. Energy Environ.* 8, e336.
- Gsänger, S., Pitteloud, J.-D., 2015. *Small Wind World Report 2015*.
- Guntur, S., Sørensen, N.N., Schreck, S., Bergami, L., 2016. Modeling dynamic stall on wind turbine blades under rotationally augmented flow fields. *Wind Energy* 19, 383–397.
- Haan, F.L., Kareem, A., 2009. Anatomy of Turbulence Effects on the Aerodynamics of an Oscillating Prism. *J. Eng. Mech.* 135, 987–999.
- Haan, F.L., Kareem, A., Szewczyk, A.A., 1998. The effects of turbulence on the pressure distribution around a rectangular prism. *J. Wind Eng. Ind. Aerodyn.* 77–78, 381–392.
- Haarstad, H., Wathne, M.W., 2019. Are smart city projects catalyzing urban energy sustainability? *Energy Policy* 129, 918–925.
- Hall, N., Ashworth, P., Devine-Wright, P., 2013. Societal acceptance of wind farms: Analysis of four common themes across Australian case studies. *Energy Policy* 58, 200–208.
- Hamza, N., 2015. Urban wind energy: exposing sustainability symbolism or a hidden existence. In: *Trends and Challenges for Wind Energy Harvesting: Workshop*. Coimbra, Portugal.
- Hancock, P.E., Bradshaw, P., 1983. The Effect of Free-Stream Turbulence on Turbulent Boundary Layers. *J. Fluids Eng.* 105, 284.
- Hand, M.M., Kelley, N.D., Balas, M.J., 2003. Identification of Wind Turbine Response to Turbulence Inflow Structures. In: *4th ASME/JSME Joint Fluids Engineering Conference*. Honolulu, Hawaii, p. 13.
- Hanjalic, K., 2005. Will RANS Survive LES? A View of Perspectives. *J. Fluids Eng.* 127, 831.
- Hansen, K., Breyer, C., Lund, H., 2019. Status and perspectives on 100% renewable energy systems. *Energy* 175, 471–480.
- Hansen, K.S., Barthelmie, R.J., Jensen, L.E., Sommer, A., 2012. The impact of turbulence intensity and atmospheric stability on power deficits due to wind turbine wakes at Horns Rev wind farm. *Wind Energy* 15, 183–196.
- Hansen, M., 2015. *Aerodynamics of wind turbines*.
- Hansen, M.H., 2007. Aeroelastic instability problems for wind turbines. *Wind Energy* 10, 551–577.
- Hansen, M.O.L., Aagaard Madsen, H., 2011. Review Paper on Wind Turbine Aerodynamics. *J. Fluids Eng.* 133, 114001.
- Hansen, M.O.L., Sørensen, J.N., Voutsinas, S., Sørensen, N.N., Madsen, H.A., 2006. State of the art in wind turbine aerodynamics and aeroelasticity. *Prog. Aerosp. Sci.* 42, 285–330.
- Harms, F., Berbekar, E., Lübcke, M., Leitl, B., 2013. Flow and dispersion processes in an idealized urban roughness. In: *PHYSMOD 2013 – International Workshop on Physical Modeling of Flow and Dispersion Phenomena*. Surrey, UK.

- Hasager, C., Rasmussen, L., Peña, A., Jensen, L., Réthoré, P.-E., Hasager, C.B., Rasmussen, L., Peña, A., Jensen, L.E., Réthoré, P.-E., 2013. Wind Farm Wake: The Horns Rev Photo Case. *Energies* 6, 696–716.
- Hatuka, T., Rosen-Zvi, I., Birmhack, M., Toch, E., Zur, H., 2018. The Political Premises of Contemporary Urban Concepts: The Global City, the Sustainable City, the Resilient City, the Creative City, and the Smart City. *Plan. Theory Pract.* 19, 160–179.
- Hau, E., 2013. *Wind turbines: Fundamentals, technologies, application, economics*, 3rd ed, Springer-Verlag. Berlin Heidelberg.
- Hdidouan, D., Staffell, I., 2017. The impact of climate change on the levelised cost of wind energy. *Renew. Energy* 101, 575–592.
- He, J., Song, C.C., 1999. Evaluation of pedestrian winds in urban area by numerical approach. *J. Wind Eng. Ind. Aerodyn.* 81, 295–309.
- Hemida, H., 2014. Large-eddy simulation of the above roof flow of a high-rise building for micro-wind turbines. In: 11th UK Conference on Wind Engineering.
- Hemida, H., 2016. On the Understanding of the Above Roof Flow of a High-rise Building for Wind Energy Generation. In: SBE16 - Europe and the Mediterranean Towards a Sustainable Built Environment. Malta.
- Hemida, H., Krajnović, S., 2010. LES study of the influence of the nose shape and yaw angles on flow structures around trains. *J. Wind Eng. Ind. Aerodyn.* 98, 34–46.
- Hemida, H., Šarkic, A., Gillmeier, S., Höffer, R., 2014. Experimental investigation of wind flow above the roof of high-rise building. In: WINERCOST Workshop “Trends and Challenges for Wind Energy Harvesting.” Coimbra, Portugal, p. p.25-34.
- Hemida, H., Šarkic, A., Höffer, R., 2015. Interference effect of high-rise buildings for wind energy extraction; wind tunnel and numerical investigations. In: 14th International Conference on Wind Engineering. Porto Alegre, Brazil.
- Hertwig, D., Patnaik, G., Leitl, B., 2017. LES validation of urban flow, part II: eddy statistics and flow structures. *Environ. Fluid Mech.* 17, 551–578.
- Hevia-Koch, P., Ladenburg, J., 2019. Where should wind energy be located? A review of preferences and visualisation approaches for wind turbine locations. *Energy Res. Soc. Sci.*
- Hidalgo, J., Masson, V., Baklanov, A., Pigeon, G., Gimeno, L., 2008. Advances in urban climate modeling. *Ann. N. Y. Acad. Sci.* 1146, 354–374.
- Hinze, J.O., 1975. *Turbulence*. McGraw-Hill.
- Hoffmann, J.A., 1981. Effects of Free-Stream Turbulence on Diffuser Performance. *J. Fluids Eng.* 103, 385.
- Hoffmann, J.A., 1991. Effects of freestream turbulence on the performance characteristics of an airfoil. *AIAA J.* 29, 1353–1354.
- Hölling, M., Peinke, J., Ivanell, S. (Eds.), 2014. *Wind Energy - Impact of Turbulence*, Research Topics in Wind Energy. Springer-Verlag, Berlin, Heidelberg.
- Holmes, J.D., 1990. Analysis and synthesis of pressure fluctuations on bluff bodies using eigenvectors. *J. Wind Eng. Ind. Aerodyn.* 33, 219–230.
- Hou, P., Enevoldsen, P., Hu, W., Chen, C., Chen, Z., 2017. Offshore wind farm repowering optimization. *Appl. Energy* 208, 834–844.
- Hu, W., Letson, F., Barthelmie, R.J., Pryor, S.C., Hu, W., Letson, F., Barthelmie, R.J., Pryor, S.C., 2018. Wind

References

- Gust Characterization at Wind Turbine Relevant Heights in Moderately Complex Terrain. *J. Appl. Meteorol. Climatol.* 57, 1459–1476.
- Huang, R.F., Lee, H.W., 1999. Effects of Freestream Turbulence on Wing-Surface Flow and Aerodynamic Performance. *J. Aircr.* 36, 965–972.
- Hurst, D., Vassilicos, J.C., 2007. Scalings and decay of fractal-generated turbulence. *Phys. Fluids* 19, 035103.
- Hussein, H.J., Capp, S.P., George, W.K., 1994. Velocity measurements in a high-Reynolds-number, momentum-conserving, axisymmetric, turbulent jet. *J. Fluid Mech.* 258, 31.
- IEC 61400-1:2019 Wind energy generation systems - Part 1: Design requirements, 2019.
- IEC 61400-2:2013 Wind turbines - Part 2: Small wind turbines, 2013.
- Ikeda, Y., Hagishima, A., Ikegaya, N., Tanimoto, J., Razak, A.A., 2015. Estimation of Wind Speed in Urban Pedestrian Spaces on the Basis of Large-Eddy Simulation. *J. Environ. Eng. (Transactions AIJ)* 80, 259–267.
- Ikegaya, N., Ikeda, Y., Hagishima, A., Razak, A.A., Tanimoto, J., 2017. A prediction model for wind speed ratios at pedestrian level with simplified urban canopies. *Theor. Appl. Climatol.* 127, 655–665.
- Immer, M.C., 2016. Time-resolved measurement and simulation of local scale turbulent urban flow. ETH-Zürich.
- Isaza, J.C., Salazar, R., Warhaft, Z., 2014. On grid-generated turbulence in the near- and far field regions. *J. Fluid Mech.* 753, 402–426.
- Ishugah, T.F., Li, Y., Wang, R.Z., Kiplagat, J.K., 2014. Advances in wind energy resource exploitation in urban environment: A review. *Renew. Sustain. Energy Rev.* 37, 613–626.
- Isyumov, N., Davenport, A.G., 1976. The Ground Level Wind Environment in Built Up Areas. In: *Proceedings of the Fourth International Conference on Wind Effects on Buildings and Structures*. Cambridge University Press, U.K., pp. 403–422.
- Jacob, J., Sagaut, P., 2018. Wind comfort assessment by means of large eddy simulation with lattice Boltzmann method in full scale city area. *Build. Environ.* 139, 110–124.
- Jacobson, M.Z., Delucchi, M.A., 2011. Providing all global energy with wind, water, and solar power, Part I: Technologies, energy resources, quantities and areas of infrastructure, and materials. *Energy Policy* 39, 1154–1169.
- Jacobsson, S., Bergek, A., Finon, D., Lauber, V., Mitchell, C., Toke, D., Verbruggen, A., 2009. EU renewable energy support policy: Faith or facts? *Energy Policy* 37, 2143–2146.
- Jangamshetti, S.H., Ran, V.G., 2001. Optimum siting of wind turbine generators. *IEEE Trans. Energy Convers.* 16, 8–13.
- Jarrin, N., Benhamadouche, S., Laurence, D., Prosser, R., 2006. A synthetic-eddy-method for generating inflow conditions for large-eddy simulations. *Int. J. Heat Fluid Flow* 27, 585–593.
- Jovanović, J., 2004. *The Statistical Dynamics of Turbulence*. Springer-Verlag, Berlin, Heidelberg, New York.
- Junker, R.G., Azar, A.G., Lopes, R.A., Lindberg, K.B., Reynders, G., Relan, R., Madsen, H., 2018. Characterizing the energy flexibility of buildings and districts. *Appl. Energy* 225, 175–182.
- Kaimal, J.C., Wyngaard, J.C., Haugen, D.A., Coté, O.R., Izumi, Y., Caughey, S.J., Readings, C.J., 1976. Turbulence Structure in the Convective Boundary Layer. *J. Atmos. Sci.*
- Kaiser, K., Langreder, W., Hohlen, H., Højstrup, J., 2007. Turbulence correction for power curves. *Wind Energy*.
- Kanda, M., 2007. Progress in Urban Meteorology :A Review. *J. Meteorol. Soc. Japan* 85B, 363–383.
- Kang, H.S., Chester, S., Meneveau, C., 2003. Decaying turbulence in an active-grid-generated flow and

- comparisons with large-eddy simulation. *J. Fluid Mech.* 480, 129–160.
- Kareem, A., Wu, T., 2013. Wind-induced effects on bluff bodies in turbulent flows: Nonstationary, non-Gaussian and nonlinear features. *J. Wind Eng. Ind. Aerodyn.* 122, 21–37.
- KC, A., Whale, J., Urmee, T., 2019. Urban wind conditions and small wind turbines in the built environment: A review. *Renew. Energy* 131, 268–283.
- Kelly, M., Larsen, G., Dimitrov, N.K., Natarajan, A., 2014. Probabilistic Meteorological Characterization for Turbine Loads. *J. Phys. Conf. Ser.* 524, 012076.
- Khayrullina, a, van Hooff, T. a J., Blocken, B.J.E., 2013. A study on the wind energy potential in passages between parallel buildings 1-8 BT-Proceedings of the 6th European-African.
- Kim, J.W., Haeri, S., Joseph, P.F., 2016. On the reduction of aerofoil–turbulence interaction noise associated with wavy leading edges. *J. Fluid Mech.* 792, 526–552.
- Kim, S.-H., Shin, H.-K., Joo, Y.-C., Kim, K.-H., 2015. A study of the wake effects on the wind characteristics and fatigue loads for the turbines in a wind farm. *Renew. Energy* 74, 536–543.
- Kim, Y., Castro, I.P., Xie, Z.-T., 2013. Divergence-free turbulence inflow conditions for large-eddy simulations with incompressible flow solvers. *Comput. Fluids* 84, 56–68.
- Kim, Y., Xie, Z.-T., 2016. Modelling the effect of freestream turbulence on dynamic stall of wind turbine blades. *Comput. Fluids* 129, 53–66.
- Kistler, A.L., Vrebalovich, T., 2006. Grid turbulence at large Reynolds numbers. *J. Fluid Mech.* 26, 37.
- Kiya, M., Sasaki, K., 1985. Structure of a turbulent separation bubble. *J. Fluid Mech.* 137, 83.
- Klein, M., Sadiki, A., Janicka, J., 2003. A digital filter based generation of inflow data for spatially developing direct numerical or large eddy simulations. *J. Comput. Phys.* 186, 652–665.
- Kolokotsa, D., 2016. The role of smart grids in the building sector. *Energy Build.* 116, 703–708.
- Kosasih, B., Saleh Hudin, H., 2016. Influence of inflow turbulence intensity on the performance of bare and diffuser-augmented micro wind turbine model. *Renew. Energy* 87, 154–167.
- Kozmar, H., Allori, D., Bartoli, G., Borri, C., 2016. Complex terrain effects on wake characteristics of a parked wind turbine. *Eng. Struct.* 110, 363–374.
- Kruyt, B., Dujardin, J., Lehning, M., 2018. Improvement of Wind Power Assessment in Complex Terrain: The Case of COSMO-1 in the Swiss Alps. *Front. Energy Res.* 6.
- Kubota, T., Miura, M., Tominaga, Y., Mochida, A., 2008. Wind tunnel tests on the relationship between building density and pedestrian-level wind velocity: Development of guidelines for realizing acceptable wind environment in residential neighborhoods. *Build. Environ.* 43, 1699–1708.
- Kurian, T., Fransson, J.H.M., 2009. Grid-generated turbulence revisited. *Fluid Dyn. Res.* 41, 021403.
- Kylili, A., Fokaides, P.A., 2015. European smart cities: The role of zero energy buildings. *Sustain. Cities Soc.* 15, 86–95.
- Lalas, D.P., 1985. Wind Energy Estimation and Siting in Complex Terrain. *Int. J. Sol. Energy* 3, 43–71.
- Laneville, A., 1973. Effects of turbulence on wind-induced vibrations of bluff cylinders. University of British Columbia, Vancouver, Canada.
- Laneville, A., Gartshore, I., Parkinson, G., 1975. An explanation of some effects of turbulence on bluff bodies. ... Fourth Int. Conf. Wind
- Larsen, J. V., Deavenport, W.J., 2011. On the generation of large-scale homogeneous turbulence. *Exp. Fluids* 50,

- 1207–1223.
- Lawson, T.V., Penwarden, A.D., 1976. The Effects of Wind on People in the Vicinity of Buildings. In: Proceedings of the Fourth International Conference on Wind Effects on Buildings and Structures. pp. 605–622.
- Lee, B.E., 1975. Some effects of turbulence scale on the mean forces on a bluff body. *J. Wind Eng. Ind. Aerodyn.* 1, 361–370.
- Lee, D.O., 1979. The influence of atmospheric stability and the urban heat island on urban-rural wind speed differences. *Atmos. Environ.* 13, 1175–1180.
- Lee, S., Churchfield, M., Moriarty, P., Jonkman, J., 2012. Atmospheric and wake turbulence impacts on wind turbine fatigue loadings.
- Leishman, J.G., 2000. Principles of Helicopter Aerodynamics, 2nd ed. Cambridge University Press, Cambridge, UK.
- Leishman, J.G., 2002a. Challenges in Modeling the Unsteady Aerodynamics of Wind Turbines. 21st ASME Wind Energy Symp. 40th AIAA Aerosp. Sci. Meet. 1–28.
- Leishman, J.G., 2002b. Challenges in modelling the unsteady aerodynamics of wind turbines. *Wind Energy* 5, 85–132.
- Letzel, M.O., Helmke, C., Ng, E., An, X., Lai, A., Raasch, S., 2012. LES case study on pedestrian level ventilation in two neighbourhoods in Hong Kong. *Meteorol. Zeitschrift* 21, 575–589.
- Li, Q., Kamada, Y., Maeda, T., Murata, J., Nishida, Y., 2016. Effect of turbulent inflows on airfoil performance for a Horizontal Axis Wind Turbine at low Reynolds numbers (Part II: Dynamic pressure measurement). *Energy* 112, 574–587.
- Lindeboom, R.C.J., 2010. Determination of unsteady loads on a DU96W180 airfoil with actuated flap using Particle Image Velocimetry.
- Liu, J., Niu, J., Du, Y., Mak, C.M., Zhang, Y., 2019. LES for pedestrian level wind around an idealized building array—Assessment of sensitivity to influencing parameters. *Sustain. Cities Soc.* 44, 406–415.
- Liu, J., Niu, J., Mak, C.M., Xia, Q., 2017. Detached eddy simulation of pedestrian-level wind and gust around an elevated building. *Build. Environ.* 125, 168–179.
- Liu, Q., Lei, Q., Xu, H., Yuan, J., 2018. China’s energy revolution strategy into 2030. *Resour. Conserv. Recycl.* 128, 78–89.
- Lu, L., Ip, K.Y., 2009. Investigation on the feasibility and enhancement methods of wind power utilization in high-rise buildings of Hong Kong. *Renew. Sustain. Energy Rev.* 13, 450–461.
- Lubitz, W.D., 2014. Impact of ambient turbulence on performance of a small wind turbine. *Renew. Energy* 61, 69–73.
- Luhur, M.R., Peinke, J., Schneemann, J., Wächter, M., 2015. Stochastic modeling of lift and drag dynamics under turbulent wind inflow conditions. *Wind Energy* 18, 317–337.
- Lumley, J.L., 1979. Computational Modeling of Turbulent Flows. *Adv. Appl. Mech.* 18, 123–176.
- Lund, H., 2007. Renewable energy strategies for sustainable development. *Energy* 32, 912–919.
- Lund, H., Østergaard, P.A., 2000. Electric grid and heat planning scenarios with centralised and distributed sources of conventional, CHP and wind generation. *Energy* 25, 299–312.
- Lund, T.S., Wu, X., Squires, K.D., 1998. Generation of Turbulent Inflow Data for Spatially-Developing Boundary

- Layer Simulations. *J. Comput. Phys.* 140, 233–258.
- Mainali, B., Silveira, S., 2013. Alternative pathways for providing access to electricity in developing countries. *Renew. Energy* 57, 299–310.
- Makita, H., 1991. Realization of a large-scale turbulence field in a small wind tunnel. *Fluid Dyn. Res.* 8, 53–64.
- Makita, H., Sassa, K., 1991. Active Turbulence Generation in a Laboratory Wind Tunnel. In: Johansson, A. V., Alfredsson, P.H. (Eds.), *Advances in Turbulence 3: Proceedings of the Third European Turbulence Conference Stockholm, July 3–6, 1990*. Springer Berlin Heidelberg, Berlin, Heidelberg, pp. 497–505.
- Maldonado, V., Castillo, L., Thormann, A., Meneveau, C., 2015. The role of free stream turbulence with large integral scale on the aerodynamic performance of an experimental low Reynolds number S809 wind turbine blade. *J. Wind Eng. Ind. Aerodyn.* 142, 246–257.
- Mannini, C., Marra, A.M., Pigolotti, L., Bartoli, G., 2017. The effects of free-stream turbulence and angle of attack on the aerodynamics of a cylinder with rectangular 5:1 cross section. *J. Wind Eng. Ind. Aerodyn.* 161, 42–58.
- Martin, S.L., 2009. Wind Farms and NIMBYs: Generating Conflict, Reducing Litigation. *Fordham Environ. Law Rev.* 20.
- Martínez, E., Sanz, F., Pellegrini, S., Jiménez, E., Blanco, J., 2009. Life cycle assessment of a multi-megawatt wind turbine. *Renew. Energy* 34, 667–673.
- Matyushenko, A.A., Kotov, E. V., Garbaruk, A. V., 2017. Calculations of flow around airfoils using two-dimensional RANS: an analysis of the reduction in accuracy. *St. Petersburg. Polytech. Univ. J. Phys. Math.* 3, 15–21.
- Mazria, E., 2003. It's the Architecture, Stupid! *Sol. Today* 48–51.
- McCauley, D., Ramasar, V., Heffron, R.J., Sovacool, B.K., Mebratu, D., Mundaca, L., 2019. Energy justice in the transition to low carbon energy systems: Exploring key themes in interdisciplinary research. *Appl. Energy* 233–234, 916–921.
- McKeough, P.J., 1976. Effects of turbulence on aerofoils at high incidence. University of London.
- Mehta, D., van Zuijlen, A.H., Koren, B., Holierhoek, J.G., Bijl, H., 2014. Large Eddy Simulation of wind farm aerodynamics: A review. *J. Wind Eng. Ind. Aerodyn.* 133, 1–17.
- Mehta, R.D., 1979. The aerodynamic design of blower tunnels with wide-angle diffusers. *Prog. Aerosp. Sci.* 18, 59–120.
- Melbourne, W.H., 1978. Criteria for environmental wind conditions. *J. Wind Eng. Ind. Aerodyn.* 3, 241–249.
- Melina, G., Bruce, P.J.K., Vassilicos, J.C., 2016. Vortex shedding effects in grid-generated turbulence. *Phys. Rev. Fluids* 1, 044402.
- Merlier, L., Jacob, J., Sagaut, P., 2018. Lattice-Boltzmann Large-Eddy Simulation of pollutant dispersion in street canyons including tree planting effects. *Atmos. Environ.* 195, 89–103.
- Mertens, S., 2006. Wind Energy in the Built Environment Concentrator Effects of Buildings Wind Energy in the Built Environment Concentrator Effects of Buildings 1–180.
- Miao, S., Li, P., Wang, X., 2009. Building morphological characteristics and their effect on the wind in Beijing. *Adv. Atmos. Sci.* 26, 1115–1124.
- Micallef, D., van Bussel, G., 2018. A Review of Urban Wind Energy Research: Aerodynamics and Other Challenges. *Energies* 11, 2204.

References

- Milan, P., Wächter, M., Peinke, J., 2013. Turbulent character of wind energy. *Phys. Rev. Lett.* 110, 138701.
- Miley, S., 1982. A catalog of low Reynolds number airfoil data for wind turbine applications.
- Millward-Hopkins, J.T., Tomlin, A.S., Ma, L., Ingham, D., Pourkashanian, M., 2012. The predictability of above roof wind resource in the urban roughness sublayer. *Wind Energy* 15, 225–243.
- Mish, P.F., Devenport, W.J., 2006. An experimental investigation of unsteady surface pressure on an airfoil in turbulence—Part 1: Effects of mean loading. *J. Sound Vib.* 296, 417–446.
- Mohamed, M.S., Larue, J.C., 1990. The decay power law in grid-generated turbulence. *J. Fluid Mech.* 219, 195.
- Morenko, I. V., Fedyayev, V.L., 2017. Influence of turbulence intensity and turbulence length scale on the drag, lift and heat transfer of a circular cylinder. *China Ocean Eng.* 31, 357–363.
- Mouzakis, F., Morfiadakis, E., Dellaportas, P., 1999. Fatigue loading parameter identification of a wind turbine operating in complex terrain. *J. Wind Eng. Ind. Aerodyn.* 82, 69–88.
- Mücke, T., Kleinhans, D., Peinke, J., 2011. Atmospheric turbulence and its influence on the alternating loads on wind turbines. *Wind Energy* 14, 301–316.
- Mueller, T.J., Pohlen, L.J., Conigliaro, P.E., Jansen, B.J., 1983. The influence of free-stream disturbances on low Reynolds number airfoil experiments. *Exp. Fluids* 1, 3–14.
- Mulvaney, K.K., Woodson, P., Prokopy, L.S., 2013. A tale of three counties: Understanding wind development in the rural Midwestern United States. *Energy Policy* 56, 322–330.
- Mydlarski, L., Warhaft, Z., 2006. On the onset of high-Reynolds-number grid-generated wind tunnel turbulence. *J. Fluid Mech.* 320, 331.
- Nakamura, Y., 1993. Bluff-body aerodynamics and turbulence. *J. Wind Eng. Ind. Aerodyn.* 49, 65–78.
- Nakamura, Y., Ohya, Y., Ozono, S., 1988. The effects of turbulence on bluff-body mean flow. *J. Wind Eng. Ind. Aerodyn.* 28, 251–259.
- Nedić, J., Vassilicos, J.C., 2015. Vortex Shedding and Aerodynamic Performance of Airfoil with Multiscale Trailing-Edge Modifications. *AIAA J.* 53, 3240–3250.
- Nicoud, F., Ducros, F., 1999. Subgrid-scale stress modelling based on the square of the velocity gradient tensor. *Flow, Turbul. Combust.* 62, 183–200.
- Norman, B., 2018. Are autonomous cities our urban future? *Nat. Commun.* 9, 2111.
- Norman, J., MacLean, H.L., Kennedy, C.A., 2006. Comparing High and Low Residential Density: Life-Cycle Analysis of Energy Use and Greenhouse Gas Emissions. *J. Urban Plan. Dev.* 132, 10–21.
- Ohya, Y., 2004. Drag of circular cylinders in the atmospheric turbulence. *Fluid Dyn. Res.* 34, 135–144.
- Oppenheim, D., Owen, C., White, G., 2004. Outside the square: Integrating wind into urban environments. *Refocus* 5, 32–35.
- Ozmen, Y., Baydar, E., van Beeck, J.P.A.J., 2016. Wind flow over the low-rise building models with gabled roofs having different pitch angles. *Build. Environ.* 95, 63–74.
- Pagnini, L.C., Burlando, M., Repetto, M.P., 2015. Experimental power curve of small-size wind turbines in turbulent urban environment. *Appl. Energy* 154, 112–121.
- Panofsky, H.A., Dutton, J.A., 1984. *Atmospheric turbulence: models and methods for engineering applications.* Wiley-Interscience.
- Patrino, L., Ricci, M., 2017. On the generation of synthetic divergence-free homogeneous anisotropic turbulence. *Comput. Methods Appl. Mech. Eng.* 315, 396–417.

References

- Peeringa, J., Brood, R., Ceyhan, O., 2015. Upwind 20 MW Wind Turbine Pre-Design. Wind Energy.
- Peter, J., 2019. How does climate change affect electricity system planning and optimal allocation of variable renewable energy? *Appl. Energy* 252, 113397.
- Peyrin, F., Kondjoyan, A., 2002. Effect of turbulent integral length scale on heat transfer around a circular cylinder placed cross to an air flow. *Exp. Therm. Fluid Sci.* 26, 455–460.
- Piomelli, U., 2008. Wall-layer models for large-eddy simulations. *Prog. Aerosp. Sci.* 44, 437–446.
- Piringer, M., Joffre, S., Baklanov, A., Christen, A., Deserti, M., De Ridder, K., Emeis, S., Mestayer, P., Tombrou, M., Middleton, D., Baumann-Stanzer, K., Dandou, A., Karppinen, A., Burzynski, J., 2007. The surface energy balance and the mixing height in urban areas - Activities and recommendations of COST-Action 715. *Boundary-Layer Meteorol.* 124, 3–24.
- Poletto, R., Craft, T., Revell, A., 2013. A New Divergence Free Synthetic Eddy Method for the Reproduction of Inlet Flow Conditions for LES. *Flow, Turbul. Combust.* 91, 519–539.
- Pope, S.B., 2000. *Turbulent Flows*, Cambridge University Press.
- Porté-Agel, F., Lu, H., Wu, Y., 2014. Interaction between Large Wind Farms and the Atmospheric Boundary Layer. *Procedia IUTAM* 10, 307–318.
- Raasch, S., Schröter, M., 2001. PALM - A large-eddy simulation model performing on massively parallel computers. *Meteorol. Zeitschrift* 10, 363–372.
- Rajasekar, U., Chakraborty, S., Bhat, G., 2018. *Climate Resilient Smart Cities: Opportunities for Innovative Solutions in India*. Springer, Cham, pp. 203–227.
- Rasmussen, F., Hansen, M.H., Thomsen, K., Larsen, T.J., Bertagnolio, F., Johansen, J., Madsen, H.A., Bak, C., Hansen, A.M., 2003. Present status of aeroelasticity of wind turbines. *Wind Energy* 6, 213–228.
- Resch, G., Liebmann, L., Geipel, J., Janeiro, L., Klessmann, C., Ragwitz, M., Held, A., del Rio, P., 2019. Assessment of Policy Pathways for Reaching the EU Target of (At Least) 27% Renewable Energies by 2030. In: *The European Dimension of Germany's Energy Transition*. Springer International Publishing, Cham, pp. 45–65.
- Rezaeiha, A., Kalkman, I., Blocken, B., 2017. Effect of pitch angle on power performance and aerodynamics of a vertical axis wind turbine. *Appl. Energy* 197, 132–150.
- Rezaeiha, A., Montazeri, H., Blocken, B., 2018. Towards optimal aerodynamic design of vertical axis wind turbines: Impact of solidity and number of blades. *Energy* 165, 1129–1148.
- Ricci, A., Kalkman, I., Blocken, B., Burlando, M., Freda, A., Repetto, M.P., 2018. Large-scale forcing effects on wind flows in the urban canopy: Impact of inflow conditions. *Sustain. Cities Soc.* 42, 593–610.
- Roach, P.E., 1987. The generation of nearly isotropic turbulence by means of grids. *Int. J. Heat Fluid Flow* 8, 82–92.
- Roshko, A., 1955. On the Wake and Drag of Bluff Bodies, *Journal of the Aeronautical Sciences*. Institute of the Aeronautical Sciences.
- Roshko, A., 1993. Perspectives on bluff body aerodynamics. *J. Wind Eng. Ind. Aerodyn.* 49, 79–100.
- Roth, M., 2000. Review of atmospheric turbulence over cities. *Q. J. R. Meteorol. Soc.* 126, 941–990.
- Saarinén, P., Koskela, H., Siikonen, T., 2016. An easy-to-use turbulent inlet boundary condition for large-eddy simulation of radial diffusers. *Build. Simul.* 9, 569–581.
- Saathoff, P.J., Melbourne, W.H., 1987. Freestream turbulence and wind tunnel blockage effects on streamwise

- surface pressures. *J. Wind Eng. Ind. Aerodyn.* 26, 353–370.
- Saathoff, P.J., Melbourne, W.H., 1997. Effects of free-stream turbulence on surface pressure fluctuations in a separation bubble. *J. Fluid Mech.* 337, S0022112096004594.
- Sagaut, P., 2006. *Large eddy simulation for incompressible flows : an introduction*. Springer-Verlag.
- Samu, R., Fahrioglu, M., Ozansoy, C., 2019. The potential and economic viability of wind farms in Zimbabwe. *Int. J. Green Energy* 1–8.
- Sareen, A., Sapre, C.A., Selig, M.S., 2012. Effects of Leading-Edge Protection Tape on Wind Turbine Blade Performance. *Wind Eng.* 36, 525–534.
- Šarkić Glumac, A., Hemida, H., Höffer, R., 2018. Wind energy potential above a high-rise building influenced by neighboring buildings: An experimental investigation. *J. Wind Eng. Ind. Aerodyn.* 175, 32–42.
- Sasaki, K., Kiya, M., 1983. Free-stream turbulence effects on a separation bubble. *J. Wind Eng. Ind. Aerodyn.* 14, 375–386.
- Sasaki, K., Kiya, M., 1985. Effect of Free-Stream Turbulence on Turbulent Properties of a Separation-Reattachment Flow. *Bull. JSME* 28, 610–616.
- Schlichting, H., Gersten, K., 2000. *Boundary Layer Theory*. Springer-Verlag, Berlin, Heidelberg.
- Seddighi, M., Soltani, M., 2007. The Influence of Free Stream Turbulence Intensity on the Unsteady Behavior of a Wind Turbine Blade Section. In: 45th AIAA Aerospace Sciences Meeting and Exhibit. American Institute of Aeronautics and Astronautics, Reston, Virginia.
- Seoud, R.E., Vassilicos, J.C., 2007. Dissipation and decay of fractal-generated turbulence. *Phys. Fluids* 19, 105108.
- Seto, K.C., Dhakal, S., Bigio, A., Blanco, H., Delgado, G.C., Dewar, D., Huang, L., Inaba, A., Kansal, A., Lwasa, S., McMahon, J.E., Müller, D.B., Murakami, J., Nagendra, H., Ramaswami, A., 2014. Human Settlements, Infrastructure and Spatial Planning. In: Edenhofer, O., Pichs-Madruga, R., Sokona, Y., Farahani, E., Kadner, S., Seyboth, K., Adler, A., Baum, I., Brunner, S., Eickemeier, P., Kriemann, B., Savolainen, J., Schlömer, S., von Stechow, C., Zwickel, T., Minx, J.C. (Eds.), *Climate Change 2014: Mitigation of Climate Change. Contribution of Working Group III to the Fifth Assessment Report of the Intergovernmental Panel on Climate Change*. Cambridge University Press, Cambridge, United Kingdom and New York, NY, USA, pp. 1–78.
- Sheikh, N.J., Kocaoglu, D.F., Lutzenhiser, L., 2016. Social and political impacts of renewable energy: Literature review. *Technol. Forecast. Soc. Change* 108, 102–110.
- Shen, L., Han, Y., Cai, C.S., Dong, G., Zhang, J., Hu, P., 2017. LES of wind environments in urban residential areas based on an inflow turbulence generating approach. *Wind Struct.* 24, 1–24.
- Shur, M.L., Spalart, P.R., Strelets, M.K., Travin, A.K., 2008. A hybrid RANS-LES approach with delayed-DES and wall-modelled LES capabilities. *Int. J. Heat Fluid Flow* 29, 1638–1649.
- Sicot, C., Aubrun, S., Loyer, S., Devinant, P., 2006a. Unsteady characteristics of the static stall of an airfoil subjected to freestream turbulence level up to 16%. *Exp. Fluids* 41, 641–648.
- Sicot, C., Devinant, P., Laverne, T., Loyer, S., Hureau, J., 2006b. Experimental study of the effect of turbulence on horizontal axis wind turbine aerodynamics. *Wind Energy* 9, 361–370.
- Sicot, C., Devinant, P., Loyer, S., Hureau, J., 2008. Rotational and turbulence effects on a wind turbine blade. Investigation of the stall mechanisms. *J. Wind Eng. Ind. Aerodyn.* 96, 1320–1331.

References

- Sieros, G., Chaviaropoulos, P., Sørensen, J.D., Bulder, B.H., Jamieson, P., 2012. Upscaling wind turbines: theoretical and practical aspects and their impact on the cost of energy. *Wind Energy* 15, 3–17.
- Simiu, E., Scanlan, R.H., 1986. *Wind Effects on Structures: An Introduction to Wind Engineering*, Wiley. ed. New York.
- Simmons, L.F.G., Salter, C., 1934. Experimental Investigation and Analysis of the Velocity Variations in Turbulent Flow. *Proc. R. Soc. London A Math. Phys. Eng. Sci.* 145.
- Simões, T., Estanqueiro, A., 2016. A new methodology for urban wind resource assessment. *Renew. Energy* 89, 598–605.
- Smirnov, A., Shi, S., Celik, I., 2001. Random Flow Generation Technique for Large Eddy Simulations and Particle-Dynamics Modeling. *J. Fluids Eng.* 123, 359.
- Snel, H., 2003. Review of aerodynamics for wind turbines. *Wind Energy* 6, 203–211.
- Sørensen, J.N., 2011. Aerodynamic Aspects of Wind Energy Conversion. *Annu. Rev. Fluid Mech.* 43, 427–448.
- Sørensen, J.N., Shen, W.Z., 2002. Numerical Modeling of Wind Turbine Wakes. *J. Fluids Eng.* 124, 393.
- Spalart, P.R., 2009. Detached-Eddy Simulation. *Annu. Rev. Fluid Mech.* 41, 181–202.
- Sreenivasan, K.R., 1995. On the universality of the Kolmogorov constant. *Phys. Fluids* 7, 2778–2784.
- St Martin, C.M., Lundquist, J.K., Clifton, A., Poulos, G.S., Schreck, S.J., 2016. Wind turbine power production and annual energy production depend on atmospheric stability and turbulence.
- Stainback, P.C., Nagabushana, K.A., 1993. Review of hot-wire anemometry techniques and the range of their applicability for various flows. *J. Fluids Eng.* 1, 1–54.
- Stankovic, S., Campbell, N., Harries, A., 2009. *Urban Wind Energy*. Earthscan.
- Stathopoulos, T., 2002. The numerical wind tunnel for industrial aerodynamics: Real or virtual in the new millennium? *Wind Struct.* 5, 193–208.
- Stathopoulos, T., 2006. Pedestrian level winds and outdoor human comfort. *J. Wind Eng. Ind. Aerodyn.* 94, 769–780.
- Stathopoulos, T., Alrawashdeh, H., 2019. *Urban Wind Energy: A Wind Engineering and Wind Energy Cross-Roads*. Springer, Cham, pp. 3–16.
- Stathopoulos, T., Alrawashdeh, H., Al-Quraan, A., Blocken, B., Dilimulati, A., Paraschivoiu, M., Pilay, P., 2018. Urban wind energy: Some views on potential and challenges. *J. Wind Eng. Ind. Aerodyn.* 179, 146–157.
- Stathopoulos, T., Wu, H., Bédard, C., 1992. Wind environment around buildings: A knowledge-based approach. *J. Wind Eng. Ind. Aerodyn.* 44, 2377–2388.
- Stensgaard Toft, H., Svenningsen, L., Moser, W., Dalsgaard Sørensen, J., Lybech Thøgersen, M., 2016. Wind Climate Parameters for Wind Turbine Fatigue Load Assessment. *J. Sol. Energy Eng.* 138, 031010.
- Stork, C.H.J., Butterfield, C.P., Holley, W., Madsen, P.H., Jensen, P.H., 1998. Wind conditions for wind turbine design proposals for revision of the IEC 1400-1 standard. *J. Wind Eng. Ind. Aerodyn.* 74–76, 443–454.
- Stratford, B.S., 1959. The prediction of separation of the turbulent boundary layer. *J. Fluid Mech.* 5, 1.
- Stull, R.B., 1988. *An Introduction to Boundary Layer Meteorology*, Springer Netherlands.
- Subramanian, B., Chokani, N., Abhari, R.S., 2016. Aerodynamics of wind turbine wakes in flat and complex terrains. *Renew. Energy* 85, 454–463.
- Sunderland, K., Woolmington, T., Blackledge, J., Conlon, M., 2013. Small wind turbines in turbulent (urban) environments: A consideration of normal and Weibull distributions for power prediction. *J. Wind Eng. Ind.*

References

- Aerodyn. 121, 70–81.
- Suryadi, A., Herr, M., 2015. Wall Pressure Spectra on a DU96-W-180 Profile From Low to Pre-Stall Angles of Attack. In: 21st AIAA/CEAS Aeroacoustics Conference. American Institute of Aeronautics and Astronautics, Reston, Virginia.
- Swalwell, K., Sheridan, J., 2001. The effect of turbulence intensity on stall of the NACA 0021 aerofoil. 14th Australas.
- Swalwell, K., Sheridan, J., Melbourne, W., 2004. The effect of turbulence intensity on performance of a NACA 4421 airfoil section. 42nd AIAA Aerosp.
- Tabor, G.R., Baba-Ahmadi, M.H., 2010. Inlet conditions for large eddy simulation: A review. *Comput. Fluids* 39, 553–567.
- Tabrizi, A.B., Whale, J., Lyons, T., Urmee, T., 2014. Performance and safety of rooftop wind turbines: Use of CFD to gain insight into inflow conditions. *Renew. Energy* 67, 242–251.
- Tabrizi, A.B., Whale, J., Lyons, T., Urmee, T., 2015. Extent to which international wind turbine design standard, IEC61400-2 is valid for a rooftop wind installation. *J. Wind Eng. Ind. Aerodyn.* 139, 50–61.
- Tadie Fogaing, M.B., Gordon, H., Lange, C.F., Wood, D.H., Fleck, B.A., 2019. A Review of Wind Energy Resource Assessment in the Urban Environment. Springer, Cham, pp. 7–36.
- Tamura, T., 2008. Towards practical use of LES in wind engineering. *J. Wind Eng. Ind. Aerodyn.* 96, 1451–1471.
- Tamura, Y., Suganuma, S., Kikuchi, H., Hibi, K., 1999. Proper orthogonal decomposition of random wind pressure field. *J. Fluids Struct.* 13, 1069–1095.
- Tangler, J., 2002. The nebulous art of using wind-tunnel airfoil data for predicting rotor performance. ASME 2002 Wind Energy
- Tangler, J.L., 2004. Insight into wind turbine stall and post-stall aerodynamics. *Wind Energy* 7, 247–260.
- Tanner, M., Harpham, T., 2014. Urban health in developing countries: progress and prospects.
- Taylor, G.I., 1935. Statistical Theory of Turbulence. *Proc. R. Soc. London A Math. Phys. Eng. Sci.* 151.
- Thomsen, K., Sørensen, P., 1999. Fatigue loads for wind turbines operating in wakes. *J. Wind Eng. Ind. Aerodyn.* 80, 121–136.
- Timmer, W.A., 2010. Aerodynamic characteristics of wind turbine blade airfoils at high angles-of-attack. In: TORQUE 2010: The Science of Making Torque from Wind. pp. 71–78.
- Timmer, W.A., van Rooij, R.P.J.O.M., 2003. Summary of the Delft University Wind Turbine Dedicated Airfoils. In: ASME 2003 Wind Energy Symposium. ASME, pp. 11–21.
- Toft, H.S., Svenningsen, L., Sørensen, J.D., Moser, W., Thøgersen, M.L., 2016. Uncertainty in wind climate parameters and their influence on wind turbine fatigue loads. *Renew. Energy* 90, 352–361.
- Toja-Silva, F., Kono, T., Peralta, C., Lopez-Garcia, O., Chen, J., 2018. A review of computational fluid dynamics (CFD) simulations of the wind flow around buildings for urban wind energy exploitation. *J. Wind Eng. Ind. Aerodyn.* 180, 66–87.
- Toja-Silva, F., Peralta, C., Lopez-Garcia, O., Navarro, J., Cruz, I., 2015a. Roof region dependent wind potential assessment with different RANS turbulence models. *Jnl. Wind Eng. Ind. Aerodyn.* 142.
- Toja-Silva, F., Peralta, C., Lopez-Garcia, O., Navarro, J., Cruz, I., 2015b. On Roof Geometry for Urban Wind Energy Exploitation in High-Rise Buildings. *Computation* 3, 299–325.
- Tolias, I.C., Koutsourakis, N., Hertwig, D., Efthimiou, G.C., Venetsanos, A.G., Bartzis, J.G., 2018. Large Eddy

- Simulation study on the structure of turbulent flow in a complex city. *J. Wind Eng. Ind. Aerodyn.* 177, 101–116.
- Tominaga, Y., Mochida, A., Shirasawa, T., Yoshie, R., Kataoka, H., Harimoto, K., Nozu, T., 2004. Cross Comparisons of CFD Results of Wind Environment at Pedestrian Level around a High-rise Building and within a Building Complex. *J. Asian Archit. Build. Eng.* 3, 63–70.
- Toparlar, Y., Blocken, B., Maiheu, B., van Heijst, G.J.F., 2017. A review on the CFD analysis of urban microclimate. *Renew. Sustain. Energy Rev.* 80, 1613–1640.
- Tsang, C.W., Kwok, K.C.S., Hitchcock, P.A., 2012. Wind tunnel study of pedestrian level wind environment around tall buildings: Effects of building dimensions, separation and podium. *Build. Environ.* 49, 167–181.
- Tummala, A., Velamati, R.K., Sinha, D.K., Indrajha, V., Krishna, V.H., 2016. A review on small scale wind turbines. *Renew. Sustain. Energy Rev.* 56, 1351–1371.
- Uberoi, M.S., 1956. Effect of Wind-Tunnel Contraction on Free-Stream Turbulence. *J. Aeronaut. Sci.* 23, 754–764.
- United Nations - Department of Economic and Social Affairs - Population Division, 2019. *World Urbanization Prospects: The 2018 Revision*. New York: United Nations.
- van Kuik, G., Ummels, B., Hendriks, R., 2006. Perspectives of Wind Energy 23–25.
- van Kuik, G.A.M., Peinke, J., Nijssen, R., Lekou, D., Mann, J., Sørensen, J.N., Ferreira, C., van Wingerden, J.W., Schlipf, D., Gebraad, P., Polinder, H., Abrahamsen, A., van Bussel, G.J.W., Sørensen, J.D., Tavner, P., Bottasso, C.L., Muskulus, M., Matha, D., Lindeboom, H.J., Degraer, S., Kramer, O., Lehnhoff, S., Sonnenschein, M., Sørensen, P.E., Künneke, R.W., Morthorst, P.E., Skytte, K., 2016. Long-term research challenges in wind energy – a research agenda by the European Academy of Wind Energy. *Wind Energy Sci.* 1, 1–39.
- Vasaturo, R., Kalkman, I., Blocken, B.J.E., van Wesemael, P.J.V.J.V., 2018. Large eddy simulation of the neutral atmospheric boundary layer: performance evaluation of three inflow methods for terrains with different roughness. *J. Wind Eng. Ind. Aerodyn.* 173, 241–261.
- Vermeer, L.J., Sørensen, J.N., Crespo, A., 2003. Wind turbine wake aerodynamics. *Prog. Aerosp. Sci.* 39, 467–510.
- Vickery, B.J., 1966. Fluctuating lift and drag on a long cylinder of square cross-section in a smooth and in a turbulent stream. *J. Fluid Mech.* 25, 481.
- Vita, G., Hemida, H., Andrienne, T., Baniotopoulos, C., 2018a. Generating atmospheric turbulence using passive grids in an expansion test section of a wind tunnel. *J. Wind Eng. Ind. Aerodyn.* 178, 91–104.
- Vita, G., Hemida, H., Baniotopoulos, C.C., 2016. Effect of atmospheric turbulence on the aerodynamics of wind turbine blades: a review. In: *Proceedings of the 1st WinerCost International Conference*, Ankara, TR.
- Vita, G., Hemida, H., Baniotopoulos, C.C., 2017a. On the influence of the shape of buildings in urban wind energy harvesting. In: *7th European and African Conference on Wind Engineering, EACWE 2017*.
- Vita, G., Hemida, H., Baniotopoulos, C.C., 2017b. Improving Sustainability and Resilience of Future Cities. Positioning of Wind Turbines within the Urban Environment. In: *CESARE'17 Conference*, 3-8.05.17, Dead Sea, JO. Dead Sea, JO.
- Vita, G., Hemida, H., Chaudhari, A., Baniotopoulos, C.C., 2018b. Turbulent inlet boundary conditions for large eddy simulation: an urban wind energy test-case. In: *2nd International WINERCOST and Aeolus4Future*

- Conference, WINERCOST'18, 21-23.03.18, Catanzaro, IT. Catanzaro, IT.
- Walker, S.L., 2011. Building mounted wind turbines and their suitability for the urban scale—A review of methods of estimating urban wind resource. *Energy Build.* 43, 1852–1862.
- Walsh, C., Pineda, I., 2019. Wind energy in Europe in 2018. Trends and statistics.
- Wang, S., Zhou, Y., Alam, M.M., Yang, H., 2014. Turbulent intensity and Reynolds number effects on an airfoil at low Reynolds numbers. *Phys. Fluids* 26, 115107.
- Wang, W., Xu, Y., Ng, E., 2018. Large-eddy simulations of pedestrian-level ventilation for assessing a satellite-based approach to urban geometry generation. *Graph. Models* 95, 29–41.
- Wendling, L.A., Huovila, A., zu Castell-Rüdenhausen, M., Hukkalainen, M., Airaksinen, M., 2018. Benchmarking Nature-Based Solution and Smart City Assessment Schemes Against the Sustainable Development Goal Indicator Framework. *Front. Environ. Sci.* 6, 69.
- Wilczek, M., Daitche, A., Friedrich, R., 2011. On the velocity distribution in homogeneous isotropic turbulence: correlations and deviations from Gaussianity. *J. Fluid Mech.* 676, 191–217.
- Wu, H., Stathopoulos, T., 1993. Wind-Tunnel Techniques for Assessment of Pedestrian-Level Winds. *J. Eng. Mech.* 119, 1920–1936.
- Wu, Y.-T., Porté-Agel, F., 2012. Atmospheric Turbulence Effects on Wind-Turbine Wakes: An LES Study. *Energies* 5, 5340–5362.
- XING, T., 2015. A general framework for verification and validation of large eddy simulations. *J. Hydrodyn. Ser. B* 27, 163–175.
- Yoshie, R., Mochida, A., Tominaga, Y., Kataoka, H., Harimoto, K., Nozu, T., Shirasawa, T., 2007. Cooperative project for CFD prediction of pedestrian wind environment in the Architectural Institute of Japan. *J. Wind Eng. Ind. Aerodyn.* 95, 1551–1578.
- Younis, N., Ting, D.S.K., 2012. The subtle effect of integral scale on the drag of a circular cylinder in turbulent cross flow. *Wind Struct.* 15, 463–480.
- Zdravkovich, M.M., 1997. *Flow Around Circular Cylinders, Flow around circular cylinders.*
- Zhang, X., Tse, K.T., Weerasuriya, A.U., Kwok, K.C.S., Niu, J., Lin, Z., Mak, C.M., 2018. Pedestrian-level wind conditions in the space underneath lift-up buildings. *J. Wind Eng. Ind. Aerodyn.* 179, 58–69.
- Zhao, H., Magoulès, F., 2012. A review on the prediction of building energy consumption. *Renew. Sustain. Energy Rev.* 16, 3586–3592.
- Zhiyin, Y., 2015. Large-eddy simulation: Past, present and the future. *Chinese J. Aeronaut.* 28, 11–24.